Thermodynamics and Kinetics of Ceramic/Metal Interfacial Interactions

by

Raymundo Arróyave

B.S., Instituto Tecnológico y de Estudios Superiores de Monterrey (1996)
S.M., Massachusetts Institute of Technology (2000)

Submitted to the Department of Materials Science and Engineering
in partial fulfillment of the requirements for the degree of

Doctor of Philosophy in Materials Science

at the

MASSACHUSETTS INSTITUTE OF TECHNOLOGY

February 2004

Author .....
Department of Materials Science and Engineering
November 25, 2003

Certified by .....
Thomas W. Eagar
Thomas Lord Professor of Materials Engineering and Engineering Systems
Thesis Supervisor

Accepted by .....
Harry S. Tuller
Professor of Ceramics and Electronic Materials
Chairman, Department Committee on Graduate Students

Thermodynamics and Kinetics of Ceramic/Metal Interfacial Interactions

by

Raymundo Arróyave

Submitted to the Department of Materials Science and Engineering
on November 25, 2003, in partial fulfillment of the
requirements for the degree of
Doctor of Philosophy in Materials Science

Abstract

Ceramic/metal interfaces occur in a great number of important applications, such as ceramic/metal composites, microelectronics packaging, ceramic/metal seals, and so forth. Understanding the formation and evolution of such interfaces is therefore essential for the better design and optimization of these technologies.

In this thesis, a methodology for the study of the thermochemical interactions at ceramic/metal interfaces, during both their formation and evolution, is proposed. Because of the importance of zirconia-based ceramics in increasingly important applications such as structural composites, thermal barrier coatings and Solid Oxide Fuel Cells, it was decided to illustrate the concepts developed in this thesis through the study of the interactions between zirconias and active metals.

Semi-empirical thermodynamic models of all the phases likely to take part in the ceramic/metal interfacial interactions studied were developed. Phase diagram data and thermochemical information were critically assessed and use to adjust the thermodynamic parameters that allowed the description of the Ag-Cu-Ti, Cu-Ti-Zr, Ti-Zr-O, Cu-Ti-O and Cu-Zr-O systems.

The thermodynamic models were used to predict the diffusion paths across zirconia/active metal interfaces through metastable phase diagrams calculations. Additionally, equilibrium calculations of activity diagrams were used to understand the complex interfacial reactions occurring during the active metal brazing of zirconia-based ceramics. By using simple one-dimensional inter-diffusion simulations, it was demonstrated that the base metal in ceramic/metal joints plays an essential role in determine the thermochemical interactions at the ceramic/metal interface during ceramic/metal joining operations. In general it was found that, using all these techniques, it was possible to explain diffusion paths and reaction sequences observed in a great number of zirconia/active-metal systems, both in the solid and in the liquid states.

In many cases, the morphology of the reaction layers formed at ceramic/metal interfaces determine their final properties. To address this problem, empirical ther-

modynamic models of the likely reaction products at zirconia/metal interfaces were coupled to kinetic models using the diffuse-interface formalism to successfully describe the formation and evolution of complex ceramic/metal interfacial structures.

Thesis Supervisor: Thomas W. Eagar
Title: Thomas Lord Professor of Materials Engineering and Engineering Systems

Acknowledgments

This thesis is dedicated to my parents, Graciela and Raymundo Arróyave. I could not have come all the way to this stage in my academic life if it not were because of their encouragement, support and love, Gracias Papás!.

First of all, I would like to thank my advisor, Prof. Thomas W. Eagar. I cannot think of any other advisor from whom I could have learned as much as I did. He was not only available when I needed counsel regarding the direction of my research, but he was also there when I needed career and even personal advise. I deeply admire the respect that he has for all his students, and for the fact that, for him, our personal well-being is as important (or even more important, indeed) as our performance as researchers. He is a great human being, and I hope that I not only learned from his vast knowledge in the field of Materials Science but also from his even greater knowledge of life and human character. I don't know if this happens very often at MIT, but Prof. Eagar took the risk of giving me freedom to pursue the research path that best fitted my interests and goals and for that I'm deeply thankful. I hope that this work is up to his expectations.

I would also like to thank the other members of my committee. I thank Dr. Larry Kaufman for all the help that he gave me when I was starting to explore thermodynamic modeling as a possible way to approach the problem of ceramic/metal interactions. I consider myself very fortunate to have had the opportunity to interact with one of the pioneers in the field of computational thermodynamics, but I consider my self even more fortunate and honored for his friendship. I would also like to thank one of the great ones in Thermodynamics of Materials, Prof. Claude Lupis. I've read his book I don't know how many times, and I still learn new concepts every time I read it. More important than his vast knowledge is the fact that he is, without a doubt, one of the finest persons that I met at MIT. I would also like to thank Prof. Carter. I had the opportunity of being his TA for 3.00 and it was there that I learned how important it is to enjoy the subject (Thermodynamics) that you teach. All I have left to say is that it has been a great honor to have all these great material scientists and more important, persons, as members of my committee.

I could not have done this without the help and support from all the members of the Welding and Joining Group. I would like to thank Don Galler for all the advise and help he provided while seting up my experimental apparatus. I thank Jeri for all her patience and for all the interesting conversations about movies that we had while waiting for my meetings with Tom. I would like to thank Chris Musso for his friendship and all his help in designing my experimental aparatus, and also for all the great discussions (sometimes a tad heated, but always respectful) about so many topics. Neil: you are a weird guy...just kidding, it was great to meet you and is an honor to be considered your friend. Joel: thank you for all the drawings and all your help with my experiments. I would also like to thank Harold for all his help and support. Finally, I would like to thank my old labmates Mike, Burke, Patricio,

Jocelyn and Jin-Woo, for their friendship and help.

Life at MIT can be sometimes a little bit rough (no sarcasm here). To keep sanity, everyone must have his/her support group of equally stressed out, depressed, confused, students. I was very fortunate to have met so many smart and great people in my particular support group. I thank my friend, cousin, former roommate and even former labmate Chorro for his help and support during my first years here at MIT. Jorge Carretero: we've been through regular, bad, and even worse times. Thanks for your friendship. I would also like to thank Jorge Feuchtwanger, not only a good friend, but also one of the few persons that did not have to read this thesis, and despite this, he read it and gave me valuable advise! I also thank my favorite roommie, Gina, for her friendship and support. I thank the rest of the Mexican Gang: Ante, Juan Gonzalez, Ulises, Oso, Antonio, Nuria, Lula. I want to thank especially Kate Baty, who is an angel that worked uder the cover of Director of The Host Families Program for International Students at MIT. She adopted me in the great and numerous Baty Family and gave me something that is always missed: the feeling of being home. Finally, I would also like to thank Gerardo Trápaga, who, during my first two years at MIT provided me with invaluable advise and more importantly, with his frienship.

Back in Monterrey Mexico, there are many people that I want to thank. First of all, I thank my Mom and Dad for their unconditional love and support. I also thank Grace and Jorge for being the coolest sister and brother one can have. Bere: I love you and I thank you for being so supportive during the past couple of long, crazy months. I deeply thank my Aunt Nene, since it was thanks to her that I had financial support during my undergraduate years at ITESM. Without her support, I might not have been able to come here. Abuelita: thanks for all your prayers and your love. I thank all my uncles, aunts, cousins, nephews and nieces back in Monterrey for their moral support. I thank also all my friends in Monterrey. They have helped me keep my feet on the ground. To them I'm only Ray, and I hope that I will always remain that way.

Contents

List of Figures

List of Tables

Nomenclature

${}^{id}G_m^{\phi}$ Ideal mixing contribution to the total Gibbs energy of phase ϕ, . Units: $\frac{J}{mol}$, see equation (A.4), page 177

${}^{xs}G_m^{\phi}$ Excess contribution to the total Gibbs energy of phase ϕ. Units: $\frac{J}{mol}$, see equation (A.4), page 177

$(A,B)_i\,(C,D)_j$ Sublattice notation. Phase with two sublattices with i and j sites in each sublattice. Elements A, B in first sublattice, while C, D are in second sublattice. , see equation (3.0), page 24

$\underline{A}$ Solute A dissolved in solvent , see equation (2.5), page 7

a_A Chemical activity of element A , see equation (2.6), page 7

A_j Partial quantity from molar quantity A_m , see equation (A.21), page 183

C_j Molar concentration. Units: $\frac{mol}{m^3}$, see equation (6.2), page 123

D_{kj}^n Diffusion coefficient in the $(n-1)$ by $(n-1)$ diffusion matrix. Units: $\frac{m^2}{s}$, see equation (6.2), page 123

$e^{'}$ Electron.

e_i^j Interaction coefficient of j over i in solvent M, on a weight percent basis , see equation (4.8), page 57

E_g Bandgap Energy, eV , see equation (2.15), page 13

F Free energy of system , see equation (7.4), page 142

G^{ϕ} Gibbs free energy of phase ϕ , see equation (A.1)

G_{ij}^{ϕ} Gibbs free energy of compound ij in crystalline structure ϕ. Units: $\frac{J}{mol}$, see equation (A.3), page 177

$GHSER_i$ Gibbs energy with respect to enthalpy of standard element reference state (SER). Units $\frac{J}{mol}$, see equation (A.3), page 177

h Computational grid spacing.

I_i First ionization potential , see equation (2.14), page 11

J_k Mass flux. Units: $\frac{mol}{m^2\,s}$, see equation (6.2), page 123

k Gradient energy coefficient , see equation (7.10), page 144

$K_D\,(T)$ Equilibrium constant for oxide dissolution reaction , see equation (2.6), page 7

K_{eq} Equilibrium constant , see equation (3.2), page 28

$L^{\phi}_{A:C,D}$ Interaction parameter between C and D in second sublattice of phase ϕ when A is present in second sublattice ., see equation (A.17), page 182

$L^{\phi}_{i,j,k}$ The ternary interaction parameter between elements i, j, k in substitutional phase ϕ , see equation (3.4), page 34

L_{ij} Regular solution interaction parameter between components i and j. Units: $\frac{J}{mol}$, see equation (A.6), page 178

M_i Molecular weight of element i.

n_h Hole concentration in valence band , see equation (2.15), page 13

n_h^0 Constant.

O_O^X Oxygen in oxygen site , see equation (5.0), page 77

$P_{I0}\,(Y)$ Zeroth-order product of site fractions ., see equation (A.15), page 181

p_{O_2} Oxygen partial pressure , see equation (3.2), page 28

R Universal gas constant. $R = 8.314\,\frac{J}{mol\,K}$

r Interatomic distance at ceramic/metal interface , see equation (2.14), page 11

T Temperature, K

t Time.

v_ξ Velocity of interface ξ. Units: m/s , see equation (6.3), page 123

$V_O^{\bullet\bullet}$ Oxygen vacancy , see equation (5.0), page 77

Va Vacancy.

W_{ad} Work of adhesion. Units: J/m^2 , see equation (2.2), page 6

x_i Mole fraction of component i.

x_O^D Molar fraction of oxygen dissolved in the melt when oxide A_mO_n is in equilibrium with it , see equation (2.9), page 8

x_O^P Molar fraction of oxygen in melt when it is at equilibrium with reaction product , see equation (2.13), page 10

$y_i^n 1$ Site fraction of element i in sublattice n ., see equation (A.12), page 181

${}^0G^{\phi}_{(i)_1(j)_1}$ Gibbs free energy of the reference compound ij in the crystal structure ϕ ., see equation (A.14), page 181

α_i Polarizability of element i , see equation (2.14), page 11

$\Delta^0 G_f^{\phi}$ Gibbs free energy of formation for phase ϕ

ΔG_f^{Int} Gibbs free energy for interface formation , see equation (2.1), page 6

$\Delta^0 G_f^{A_m O_n}$ Gibbs free energy of formation of $A_m O_n$ oxide. Units: J/mol , see equation (2.6), page 7

$\Delta^0 H_f^{MO}$ Enthalpy of formation of MO oxide , see equation (2.14), page 11

δ Interface thickness , see equation (7.18), page 150

ϵ_i^j Wagner first order interaction coefficient between element i and element j dissolved in solvent M.

γ_i Chemical activity coefficient for element i.

γ_i^{∞} Chemical activity coefficient for element i at infinite dilution.

${}^0\Delta H^{\phi}_{ij,f}$ Standard enthalpy of formation of compound ij. Units: $\frac{J}{mol}$, see equation (A.3), page 177

$\mu(i)$ Chemical potential of element i.

Ω Molar volume , see equation (7.4), page 142

${}^0\Delta S^{\phi}_{ij,f}$ Standard entropy of formation of compound ij. Units: $\frac{J}{mol \cdot K}$, see equation (A.3), page 177

σ Surface energy. Units: $\frac{J}{m^2}$, see equation (7.8), page 143

σ_{LV} Surface energy of liquid/vapor interface. Units: J/m^2 , see equation (2.1), page 6

σ_{SL} Solid/liquid interfacial energy. Units: J/m^2 , see equation (2.1), page 6

σ_{SV} Surface energy of solid/vapor interface. Units: J/m^2 , see equation (2.1), page 6

θ Contact angle, in degrees , see equation (2.3), page 6

$K_P(T)$ Equilibrium constant for precipitation , see equation (2.12), page 10

Chapter 1

Introduction

A wide range of ceramic/metal interfaces occurs naturally. In general, thin oxide layers cover the surfaces of most metals under normal conditions. This metal/oxide system constitutes an excellent example of a typical ceramic/metal C/M interface. This work, however, is concerned with synthetic interfaces created during ceramic/metal joining, coating processes and so on. Understanding of the thermo-kinetic phenomena occurring at ceramic metal interfaces comprises three different levels:

i Thermodynamic interactions between the different phases present in the system. This implies the determination of the driving forces for any further interfacial interaction, such as dissolution, diffusion, precipitation of reaction products, etc.

ii Once the thermodynamic driving forces have been determined, it is possible to analyze the kinetic processes occurring at C/M interfaces, such as charge and/or mass transfer.

iii Determination/prediction of the microstructural evolution of the interfaces when subjected to arbitrary thermo-mechanical and chemical conditions.

These three hierarchical levels of analysis warrant varying degrees of complexity, depending on the number of elements and phases involved, stoichiometry of the ceramic and possible reaction products, nature of transport mechanisms across interfaces, moving boundaries, morphological instabilities, and so forth.

In this work, a methodology for the study of the thermochemical interactions at ceramic/metal interfaces is proposed. In order to illustrate the concepts developed in this thesis, the nature of the interfacial interactions between zirconia-based ceramics and active metals was selected. The selection of zirconia/active metal interfaces was based on the importance of these ceramic/metal systems in established and emerging technologies, such as solid oxide fuel cells, thermal barrier coatings for turbine blades, biomedical materials, structural ceramic/metal composites, etc.

Through the use of thermodynamic models based on the *CALPHAD* formalism it will be shown that it is possible to perform metastable thermodynamic calculations that allow the prediction of diffusion paths across zirconia/active-metal interfaces. Additionally, equilibrium calculations of activity diagrams will be applied to the understanding of the complex interfacial reactions occurring during active metal brazing of zirconia-based ceramics. By using simple inter-diffusion simulations, it will be demonstrated that the base metal in ceramic/metal joints may play an essential role in determining the thermochemical interactions at the ceramic/metal interface. In many cases, the morphology of the reaction layers formed at ceramic/metal interfaces determines the final properties. Thermodynamic calculations and one-dimensional diffusion simulations are incapable of describing the morphological evolution of these interfaces. In this thesis, it will be demonstrated that thermodynamic models of the likely reaction products at zirconia/metal interfaces can be coupled to kinetic models using the diffuse-interface formalism to describe the formation and evolution of complex ceramic/metal interfacial structures.

The organization of this work is as follows:

In Chapter 2, the main physico-chemical aspects of *C/M* interfaces are discussed. A review of the most relevant work on the nature and characteristics of *C/M* interfaces is presented. Subsequently, the implications of these theories on the problem at hand: the creation of synthetic *C/M* interfaces is discussed.

Although ceramic/metal interfaces have been experimentally investigated for several decades, thermodynamic models to describe even the most simple systems are still lacking. For the problem at hand, it was found that there were no thermodynamic assessments for many of the systems that were needed to achieve a complete thermodynamic description of the system under study.

Despite the widespread use of $Ag-Cu-Ti$ alloys in ceramic/brazing applications, no thermodynamic assessment for this system has been published before. In Chapter 3, the thermodynamic model for this system is presented and the available experimental information is critically assessed. In addition to the $Ag-Cu-Ti$ system, active brazes based on amorphous $Cu-Ti-Zr$ alloys are becoming important in ceramic/metal brazing applications, mainly due to the higher operating temperature of this system. Chapter 3 presents a thermodynamic assessment for this system.

Despite the fact that it has been used commercially for several decades, there has been very limited thermodynamic investigations of the $Zr-O$ system, from the *CALPHAD* point of view. In Chapter 4 a thermodynamic assessment for this system is presented. Additionally, a previously developed thermodynamic model for the $Cu-Ti-O$ system is refined. In Chapter 4, a thermodynamic description for the $Ti-Zr-O$ system is also developed. These last systems are of fundamental importance for the understanding of zirconia/active-metal interactions. Finally, a critical assessment of the scarce thermochemical data for the $Cu-O-Zr$ is presented.

In Chapter 5, the thermodynamic models developed in Chapter 3 and Chapter 4 are used to describe the complex reaction sequences observed in experiments on ceramic/metal interactions. In the case of ZrO_2/Ti interactions, metastable thermodynamic calculations are used to determine the likely diffusion paths in both solid/solid and solid/liquid interfacial processes. Activity diagrams calculated based on the model for the $Cu-Ti-O$ system are used to understand the interfacial structure resulting from active brazing experiments of zirconia to metals and to itself.

In Chapter 6, the effect of the substrate metal on the thermochemistry of the active brazing alloy during ceramic/metal brazing operations is studied. By using simple diffusion simulations, the interdiffusion processes occurring at the metal/braze interface are elucidated and quantified.

In Chapter 7, the coupled growth of typical reaction layers formed due to ZrO_2/Ti solid state diffusional reactions are investigated using the Phase-Field approach. By combining semi-empirical thermodynamic models with the diffuse interface formalism, it is shown that the reaction layer sequencing and morphology observed in the zirconia/titanium system can be explained, at least in a qualitative manner. In this chapter is also shown that the model developed can be generalized to other complex interfacial phenomena in other systems.

Chapter 2

Ceramic/Metal Interfaces: Basic Ideas, Joining Processes

2.1 Introduction

Ceramics and metals have different electronic structures [1]. While the bonding electrons in metals are highly delocalized, electrons in ceramics are highly localized around the ions in the crystalline lattice. Since the nature of the inter-atomic bonding, as well as the electronic density, change abruptly at *C/M* interfaces, it is to be expected that these interfaces will be energetically unstable*.

In this chapter, the main physico-chemical aspects of *C/M* interfaces are discussed. A review of the most relevant works on the nature and characteristics of *C/M* interfaces will be presented. Subsequently, the implications of these theories on the problem at hand: the creation of synthetic *C/M* interfaces will be discussed.

2.2 Wetting as a Metric of Ceramic/Metal Interfacial Energetics

Quantification of the energetics of ceramic/metal interfacial interactions † is only possible when the proper metric is used. In the solid/solid case, a measure of the strength of such interactions could be the shear stress necessary to separate the *C/M* interface. This metric, however, is of little practical use in this case because the mechanical strength of a ceramic/metal interface is not only determined by interfacial energetics, or *adhesion*, but also by the mechanical state (i.e. stored elastic/plastic energy due to differences in thermo-mechanical properties) of the bulk materials themselves (see for example Park et al. [2]). Since the final state of the system is a function of the actual process of *C/M* interface formation, it is difficult to de-couple the energetics of *C/M* interfacial adhesion from the mechanical state of the system.

*This statement refers to non-reactive metal/ceramic systems. In the case of reactive systems, the chemical affinity between the ceramic cations and the active metal is such that a reaction product forms at the *C/M* interface. It is highly likely that this reaction product in turn has intermediate properties to those of the reactive alloy and the ceramic.

†The metal could be either in the solid or the liquid state

This problem becomes more tractable in the case of solid/liquid interfaces, since the metric of the interfacial energetics is much easier to access and is not coupled*to other (mechanical) energetic contributions to the total energy of the system. This metric is the wetting behavior of the solid/liquid system.

In general, the driving force for the formation of a ceramic/metal interface is the decrease in free energy that occurs when intimate contact is established between the two substrates [3]. This change in energy (per unit area) is given by:

$$\Delta G_f^{Int} = \sigma_{SV} + \sigma_{LV} - \sigma_{SL} \tag{2.1}$$

where ΔG_f^{Int} is the Gibbs free energy for interface formation, and σ_{SV} and σ_{LV} are the surface energies of the solid and the liquid, while σ_{SL} represents the interfacial energy of the *Solid/Liquid* interface. In the case when only chemical bonding has occurred and the ceramic and metal remain free of plastic deformation, ΔG is identical to the work of adhesion, W_{ad}, necessary to separate a unit area of interface into the two original surfaces [4]:

$$W_{ad} = \sigma_{SV} + \sigma_{LV} - \sigma_{SL} \tag{2.2}$$

As indicated by Eq. 2.2, (known as the *Dupré* equation) the work of adhesion, W_{ad}, increases as the S/L interfacial energy becomes smaller than the surface energies of the solid and liquid phases. A greater W_{ad} implies a greater S/L interfacial stability.

If the system is considered to be at equilibrium, the surface and interfacial energies balance each other and the following relationship can be established:

$$\sigma_{SV} = \sigma_{Sl} + \sigma_{LV} cos\theta \tag{2.3}$$

Eq. 2.3 is also known as the *Young's* equation†, and it can be combined with Eq. 2.2 so the work of adhesion, W_{ad}, can be related to the more accessible contact angle, θ, between the liquid metal and the solid substrate:

$$W_{ad} = \sigma_{LV} \left(1 + \cos\theta\right) \tag{2.4}$$

*The de-coupling of adhesion from the total strain energy of a liquid/solid *C/M* interface occurs because the liquid cannot be subjected to shear stresses.

†Note that Young's equation is only an approximation and should be used with care when considering the real 3D-shape of liquid droplets wetting a surface. Moreover, Young's equation only applies at equilibrium conditions.

By convention, wetting can be defined as the condition at which the contact angle between the liquid metal and the solid substrate is below 90^0. As $\theta \rightarrow 0^0$, complete spreading occurs, and the work of adhesion reaches the maximum allowable value, namely $2\,\sigma_{LV}$.

By measuring the contact angle between a liquid and a solid substrate, it is thus possible to establish the stability of the C/M interface. In the following section, the wettability of liquid metals over ceramic substrates will be addressed from the point of view of the the reactivity or non-reactivity of the metal.

2.3 Reactive vs. Non-Reactive Wetting

At high temperatures, there is always a certain degree of dissolution of a ceramic substrate when is in contact with a liquid metal, regardless of the reactivity of the latter. To establish a relationship between the reactivity (or chemical activity) of the liquid metal and the thermodynamic driving force for the formation of a ceramic/metal interface, one has to establish first a quantitative measure of the reactivity of the system. The extent of oxide dissolution in the liquid metal provides with a good indication of the latter's reactivity [5, pp. 198-199]. In this section, the dissolution of a ceramic substrate in a liquid metal will be considered under both reactive and non-reactive conditions, and a relationship between reactivity and wettability will be presented.

2.3.1 Ceramic Dissolution: Non-reactive Case

Consider for example the following dissolution reaction:

$$\frac{1}{m}A_mO_n \leftrightarrow \underline{A} + \frac{n}{m}\underline{O} \tag{2.5}$$

where A_mO_n is the ceramic substrate and M is the liquid metal.

The equilibrium constant, $K_D(T)$ for this reaction [5, p. 199] is given by:

$$K_D\,(T) = a_A \cdot a_O^{n/m} = \exp\left(\frac{+\Delta^0 G_f^{A_mO_n}}{m \cdot RT}\right) \tag{2.6}$$

Assuming constant chemical activity coefficients, $\gamma_i \sim \gamma_i^{\infty}$

$$a_A = x_A\gamma_A^{\infty} \quad a_O = x_O\gamma_O^{\infty} \tag{2.7}$$

Eq. 2.6 can then be written as follows:

$$K_D\,(T) = x_A\gamma_A^{\infty} \cdot \{x_O\gamma_O^{\infty}\}^{n/m} \tag{2.8}$$

If the only source of elements A and O is the oxide substrate, the molar fractions

of O and A are then related by $m \cdot x_O = n \cdot x_A$.

The equilibrium molar fraction of oxygen, x_O^D is given by:

$$x_O^D = \left(\frac{n}{m}\right)^{\frac{m}{m+n}} \cdot K_D^{'}(T)^{\frac{m}{m+n}} \tag{2.9}$$

where

$$K_D^{'}(T) = \frac{K_D(T)}{\gamma_A^{\infty} \cdot (\gamma_O^{\infty})^{n/m}}$$

Eustathopoulos et al. [5] have compiled a large number of ceramic oxide/metal wetting experiments in which the contact angle between the liquid and the solid substrate has been measured using the sessile drop technique. By calculating the oxygen molar fraction in the liquid metal (x_O^D) using homogeneous thermodynamic properties for the oxides and approximate values for the activity coefficients of both oxygen and the cation of the ceramic in the melts, Eustathopoulos et al. [5] found a relationship between the extent of oxide dissolution, as measured by x_O^D, and the contact angle at the ceramic/metal junction. Their findings can be summarized as follows (see Fig. 2-1):

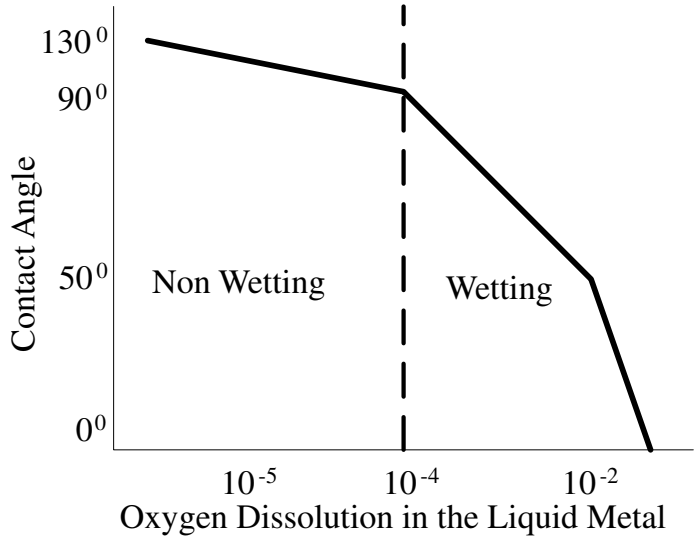

Figure 2-1: Schematic of experimental compilation by Eustathopoulos et al. [5]. This diagram is not at scale.

i) For the range $x_O^D < 10^{-5}$, the observed contact angle was virtually independent of the extent of dissolution of the ceramic oxide in the metal. The contact angles observed under these conditions were within the $100^0 < \theta < 140^0$ range.

ii) As the extent of oxide dissolution increased above the $x_O^D > 10^{-5}$ value, the contact angle started to decrease.

iii) At about $x_O^D \sim 10^{-4}$, all the sessile drop experiments that were examined exhibited a contact angle of $\sim 90^0$, which corresponds to the *wetting/non-wetting* transition.

iv) At even greater oxide dissolution, the contact angle approaches 0^0 degrees. These low contact angles, however, were due to the formation of a wettable reaction layer between the liquid metal and the ceramic substrate. The liquid metals in these cases were invariably highly reactive and the free energy of formation of their oxides was highly negative.

From the observations by Eustathopoulos et al. [5], the limit between wetting and non-wetting seems to be $x_O^D \sim 10^{-5}$. It is important to note that the calculated extents of dissolution did not consider the effect that the furnace atmosphere has on the chemistry of the liquid metal. For extremely reactive systems, providing there is a low enough p_{O_2} surrounding the samples, the effect of the furnace atmosphere is not expected to affect the thermochemistry at the ceramic/metal interface. For non-reactive systems,however, the effect can be significant [5].

2.3.2 Addition of Reactive Elements

In general, even if it is possible to reduce the contact angle observed in non-reactive metal systems by the addition of solutes that decrease the surface tension of the liquid [5, section 6.5] or promote the segregation of oxygen to the ceramic/metal interface (see Section 2.4), the contact angle between a liquid metal and a ceramic substrate cannot be reduced to values below $\sim 60^0$ unless active elements are added to the liquid.

One can consider again the dissolution reaction [5]:

$$\frac{1}{m} A_m O_n \leftrightarrow (A)_M + \frac{n}{m} (O) \tag{2.10}$$

If a second element, Re is added to the liquid M and this element has a significant oxygen affinity, Eq. 2.9 can be modified in the following manner:

$$x_O^D = \left(\frac{n}{m}\right)^{\frac{m}{m+n}} \cdot K_D^{'} (T)^{\frac{m}{m+n}} \cdot \exp\left(-\frac{n}{m+n} \varepsilon_O^{Re} \cdot x_{Re}\right) \tag{2.11}$$

where ε_O^{Re} is the Wagner's first-order interaction coefficient between O and Re in liquid M*.

According to Eq. 2.11, if $\varepsilon_O^{Re} < 0$, the amount of oxygen in the liquid $M - Re$ that is in equilibrium with the oxide $A_m O_n$ increases rapidly as the amount of B increases. If the interaction between the reactive element R and oxygen is very negative $\varepsilon_O^{Re} << 0$, the precipitation of an oxide $Re_y O_z$ can be promoted:

*It has been assumed that the remaining interaction coefficients are negligible compared to ε_O^{Re}.

$$y\underline{Re} + z\underline{O} \leftrightarrow Re_yO_z$$

The equilibrium constant for this reaction, $K_P(T)$ will then be given by:

$$K_P(T) = \{x_{Re}\gamma_{Re}\}^y \cdot \{x_O\gamma_O^\infty\}^z = \exp\left(\frac{\Delta^0 G_f^{\mathrm{Re}_yO_z}}{RT}\right) \tag{2.12}$$

The mole fraction of oxygen in the liquid M in equilibrium with the reaction product Re_yO_z is given by:

$$x_O^P = K_P^{'}(T)\, x_{Re}^{-y/z} \exp\left(-\varepsilon_{Zr}^O x_{Re}\right) \tag{2.13}$$

where

$$K_P^p(T) = K_P(T)^{1/z} \cdot \gamma_{Re}^{y/z} \cdot (\gamma_O^\infty)^{-1}$$

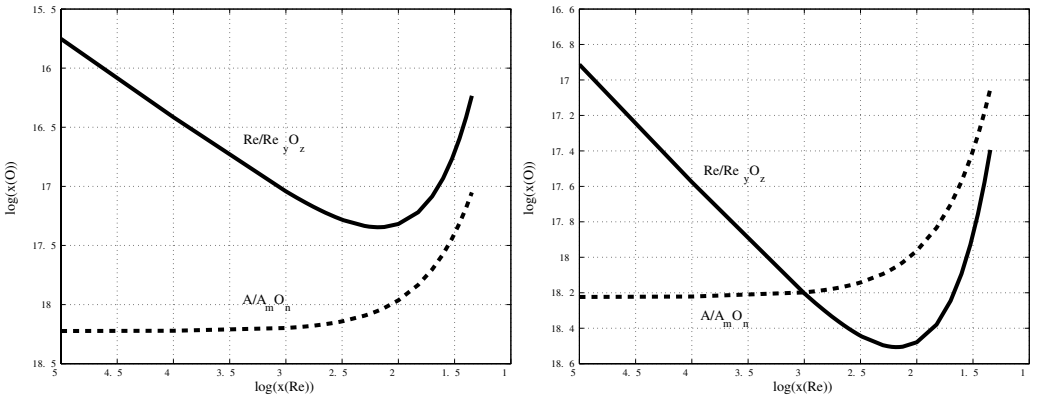

(a) Slightly reactive element addition. Graphical representation of Eq. 2.11 and Eq. 2.13.

(b) Strongly reactive element addition. Graphical representation of Eq. 2.11 and Eq. 2.13.

Figure 2-2: Effects of active element additions on the dissolution of ceramic oxide substrates.

Fig. 2-2 is a graphical representation of the two different behaviors that can be expected when active elements are added to non-reactive liquid metals in contact with ceramic substrates. In both cases, it can be seen that the ceramic dissolution increases dramatically as the concentration of the active element in the liquid increases. In Fig. 2-2(a) the active element, however, does not react with the oxygen dissolved in the metal to form a reaction product, as the A/A_mO_n and Re/Re_yO_z equilibrium curves never intersect [5, p. 249]. Fig. 2-2(b) illustrates the case in which the reactive element has such a strong affinity for oxygen ($\varepsilon_O^{\mathrm{Re}} << 0$), that the precipitation of a Re_yO_z oxide occurs, as is illustrated by the interception of the A/A_mO_n and Re/Re_yO_z equilibrium curves. It is to be expected that, while the active element

addition in Fig. 2-2(a) will decrease the contact angle in a noticeable manner, the precipitation of a reaction product, as shown in Fig. 2-2(b), will promote the greatest wettability, provided the reaction product is *wettable*.

In the following section, a brief review of the most successful description of the energetics of ceramic/metal interfaces will be presented. Wettability will then be related to the intrinsic electronic structure of ceramics and metals. Although the models are principally focused on the interaction of non-reactive liquids on ceramic substrates, it will be seen (see Section 2.6) that the models can also explain the different degrees of wettability observed in reactive C/M systems.

2.4 Non-reactive Metal-Ceramic Wetting: Influence of the Electronic Structure

Although there have been several attempts at understanding the nature of ceramic/metal interactions, there are very few models capable of describing the full set of trends and behaviors that have been observed in experiments. For example, early attempts to describe the metal M - oxide AO interaction at the C/M interface focused on finding a correlation between the energetics of the interface (W_{ad}, for example) and the formation enthalpy or Gibbs energy of formation of the MO oxide [5]. Such a correlation would indicate a chemical interaction between the ceramic substrate AO and the metal M at the interface, even though a chemical reaction would not necessarily occur. According to these models, W_{ad} (see Section 2.2) would be related to the bond energies between the anion and the metal. One such model was proposed by MacDonald and Eberhart [6]:

$$W_{ad} = a\Delta^0 H_f^{MO} + b\frac{\alpha_M \alpha_O}{r^6} \cdot \frac{I_M I_O}{I_M + I_O} \tag{2.14}$$

where $\triangle H^0_{f,MO}$ is the enthalpy of formation of the oxide MO, α_i are the polarizabilities of the oxygen and metal atoms, I_i are the first ionization potentials, r is the interatomic distance at the ceramic/metal interface and a and b are proportionality constants.

This model requires the addition of a 'chemical' ($a\Delta^0 H_f^{MO}$) and a 'physical' ($b\frac{\alpha_M \alpha_O}{r^6} \cdot \frac{I_M I_O}{I_M + I_O}$) interaction term. The chemical interaction term is the enthalpy of formation of the liquid metal oxide. The physical interaction term takes into account a dipole-dipole interaction between the ceramic anion and the liquid metal and is essentially constant for most metals [7].

Table 2.1 shows that the *McDonald-Eberhart* model does not predict the correct tendencies according to Eq. 2.14. Note that while the enthalpy of formation of SnO is twice that of CuO, the work of adhesion at the Sn/Al_2O_3 is half that of the Cu/Al_2O_3 case. It is evident that this model (and all models that try to correlate $M-O$ bond

Table 2.1: Test of Eberhart model. Wetting of metals on sapphire (Al_2O_3)

Metal	**Contact Angle** [7]	**Work of adhesion** $\frac{mJ}{m^2}$ [7]	**Formation enthalpy** [8] kJ/mol
Cu	130	450	-156
Sn	122	225	-287

energies to W_{ad}) does not agree with the observed experimental facts.

One of the best models for describing non-reactive ceramic/metal C/M interfacial interactions was proposed by Li [9]. He examined the dependency of the work of adhesion, W_{ad}, of a metal/oxide system on the electronic properties of both the (liquid) metal and the ceramic substrate. In his analysis, Li [9] excluded metallic systems that reacted with ceramic substrates forming reaction products, since this necessarily changes the nature of the original C/M interface. From this analysis, a correlation between the electronic properties of the C/M system and the work of adhesion was found (See Fig. 2-3).

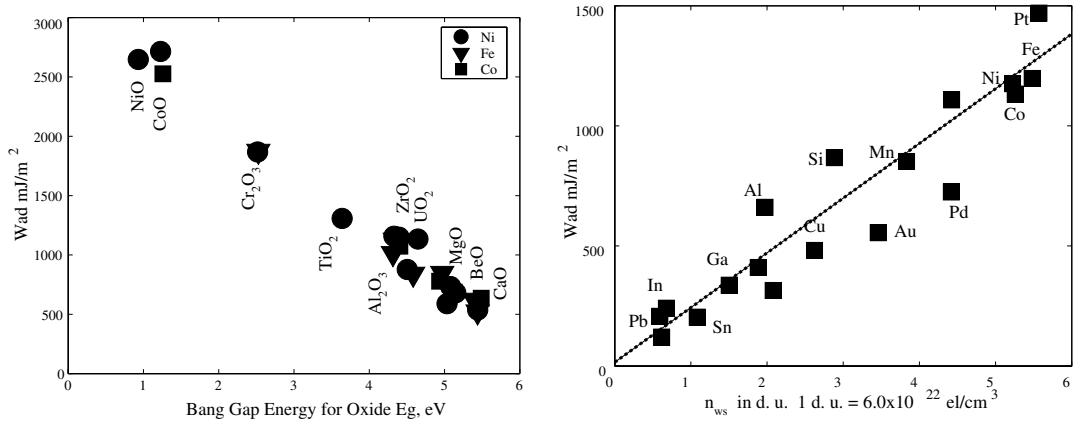

(a) Work of adhesion W_{ad} of molten Co, Fe, Ni as a function of the bandgap energy Eg of different oxides [9]. The data was originally presented as W_{ad} vs. $\triangle G_f^0$. It was modified using the plots of Eg vs. $\triangle G_f^0$ found also in Li [9]

(b) Work of adhesion W_{ad} of different liquid metals with alumina vs. the electron density n_{ws} at the boundary of the Wigner-Seitz cell.

Figure 2-3: Correlation between the work of adhesion W_{ad} of a ceramic/metal interface and the electronic properties of both ceramic substrates and liquid metals.

Based on the correlations depicted in Fig. 2-3, Li [9] formulated a model to describe the energetics of C/M interactions between non-reactive metals and ionic-covalent oxides as a function of the electronic properties of both bulk materials.

According to this model, the stability of a non-reactive C/M interface is increased by greater electron transfer from the metal conduction band into the oxide valence band. When a metal comes into contact with a ceramic surface (in the case examined by Li [9], an oxide), the thermally created holes in the valence band can be filled by the free electrons of the conduction band of the metallic lattice. The ceramic surface can thus be stabilized by the presence of a foreign metallic phase. This interaction is metallic-like in nature and therefore is expected to have long range character, as has been observed in some first-principle calculations [5, chap. 6]. Such a transfer would be favored by a large electronic density, n_{ws} on the metal side of the C/M interface*. Fig. 2-3(b) shows how the work of adhesion between several molten non-reactive metals and alumina changes with n_{ws}. As can be seen, Li's model agrees with the trends observed in Fig. 2-3(b).

Another implication of the model by Li [9] is that electron transfer across a C/M interface will be favored in cases for which the valence band in the ceramic material has a large concentration of holes. For an idealized oxide crystal, free of impurities, the concentration of holes in the valence band is given by:

$$n_h = n_h^0 exp^{\frac{-E_g}{2KbT}} \tag{2.15}$$

where E_g is the bandgap energy. According to Eq. 2.15, as E_g increases, the concentration of holes n_h decreases at an exponential rate. According to Li's model, insulating materials with large E_g would then interact in a weakly manner with liquid metals. This behavior can be observed in Fig. 2-3(a). Another conclusion from this model is that W_{ad} (θ would decrease) would increase with temperature, as was experimentally observed by Rivollet [11].

In general, E_g is correlated to the Gibbs free energy of formation $\triangle G_f^0$ of the ceramic (See Fig. 2-4). Thus, a correlation between ceramic stability and work of adhesion should then be observed. According to the experimental data presented by Li [9], the work of adhesion of the corresponding C/M interface decreases as the Gibbs free energy of formation of the oxide increases (using the same liquid metal).

Although the model described above focused on the interactions between non-reactive liquids and metals, it is possible to extend the conclusions of the model to solid/solid systems. In fact, Li [9] found experimental evidence [14] that showed a linear correlation between the work of adhesion of solid metal/Al_2O_3 interfaces, and the electronic density of the respective metals, n_{ws} (see Fig. 2-3(b)). This means that the nature of bonding at solid/solid C/M interfaces is very similar to that in liquid/solid C/M systems. Despite the similarities, it is important to consider that,

*The electronic density, n_{ws}, is one of the terms used in Miedema's model to describe cohesion in metallic systems and it corresponds to the electron density at boundaries of the Wigner-Seitz cells [10].

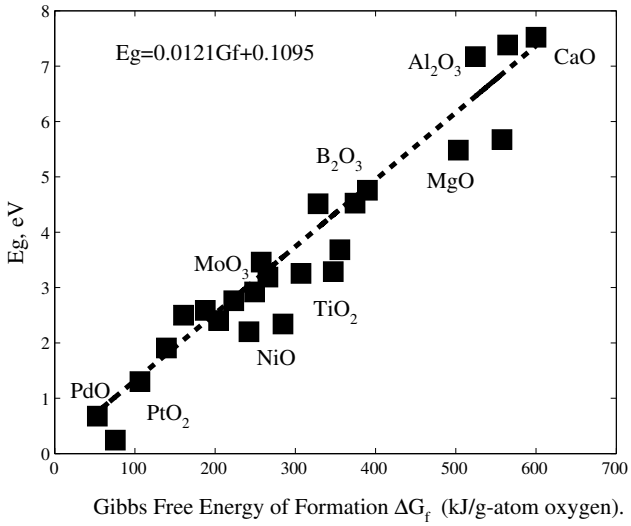

Figure 2-4: Relationship between bandgap energies [12] and Gibbs free energy of formation [13] for several oxide ceramics

contrary to S/L interfaces, in the case of S/S interfaces large strain energies can be generated at the ceramic/metal interface as it is cooled from the joining temperature. These strain energies arise due to differences in the thermo-mechanical properties of the materials. The addition of this extra strain energy can result in an actual rupture of the interface if its value is greater than the interfacial work of adhesion.

It is important to note that the model described above only applies when considering pure metal-ceramic interactions, with no surface contamination and under high-vacuum conditions. Adsorption of surface active elements, such as oxygen, onto the liquid metal surface will decrease the liquid surface tension and, according to Young's equation (Eq. 2.3), decrease θ. Additionally, alloying the liquid metal with another metallic solute with much smaller surface tension and a strong tendency for segregation will also decrease the contact angle between the molten metal and the ceramic.

The model described in this section applies only to non-reactive C/M interactions for the simple reason that the product of a reactive system would permanently alter the nature of the original C/M interface. With an interfacial reaction product, a new set of interfaces would have to be considered and the analysis would then be more complicated than the simple model outlined above. Nevertheless, we can expect that the resulting C/M interface can be analyzed under the assumptions of Li's model.

2.5 Joining Ceramics to Metals

Joining facilitates the use of structural ceramics -as well as other types of ceramic materials- by providing a means to manufacture structures which cannot be made in one piece or which can be made less expensively by joining. Because of their intrinsic

brittleness, most ceramics are fabricated using diverse joining techniques, thus avoiding large mechanical loads involved in bulk processing.

Furthermore, ceramic/metal, *C/M*, joining is particularly useful when trying to combine the mechanical and/or chemical properties of both ceramics and metals in the same device -i.e. *C/M* composites, protective coatings, etc. Of all the current *C/M* joining applications, one of the most important is the attachment of ceramic components operating at high temperatures to structures or moving parts which must withstand stresses or temperature gradients too great for ceramics, and which are usually made of metals.

When designing a *C/M* joint, one always has to face the fact that the different nature of the materials makes the joining process a difficult task. In order to optimize the design of a successful *C/M* joint it is crucial to overcome two different although inter-related problems:

- *C/M* interfaces tend to be thermodynamically unstable. Since the electronic structures of the ceramic and metallic lattices are different (see Section 2.4), the ceramic/metal interfacial energy is usually greater than the free surface energy of the ceramic itself. Therefore, the ceramic free surface is usually more stable than a *C/M* interface.
- *C/M* interfaces are mechanically unstable*. Because of the usually different mechanical and thermo-mechanical properties of the ceramics and metals, *C/M* interfaces are usually subjected to large stresses, especially when the joint must operate at high temperatures.

The resulting *C/M* interfaces usually have to be stable over a wide range of temperature conditions. At the same time, the joint must be able to withstand the large stresses generated due to the different thermo-mechanical properties of both ceramics and metals.

As a way of summarizing the broad spectrum of possible *C/M* joining techniques, one can classify them into one of the following major groups:

i) Mechanical joining: Used in both traditional and new applications such as securing of furnace roof refractories with metal hooks. Press-and-shrink fitting is another type of mechanical joining technique that is widely employed in mass production processes.

ii) Direct joining: Achieved by pressing together very flat surfaces to achieve bonding via solid-state diffusion processes. In these type of processes, no intermediate materials are needed to create a joint between dissimilar materials.

*This is only true when both substrates are in the solid steta

iii) Indirect joining: This is the most common method for obtaining high-integrity joints. It uses a wide range of intermediate materials such as organic adhesives, glasses or glass-ceramic composites, oxide mixtures, or metals. Metal interlayers are used in both solid and liquid phase diffusion processes, brazing, etc. In these techniques, pretreatment of the ceramic surface is sometimes needed to guarantee good wetting properties.

The choice of a particular joining technique, as has been noted above, depends on the nature of the ceramic and the metal, as well as on the operating conditions for which the joint is being designed. Nevertheless, no matter which process is chosen, the formation of a successful joint depends on the achievement of intimate contact between the work pieces; the conversion of these contacting surfaces into an atomically bonded interface; and finally, on the ability of this interface to accommodate thermally-induced stresses which are generated either during cooling from the joining temperature or by temperature gradients due to the normal operating conditions of the part.

One of the purposes of this thesis is to investigate some of the basic aspects of the thermochemical interactions occurring at *C/M* interfaces. It is hoped that this understanding will make a contribution to the development of synthetic *C/M* interfaces of practical use. Due to the complexity of this problem, it is necessary to narrow the scope of this work, while at the same time extracting general principles that would allow a better design and understanding of practical *C/M* interfaces. *C/M* active metal brazing (to be described in Section 2.6) has been chosen as the primary example. Specifically, the thermochemical phenomena occurring at *C/M* brazed joints will be addressed. By choosing relevant *C/M* systems, it is expected that generalizations applicable not only to *C/M* joining but to the more general field of *C/M* interfacial thermochemistry can be made. While *C/m* active brazing is the main example studied in this work, other instances where ceramic/metal interactions are important are examined. In all the cases explored zirconia has been selected as the ceramic substrate, for reasons outlined elsewhere in this thesis (see Section 5.2).

2.6 Active Brazing

According to Li's model (See Section 2.4) the electronic structure of both the ceramic and the metal substrates determine the energetics of ceramic/metal *C/M* interfaces. In general, non reactive-metal/ceramic systems show contact angles above 90^0. This large contact angle implies that most non-reactive *C/M* interfaces would tend to be energetically unstable. If one were to create a synthetic *C/M* interface by indirect joining of a ceramic substrate to a metal part (as outlined in Section 2.5) it would be necessary to change the energetics of the resulting interfacial interactions in such a way that a stable interface can be created.

Of the ceramic/metal joining techniques described in Section 2.5, one of the most widely used is active brazing. In general, brazing can be defined as any joining tech-

nique that relies on the presence of a liquid interlayer between two solid substrates. The interlayer should have a melting point lower than those of the joined substrates. After the interlayer solidifies, a joint is created, whose mechanical properties will be determined by the adhesion between the interlayer and the substrates as well as by the resulting mechanical stresses generated when the interface is cooled from the joining temperature*.

As noted above, common brazing techniques cannot be applied to C/M joining applications because the metals normally used in these techniques (copper, silver, nickel) do not wet most ceramic substrates†. Fortunately, these alloying systems can be modified to promote wetting ($\theta << 90^0$) on even the most stable ionically bonded ceramic oxides (such as Al_2O_3, ZrO_2, etc.) [15].

One of theories that have been developed to explain the beneficial effects of adding active elements to non-reactive brazing alloys is that the evolved heat from the dissolution and precipitation reactions constitutes a negative contribution to the formation energy of the C/M interface. If this were the only contribution of reactive brazing, a greater C/M work of adhesion (or smaller contact angle θ) would result as the interfacial interaction became more intense. In general the intensity of the C/M interfacial interaction could be indicated by the relative thickness of the interfacial reaction product. Following this reasoning, a greater reaction layer thickness would have to be associated with a smaller contact angle θ. Table 2.2 shows that, at least for some systems, this is not the case.

Table 2.2: Wettability and interfacial chemistry of $Cu-Pd-Ti$/oxide sessile drop experiment at $T = 1200^0C$ [16].

Substrate	**Contact Angle**	**Interfacial Product**	**Thickness,** μm
Alumina	34	Ti_2O_3	0.5
Mullite	32	Ti_2O_3	1.0
Silica	35	Ti_2O_3	10.0

Although in many cases the presence of a continuous reaction layer promotes wetting in C/M systems, there are some cases in which this is not the case. One example of these situations is the sessile droplet experiments of liquid Ag over a SiC substrate reported by [17]. At high temperatures ($T \sim 1100^0C$), Ag dissolves SiC forming Si dissolved in Ag and graphite. Before graphite is formed, the molten Ag wets the SiC substrate ($\theta << 90^0$). Nevertheless, as soon as a continuous graphite layer forms at

*These mechanical stresses originate from the different thermo-mechanical properties of the materials to be joined, such as coefficient of thermal expansion, elastic moduli, etc.

†This non-wetting is particularly evident for the most thermodynamically-stable ceramics, such as highly ionic oxides (See Section 2.4).

the ceramic/braze interface, de-wetting occurs ($\theta >> 90^0$).

Table 2.3: Contact angle and W_{ad} of $CuPd$-Ti/alumina sessile drop experiments [18]

Ti **content in braze**	**Oxide**	**Bonding Character**	**Contact Angle**	W_{ad}, $\frac{mJ}{m^2}$
0	Al_2O_3	Insulating	127	560
4	Ti_3O_5	Semi-metallic	92	1350
7	Ti_2O_3	Semi-metallic	70	1880
24.7	$TiO_{1.2}$	Metallic	18	2730

A greater insight on the beneficial effects of active element additions to brazing alloys can be gained by examining Table 2.3. From this table, it is apparent that the nature of the reaction layer (wether is conducting or insulating) formed due to the interaction between the $CuPd$-Ti braze alloy and the alumina substrate has a great influence on the C/M interfacial adhesion. This result can be examined in light of the model developed by Li [9] , described in Section 2.4. As the electronic bonding character of the reaction layer changes from insulating to metallic, electron transfer across the C/M interface increases. This increased electronic interaction (a long-range interaction of metallic-like characteristics) increases the resulting interfacial work of adhesion W_{ad}. According to Eq. 2.4, the contact angle θ should decrease as W_{ad} increases. This seems to be supported by the experimental evidence presented in Table 2.3.

It is important to note that in some active brazing applications the precipitation of a reaction layer is not thermodynamically possible. Nevertheless, dissolution of the ceramic substrate is promoted because of the strong affinity between the active element and the ceramic anion. Oxygen tends to segregate* to metal free surfaces [19, chap. XIV], lowering σ_{LV} in Eq. 2.4. Naidich [20] proposed that the dissolved oxygen and the active metal form clusters (because of the strong chemical interaction) that have partially ionic character due to the charge transfer from the metal to the oxygen atom. Due to this ionic character, these clusters can interact with ionically-bonded solid substrates and segregate to the *solid/liquid* interface. This interaction, in turn, lowers σ_{SL} in Eq. 2.4. If $|\delta\sigma_{SL}| > |\delta\sigma_{LV}|$, as has been observed in some systems (See Naidich [20]), then $|\delta W_{ad}| > 0$ and therefore $|\delta\theta| < 0$. Wetting, thus, can be improved in reactive brazing systems by just promoting further oxide dissolution into the liquid braze.

*The reason for this segregation is that the perturbations in the structure and energy of bulk metals can be better relaxed in 2D geometries [5, chap. 6].

The effectiveness of active brazing in *C/M* joining applications is thus derived from two main factors:

i) The active element can promote a greater ceramic dilution. Dissolved oxygen reduces the *Solid/Liquid* interfacial energy and increases the work of adhesion of the *C/M* system.

ii) If the interaction between the active element and the anion is strong, the precipitation of a reaction layer can be promoted. If this reaction layer has the appropriate electronic properties* wetting is further promoted and the work of adhesion increases to levels that make *C/M* interfaces practical.

When the reaction product formed at the *ceramic/liquid* interface is ionically or covalently-bonded, chances are that the liquid metals will not wet the substrate (or de-wetting can occur). In this case, the use of active brazing alloys for the joining of ceramic to metals will be ineffective.

In order to accelerate the development of effective ceramic/metal joining techniques (in this particular case, brazing) it is desirable to be able to predict what kind of interfacial interactions would occur in a particular ceramic/metal system. By predicting the reaction products more likely to be observed under a particular thermochemical condition, it will be possible to assess the effectiveness of a particular ceramic/metal joining approach. At the same time, with a sound knowledge of the thermochemistry of ceramic/metal interaction, the interpretation and rationalization of experimental results will be more straightforward.

2.7 Understanding Ceramic/Metal Interfacial Interactions: The need for Thermodynamic Databases.

Because of their industrial importance, thermodynamic databases for material systems such as Fe and Ni-based alloys have reached a mature stage and the application of such thermodynamic data to practical applications has become routine†. Unfortunately, this cannot be said of many other material systems that, although important, are either too recent in their developmental stage or have applications which are too specific and hence they have not captured the interest of researchers dedicated to the assessment and modelling of phase diagrams. In the particular case of ceramic/metal joining applications, it is possible to identify key systems that require either further study or a completely new analysis:

- **Active brazing alloys**. As noted in Section 2.6, by using active chemical additives it is possible to improve the wetting behavior of conventional brazing alloys. Obviously, it is important to understand the thermochemistry of such

*i.e. metallic in character.

†For examples of such applications, please refer to Saunders and Miodownik [21, chapter 10]

alloys. Except for the work by Paulasto et al. [22], no attempt has been made to develop a thermodynamic model for these systems *.

- **Ceramic oxide systems**. In order to model the interfacial interactions of ceramic/metal systems it is necessary to have an accurate representation of the thermodynamics of the ceramics of interest. Additionally, since many of the possible reaction products are oxides themselves, it is essential to have as complete a description as possible of such oxides. Although there is a lot of experimental work on the study of interfacial reactions and reaction products, almost no thermodynamic descriptions of these systems are available.

The purpose of this work is to provide a general methodology for the study of the thermochemical interactions occurring at C/M interfaces. More specifically, the focus of this thesis is the study of the interactions between zirconia-based ceramics and metals, particularly during active brazing, although other cases are also studied. A description of the $Zr-O$ system is fundamental. Because no satisfactory description was available, a complete set of thermodynamic models for the principal phases of this system was developed.

According to Section 2.4, the more stable the ceramic is, the less likely that there will be a sufficiently strong work of adhesion W_{ad} at the corresponding C/M interface. From Fig. 2-3(a) it is obvious that ZrO_2 is not likely to be wetted by most commercial brazing alloys. Active brazing alloys belonging to the $Ag-Cu-Ti$ family, for example, should be used when attempting to join these stable ceramics to metals. A thermodynamic description of the $Ag-Cu-Ti$ (and other braze systems such as the $Cu-Ti-Zr$, etc.) is therefore necessary for this work. Putting $Cu-Ti$ alloys in contact with ceramic oxides implies the possible presence of reaction layers belonging to the complex $Cu-Ti-O$ family of oxides [23]. A thermodynamic description of the $Cu-Zr-O$ and $Ti-Zr-O$ systems is also of importance if a comprehensive thermochemical analysis of all the possible interfacial reactions is to be achieved. As will be shown later in this thesis, a correct thermodynamic description not only sheds light on the nature of C/M chemical interactions but also can be used to gain a deeper understanding of kinetics aspects of such interactions such as diffusion paths, interfacial morphology, etc.

In Appendix A, a general introduction to thermodynamic modelling is presented. The two following chapters present a thermodynamic assessment of the metallic and oxide systems of interest for this thesis. A detailed review of the available models and experimental information will be presented. Discrepancies between the observed and calculated thermodynamic properties of the systems will also be discussed.

*In the paper by Paulasto et al. [22] the parameters of the thermodynamic models were not reported.

Chapter 3

Development of Thermodynamic Database for Active-Brazing Alloys

3.1 Development of Active Brazing Thermodynamic Database: Introduction

As noted in Section 2.7, very few attempts have been made at obtaining a self-consistent and reliable thermodynamic database for active brazing alloys. Although considerable research has been done regarding ceramic/metal active brazing techniques and processes, many of the key aspects of the resulting ceramic/metal interfaces, such as the reaction products formed, cannot be predicted, or even rationalized, due to the lack of understanding of the thermochemical behavior of the active metal brazing alloys used in those studies.

Even for the very important $Ag-Cu-Ti$ ternary system used in the majority of ceramic/metal active brazing applications, thermodynamic models are incomplete. The lack of a reliable thermodynamic description for this system makes it difficult to design better brazing alloys. Because of this, an optimization of the brazing parameters for a particular ceramic/metal joining application cannot include active braze composition as an optimizable parameter, unless one is willing to obtain (perhaps at a great cost) a great number of experimental data points. It is therefore no surprise that the actual active brazing alloys based in the $Ag-Cu-Ti$ system are limited to a handful of compositions.

In addition to the widely used $Ag-Cu-Ti$ alloy system, novel brazing filler metals based on the $Cu-Ti-Zr$ system have been developed for brazing of Ti-based alloys [24]. Moreover, several workers have been exploring the use of such novel filler metals in ceramic/metal joining applications [25]. The use of active brazing alloys based on this system provides a high-temperature alternative to the lower-temperature active brazing alloys based on the $Ag-Cu-Ti$ system*. Although the use of brazing alloys based on the $Cu-Ti-Zr$ ternary system is not as extensive as

*The melting range of the $Cu-Ti-Zr$ system (900^0C) is about 100^0C higher than the melting range for widely used alloys belonging to the $Ag-Cu-Ti$ system.

that of $Ag-Cu-Ti$ alloys, it is to be expected that its use will increase in importance over time. It is therefore desirable to have a reliable thermodynamic model capable of describing the thermochemical behavior of this system,

In the present chapter, thermodynamic models for both the $Ag-Cu-Ti$ and $Cu-Ti-Zr$ active brazing systems will be developed using the often-called *CALPHAD* formalism presented in Appendix A. Given the fact that the complete procedure for the thermodynamic assessment of these two systems has been [26] or will be made public in the near future, only the basics of the actual assessment procedures and results will be presented.

The optimization of the thermodynamic parameters and the calculation of the resulting phase diagrams was done using the computational thermodynamics software Thermo-Calc®. The parameters for all of the thermodynamic models described in this chapter can be found in Appendix C.

3.2 Assessment of the $Ag-Cu-Ti$ System

As mentioned in Section 2.6, molten metals do not usually wet ceramic substrates*, especially if the ceramics in question are stable, ionically-bonded oxides, such as Al_2O_3, ZrO_2, etc. When using liquid-based bonding procedures (such as brazing), wetting of the substrates to be joined is of fundamental importance. In ceramic/metal brazing applications, it is necessary to chemically modify the liquid brazing alloy so wetting is promoted. Because of its chemical reactivity †, Ti‡ is usually the additive of choice when attempting to improve the wetting behavior of chemically-inactive brazing alloys.

The $Ag-Cu$ family of alloys is widely used in conventional brazing applications. It was thus logical to attempt its use in ceramic/metal brazing applications. In order to promote the wettability of these alloys, Ti began being used as the reactive additive and the $Ag-Cu-Ti$ system began to be extensively used in ceramic/metal joining applications several decades ago. The low liquidus temperatures of the $Ag-Cu$ eutectic allows brazing at reasonably low temperatures, while the presence of Ag increases the activity of Ti very noticeably [27], promoting interfacial reactions with even the most stable ceramics. Understanding the chemical behavior of the $Ag-Cu-Ti$ system is important when trying to understand the mechanisms of reactive wetting [28]. Although the $Ag-Cu-Ti$ system has been modelled before [22], no thermodynamic description has been made available. In this section, a model for the ternary $Ag-Cu-Ti$ system will be proposed and phase diagram and thermochemical calculations will be compared with the experimental evidence available.

*This is especially true when the molten metals in question do not have active element additions.

†Titanium has a great affinity for the anionic components of important industrial ceramic families such as oxides, nitrides, carbides, etc.

‡Zr, Hf are also used, although on a much smaller scale.

3.2.1 Assessment of the $Ag-Ti$ Subsystem

One of the greatest advantages of the *CALPHAD* methodology (see A) is that thermodynamic descriptions for low-order systems (binaries) can be easily expanded to describe higher-order (ternary) systems by including higher-order interaction terms and, when necessary, descriptions for ternary compounds [21]. In the case of the $Ag-Cu-Ti$ system, by using the already developed thermodynamic descriptions for $Ag-Cu$ [29], $Cu-Ti$ [30] and $Ag-Ti$ [31] it is possible to make the extensions to the third-order $Ag-Cu-Ti$ ternary system with minimum effort, provided the assessments of the binary subsystems are reliable. While the thermodynamic descriptions for the $Ag-Cu$ and $Cu-Ti$ systems can be considered to be adequate*, it was necessary to carefully re-examine the description for the $Ag-Ti$ binary since recent results regarding the thermochemistry of $Ag-Ti$ alloys [32, 33] contradict the early thermodynamic assessment of this system [31].

3.2.1.1 Phases Present in the $Ag-Ti$ System

According to the assessment by Murray and Bhansali [31], the $Ag-Ti$ system is comprised of the following phases:

- **The Liquid Phase:** Murray and Bhansali [31] observed that the steep slope of the liquidus near the Ti and Ag-rich ends of the diagram, with an apparent flattening in the central compositional range, hints at the existence of a metastable liquid miscibility gap [31]. Although this miscibility gap does not appear in the binary equilibrium phase diagram†, its presence has been confirmed in experimental observations concerning the $Ag-Cu-Ti$ ternary (See below). The existence of this metastable miscibility gap is a consequence of the highly positive $Ag-Ti$ chemical interaction and is therefore an indication of the high Ti chemical activity in Ag-rich melts. Thanks to this reactivity, Ag-based brazing alloys need relatively small Ti additions in order to make them reactive enough so wetting of ceramic substrates is promoted.

  The liquid phase can be modelled using the substitutional random sublattice model, described in Appendix A, having at a least a regular solution parameter so the positive interaction energy between Ag and Ti can be represented with the following notation:

$$(Ag,Ti)_1$$

*The systems have been critically assessed and there have been no cases in which two sets of experimental information were mutually excluding [29, 30].

†The critical temperature for the liquid miscibility gap is lower than the solidus temperature observed in the equilibrium phase diagram.

- **Solid Solution Phases:** According to the assessment by Murray and Bhansali [31], the solubility of Ti in the fcc, Ag-rich solid solution is small, providing further indication of a strongly positive $Ag - Ti$ chemical interaction energy. Although the solubility of Ag in bcc and hcp Ti-rich solid solutions is higher, it is reasonable to expect a similar positive interaction in these phases as well. The solid solution phases, fcc, hcp and bcc can be modelled using the sublattice formalism for an interstitial phase*:

  $$(Ag, Ti)_1 (Va)_c$$

  where c is the ratio between interstitial and 'normal' sites in the solid solutions. As noted above, c has a value of 0.5, 1 and 3 for the hcp, fcc and bcc structures, respectively †.

- **The $AgTi$ Phase:** The $AgTi$ phase is iso-structural with $CuTi$. Experimental evidence suggest that both phases present a certain degree of non-stoichiometry. Because of their similarity, it was reasonable to expect that the model already available to describe the $CuTi$ phase [30] could be applied to the $Ag-Ti$ system.

  In their assessment of the $Cu - Ti$ system, Hari Kumar et al. [30] modelled the $CuTi$ phase considering that for the perfectly stoichiometric composition, Ti would occupy one sublattice, while Cu would occupy the other one. To model the observed non-stoichiometric deviations it was supposed that point defects (anti-structure atoms ‡) were also present in the phase§. Using the sublattice notation, this phase was represented by $(Cu, Ti)_1 (Ti, Cu)_1$. Given that the $AgTi$ phase is iso-structural with $CuTi$, it is reasonable to use the same sublattice formalism to describe its thermodynamic behavior:

  $$(Ag, Ti) (Ti, Ag)$$

*This allows the further modification of the model so interstitials such as O can be later introduced.

†When considering substitutional solutions in these phases the actual site ratio between normal sites to interstitial sites is not important. On the other hand, this ratio has a very physical significance when considering interstitial solutions. In the case of the fcc phase, there are one normal site per interstitial site, while for the bcc phase, there is one normal site per three interstitial sites. Although the hcp phase has a site ratio of $1:1$, elastic interactions between interstitials effectively reduce this ratio to $1:0.5$ [34].

‡Anti-structure atoms are point defects corresponding to a complete inversion of the occupation within the structure. For example, the anti-structure of $CuTi_4$ is $TiCu_4$ where the Cu atoms are replaced by Ti and viceversa.

§This model is called the Wagner-Shottky model [35]. This formalism considers that an intermetallic phase can have point defects such as vacancies and anti-structure atoms and defines the Gibbs free energy of such a phase using the Gibbs free energy of the perfect stoichiometric compound, plus additions representing the Gibbs energy of formation of its point defects.

- **The $AgTi_2$ Phase:** There is no consistent experimental evidence regarding the non-stoichiometry of the $AgTi_2$ phase (it is iso-structural with $MoSi_2$). In their assessment, Murray and Bhansali [31] noted that this phase could be considered as being perfectly stoichiometric. Therefore, a stoichiometric model was used to describe this phase:

$$(Ag)(Ti)_2$$

3.2.1.2 Assessment Results

Using only phase diagram data* it is possible to obtain approximate values for the model parameters describing the thermodynamics of a system. The problem with this approach, however, is that, in principle, there is a great number of 'correct' solutions to the thermodynamic optimization problem. It is desirable then to constrain the problem in such a way that this optimization results in a realistic thermodynamic description†. Using thermochemical measurements (such as enthalpies, chemical activities, etc.) of any given phase, it is possible to unambiguously define the parameters describing its thermodynamic behavior. If there is experimental data on equilibria between that phase and another one, the already optimized description can be used, in conjunction with experimental data, to further restrict the possible values that the parameters describing the second phase must have in order to obtain an 'optimal' description of the thermodynamics of the system.

Unfortunately, thermochemical information on the $Ag-Ti$ system is scarce and, as will be seen later (see 3.2.1.3), in conflict with well-accepted phase diagram features. Therefore, in the preliminary re-assessment of the $Ag-Ti$ system, the thermochemical measurements reported by Fitzner and Kleppa [32], Wei et al. [33] were ignored and the optimization procedure was performed using only phase diagram data. In light of the resulting optimized description, the thermochemical measurements reported by Fitzner and Kleppa [32], Wei et al. [33] were critically examined and, as will be seen below, were determined to be non-reliable.

As can be seen in Table 3.1 there is excellent agreement between the calculated and experimental invariant points‡. Although agreement with experimental invariant points does not necessarily guarantee the reliability of the model, it indicates that the models used are at least a good first-order approximation. In order to establish a higher degree of confidence on the models developed, it would be necessary to have additional *independent* data that could be used to further constrain the set of parameters necessary to describe the system. In this particular case, experimental phase boundary data involving equilibria between four different phases were used as

*Phase boundaries, invariant reactions, etc.

†A realistic description would represent both phase diagram topological features and thermochemical properties with a high degree of reliability. Additionally, such a description could be confidently used in both metastable and higher-order equilibria calculations.

‡Initial values for the parameters were taken from the model proposed by Kaufman [36]

Table 3.1: Comparison between calculated and experimental invariant points in the $Ag-Ti$ system.

Invariant Reaction	**at.%Ag of Respective Phases**			**Temp. ^{0}C**	
$bcc + L \rightleftharpoons AgTi$	15.5	~ 94	~ 48	1020 ± 5	Exp.
	16.35	91.5	49.5	1024	Calc.
$bcc + AgTi \rightleftharpoons AgTi_2$	~ 12	~ 48	33.33	940 ± 5	Exp.
	11.5	49	33.33	943	Calc.
$bcc \rightleftharpoons hcp + AgTi_2$	7.6	~ 4.7	33.33	855 ± 5	Exp.
	6.7	4.2	33.33	853	Calc.
$L \rightleftharpoons AgTi + fcc$	~ 95	~ 50	~ 95	959 ± 1	Exp.
	93.86	50	94.3	959	Calc.

a further constraint to the thermodynamic optimization:

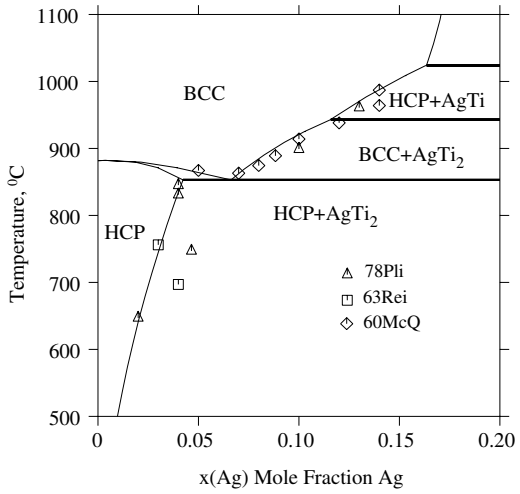

Figure 3-1: Experimental ([37–39]) vs. calculated phase boundaries in $Ag-Ti$ system.

Fig. 3-1 shows good agreement between calculated and experimental phase boundaries in the Ti-rich region of the phase diagram*. This agreement is encouraging, since a correct prediction of the solubility limits for solid solution phases in equilibrium with intermetallic phases (as in this case) provides additional corroboration for the chosen parameters used to describe such compounds. It is necessary to emphasize, again,

*The agreement is not perfect: there are conflicting sets of experimental phase boundary data points.

that information regarding the thermochemical behavior of this system would be fundamental to remove any remaining uncertainty regarding the ability of the models used to correctly represent the thermodynamic behavior of the $Ag-Ti$ system. As will be seen in 3.2.1.3, such measurements have recently been made available.

According to the optimization results, the interaction parameters for all the solution phases in the $Ag-Ti$ system are positive (See Appendix C). As will be seen in Section 3.2.2, the liquid phase in the $Ag-Cu-Ti$ ternary system shows a miscibility gap, which is caused, in part, by strong positive $Ag-Ti$ and $Ag-Cu-Ti$ interaction energies. This result is also consistent with the high Ti chemical activity in Ag melts observed in many ceramic/metal brazing experiments [28]*.

3.2.1.3 Problematic Thermochemical Measurements

In order to refine the above assessment, it was attempted to include recent thermochemical experimental information obtained by Fitzner and Kleppa [32]. Through calorimetric measurements these authors determined the enthalpy of infinitely diluted Ti in *liquid* Ag to be $-52\ kJ/mol$. This constitutes a large negative deviation from ideality and is contrary to the values obtained from the thermodynamic optimization using phase diagram data ($+25\ kJ/mol$). This negative contribution to the Gibbs energy of the liquid phase would promote the existence of a deep eutectic at the Ag-rich side of the phase diagram, however, the accepted $Ag-Ti$ phase diagram shows a eutectic temperature of only 1^0C below the melting point of Ag.
Further evidence against the measurements by Fitzner and Kleppa [32] comes from analyzing the very similar $Cu-Ti$ system. This system has far more intermetallic compounds than the $Ag-Ti$ system (6 vs. 2), so it is expected that the Gibbs energy of the liquid phase would present a larger negative deviation from ideality†. From the assessment by Hari Kumar et al. [30], the enthalpy of liquid Ti at infinite dilution in liquid Cu is $-9.95\ kJ/mol$. Using as an argument the fact that Ag and Cu have very similar chemical properties, and considering the difference in the number of stable intermetallic compounds, it is possible to consider $-9.95\ kJ/mol$ as a lower bound for the value of the enthalpy of liquid Ti in liquid Ag at infinite dilution.

Wei et al. [33] used the Electromotive Force Method, *EMF*, to measure the chemical activity of Ti in Ag silver melts. They placed the liquid solutions in alumina crucibles and observed the reaction products formed at the alumina/melt interface. Because Ti has a very high affinity for oxygen, they determined the chemical activity of Ti by measuring the equilibrium oxygen partial pressure in the melt, considering the following reaction:

*Evidence for this high chemical activity comes from the nature of reaction products observed in ceramic/metal joints using brazing alloys based on the $Ag-Ti$ system

†In general, the presence of a large number of intermetallic phases indicates a negative deviation from ideality in the liquid phase. See Bakker [40] for a more comprehensive discussion on this observed trend.

$$x\underline{Ti} + \frac{1}{2}O_2(g) = Ti_xO(s) \tag{3.1}$$

where x defines the stoichiometry of the titanium oxide present, and the $\underline{Ti}$ represents titanium dissolved in the Ag melt.

From Eq. 3.1, it can be seen that the equilibrium oxygen partial pressure is determined by the chemical activity of Ti in the melt and the titanium oxide in equilibrium with the $Ag-Ti$ liquid:

$$K_{eq} = \frac{1}{a_{Ti}^{x}(p_{O_2})^{1/2}} \tag{3.2}$$

One of the key parameters used in the calculation of the chemical activity of Ti was the $Ti-O$ oxide phase in equilibrium with the melt. Wei et al. [33] used XRD to identify the phase and were surprised to find Ti_2O (essentially, $hcp-Ti$ saturated with O interstitials) as the equilibrium phase. This phase, however, has been observed to be present when the activity levels of Ti are very high [28]. Despite this evidence, the authors interpreted the observed phase as the result of a solid-state transformation from $\beta\, TiO$ to Ti_2O.

Extrapolating the mathematical fitting of the measured data down to infinite dilution, Wei et al. [33] obtained an enthalpy of Ti at infinite dilution in liquid Ag of $-27,850\, J/mol$. Again, a negative deviation from ideality is observed, although this deviation is considerably less than the one obtained by Fitzner and Kleppa [32]. This value, however, cannot be reconciled with the features of the accepted experimental $Ag-Ti$ phase diagram.

It may be possible to question the results by Wei et al. [33] in light of the misidentification of the oxide (TiO_x vs. Ti_2O) formed at the crucible/melt interface. By using the Gibbs energy of formation for Ti_2O reported by Pak et al. [28], and, taking the measured values for the oxygen partial pressures as the correct ones, an increase of an order of magnitude in the values for the activities of Ti in Ag melts can be obtained. This new interpretation of the work by Wei et al. [33], however, is not enough to reconcile these measurements with the accepted features of both the $Ag-Ti$ and $Ag-Cu-Ti$ phase diagrams, and the apparent high chemical activity of Ti when dissolved in Ag melts.

In their study on the thermochemical behavior of the $Ag-Cu-Ti$ liquid alloys, Pak et al. [28] used an EMF method similar to that used by Wei et al. [33] to obtain the chemical activity of Ti in $Ag-Cu$ melts. Although Pak et al. [28] focused their investigations of the thermochemistry of Ti in $Ag-Cu$ melts, they report a single measurement of the chemical activity of Ti in a Ag liquid solution with no Cu. The measurement cannot be extrapolated to infinite dilution(there is only one data point), but it clearly shows a very positive deviation from ideality. This result contradicts the results obtained by Wei et al. [33] but is consistent with the accepted experimental phase diagram.

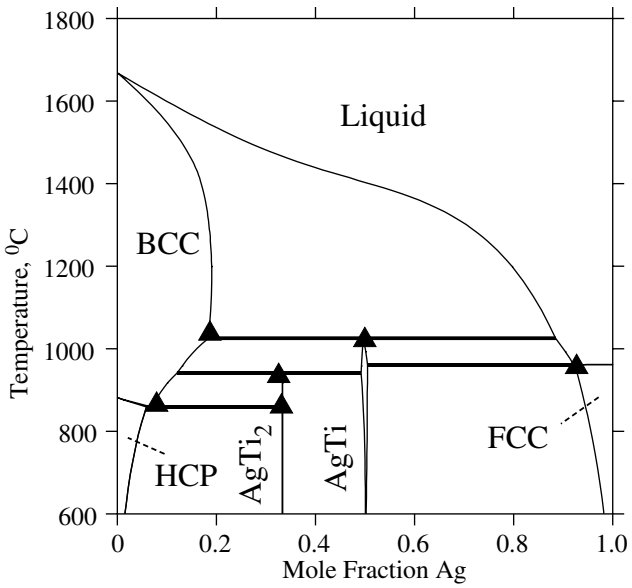

Figure 3-2: Calculated $AgTi$ phase diagram. Triangles indicate experimental invariant points.

Although there are enough reasons to question the results obtained by Fitzner and Kleppa [32] and Wei et al. [33], the fact that two independent and un-related thermochemical measurements offered results contrary to what would be expected according to accepted phase diagram features makes it impossible to reject them completely. A sensitivity analysis on the effect of varying the values of the interaction parameters for the liquid and fcc phases on the compositional coordinate of the reaction $L \rightleftharpoons AgTi + fcc$ (fixing the reaction temperature at the accepted 960^0C), shows that as the binary chemical interaction parameter on both phases became less positive (going towards the values proposed by [32, 33]), the eutectic composition was displaced towards the Ti rich side of the diagram. With a negative interaction coefficient, a eutectic point was present at the middle of the phase diagram, and the width of the $bcc - Ti$ single-phase field was decreased to values much lower than the accepted solubility limits. Using this sensitivity analysis, along with the independent data by Pak et al. [28], it was decided that the phase diagram measurements were to be accepted, while the data by Fitzner and Kleppa [32], Wei et al. [33] were to be discarded, at least until more reliable thermochemical measurements are made available.

This section has shown how the *CALPHAD* approach, when followed properly, constitutes a self-consistent method that can be used to discriminate between conflicting pieces of experimental evidence. Thus, the *CALPHAD* approach not only provides a systematic way to model the thermodynamic properties of material phases but also allows one to determine the reliability of the experimental data used to construct such models.

3.2.2 *Assessment of the* $Ag - Cu - Ti$ *Ternary*

Once the reliability of the thermodynamic models of the $Ag - Ti$, $Ag - Cu$ and $Cu - Ti$ sub-systems has been established, a thermodynamic description of the ternary $Ag - Cu - Ti$ system can be obtained by using available experimental information.

3.2.2.1 Phases Present in the $Ag - Cu - Ti$ *System*

Eremenko et al. [41, 42, 43, 44] assessed the $Ag - Cu - Ti$ system at several temperatures and over the entire compositional range. From their work, the following condensed phases can be identified*:

- **Liquid Phase:** The liquid phase can be modelled using a regular random solution single sublattice model. This phase was observed [41] to undergo phase separation in the central region of the phase diagram. Since this liquid miscibility gap was not observed in the binary sub-systems, they assumed that the miscibility gap would have a closed topology. The model can be represented by:

$$(Ag, Cu, Ti)$$

- MTi_2 **Phase:** Eremenko et al. [42] concluded that the $CuTi_2$ and $AgTi_2$ phases were iso-structural ($MoSi_2$ is their prototype). At the $x_{Cu} = 0.33$ composition and low temperatures, they found that the lattice parameters changed continuously from $CuTi_2$ to $AgTi_2$, implying complete solid solubility among the two phases. It was natural, then, to model the two phases as if they were a single phase. Using the sublattice formalism, this phase can be modelled as:

$$(Cu, Ag)_1 (Ti)_2$$

  This model allows random mixing of Cu and Ag atoms in the first sublattice, as evident from the experimental results by Eremenko et al. [43, 44] and Paulasto et al. [22].

- MTi **Phase:** The $CuTi$ and $AgTi$ phases are iso-structural [42]. Nevertheless, they do not form solid solutions and are not even in equilibrium with each other at any temperature, although both phases exhibit noticeable penetration in the ternary compositional triangle [22, 42]. Therefore, it was decided to represent them as a single phase, using the model proposed by Hari Kumar et al. [30], allowing for mixing of all three atoms in the two sublattices:

$$(Cu, Ag, Ti)_1 (Cu, Ag, Ti)_1$$

*Only the phases actually assessed during this work are included in this description

3.2.2.2 Experimental Data used in the Assessment of the $Ag-Cu-Ti$ Ternary

In a series of papers spanning two years, Eremenko et al. [41, 42, 43, 44] generated the most important collection of phase diagram data on the $Ag-Cu-Ti$ system at different temperatures to date. Through their work, they discovered a miscibility gap in the liquid phase [41] (not observed in any of the binary sub-systems), the phase relationships of the ternary section at 700^0C, along with the liquidus surface and a series of invariant ternary reactions involving the liquid phase [43].

Paulasto et al. [22] used the diffusion couple method to study the $Ag-Cu-Ti$ system at 900^0C, 950^0C and 1000^0C and at different compositions. In these series of experiments, Paulasto et al. [22], observed the formation of two liquid phases with different densities, confirming the results by Eremenko et al. [41]. At 950^0C, extensive penetration of the $CuTi$ phase into the ternary composition triangle was observed.

Pak et al. [28] used the *EMF* Method* to measure the chemical activity of Ti in $CuAg$ eutectic melts. They placed the liquid solutions in alumina and zirconia crucibles and observed the reaction products formed at the crucible/melt interface. Because Ti has a very high affinity for oxygen, they determined the chemical activity of Ti by measuring the equilibrium oxygen partial pressure in the melt using the following equilibrium reaction:

$$x\underline{Ti} + \frac{1}{2}O_2(g) = Ti_xO(s) \tag{3.3}$$

where x defines the stoichiometry of the titanium oxide present, and the underlined Ti represents titanium dissolved in the $CuAg$ melt.

3.2.2.3 Optimization of the $Ag-Cu-Ti$ System

In order to assign values to the parameters of the models outlined in 3.2.2.1, the phase diagram, invariant equilibria, diffusion and electrochemical data briefly described in 3.2.2.2 were used. Existing assessments of the $Ag-Cu$ [29] and $Cu-Ti$ [30] systems were also incorporated into the optimization.

Fig. 3-4 presents the calculated $Ag-Cu-Ti$ phase diagram, along with experimental data points obtained from the literature (See [22, 42]). In general, the agreement is quite good:

i) Fig. 3-4(a) shows the calculated and experimental $Ag-Cu-Ti$ phase diagram at 700^0C. As can be seen, in most of the compositional triangle the agreement is excellent and the single, two- and three-phase fields have adequate compositional ranges and all the important features of the experimental diagram are

*Electromotive force measurements consist of measuring the chemical potential of an anionic species through the measurement of the electric potential across a membrane capable of maintaining a gradient of chemical potential of such anion across its thickness.

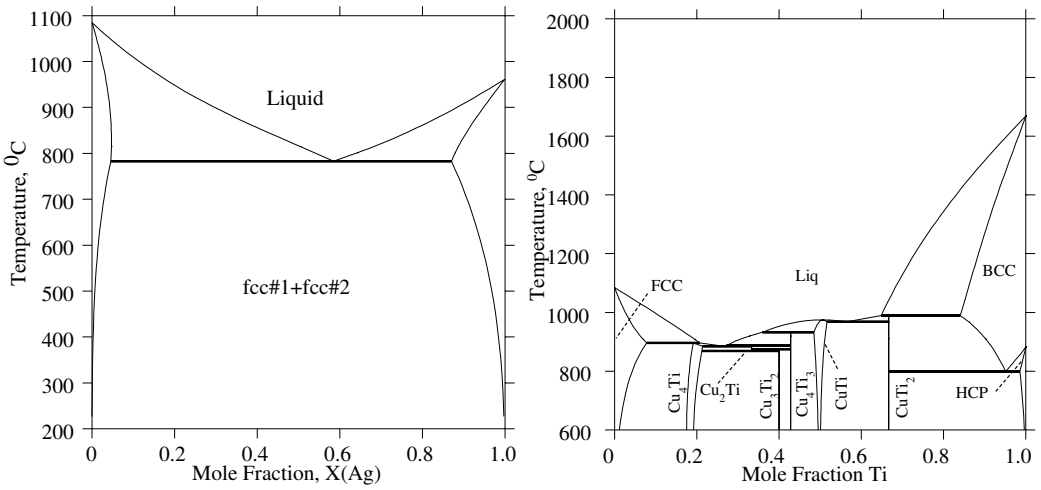

(a) Calculated $Ag - Cu$ system, after model by Hayes et al. [29].

(b) Calculated $Cu - Ti$ system, after model by Hari Kumar et al. [30]

Figure 3-3: Calculated subsystems of the $Ag - Cu - Ti$ ternary system.

reproduced.

ii) Fig. 3-4(b) shows the experimental and calculated ternary $Ag - Cu - Ti$ phase diagram at 1000^0C. As can be seen, the $liquid - bcc$ two-phase equilibrium is well-reproduced. This two-phase equilibrium was also reported by Eremenko et al. [41], although they did not report the exact compositions of the phase boundaries.The direction of the tie-lines indicating regions across the miscibility gap at thermochemical equilibrium also correspond to reported experimental results [41].

As noted above, Eremenko et al. [43] used metallographic and thermal analysis techniques to determine the existence of three invariant transformations taking place on alloys within the $Ag - Cu - Ti$ system during heating or cooling. These three invariant transformations occur when the three simultaneous crystallization curves for the phases βTi and $CuTi_2$; $CuTi_2$ and $CuTi$; $CuTi$ and Cu_4Ti_3 starting from the $L \rightleftharpoons \beta Ti + CuTi_2$, $L \rightleftharpoons CuTi_2 + CuTi$ and $L + CuTi \rightleftharpoons Cu_4Ti_3$ binary invariant points meet the boundary of the miscibility gap region of the ternary system.

As can be seen in Table 3.2, the agreement between experimental and calculated invariant points is good. There are some discrepancies, however, in the temperatures for the invariant reactions. The largest discrepancy is for the invariant reaction $L\#1 + CuTi \rightleftharpoons L\#2 + Cu_4Ti_3$. Since the thermodynamic properties of the $CuTi$ and Cu_4Ti_3 phases are already defined and verified trough the assessment of the binary $Cu-Ti$ by Hari Kumar et al. [30], the only possible explanation for this discrepancy lies in the ternary interaction parameter used to describe the Gibbs energy of the liquid phase. The fact that the calculated temperature for all the invariant reactions is lower than the experimental temperatures, indicates that the liquid phase might be too stable,

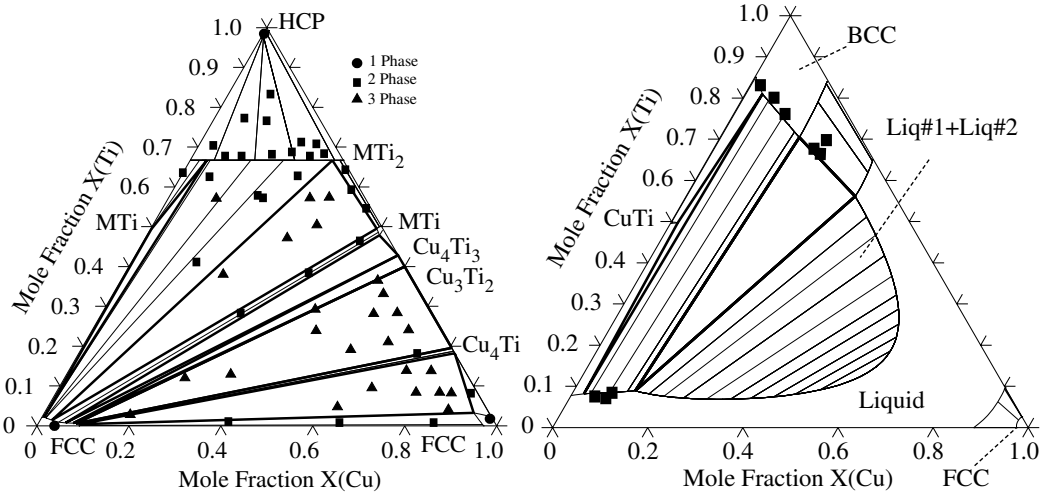

(a) Calculated and experimental phase diagram of the $Ag-Cu-Ti$ system at 700^0C. The experimental data was obtained from [42].

(b) Calculated and experimental phase diagram for the $Ag-Cu-Ti$ system at 1000^0C. Experimental data after [22].

Figure 3-4: Calculated phase diagram of the $Ag-Cu-Ti$ at two different temperatures. Experimental data points are incorporated for comparison.

and a more positive deviation from ideality might correct the discrepancy. From a sensitivity analysis on the ternary interaction parameter of the liquid phase it was found that, when the interaction parameter had values above $40,000\,J/mol$ it was impossible to find equilibria involving the invariant reactions presented in Table 3.2. It is possible, however, that this problem could be resolved if the ternary interaction parameter for the liquid phase were implemented in its asymmetrical form (please refer to Appendix A):

Table 3.2: Experimental [43] and calculated invariant points in the ternary $Ag-Cu-Ti$ system

Invariant Reaction	**Temp.^{0}C**		**x_{Cu}**		**x_{Ti}**	
	exp.	**calc.**	**exp.**	**calc.**	**exp.**	**calc.**
$L\#1+\beta\,Ti \rightleftharpoons L\#2+CuTi_2$	980	996	$\sim$ 0.25	0.22	~ 0.6	0.55
$L\#1 \rightleftharpoons L\#2+CuTi_2+CuTi$	954	991	~ 0.4	0.27	$\sim$ 0.55	0.52
$L\#1+CuTi \rightleftharpoons L\#2+Cu_4Ti_3$	900	837	$\sim$ 0.62	0.57	$\sim$ 0.37	0.38

$$L^{\phi}_{i,j,k} = \sum_{i} x^{\phi}_{i} L^{\phi}_{i,j,k} \tag{3.4}$$

where $L^{\phi}_{i,j,k}$ is the ternary interaction parameter between elements i, j, k in substitutional phase ϕ.

The problem with this approach, however, is that more degrees of freedom are introduced to the thermodynamic optimization, and the numerical values used to fit the experimental results could lead to anomalous extrapolations in regions away from the compositions explored by the experimental work. Additionally, there is also the possibility of experimental inconsistencies due to the fact that liquid alloys involving the $Ag - Cu - Ti$ system are likely to undergo extensive Ag evaporation at high temperatures [31]. Thus, since the reliability of the experiments could not be fully established, it was judged appropriate to consider the calculated results as good enough for the purposes of this work.

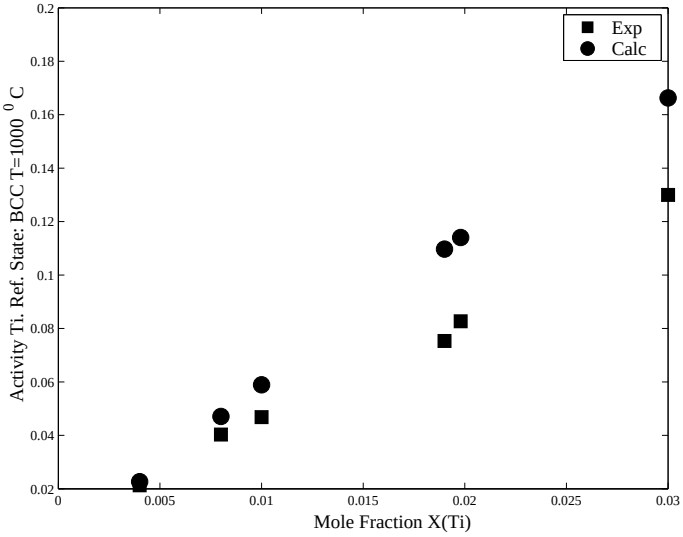

Figure 3-5: Calculated and experimental chemical activity of Ti in the eutectic melt $Ag-Cu$ at 1000^0C. The experimental data points are taken from [28]

3.2.3 Summary

In ceramic/metal joining applications that use active brazing, the chemical activity of Ti in the liquid brazing alloy is perhaps the most important factor when trying to predict the reaction products formed at the ceramic/metal interface. Thus, a reasonable calculation of the chemical activity of Ti in liquid $Ag - Cu - Ti$ melts is desired. Fig. 3-5 shows the comparison between experimental and calculated Ti chemical activities in eutectic $Ag - Cu$ melts. As can be seen, the agreement is quite good. It is important to note, however, that the calculated values are higher than the

experimental ones. This implies a higher calculated positive deviation from ideality than experimentally observed.

The correct calculation of the ternary $Ag-Cu-Ti$ system contributes to the verification of the reliability of the parameters used for the binary $Ag-Ti$ system. This is a significant result, since many inconsistencies between calculation and experiments have become evident in the analysis of this binary system (See 3.2.1). Since the $Ag-Cu-Ti$ system is extensively used in ceramic/metal joining applications, the results from this work will contribute to better understanding and optimization of technologically relevant ceramic/metal interface engineering.

3.3 Assessment of the $Cu-Ti-Zr$ System

The assessment of the $Ag-Cu-Ti$ presented in Section 3.2 is key to understanding of the thermochemical behavior of an important family of active brazing alloys [22]. Despite the successful use of this brazing alloy, a need for higher-melting active brazing alloys has recently emerged, especially in ceramic/metal joining applications involving zirconia-based ceramics. Such brazing alloys are based on novel amorphous metallic systems based on the $Cu-Ti-Zr$ ternary. It is therefore desirable to obtain a reliable description of this system that could not only be used to design better active brazing alloys but also would aid the development of novel amorphous alloys, as stated in [26].

3.3.1 Description of the $Cu-Ti-Zr$ System

Woychik and Massalski [45] studied the isothermal section of the $Cu-Ti-Zr$ system at 700^0C. Microstructures of the resulting samples were analyzed using optical microscopy, while their chemical composition was determined using electron microprobe analysis. The phase relationships at 700^0C were determined by fitting of the corresponding three-phase triangles.

One of the dominant features of the 700^0C section was the presence of the ternary phase Cu_2TiZr. This phase greatly influences the shape of the liquidus at the central region of the phase diagram and is expected to be an important competing crystalline phase in amorphous solidification processing involving this system. It was also observed that this phase enters into pseudo-binary equilibrium with most of the stable phases of the system at the experimental temperatures.

To determine any possible eutectic reactions involving this phase, Woychik and Massalski [45] used the Transient Liquid Phase (TLP) bonding technique [46]. In this procedure, two phases, A and B, are brought into contact and assembled into a sandwich structure- A/B/A, for example- at a temperature higher than the invariant point involving these phases. If there were a eutectic-type reaction involving these two phases, inter-diffusion processes would eventually lead to the formation of a liquid layer at the A/B interfaces. A liquid thus formed, gradually disappears as the

inter-diffusion process continues. However, if the liquid is quenched before it disappears, the eutectic regions can be identified in the quenched microstructure and the composition of the liquid at the eutectic point can be determined. Woychik and Massalski [45] used diffusion couples involving Cu_2TiZr and either $CuTi$, $CuZr$ or $CuZr_2$. From these experiments, the three eutectic reactions involving the Cu_2TiZr phase were determined.

Chebotnikov and Molokanov [47] studied the $CuTi_2$-$CuZr_2$ vertical region of the $Cu-Ti-Zr$ system by preparing several alloys along the $x_{Cu} = 0.33$ iso-compositional line. *XRD* analyses were performed both at high (297-697 ^{0}C) temperatures and at room temperature. Furthermore, *DTA* analysis was done on each of the samples for the entire temperature range until complete melting was detected.

XRD analyses showed that the alloys had linearly increasing a and c unit-cell parameters -while the $^c/_a$ ratio decreased- as the amount of Zr increased over the entire compositional range. This indicated that the alloys formed a single phase in which Zr and Ti atoms could be exchanged within the same lattice site of the unit cell. In these *XRD* analyses, small amounts of a ternary phase (of un-reported composition) in the central region of this iso-compositional section were detected. This ternary phase may correspond to the Cu_2TiZr phase observed by Woychik and Massalski [45].

3.3.2 Phases Described in the $Cu-Ti-Zr$ *System*

According to the experimental studies presented in 3.3.1 and the previous assessments for the subsystems $Cu-Ti$, $Cu-Zr$ and $Ti-Zr$ [30, 48, 49], the main phases present in this system are:

- **Solution Phases:** The liquid phase was modelled using a single-lattice random solution model. Since all the elements comprising this system form substitutional *fcc*, *hcp* and *bcc* solutions, they could also be modelled using the same single-lattice random solution model used for the liquid phase:

  $$(Cu, Ti, Zr)$$

  However, if one is to allow further modifications of the solid solutions (allowing the incorporation of interstitials into the solid phases) it is necessary to use a two-sublattice model:

  $$(Cu, Ti, Zr)_1 (Va)_c$$

  where c is 0.5, 1 or 3 for the *hcp*, *bcc* and fcc phases, respectively.
  The models describing the thermodynamic behavior of the solid solution phases fcc, and *hcp* were not re-assessed. The liquid and bcc phases, however, were further modified by adding an extra term to the expression for ${}^{ex}G_m^{\phi}$ (See 198).

- CuM_2 **Phase:** In their experimental work on the $Cu-Ti-Zr$ system Chebot-

nikov and Molokanov [47] determined that the phases $CuTi_2$ and $CuZr_2$ form a continuous series of solid solutions across the entire $x_{Ti} + x_{zr} = 2/3$ isocompositional line. Therefore, it was decided to model this phase as a single phase using a two-sublattice model. Cu would occupy the first sublattice while Ti and Zr atoms formed a random solution within the second sublattice. Accordingly, the sublattice notation for this phase is:

$$(Cu)\,(Ti, Zr)_2$$

- Cu_2TiZr **Phase:** In their study of the isothermal section of the $Cu - Ti - Zr$ system, Woychik and Massalski [45] identified the ternary Cu_2TiZr Laves phase in the central region of the phase diagram. Since no information on its solubility limits is available, it was decided to represent this phase as a stoichiometric compound:

$$(Cu)_2\,(Ti)_1\,(Zr)_1$$

3.3.3 Optimization of the $Cu - Ti - Zr$ System: Results

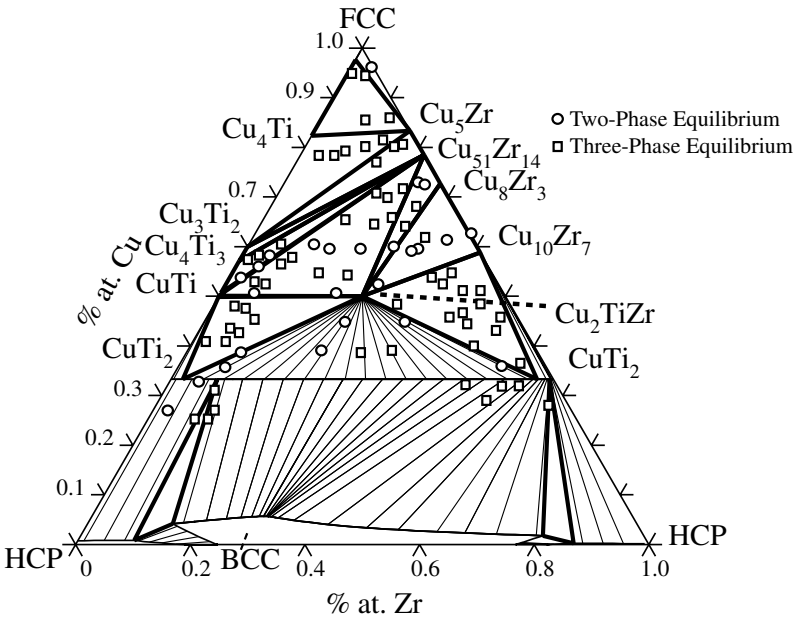

Figure 3-6: Experimental vs. calculated $Cu - Ti - Zr$ isothermal section at 703^0C

Fig. 3-6 shows the calculated and experimental [45] ternary section for the $Cu - Ti - Zr$ system at 703^0C. The agreement in most of the phase diagram is good, although there are some important discrepancies. First, Woychik and Massalski [45] have established the existence of a two-phase equilibrium phase field between the phases Cu_3Zr_2 and Cu_3Ti_2. It was found that it was not possible to reproduce this feature of the phase diagram without modifying the descriptions for the Gibbs

energies of formation for the binary phases in the $Cu-Ti$ and $Cu-Zr$ systems, as obtained by Hari Kumar et al. [30], Zeng et al. [48]. The other important discrepancy is the reported existence of a three-phase field involving the phases *hcp*, $CuZr_2$ and Cu_2TiZr. This contradicts the experiments done by Chebotnikov and Molokanov [47].

One of the most important kinds of experimental data in terms of its usefulness for thermodynamic modelling is the determination of invariant equilibrium points. The consistency between experimental and calculated invariant equilibria constitutes a good indicator of the validity of the thermodynamic descriptions used. Table 3.3 presents a comparison between the calculated and experimental invariant points, including reaction temperatures. One of the most satisfactory results was the successful calculation of the temperatures for the invariant reactions. From *TLP* experiments it is not possible to determine the temperatures at which the invariant reaction occurred. Nevertheless, all the *TLP* experiments occurred at temperatures between 855^0C and 867^0C. In order to observe eutectic (or peritectic) transformations upon quenching of the *TLP* diffusion couples, these invariant reactions must have occurred at temperatures below that temperature range. Table 3.3 shows that this is, indeed, what has been calculated.

Table 3.3: Comparison between calculated and experimental invariant points in the $Cu-Ti-Zr$ system.

Invariant Reaction	**at.%Cu**		**at.%Ag**		**Temp. ^{0}C**
	exp	**calc**	**exp**	**calc**	
$L \rightarrow CuZr + CuZr_2 + Cu_2TiZr$	48.6	44.5	37.5	41.2	833
$L \rightarrow bcc + CuZr_2 + Cu_2TiZr$	39.4	38.5	43.2	29.5	827
$L + CuTi_2 \rightarrow CuTi + Cu_2TiZr$	47.6	44.9	17.8	14.5	856

Fig. 3-7 shows the calculated and experimental [47] pseudo-binary section $CuTi_2-CuZr_2$. As can be seen, very good agreement has been achieved between the points describing the solidus and liquidus lines and the calculated pseudo-phase boundaries. According to the experiments, a minimum in the liquidus temperature is reached in the central region of the phase diagram ($33\,at.\,\%$) calculated vs. $36.7\,at.\,\%$ experimental). At this point, the liquid phase is stable down to 839^0C, which compares well with the calculated value of $\sim 827^0C$. It can also be seen that the calculation shows that a continuous series of compositions based on the $(Cu)_1\,(Ti,Zr)_2$ formula exist at temperatures below 827^0C. The stability of the CuM_2 phase over the entire compositional range from $CuTi_2$ to $CuZr_2$ has been verified experimentally. Chebotnikov and Molokanov [47] observed the presence of a ternary phase (they did not identify it) near the minimum of the liquidus in the pseudo-binary section. Fig. 3-7 shows two

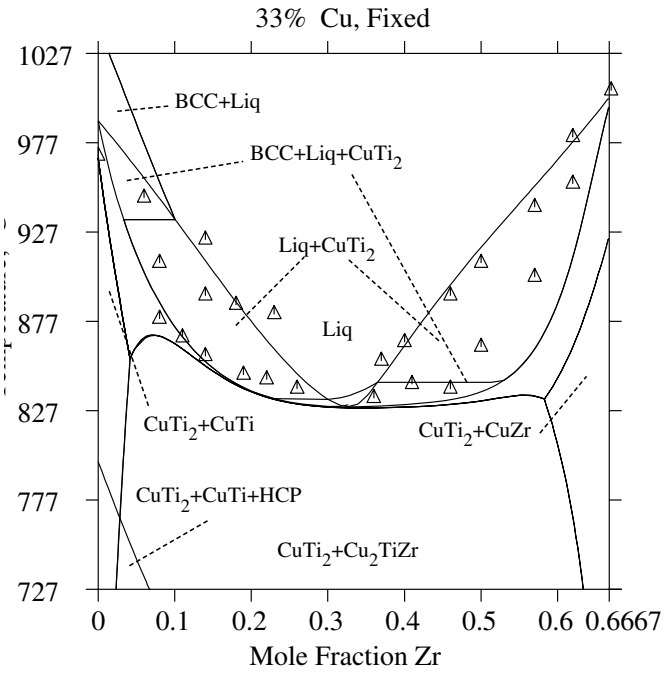

Figure 3-7: Calculated and experimental pseudo-binary section $CuTi_2 - CuZr_2$.

invariant reactions, close to 827^0C that involve the presence of the Cu_2TiZr phase.

3.3.4 Summary

The $Cu - Ti - Zr$ system was thermodynamically assessed in order to obtain an optimized and consistent thermodynamic description of all the experimentally-observed stable phases. A new description for the phases $CuTi_2$ and $CuZr_2$ was proposed. Isothermal sections and the surface for primary solidification were calculated using the assessed models. It was found that the liquid is more stable at the central region of the phase diagram.

Chapter 4

Development of Thermodynamic Database for Ceramic Oxide Substrates and Reactive Brazing Interfacial Products

4.1 CALPHAD Modelling of Ceramic Oxide Systems: Introduction

As noted in Section 2.7, reliable thermodynamic models of ceramic substrates are needed in order to obtain a better understanding of the underlying thermochemical processes occurring at ceramic/metal, C/M interfaces. Additionally, understanding the energetics of the likely reaction products resulting from interfacial C/M interactions would allow a better prediction of the equilibrium (both stable and metastable) states of the C/M interfaces created through joining operations. Although there have been attempts to describe the thermodynamics of some important ceramic/metal interaction systems through computational thermodynamics techniques [50], much work remains to be done, especially when attempting to study ceramic/metal systems that have not been broadly investigated even from the experimental point of view.

Over the past years, ceramic/metal joining operations involving the technologically-important zirconia-based ceramics have become increasingly important due to emerging technologies that rely on the creation of stable zirconia/metal interfaces [51]. A reliable thermodynamic model of such an important ceramic system is therefore essential for a better understanding of interfacial interactions between zirconia-based substrates and metallic systems. Even though this class of ceramics have been studied for several decades, there have been very few attempts at modelling their thermodynamic properties over the entire range of compositions and temperatures [52]. As a part of this chapter, the essential aspects of the thermodynamic model for the $Zr-O$ are presented, based on the much more extensive description presented in Arroyave et al. [52].

Besides requiring accurate descriptions of the thermodynamic behavior of ceramic

substrate materials, a reliable description of the thermochemical behavior of likely ceramic/metal reaction products (in this case oxides) is necessary in order to understand (and even have predictive capabilities) of the interfacial processes occurring during ceramic/metal interactions. In the case of active-metal joining of ceramic oxide substrates to metals, a complete description of the $Cu-Ti-O$, $Cu-Zr-O$ and $Ti-Zr-O$ systems is essential for the understanding of the reaction sequences observed in the corresponding ceramic/metal interfaces.

Fortunately, as will be seen below, the relevant regions of the ternary systems in question have been experimentally accessed, making the modelling of the thermodynamic properties of these systems possible. For example, the $Cu-Ti-O$ system has been studied in the region where the M_6X compounds are stable. This region is of great importance in active metal joining operations because the usual reaction products observed belong to this M_6X family of compounds. In the case of the $Cu-Zr-O$ system, there is only one published paper on the thermochemical properties of $Cu-Zr-O$ melts at low oxygen concentrations. Although this single experimental work could, in principle, be used for the thermodynamic optimization of the liquid phase in this region of the diagram, it will be shown that these results are not reliable. The $Ti-Zr-O$ system is the most extensively investigated ternary of this set and it is therefore reasonable to expect that its assessment will be the most complete. It will be shown that this is indeed the case, allowing some unimportant discrepancies in regions of the system that have no direct impact on this thesis.

The optimization of the thermodynamic parameters and the calculation of the resulting phase diagrams was done using the computational thermodynamics software Thermo-Calc®. For an explanation of the models used to describe the systems described in this chapter, please refer to Appendix A. The parameters for all of the thermodynamic models described in this chapter can be found in Appendix C.

4.2 Assessment of the $Zr-O$ System

Understanding of the chemical behavior of the $Zr-O$ system is fundamental for a wide range of relevant industrial applications, such as glass-forming metallic alloys, *SOFC*, ceramic/metal composites, thermal barrier coatings in turbine blades and so forth (see Section 5.2).

Notwithstanding its practical importance, the only thermodynamic model available for the *elemental* $Zr-O$ system up to now was developed by Kaufman and Clougherty [53]* almost four decades ago. Since the publication of that model, considerably more experimental data has been obtained and therefore it is now possible to obtain a more accurate description of the thermodynamic behavior of such an important system.

*This is quite surprising, given the importance that this system has on several technologies developed in the past few years.

In this section, the thermodynamic model for the $Zr-O$ system will be presented. The models obtained from this work will be used in the thermochemical modelling of ceramic/metal interfacial reactions.

4.2.1 Phases present in the $Zr-O$ System

The most complete critical assessment of the phase diagram information on this system corresponds to the work by Abriata and Versaci [54]. The $Zr-O$ system is of medium complexity, having several condensed-mixture phases, stoichiometric compounds and ordered-interstitial solutions:

- **Gas Phase:** In order to calculate the oxygen-rich side of the $Zr-O$ phase diagram, the gas phase had to be considered*. The ideal gas model was used, considering the following species:

$$(O, O_2, O_3, Zr, Zr_2, ZrO, ZrO_2)$$

- **Liquid Phase:** The liquid phase goes from pure liquid zirconium to stoichiometric ionic liquid ZrO_2. Therefore, any model used would have to be able to represent the Gibbs free energy of the liquid phase from pure liquid zirconium to pure stoichiometric ZrO_2 in a continuous manner. The ionic two-sublattice model for liquids [55] has been found to be extremely useful for this purpose:

$$\left(Zr^{+4}\right)_{4-2y_{O^{-2}}} \left(O^{-2}, Va^{-4}\right)_4$$

- **Solid Solutions:** It is well-known that the stable solid phases of zirconium (*bcc* and *hcp*) dissolve oxygen interstitially into their octahedral interstitial sites [56]. The solid solutions of $Zr-O$ can be represented with the two-sublattice formalism, with one sublattice occupied by zirconium atoms and the other one occupied by both oxygen and vacancies:

$$(Zr)_1 (O, Va)_c$$

  where c corresponds to the ratio of interstitial sites to normal sites in each structure.
  For the *bcc* phase, the stoichiometry ratio c is equal to 3. For the *hcp* phase, the stoichiometry ratio used was $1/2$ †.

- **Ordered Interstitial Solutions:** In binary interstitial alloys, the solubility of interstitial elements into metals is usually so low that interstitial ordering is not

*Solid-gas equilibrium calculations were necessary to optimize the properties of the ZrO_2 solid phases.

†Although in principle it is possible for the interstitial oxygen atoms to occupy twice as many vacant cites, strain energy effects make the existence of first nearest-neighbor oxygen interstitials in *hcp* structures highly unlikely [57]

observed. However, the *hcp* phases of $IV\ A$ transition elements dissolve large amounts of oxygen in their octahedral interstitial sites. In all these systems, a tendency for ordering has been observed in the low temperature, high oxygen content region of the solid-solution fields [58]. For this work, the phases Zr_6O, Zr_3O and Zr_2O were modelled as stoichiometric compounds,

$$(Zr)_c\,(O)$$

- **The ZrO_{2-x} Phases:** The ZrO_{2-x} compound can exist, at 1 $atm.$, in three different structural modifications. The low-temperature phase, $\alpha\ ZrO_{2-x}$, has a monoclinic structure and has been reported to exhibit a certain degree of non-stoichiometry. The medium-temperature tetragonal phase,$\beta\ ZrO_{2-x}$ (prototype: HgI_2), has a higher degree of non-stoichiometry. In these phases, it has been observed that under reducing conditions, oxygen vacancies are the predominant defects[59, 60]. Although there is information regarding phase boundaries and thermochemical properties of the high-temperature cubic phase,$\gamma\ ZrO_{2-x}$ (prototype: CaF_2), there is virtually no information on the defect structure of this phase. This phase presents a large degree of non-stoichiometry and is stable at temperatures far lower than the $\beta \rightarrow \alpha$ transformation temperature for the stoichiometric phases. There are however, some other non-stoichiometric oxide systems that present large degrees of non-stoichiometry and for which a defect structure has been established, CeO_{2-x} being one example [61]. For these other oxide phases, vacancies have been used to successfully model their thermochemical properties under reducing conditions. Therefore, it is possible to consider that for the $\gamma\ ZrO_{2-x}$ phase, vacancies can be considered to be the primary defect.
  For these three phases, the formation of defects can be understood using the following reaction:

$$O^{-2}_{lattice} \rightleftharpoons \frac{1}{2}O_{2,g}\ + Va + 2e^-$$

  According to this equation, the reduction of the zirconia phase involves the formation of an oxygen vacancy plus two free electrons. In fact, experiments have shown that under reducing conditions, all the allotropes of the zirconia phase change their color from white to gray or black, indicating the presence of conduction electrons [62]. Despite this fact, it has been shown that a satisfactory description of the non-stoichiometry and its relationship to oxygen potentials is possible without considering conduction electrons [57]. In their work on the $Ti-O$ system, Waldner and Eriksson [57] used a two sublattice model to describe the fluorite-type TiO_{2-x} phase. In this work, we use the same description, giving the oxygen vacancy a double negative charge to maintain electro-neutrality of the phase:

$$\left(Zr^{+4}\right)_1\left(O^{-2}, Va^{-2}\right)_2$$

Table 4.1: Comparison between calculated and experimental invariant points in the $Zr-O$ system.

Reaction	**at.%O of Respective Phases**			**Temp. ^{0}C**	
$L + (hcp) \rightleftharpoons bcc$	10.0 ± 0.5	19.5 ± 2	10.5 ± 0.5	1970 ± 10	Exp.
	10.03	22.17	10.5	1977	Calc.
$L \rightleftharpoons hcp + \gamma\ ZrO_{2-x}$	40 ± 2	35 ± 1	62 ± 1	2062 ± 10	Exp.
	41.22	31.1	62.54	2074	Calc.
$\gamma\ ZrO_{2-x} \rightleftharpoons$ $hcp + \beta\ ZrO_{2-x}$	63.6 ± 0.4	31.2 ± 0.5	66.5 ± 0.1	~ 1525	Exp.
	63.49	30.41	66.5	1530	Calc.
$L \rightleftharpoons hcp$		25.0 ± 2		2130 ± 10	Exp.
		27.5		2127.8	Calc.

4.2.2 Model Optimization and Comparison with Experimental Results

The parameters needed for the description of the Gibbs Free Energy expressions describing all the phases present (except for Gas phase) were optimized using the *PARROT* subroutine of the Thermo-Calc® software mentioned in Section A.1. A detailed account of the optimization is presented in Arroyave et al. [52].

4.2.2.1 Comparison with Phase Diagram Data

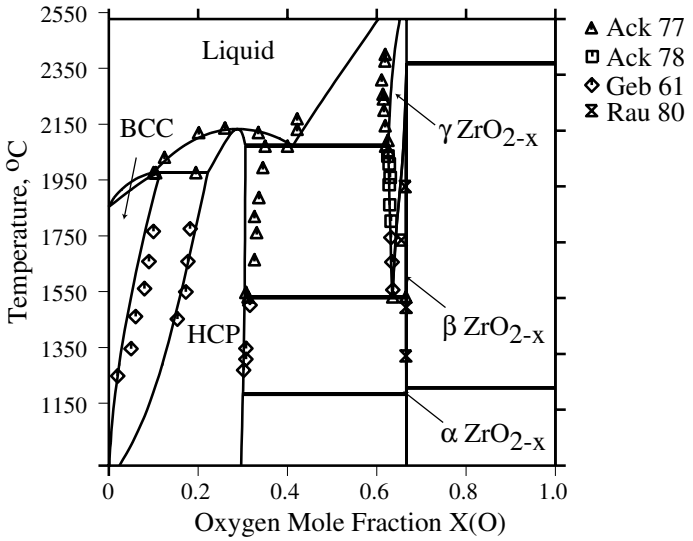

Figure 4-1: Experimental data vs. calculated $Zr-O$ phase diagram. Experimental data obtained from Ackerman et al. [63, 64], Rauh and Garg [65], Gebhardt et al. [66]

As can be seen in Fig. 4-1 and Table 4.1, the experimental and calculated phase

diagram data agree well, except for some minor discrepancies:

- The $bcc/(hcp+bcc)$ phase boundary calculated in this work presents an oxygen solubility slightly lower than that presented in the literature [66].
- One of the major discrepancies between the experimental information and the calculated phase diagram is the maximum solubility of oxygen within the *hcp* phase ($35\,at.\%\,vs.31\,at.\%$).
- Another major discrepancy is the composition at which the *hcp* melts congruently. The calculated value is $2at.\%$ higher than that reported in the literature. In similar transition metal-oxide systems, namely $Ti-O$, this composition is close to the maximum solubility composition [57], and thus there are reasons to believe that the congruent melting composition should be on the high side of the uncertainty range reported.
- The retrograde solubility observed in the lower $Liquid/(Liquid+\gamma\ ZrO_{2-x})$ phase boundary was not reproduced in the present work, but given the experimental uncertainties reported [63] we consider that the agreement is satisfactory.

4.2.2.2 Comparison with Thermochemical Data

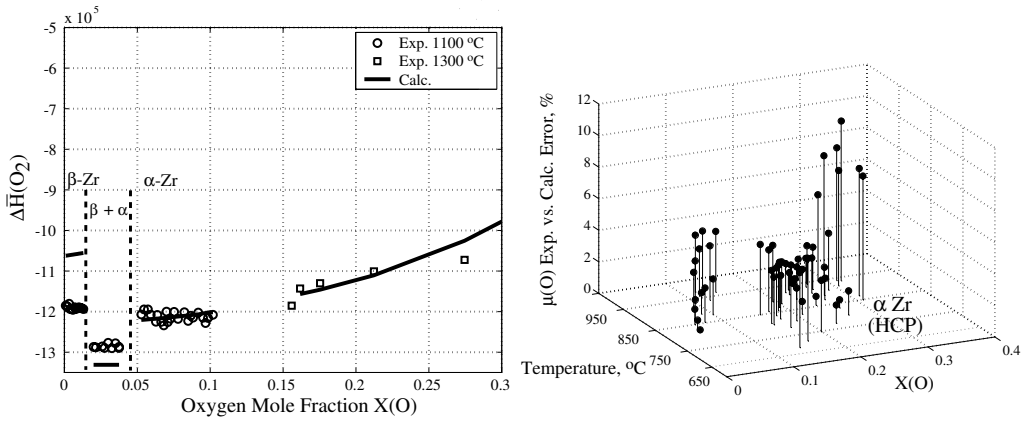

(a) Experimental [67, 68] vs. calculated partial molar enthalpies of oxygen, $\triangle\overline{H}_{O_2}$, within the *bcc*, $(bcc+hcp)$ and *bcc* phase fields.

(b) Absolute percent difference between experimental [69] and calculated chemical potential, $\mu(o)$ (Ref: $O_{2,g}$), within the *hcp phase.*

Figure 4-2: Experiment vs. calculated comparisons for the solid solution phases in the $Zr-O$ system.

Fig. 4-2(a) shows the calculated and experimental [67, 68] partial molar enthalpies of oxygen ($\triangle\overline{H}(O_2)$) within the *bcc*,$(bcc+hcp)$ and *hcp* phase fields. In general, good agreement was obtained, having a maximum error of 12% at low oxygen concentrations. From Fig. 4-2(a) it can also be seen that $\triangle\overline{H}(O_2)_{hcp}$ remains almost constant

up to $15\,at.\%$. After this composition, the molar partial enthalpy starts to increase sharply. This behavior has been observed for the $Ti-O$ system and is consistent with the presence of low-temperature ordered structures [68].

Fig. 4-2(b) shows the absolute percent difference between the experimental [69] and calculated $\mu(O)$ within the *hcp* phase field. Below $30\,at\%\ O$ there is relatively good agreement between the extensive experimental information and the calculated properties. However, when the composition approaches the solubility limit, the error increases noticeably. Near this solubility limit, Komarek and Silver [69] observed that a black layer, probably oxygen-deficient ZrO_2 was formed at the surface of the samples. Although they did not detect any weight changes, the presence of this layer may have hindered the oxidation of the metallic samples and thus affected the final compositions measured. Therefore, these experimental data should have a lower statistical weight than the ones obtained at lower oxygen concentrations.

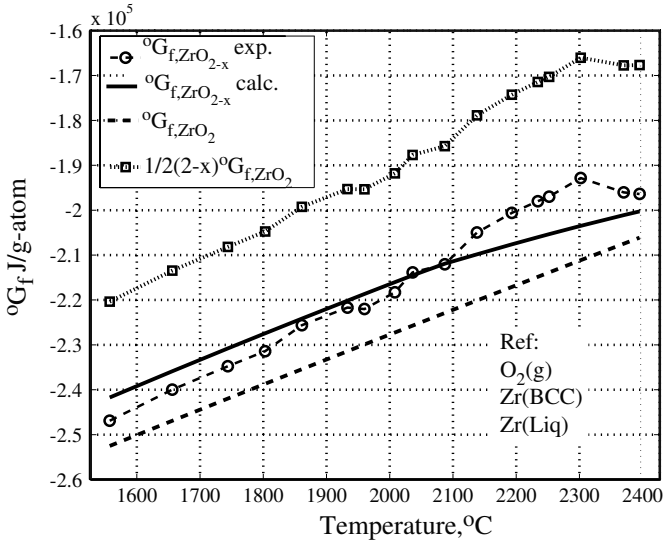

Figure 4-3: The standard Gibbs energy of formation of $\gamma\ ZrO_{2-x}$, ${}^0G_{f,\gamma\ ZrO_{2-x}}$, (experimental [70] and calculated) at the lower phase boundary-$Liquid/(Liquid+\gamma\ ZrO_{2-x})$-per mole of atoms. Comparison with ${}^0G_{f,\gamma\ ZrO_2}$ and $\frac{2-x}{2}{}^0G_{f,\gamma\ ZrO_2}$.

Fig. 4-3 shows good agreement between the experimental and calculated standard Gibbs energy of formation for the $\gamma\ ZrO_{2-x}$ high-temperature zirconia phase. As expected, the Gibbs free energy of formation for the stoichiometric phase should be more negative than that of the sub-stoichiometric phase. The experimental points were calculated using Ackerman et al. [70] mass spectroscopy measurements, together with the phase boundary data obtained in Ackerman et al. [63]. The peak observed in the experimental ${}^0G_{f,\gamma\ ZrO_{2-x}}$ curve is due to the retrograde solubility as measured by Ackerman et al. [63]. This was not reproduced using the present model and therefore in this temperature range, the discrepancies between experiments and calculations are greater. As expected, ${}^0G_{f,\gamma\ ZrO_{2-x}}$ is more negative than $\frac{2-x}{2}{}^0G_{f,\gamma\ ZrO_2}$.

This leads to a negative Gibbs energy change for the reaction [70]:

$$\frac{2-x}{2}ZrO_2(s) + \frac{x}{2}Zr(s) \rightharpoonup ZrO_{2-x}(s) \tag{4.1}$$

4.2.3 Calculated $Zr-O$ phase diagram.

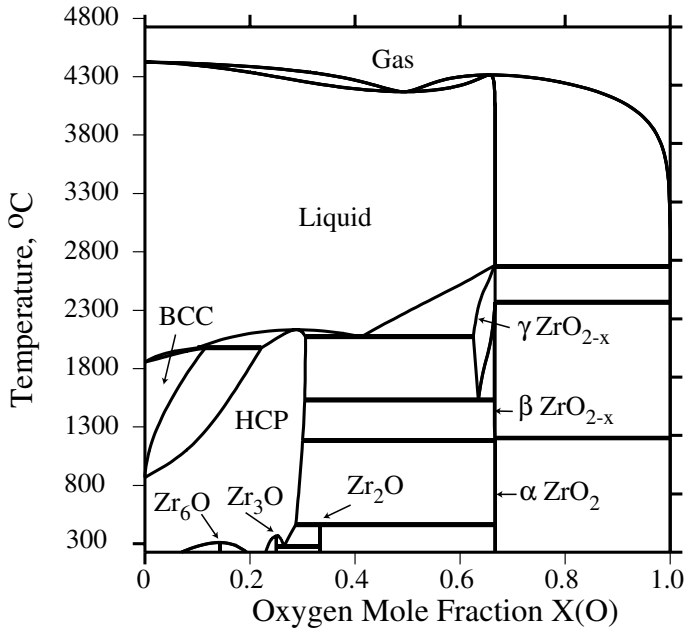

Figure 4-4: Calculated $Zr-O$ phase diagram

Fig. 4-4 shows the calculated phase diagram over the entire compositional and temperature ranges. It can be observed that the model was able to calculate the equilibrium ($CondensedPhases + Gas$) phase fields. In general, good agreement was observed between experimental and calculated phase diagram data. The invariant points and phase boundaries calculated using the model developed in this work agree well with the experimental determinations.

4.2.4 Summary

Several sets of thermochemical and phase diagram data (invariant points and phase boundaries) have been used to develop a model for the T-x phase diagram for the Zr-O system. The validity of the data used for the optimization was assessed and it was found that the data were self-consistent. This was later used to assign the relative statistical weights during the parameter optimization procedure. In general, good agreement has been observed between the experimental and calculated phase diagram and thermochemical properties.

The ordered interstitial phases present in the high-oxygen, low-temperature region of the HCP phase field have been modelled as three stoichiometric compounds. Although this does not represent the true nature of the order-disorder transformations

in interstitial *HCP-based* solid solutions, we believe that the Gibbs energies obtained are a good starting point for more complete optimizations.

Except for a few discrepancies at some invariant points, we have been able to obtain a model that is self-consistent and may serve as part of more complete databases for metallic and oxide systems. The incorporation of a more complete thermodynamic model into the studying of several technological applications involving the *Zr-O* system will allow a better understanding of the processes involved.

4.3 Modelling of the $Cu-Ti-O$ System

As noted in Section 4.1, a thermodynamic model of the $Cu-Ti-O$ system is necessary in order to understand the processes of ceramic/metal interfacial formation involving ceramic oxides and active brazing alloys. Fortunately, thermodynamic assessments of the $Cu-Ti$ [31], $Cu-O$ [71] and $Ti-O$ [34] are available and, providing these assessments are accurate enough, constitute an excellent starting point for the development of a complete thermodynamic model of the $Cu-Ti-O$ ternary system. An important characteristic of this system is that at least two ternary compounds (based on the M_6X family of compounds) play an important role as common reaction products during ceramic/metal joining operations involving oxide substrates and Ti-based active brazing alloys. In this section, a model describing the thermodynamic behavior of the $Cu-Ti-O$ system over the entire compositional range, as well as over a limited temperature interval is presented. As will be seen later in this thesis, the precise calculation of the thermodynamic properties of this system allows the understanding of reaction layer sequences in a variety of ceramic oxide/metal active brazing processes.

4.3.1 Experimental Phase Diagram of the $Cu-Ti-O$ System.

Kelkar et al. [72] studied the ternary $Cu-Ti-O$ phase relations at 945^0C around the Ti-rich corner of the phase diagram. In order to do so, they established three-phase equilibria through the mixing of powders of Ti, TiO_2, Cu and CuO with carefully controlled proportions to yield the desired overall composition. From their experiments, Kelkar et al. [72] identified the formation of two distinct M_6X-type compounds, Ti_4Cu_2O and Ti_3Cu_3O. It was found that these compounds have independent phase fields at 945^0C. These two compounds belong to the *Fd3m* space group and are iso-structural with the $\eta-carbides$ [23]. (See Table 4.2):

4.3.2 Thermal Stability range of M_6X compounds

In order to obtain a thermodynamic description of the M_6X compounds as complete as possible, it is necessary to obtain some experimental information regarding the stability ranges of the compounds in question. Kelkar and Carim [23] prepared samples of the compounds Ti_4CU_2O and Ti_3Cu_3O from Ti, TiO_2 and Cu powders. Using

Table 4.2: Phase compositions from experiments by Kelkar et al. [72]

		Phase composition (at. %)		
Sample	**Phase**	**O**	**Ti**	**Cu**
1	Ti_4Cu_2O	12.4	58.5	29.1
	Ti_2Cu	2.3	65.1	32.6
	$\alpha - Ti[O, Cu]$	19.3	79.7	1.0
2	Ti_4Cu_2O	13.1	57.7	29.2
	Ti_2Cu	2.5	64.5	33.0
	$TiCu$	1.7	49.3	49.0
3	Ti_4Cu_2O	12.4	58.5	29.1
	Ti_3Cu_3O	12.7	47.0	40.3
	$\alpha - Ti[O, Cu]$	31.0	68.1	0.6
4	Ti_3Cu_3O	13.6	43.6	42.8
	TiO	53.0	47.0	0.04
	$Cu[O, Ti]$	0.0	6.3	93.7
5	Ti_3Cu_3O	16.1	43.7	40.2
	$\alpha - Ti[O, Cu]$	32.9	66.6	0.5
	Ti_3O_2	42.7	57.1	0.3

DTA analysis techniques, the authors were able to determine the temperature range of stability of both compounds. Both M_6X compounds were observed to be stable at room temperature. The compounds were then heated under inert atmospheres at a relatively low heating rate ($3^0C/min$) until melting was detected. The melting points of Ti_4Cu_2O and Ti_3Cu_3O were found to be 1127 ± 3^0C and 1112 ± 4^0C, respectively.

4.3.3 Determination of Thermochemical Properties of M_6X Compounds

In their work, Kelkar et al. [72] used the phase compositions obtained from the microprobe analysis to determine the thermochemical properties (at 945^0C) of the M_6X compounds Ti_4O_2O and Ti_3Cu_3O. Unfortunately, their analysis was based on binary descriptions that are outdated. In this work, the most recent binary thermodynamic descriptions for the $Cu - O$, $Ti - O$, $Cu - Ti$ [30, 34, 71] are used to calculate the thermodynamic state of the experimental results obtained by Kelkar et al. [72]:

In an isothermal ternary system, a three-phase field represents a region in compositional space that is invariant with respect to the chemical potential of the elements within each of the three phases comprising this equilibrium condition. Provided that the binary phases present in this three-phase field do not exhibit pronounced ternary penetration (i.e. the third element is insoluble in the binary phases), knowledge of the individual compositions of each of the phases already *thermodynamically* described can be used to determine the thermodynamic state of the system.

In Table 4.2, the three-phase equilibrium region labelled as *Sample 1* shows that Ti_4Cu_2O is in equilibrium with $CuTi_2$ and $\alpha - Ti[O, Cu]$. Moreover, the compositional analysis shows that O is almost insoluble in $CuTi_2$ (a maximum content of $2.3\,at.\%$), while Cu is insoluble in $\alpha - Ti[Cu, O]$ (a maximum of $1.0\,at.\%$). Therefore, it can be expected that the thermodynamic state of the system can be determined from binary descriptions of the $Ti - O$ and $Cu - Ti$ systems:

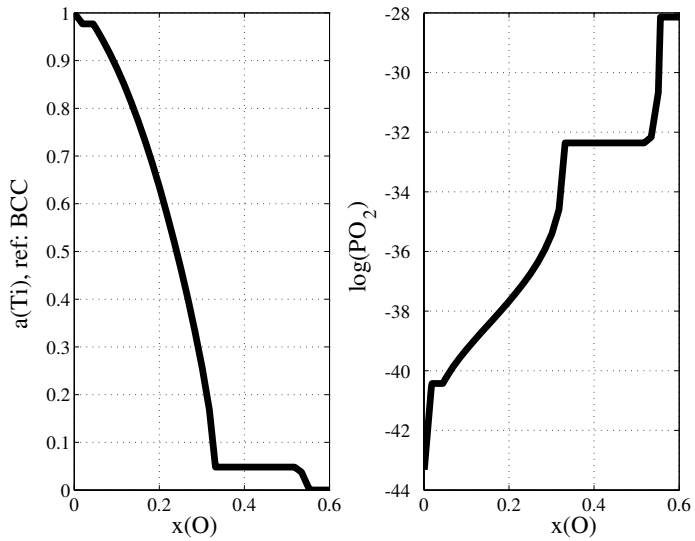

Figure 4-5: Calculated Ti and O activities in the $Ti - O$ system at 945^0C

Fig. 4-5 presents the calculated Ti and O activities in the $Ti-O$ system at 945^0C. According to Table 4.2, the Cu content in the $\alpha - Ti[O, Cu]$ phase is very low. Therefore, one could neglect any ternary thermochemical interaction between Cu, Ti and O, and therefore neglect the influence of Cu on the chemical potentials of both Ti and O in $hcp - Ti[O, Cu]$. Using the phase compositions given in Table 4.2, the activity of Ti, with respect to pure *bcc* is 0.6567, while the value for $log(PO_2)$ is -37.7899.

Fig. 4-6 shows the calculated activities (with respect to the stable structures at those temperatures) of Ti and Cu in the $Cu - Ti$ system at 945^0C. If the phase compositions presented in Table 4.2 are used, the resulting activity of Cu with respect to the fcc phase is 0.203.
Through determination of the chemical potentials of all the elements present in the

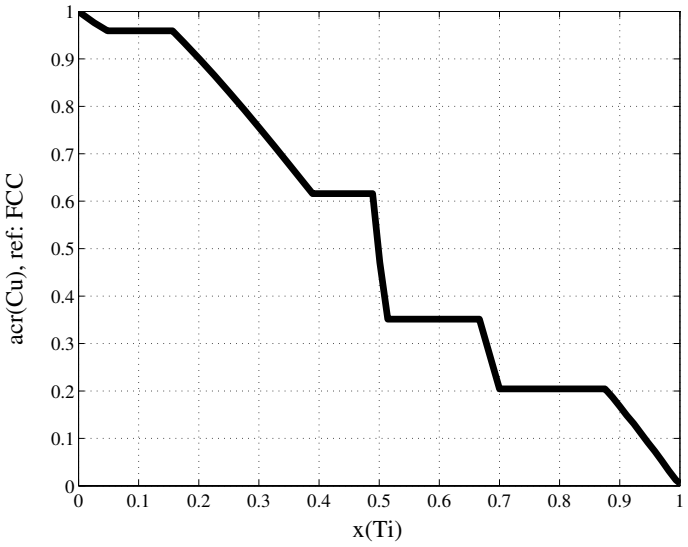

Figure 4-6: Calculated Ti and Cu activities in the $Cu - Ti$ system at 945^0C

three-phase field identified as *Sample 1*, the thermodynamic state of the system has been fully determined and it is therefore possible to obtain the Gibbs free energy for the reaction:

$$4Ti + 2Cu + \frac{1}{2}O_2 \rightarrow Ti_4Cu_2O \tag{4.2}$$

Using the standard reference states for all the components in Eq. 4.2, we can obtain the Gibbs free energy of formation of the compound Ti_4Cu_2O:

$$\begin{aligned} \Delta G_f^{Ti_4Cu_2O} &= 4\mu(Ti)^0 + 2\mu(Cu)^0 + \mu(O)^0 \\ &= RT\Big[4\ln(a_{Ti}) + 2\ln(a_{Cu}) + \frac{1}{2}\ln(P_{O_2})\Big] \end{aligned} \tag{4.3}$$

Using the values given above, the Gibbs free energy of formation of Ti_4Cu_2O at 945^0C is $-488,754\,J/mol$. Per gram-atom, this value is $-69,822\,J/g-atom$. Compared to the Gibbs free energy of formation of neighboring intermetallics, such as $CuTi_2$ (with $G_f^{CuTi_2} = -6,410\,J/g-atom$), it can be seen that this M_6X compound is very stable. The high stability of this compound implies that it would take part in a great number of equilibria, as will be seen in the phase diagram calculations below.

Once the thermodynamic state of *Sample 1* is determined, the results regarding the Gibbs free energy of formation of the other M_6X compound, Ti_3Cu_3O, can be calculated using data from other three-phase equilibrium phase fields. Sample 3 in Table 4.2 presents a three-phase equilibrium condition in which Ti_4Cu_2O, Ti_3Cu_3O and $\alpha - Ti[Cu, O]$ participate. Since the Gibbs energy of formation of Ti_4Cu_2O is already known from the previous calculation, it is possible to use only the binary description of the $\alpha - Ti[Cu, O]$ to completely determine the state of the system.

Table 4.3: Enthalpies and entropies of formation for the M_6X compounds.

Compound	$\mathbf{\Delta H_f}$	$\mathbf{\Delta S_f}$
Ti_4Cu_2O	$-631,814$	-116.51
Ti_3Cu_3O	$-655,832$	-141.67

As can be seen in Table 4.2, Cu is present in this phase in negligible quantities and therefore it is justified to ignore any thermochemical interactions between Cu and Ti, O. Moreover, since Ti presents a large thermochemical interaction with O^*, this assumption gains even more weight.

According to the results of the microprobe analysis given in Table 4.2, the composition of the $hcp - Ti[O, Cu]$ phase in thermodynamic equilibrium with Ti_4Cu_2O and Ti_3Cu_3O is 31.0 $at.\%$ for O and 68.1 $at.\%$ for Ti. With these values and aided by the results presented in Fig. 4-5, the chemical activity of Ti is 0.210, while the value for $\log(P_{O_2})$ is -35.0198. Using this values, and the reaction

$$3Ti_4Cu_2O \rightarrow 2Ti_3Cu_3O + 6Ti + \frac{1}{2}O_2 \tag{4.4}$$

the Gibbs free energy of formation for the compound Ti_3Cu_3O is given by:

$$\Delta G_f^{Ti_3Cu_3O} = \frac{1}{2}\Big(3\Delta G_f^{Ti_4Cu_2O} - RT\big[6\ln(a_{Ti}) + \frac{1}{2}\ln(P_{O_2})\big]\Big) \tag{4.5}$$

Using the values obtained for the chemical potentials of Ti and O in $hcp - Ti[Cu, O]$ and equation Eq. 4.5, the compound has a Gibbs free energy of formation of $-483,261 J/mol$, or $-69,037 J/g - atom$ at 945^0C.

From this analysis, the Gibbs free energies of formation at 945^0C of the ternary M_6X compounds have been obtained. The result, however, is not complete as no information regarding the enthalpies and entropies of formation has been obtained. In order to predict the thermal stability range of the M_6X compounds it is necessary to use the melting points[†] of the pure compounds obtained by Kelkar and Carim [23]. Using these experimental melting points, together with the thermochemical data at 945^0C it was possible to obtain the values for the enthalpies and entropies of formation of both compounds (See Table 4.3).

*Due to its high oxygen affinity

†It is not clear wether these compounds melt congruently [23]

4.3.4 *Modelling of the M_6X Compounds and Phase Diagram Calculation for the $Cu-Ti-O$ System*

In order to obtain a relatively accurate model of the two M_6X compounds, information regarding the atomic arrangement of the elements within the unit cells must be used (See Table 4.4):

Table 4.4: Structural information of Ti_4Cu_2O and Ti_3Cu_3O [73], as presented by Kelkar and Carim [23]

Compound	Ti_4Cu_2O	Ti_3Cu_3O
System	Cubic	Cubic
Space Group	Fd3m	Fd3m
Prototype	Ti_2Ni	Ti_2Ni
Atoms per unit cell	112	112
f	$48\,Ti$	$48\,Ti$
e	$32\,Cu$	$32\,Cu$
d	$16\,O$	$16\,O$
c	$16\,Ti$	$16\,Cu$

According to Table 4.4, there are four distinct atomic sites within each unit cell of the M_6X compounds. A suitable sublattice model for these M_6X compounds would be $(Ti)_3\,(Cu)_2\,(O)_1\,(Ti)_1$ for Ti_4Cu_2O and $(Ti)_3\,(Cu)_2\,(O)_1\,(Cu)_1$ for Ti_3Cu_3O. Although in the present work both compounds are modelled as stoichiometric and no specific sublattice definition is essential for the correct representation of the thermodynamic description of the phases, the present description can be useful when considering the solubility of other elements in these two compounds [74]. Once the parameters for the thermodynamic description of Ti_4Cu_2O and Ti_3Cu_3O phases have been obtained through optimization, the full ternary phase diagram can be calculated (See Fig. 4-7).

Fig. 4-7 shows the ternary phase diagram for the $Cu{-}Ti{-}O$ system at 945^0C. The triangles with the numbers indicate the experimental data points obtained by Kelkar et al. [72] and presented in Table 4.2. As can be seen, in general there is good agreement between the experimental and calculated phase equilibria.

4.3.5 *Modelling the Solubility of Al in M_6X Compounds in the $Cu{-}Ti{-}O$ System.*

In ceramic/metal brazing operations involving Al_2O_3 and active metal brazes based on the $Ag-Cu-Ti$ ternary alloy, reaction products belonging to the M_6X-type

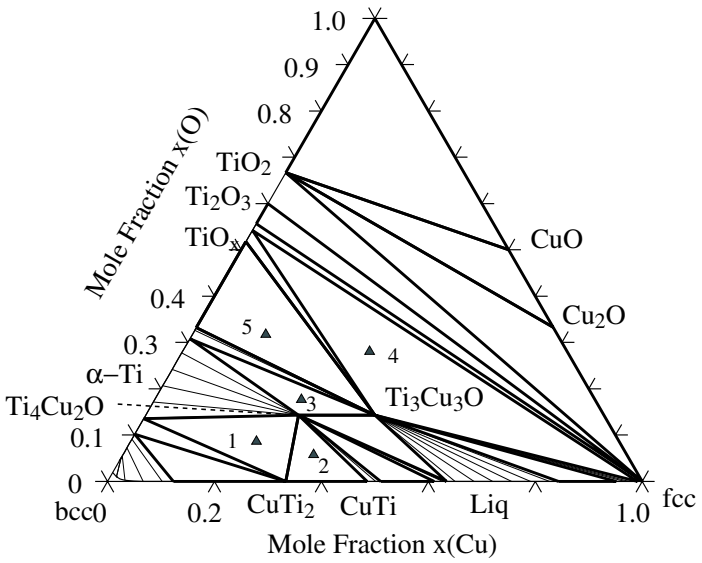

Figure 4-7: Calculated $Cu - Ti - O$ system at 945^0C.

compounds have been observed [74]. In many of these cases, the reaction products involved show a tendency to dissolve aluminum, which results from the dissolution of Al_2O_3 into the brazing alloy. In some cases, the reaction products have compositions corresponding to $(Ti, Al)_4 Cu_2O$ [75]. Under different chemical conditions, compounds with the $Ti_3 (Cu, Al)_3 O$ have also been observed [76]. It is therefore necessary to account for the solubility of Al into the M_6X compounds.

Kelkar and Carim [74] studied the Al solubility in the M_6X compounds Ti_4Cu2O and Ti_3Cu_3O by mixing Al, Ti and CuO powders and arc melting them under Ar. The resulting pellets were subsequently annealed at 945^0C for 8 days, to allow complete equilibration. By using XRD and $EPMA$ techniques, they were able to determine solubility limits for both M_6X compounds. While the Ti_4Cu_2O compound was shown to exhibit a limited Al solubility ($1.5\,at.\%$), the Ti_3Cu_3O compound exhibited a relatively large solubility range, going from Ti_3Cu_3O to Ti_3Cu_2AlO. Using the XRD results, Kelkar and Carim [74] were able to identify the location of Al in the M_6X structure, which is the location identified as c in Table 4.4. This means that for the Ti_3Cu_3O compound, Cu and Al form a random solution in the c site:

$$(Ti)_3 (Cu)_2 (O)_1 (Al, Cu)_1$$

With the compositions of the samples analyzed by Kelkar and Carim [74] and using a similar strategy to the one outlined in 4.3.3, it was possible to obtain the Gibbs free energy of formation for the Ti_3Cu_2AlO Al end-member of the $(Ti)_3 (Cu)_2 (O)_1 (Al, Cu)_1$ phase at 945^0C ($-580,000\,J/mol$). In order to obtain a temperature dependence for this Gibbs energy of formation, it was further considered that this compound undergoes melting at the same temperature as the Ti_3Cu_3O phase:

Table 4.5: Enthalpies and entropies of formation for the M_6X compounds.

Compound	$\mathbf{\Delta H_f}$	$\mathbf{\Delta S_f}$
Ti_3Cu_2AlO	$-850,000$	-221.5

4.3.6 Summary

In the present section, the solid region of the $Cu-Ti-O$ system has been critically assessed using both thermal and phase diagram information. The thermodynamic stability of the important M_6X compounds has also been determined. Because of its usual presence in ceramic/metal joining operations, Al has been incorporated to the thermodynamic description of the Ti_3Cu_3O phase.

As will be seen in Chapter 5, the M_6X compounds of the $Cu-Ti-O$ system are usually present in ceramic/metal joining applications. Therefore, the thermodynamic assessment of such compounds is of fundamental importance if one is to understand the reaction phenomena occurring during ceramic/metal joining.

4.4 Critical assessment of the $Cu-Zr-O$ liquid phase.

As noted in Section 3.3, in order to understand the nature of the chemical interactions occurring at the interface between Cu-based brazing alloys and ZrO_2-based ceramic substrates, an accurate description of the thermochemistry of $Cu-Zr-O$ melts is necessary. Fortunately, thermodynamic descriptions for the $Cu-Zr$, $Cu-O$ and $Zr-O$ are available in the literature [48, 52, 71]. In the next section it will be seen that third-order interaction parameters are not likely to play an important role in determining the chemical behavior of $Cu-Zr-O$ melts.

4.4.1 $Cu-Zr-O$ Melts

Despite the importance of its use as a de-oxidizing agent in copper-based melts (See Haessler et al. [77]), the effect of zirconium on the thermochemistry of oxygen-containing copper melts has been reported only once [78]. In that work, Sudavtsova [78] used the *EMF* technique to measure the oxygen chemical potential as a function of zirconium content in copper melts through measuring the voltage signal across an electrolytic cell using zirconia-based membranes and solid metal-metal oxide powder mixtures as reference electrodes. From these measurements (made in the $1423-1523\,K$ temperature range), Sudavtsova [78] obtained the following results:

i) The slope of a plot of $-log\,(a_O)$ vs. $-log\,(\%\,Zr)$ had a value of $\frac{1}{2}$, which, according to the reaction

$$Zr+2\,[O] \Leftrightarrow ZrO_2 \tag{4.6}$$

indicates that as soon as Zr is added to an O-containing Cu melt, ZrO_2 precip-

itates, according to the reaction constant, K:

$$K = \frac{a_{ZrO2}}{a_O^{1/2} a_Zr} \tag{4.7}$$

ii) By plotting the relationship between $-log\,(f_O)$ vs. $\%\,Zr^*$, Sudavtsova [78] found that the interaction parameter e_O^{Zr}, defined as

$$e_O^{Zr} = \left(\frac{\partial log\,(f_O)}{\partial \%Zr} \right)_{\%Zr \to 0} \tag{4.8}$$

had a value of -220. In terms of the *Raoultian* activity coefficient γ, the equivalent interaction parameter ϵ, can be calculated using(See Lupis [19, chap. VII,IX]):

$$\varepsilon_O^{Zr} = 230 \frac{M_{Zr}}{M_{Cu}} e_O^j + \frac{M_{Cu} - M_{Zr}}{M_{Cu}} \sim -75,000 \tag{4.9}$$

It is possible to use the ionic liquid two-sublattice model, as described by Hillert et al. [55] and modified by Sundman [80]:

$$\left(Cu^{+1}, Cu^{+2}, Zr^{+4}\right)_P \left(O^{-2}, Va\right)_Q \tag{4.10}$$

where $P = 2 \cdot y_{O^{-2}} + Q \cdot y_{Va}$ and $Q = 4y_{Zr^{+4}} + 2y_{Cu^{+2}} + y_{Cu^{+1}}$. By using the thermodynamic descriptions of the $Cu - Zr$, $Zr - O$ and $Cu - O$ subsystems from [48, 52, 71], it is possible to obtain a mathematical description analogous to Eq. A.32 (please refer to Appendix A):

$$\begin{aligned}
&G^{ionic} = y_{Zr^{+4}} y_{O^{-2}} \cdot {}^0G_{Zr^{+4}:O^{-2}} + y_{Cu^{+2}} y_{O^{-2}} \cdot {}^0G_{Cu^{+2}:O^{-2}} + y_{Cu^{+1}} y_{O^{-2}} \cdot {}^0G_{Cu^{+1}:O^{-2}} \\
&+Qy_{Va} \left\{ y_{Zr^{+4}} {}^0G_{Zr^{+4}:Va} + y_{Cu^{+2}} {}^0G_{Cu^{+2}:Va} + y_{Cu^{+1}} {}^0G_{Cu^{+1}:Va} \right\} \\
&+R \cdot T \left[\begin{array}{l} P \left\{ y_{Zr^{+4}} \ln\left(y_{Zr^{+4}}\right) + y_{Cu^{+2}} \ln\left(y_{Cu^{+2}}\right) + y_{Cu^{+2}} \ln\left(y_{Cu^{+2}}\right) \right\} \\ +Q \left\{ y_{O^{-2}} \ln\left(y_{O^{-2}}\right) + y_{Va} \ln\left(y_{Va}\right) \right\} \end{array} \right] \\
&+y_{Cu^{+1}} y_{Cu^{+2}} y_{O^{-2}} \cdot \left\{ L_{Cu^{+1},Cu^{+2}:O^{-2}} \right\} + y_{Cu^{+1}} y_{O^{-2}} y_{Va} \cdot \left\{ L_{Cu^{+1}:O^{-2},Va} \right\} \\
&+y_{Zr^{+4}} y_{O^{-2}} y_{Va} \cdot \left\{ L_{Zr^{+4}:O^{-2},Va} \right\} + Qy_{Va}^2 y_{Cu^{+1}} y_{Zr^{+4}} \left\{ L_{Cu^{+1},Zr^{+4}:Va} \right\} \\
&+y_{Cu^{+1}} y_{Zr^{+4}} y_{O^{-2}} y_{Va} \cdot {}^0L_{Cu^{+1},Zr^{+4}:O^{-2},Va}
\end{aligned} \tag{4.11}$$

Provided that the thermodynamic descriptions available for the subsystems $Cu - Zr$, $Zr - O$ and $Cu - O$ are reliable, the only parameter that in theory needs to be optimized to obtain an accurate description of the $Cu - Zr - O$ liquid system is

---

*f_O is the Henrian activity coefficient of oxygen having $1\,wt.\%$ as the standard state, and is defined as

$f_2 = {}^{a_2^H}/_{\%2}$. It is possible to define the value of f_2 at infinite dilution, since f_2 must become equal to the slope of the Henrian line. This means that $(f_2)_{\%2 \to 0} = 1$. For a much more comprehensive explanation, refer to Lupis [79, chap. VII].

that corresponding to the last term of Eq. 4.11, namely ${}^{0}L_{Cu^{+1},Zr^{+4}:O^{-2},Va}$. Since this parameter is multiplied by the site fractions of all the main components in the $(Cu^{+1}, Cu^{+2}, Zr^{+4})_P (O^{-2}, Va)_Q$ system ($y_{Cu^{+1}} y_{Zr^{+4}} y_{O^{-2}} y_{Va}$), it is expected that at very small dilution values of both Zr and O ($y_{Zr} \sim y_O \sim 0$), the relative importance of this parameter on the overall value of the Gibbs free energy (and the resulting oxygen chemical potential) would be small. If this assertion is true, it would be possible to use only the binary descriptions to obtain an approximate calculation of the thermochemical properties of $Cu - O - Zr$ melts at very small contents of both O and Zr. Since, as noted above, the presence of even very small quantities of Zr leads to the precipitation of ZrO_2, the calculations of the thermochemical properties of $Cu - O - Zr$ melts were done considering that the only thermodynamically stable phase was the liquid*. To make the calculations somewhat compatible with the experimental data measured by Sudavtsova, the Wagner(See [35] and [19]) approximation was used †:

$$\ln \gamma_O = \ln \gamma_0^{\infty} + \varepsilon_O^O x_O + \varepsilon_O^{Zr} x_Z r + O\left(x^2\right) \tag{4.12}$$

From the model, the following parameters were obtained:

Table 4.6: Parameters for dilute $Cu - O - Zr$ solutions, using the Wagner formalism [35].

Parameter	$\mathbf{A} + \frac{\mathbf{B}}{\mathbf{T}}$		**Range, K**
	A	**B**	
$\ln \gamma_0^{\infty}$	4.4	−8880	$T > 1473$
ε_O^O	19.4	−38390	$T > 1473$
ε_O^{Zr}	5.2	−167890	$T > 1473$

At $1473\,K$, the expression for the activity coefficient of oxygen in dilute $Cu - O - Zr$ melts is given by:

$$\ln \gamma_O = -1.6 - 6.7 x_O - 108 x_Z r \tag{4.13}$$

From Eq. 4.13, it is obvious that there is a difference of 2 orders of magnitude between the values for the ε_O^{Zr} obtained by Sudavtsova [78] ($\varepsilon_O^{Zr} \sim -75,000$) and the value calculated using the thermodynamic optimizations by [48, 52, 71] ($\varepsilon_O^{Zr} \sim -110$). In order to reconcile this difference, it is necessary to analyze the possible sources for the inconsistencies both within the thermodynamic model itself and within the experimental procedure used to measure this thermodynamic quantity.

*This is equivalent to assuming that there is a relatively large kinetic barrier for the precipitation of ZrO_2 particles in $Cu - O - Zr$ melts.

†Note that $a(O) = \gamma_O x_O \; Ref : O_{2,g}$

4.4.2 *Assessment of the Validity of the Thermodynamic Model for* $Cu-O-Zr$ *melts.*

Given the differences between the experimental and predicted value for ε_O^{Zr}, it is essential to consider the effect of third-order parameters ($^0L_{Cu^{+1},Zr^{+4}:O^{-2},Va}$ in Eq. 4.11) on the chemical potential of oxygen in $Cu-O-Zr$ melts. According to Sundman [80], $^0L_{Cu^{+1},Zr^{+4}:O^{-2},Va}$ can be given a compositional dependence*:

$$\begin{aligned} L_{Cu^{+1},Zr^{+4}:O^{-2},Va} = {}^0L_{Cu^{+1},Zr^{+4}:O^{-2},Va} + (y_{O^{-2}} - y_{Va})\,{}^1L_{Cu^{+1},Zr^{+4}:O^{-2},Va} \\ + (y_{Cu^{+1}} - y_{Zr^{+4}})\,{}^2L_{Cu^{+1},Zr^{+4}:O^{-2},Va} \end{aligned} \tag{4.14}$$

At infinite dilution (i.e. pure Cu), the effect of the ^0L parameter cannot be decoupled from the ^1L, since $(y_{O^{-2}} - y_{Va}) \sim -1$. Furthermore, since Zr is only present in very small amounts, ^0L and ^2L have almost the same effect, given the fact that $(y_{Cu^{+1}} - y_{Zr^{+4}}) \sim 1$. Thus, at infinite dilution, the compositional dependence of the $L_{Cu^{+1},Zr^{+4}:O^{-2},Va}$ can be neglected.

Assuming that the binary descriptions for the subsystems $Zr-O$, $Cu-O$ and $Cu-Zr$ are correct, reduction of the difference between the experimental results by Sudavtsova [78] and the models can only be possible by modifying the ternary interaction represented by ^0L. Fig. 4-8 illustrates the effect of varying the value of the ^0L ternary parameter on the calculated oxygen chemical potential $\mu(O)$ for a specific oxygen and zirconium concentration. As can be seen, the effects ($\pm 1 \times 10^3\, J/mol$) are small†, even for the greatest value for the ^0L parameter (i.e. $\pm 1 \times 10^6\, J/mol$). In the range of values explored, the relative difference between $\mu(O)$ calculated with and without ^0L amounted to less than 0.5 %.

Since ε_O^{Zr} is a second order parameter (See Eq. 4.12), the effect of the value of the ^0L ternary parameter on the calculated value of ε_O^{Zr} is expected to be much more pronounced than that on $\mu(O)$. Fig. 4-9 shows a plot of ε_O^{Zr} vs. ^0L. As can be seen in Fig. 4-9 the effect of varying ^0L is significant. It is therefore reasonable to assume that by thermodynamically optimizing this parameter, the experimental value obtain by Sudavtsova [78] can be reproduced. However, when an extrapolation is made on the plot depicted in Fig. 4-9 to obtain values for ε_O^{Zr} that approach the experimental ones ($\sim -75,000$), it is found that the necessary values far exceed what can reasonably be expected ($^0L \sim -1 \times 10^8\, J/mol$)‡. From this analysis it can be concluded that it is highly unlikely that the differences between the experimental and calculated ε_O^{Zr}

*Note that the Cu^{+2} species can be ignored as it is not expected to be present in significant amounts until very high levels of oxygen are present in the melt, as observed by Assal et al. [81].

†At infinite dilution, $\mu(O) \sim \mu(O)_{^0L=0} + x_{Zr} \cdot {}^0L$

‡As a manner of comparison, the value for the ^0L ternary interaction parameter for the $Ag-Cu-O$ system reported by Assal et al. [81] is only $\sim 1 \times 10^4$. Although this is clearly a different system and the thermochemical interactions between Ag and O cannot be compared to those between Zr and O, the fact that relatively small values for ^0L account for ternary experimental results indicates that, in ternary metallic oxygen-containing melts, binary parameters are dominant.

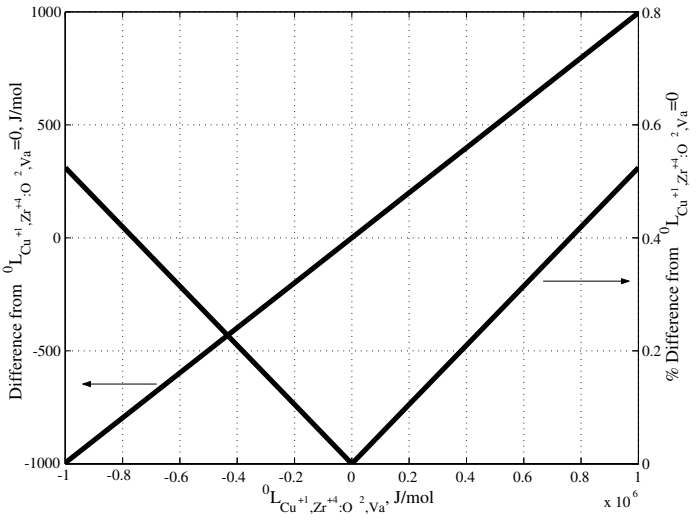

Figure 4-8: Effect of the ${}^0L$ parameter on the oxygen chemical potential (J/mol) in a copper solution with $x_O = 1 \times 10^{-6}$ and $x_{Zr} = 1 \times 10^{-3}$ at $1473\,K$

parameters can be explained by third-order interaction parameters for the ionic liquid two-sublattice model $(Cu^{+1}, Cu^{+2}, Zr^{+4})_P\,(O^{-2}, Va)_Q$

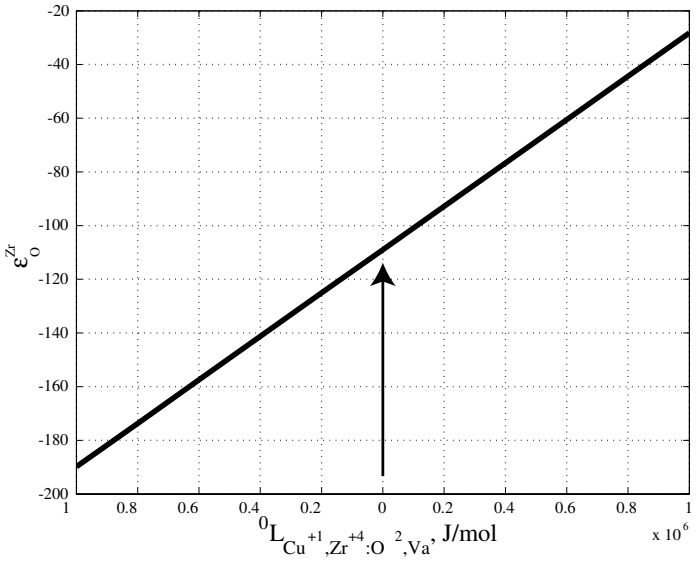

Figure 4-9: Effect of the ${}^0L_{Cu^{+1},Zr^{+4}:O^{-2},Va}$ parameter on the value for ε_O^{Zr} in $Cu - O - Zr$ melts.

4.4.3 Wagner interpolation method.

In his paper on the the chemical behavior of metallic alloys containing trace amounts of oxygen, Wagner [82], attempted to obtain an interpolation formula to determine the activity coefficient of oxygen in binary metallic mixtures. According to this analysis, oxygen atoms are considered to be present in liquid metallic melts as quasi-

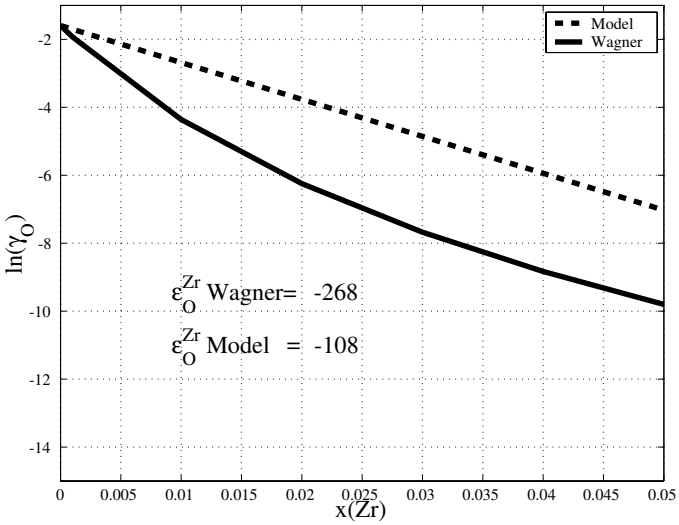

Figure 4-10: Comparison between calculated oxygen activity coefficient in $Cu - Zr - O$ metallic liquids using the two-sublattice model and Wagner [82] interpolation at $1473\,K$

interstitials*. Using an analysis analogous to standard central-atom models, Wagner obtained the following expression:

$$\gamma_O = \left[\frac{(1 - X_B)}{\left(\gamma_{O(A)}\right)^{1/Z}} + \frac{(1 - X_B)}{\left(\gamma_{O(B)}\right)^{1/Z}} \right]^{-Z} \tag{4.15}$$

where γ_O is the chemical activity coefficient, Z is the coordination number of a oxygen quasi-interstitial in its solvation cell, $X(B)$ is the mole fraction of element B and $\gamma_{O(x)}$ is the chemical potential of oxygen at infinite dilution in liquid metal X.

Using $Z = 6$† and the calculated values for the activity coefficient of oxygen at infinite dilution in Cu and Zr, it is possible to obtain an approximate value for the activity coefficient of oxygen at infinite dilution in $Cu - Zr$ metallic mixtures. In Fig. 4-10, a comparison is made between calculated (using the two-sublattice model) and interpolated (using Eq. 4.15) oxygen activity coefficient at $1473\,K$. As can be seen, there is a crude agreement between both calculations, the agreement improving as x_{Zr} decreases. However, it can be seen that both calculations yield similar values for ε_O^{Zr} ($\varepsilon_{O,Wagner}^{Zr} = -208$ vs. $\varepsilon_{O,Model}^{Zr} - 108$). Note that there is only a difference of a factor of 2 and that both values differ greatly from the experimentally determined $\epsilon_O^Z r \sim -75,000$.

*The main argument being the large difference in atomic radii between oxygen (0.66Å) and transition metals (~ 1.2Å).

†$Z = 6$ corresponds to the coordination number of a quasi-interstitial of the octahedral type in a closed-packed structure.

4.4.4 Summary

Based on this analysis, it is concluded that despite the existence of recent experimental information regarding the thermochemistry of dilute $Cu-O-Zr$ melts, it is necessary to generate more experimental information to shed light on the nature of the discrepancies between existing experiments and calculations using *CALPHAD* models. For the purpose of this work, it will be considered that the model $(Cu^{+1}, Cu^{+2}, Zr^{+4})_P\,(O^{-2}, Va)_Q$, without third-order interaction parameters constitutes a reasonable approximation to the description of ternary $Cu-O-Zr$ melts.

4.5 Thermodynamic Assessment of the $Ti-Zr-O$ System

Many zirconia-metal interfaces of practical relevance involve thermochemical interactions between the ceramic and active metals, such as Ti, Zr, Hf, etc. It is therefore necessary to have a clear understanding of the thermodynamics behavior of such zirconia-active-metal systems and, since Ti is the active metal most commonly encountered in such applications, it has been determined that the assessment of the $Ti-Zr-O$ system was essential for the understanding of such interfaces.

4.5.1 Phases Present in the $Ti-Zr-O$ System

The most complete collection of experimental work on the $Ti-Zr-O$ system has been compiled in Ondik and McMurdie [83, pp.11-14, and pp.136-140]. In this compilation, several phases have been identified. In this section, only the phases whose models have been modified (with respect to the $Ti-Zr$, $Ti-O$ and $Zr-O$ binary descriptions [34, 49, 52]) or that appear only in the ternary Gibbs triangle are described:

- **Gas Phase:** In order to calculate the oxygen-rich side of the $Ti-Zr-O$ phase diagram, the gas phase had to be considered*. The ideal gas model was used, considering the following species:

$$(O, O_2, O_3, Ti, Ti_2, TiO, TiO_2Zr, Zr_2, ZrO, ZrO_2)$$

- **Liquid Phase:** The liquid phase in the $Ti-Zr-O$ system has been observed to go from either pure metallic Ti or Zr [49] to the purely ionic liquid along the TiO_2-ZrO_2 pseudo-binary section [84]. As in the $Zr-O$ system, assessed in Section 4.2, it is therefore necessary to use a sublattice model capable of reproducing this behavior in a continuous manner. The ionic two-sublattice model for liquids [55, 80] has been found to present an accurate description of systems of such characteristics. A detailed description of this model is presented in A.2.4. In the sublattice notation, this model, for the $Ti-Zr-O$ system,

*As in Section 4.2, solid-gas equilibrium calculations were necessary to optimize the properties of the solid oxide phases.

can be represented as

$$\left(Ti^{+2}, Ti^{+3}, Ti^{+4}, Zr^{+4}\right)_P \left(O^{-2}, Va\right)_Q$$

where

$$P = 2y_{O^{-2}} + Qy_{Va}$$
$$Q = 2y_{Ti^{+2}} + 3y_{Ti^{+3}} + 4y_{Ti^{+4}} + 4y_{Zr^{+4}}$$

- **Solid Solutions:** As has been noted in Lee [34], Arroyave et al. [52], Waldner and Eriksson [57], it is well-known that the stable solid phases of zirconium and titanium (*bcc* and *hcp*) dissolve oxygen interstitially into their octahedral interstitial sites. The *metallic* solid solutions of the $Ti - Zr - O$ can be represented with the two-sublattice formalism, with one sublattice occupied by zirconium and/or titanium atoms and the other one occupied by both oxygen interstitials and vacancies:

  $$\left(Ti, Zr\right)_1 \left(O, Va\right)_c$$

  where c corresponds to the ratio of interstitial sites to normal sites in each structure.

  For the *bcc* phase, the stoichiometry ratio c is equal to 3. For the *hcp* phase, the stoichiometry ratio used was 0.5.

- **The ZrO_{2-x} Phases:** The ZrO_{2-x} compound can exist, at 1 *atm.*, in three different structural modifications (see Section 4.2). Of these three phases, the high temperature ones (βZrO_{2-x} (tetragonal) and γZrO_{2-x} (cubic)) have been observed to dissolve TiO_2 in significant quantities [85, 86]. It is therefore necessary to modify the models used in Section 4.2 to account for this fact. Because of the experimental difficulties involving the study of the higher-temperature phase (γZrO_{2-x}), and according to the $TiO_2 - ZrO_2$ assessment presented by Park et al. [84], the only zirconia phase that was modified was βZrO_{2-x}, whose sublattice model is given by:

  $$\left(Ti^{+4}, Zr^{+4}\right)_1 \left(O^{-2}, Va^{-2}\right)_2$$

  As can be seen, the fact that only Ti^{+4} is considered in the model (as opposed of titanium species with other valences, such as Ti^{+3}) implies that the βZrO_{2-x} phase behaves as a solid solution of ZrO_{2-x} and TiO_2 in the tetragonal, HgI_2, structure.

- **The *Rutile* Phase:** The *Rutile* phase has been previously modelled by Lee [34] and others with a description identical to the one used to model the high-temperature zirconia phases. This phase has been observed to dissolve signifi-

cant amounts of ZrO_2 [85] and therefore, it is necessary to describe it as:

$$\left(Ti^{+4}, Zr^{+4}\right)_1 \left(O^{-2}, Va^{-2}\right)_2$$

- **Ternary Intermetallic Solutions:** In their comprehensive review of the experimental information of the $TiO_2 - ZrO_2$ pseudo binary system, Ondik and McMurdie [83, 136-140] report that the existence of two ternary compounds, with nominal compositions $ZrTiO_4$ and $ZrTi_2O_6$. Although these phases have been observed to present certain degree of non-stoichiometry, they are considered to be stoichiometric phases in this work, with a sublattice description:

$$\left(Zr^{+4}\right)\left(Ti^{+4}\right)_A \left(O^{-2}\right)_B$$

  where $A = 1\, B = 4$ for $ZrTiO_4$ and $A = 2\, B = 6$ for $ZrTi_2O_6$.

- **Omega Phase:** According to [83], a ternary phase, identified as ω (omega) and with hexagonal structure has been identified at low temperatures in the $Ti - Zr - O$ system. From experimental data it has been possible to determine that this phase (with a broad homogeneity region) results from the transformation of the high-temperature *bcc* phase, along the $Ti_3O - Zr_3O$ iso-compositional line. The $bcc \rightarrow \omega$ transformation occurs at $\sim 1200^0C$. The ω phase has been observed to be stable at low temperatures $< 400^0C$. Because of lack of enough experimental data the presence of this phase was ignored and instead it was considered that the *bcc* phase could take its place in the phase diagram.

4.5.2 Optimization and Comparison to Experimental Data I: 1450^0C *Isothermal Section*

One of the most complete characterizations of the phase relations and invariant reactions occurring in the $Ti-Zr-O$ system was the study performed by Hoch and Dean [87]. In this work, Hoch and Dean [87] investigated the isothermal section of the $Ti-Zr-O$ system at 1450^0C. After holding the samples at 1450^0C for long enough time to ensure equilibration, the samples were analyzed using XRD, identifying all the phases present in any given sample.

According to Fig. 4-11(b) and Fig. 4-4 (see Section 4.2) it can be observed that O tends to stabilize the *hcp* solid solution. In Fig. 4-11(a), on the other hand, the mutual chemical interaction between $Ti - Zr$ tends to stabilize the *bcc* phase, with respect to the *hcp* phase. The isothermal section of the $Ti - Zr - O$ at 1450^0C reported by Hoch and Dean [87] shows that, at least at this temperature, the *bcc* phase's stability range extends from the $Ti-Zr$ binary up to the $x_O = \frac{1}{3}$ composition. In Fig. 4-11(a) it is shown that the maximum stability of the *bcc* phase is observed at the $x_{Ti} = x_{Zr} = 0.5$ composition. It is therefore reasonable to expect that this will also be the case for the isothermal section.

As can be seen in Fig. 4-12, the agreement between the experimental [87] and

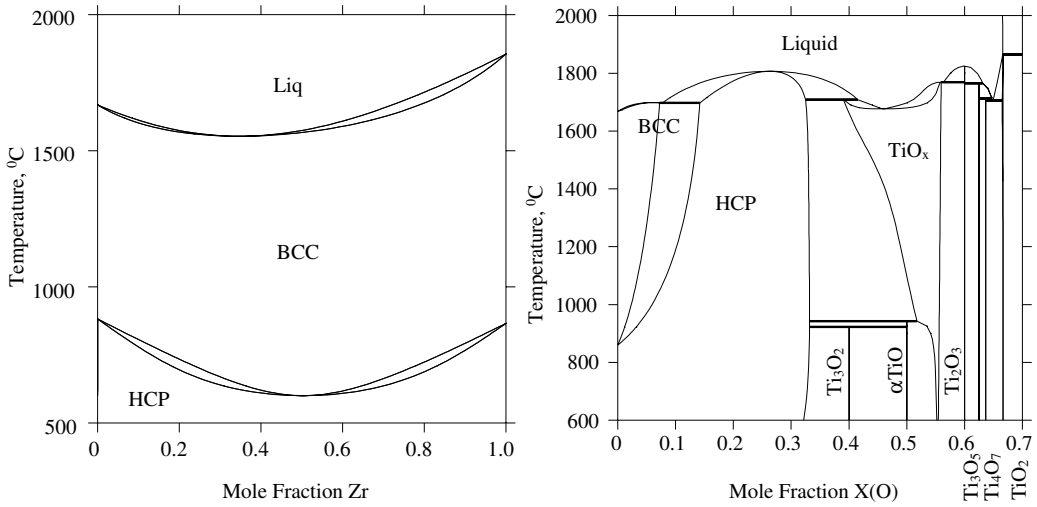

(a) Calculated $Ti - Zr$ phase diagram, from assessment by Kumar et al. [49].

(b) Calculated $O - Ti$ phase diagram, from assessment by Lee [34].

Figure 4-11: Calculated phase diagrams belonging to the $Ti - Zr - O$ system.

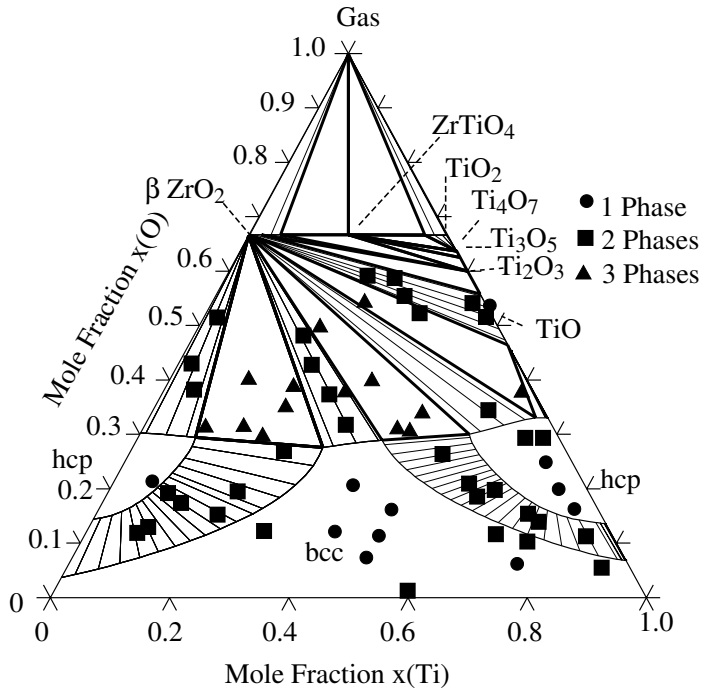

Figure 4-12: Comparison between calculated and experimental ([87]) $Ti-Zr-O$ isothermal section at 1450^0C.

calculated 1450^0C isothermal section of the $Ti - Zr - O$ phase diagram agree well. Except for very few regions of the section, the single, double and triple phase regions of the system have been accurately represented. As can be observed, the βZrO_{2-x} phase is in thermodynamic equilibrium with most of the phases present in the system.

The reason for this is the large thermodynamic stability of this phase*, with respect to any other phase in the system. The absence of any intermediate suboxide in the $Zr-O$ system is also a consequence of the great stability of this phase (see Fig. 4-4 in Section 4.2). It can also be observed that the maximum oxygen solubility observed in the ternary *bcc* phase is about $30\,at.\%$, as has been observed in Hoch and Dean [87]. This maximum solubility is not an artifice of the model (from the description in 4.5.1 it can be observed that the *bcc* phase could, in principle, dissolve much greater amounts of oxygen in its relatively open lattice.) and this constitutes additional verification of the assessment, at least for this isothermal section.

4.5.3 Optimization and Comparison to Experimental Data II: Liquidus Surface

Hoch and Dean [87] also examined the liquidus surface of the $Ti-Zr-O$ system up to the TiO_2-ZrO_2 composition. During the optimization of this set of experimental data it was observed that the liquid description had to be modified extensively, adding fourth-order interaction parameters,

$$G^{ion,ex,4^{th}} = L^{0}_{Ti^{+2},Zr^{+4}:O^{-2},Va} + (y_{O^{-2}} - y_{Va})\, L^{1}_{Ti^{+2},Zr^{+4}:O^{-2},Va}$$

in order to obtain a reasonable liquidus surface, in agreement with the experimental data. Despite numerous efforts at optimizing the thermodynamic parameters of the *liquid*, *bcc* and *hcp* phases, it was not possible to obtain complete agreement between the observed invariant reactions and the calculated ones. Several of these invariant reactions involved the βZrO_{2-x} and γZrO_{2-x} phases. Since the thermodynamic optimization of the TiO_2-ZrO_2 pseudobinary was done independently (based on the assessment by Park et al. [84]), the number of degrees of freedom available for the optimization was not the adequate, as the optimization of the TiO_2-ZrO_2 pseudobinary (see below) was deliberately fixed, once a satisfactory description of this isopleth was obtained.

*i.e. Large Gibbs free energy of formation.

Table 4.7: Comparison between calculated and experimental invariant points in the $Ti-Zr-O$ system. Experimental temperatures have an estimated variation of ± 10. Note: N/A means that the model used is not able to calculate such an invariant reaction.

Reaction		$at.\%Ti$		$at.\%O$		T, ^0C	
exp	calc	exp	calc	exp	calc	exp	calc
$L \rightarrow bcc + hcp + \beta ZrO_2$	$L + hcp \rightarrow bcc + \gamma ZrO_2$	19	20	35	38	1845	1850
$L \rightarrow bcc + hcp + \beta ZrO_2$	$L + bcc \rightarrow hcp + \gamma ZrO_2$	47	31	34	39	1825	1798
$L \rightarrow bcc$	$L \rightarrow bcc$	38	19	25	16	1930	2012
$L \rightarrow hcp + TiO + \beta ZrO_2$	$L \rightarrow hcp + TiO + \beta ZrO_2$	54	49	42	46	1750	1665
$L \rightarrow TiO + \beta ZrO_2 + \gamma ZrO_2$	N/A	34	N/A	12	N/A	1700	N/A
$L \rightarrow TiO + Ti_2O_3 + \gamma ZrO_2$	$L \rightarrow TiO + Ti_2O_3 + \beta ZrO_2$	58	60	36	32	1650	1714
$L \rightarrow Ti_2O_3 + Ti_3O_5 + \gamma ZrO_2$	N/A	58	N/A	36	N/A	1650	N/A
$L \rightarrow Ti_2O_3 + TiO_2 + TiZrO_4$	$L \rightarrow Ti_2O_3 + TiO_2 + TiZrO_4$	65	66	30	28	1700	1635
$L + Ti_3O_5 \rightarrow Ti_4O_7 + \gamma ZrO_2$	N/A	65	N/A	31	N/A	1730	N/A
$L + \gamma ZrO_2 \rightarrow Ti_4O_7 + TiZrO_4$	N/A	65	N/A	31	N/A	1710	N/A
$L + TiO_2 \rightarrow \gamma ZrO_2 + TiZrO_4$	N/A	66	N/A	20	N/A	1790	N/A

Table 4.7 shows the calculated and experimental invariant reactions obtained by Hoch and Dean [87]. One of the most common discrepancies found in the table is the

identity of the ZrO_2 phase involved in the invariant reactions. In general, the identity of the ZrO_2 is inverted. For the experimental invariant reactions involving βZrO_2, the corresponding calculated ones involve γZrO_2 and viceversa. In their experimental work, Hoch and Dean [87] report XRD analyses for their experiments on the ternary $Ti - Zr - O$ section at 1450^0C. For the liquidus surface determination, they do not report any XRD measurements so the identity of the phases involved in the detected invariant reactions is not unambiguous. However, if it is assumed that the phases taking part in the observed invariant reactions have been positively identified, then the discrepancies between calculation and experiment can be due to deficiencies in the model.

In their assessment of the $TiO_2 - ZrO_2$ pseudo-binary section, Park et al. [84] report that, although there is some evidence regarding the existence of a peritectic reaction $\gamma ZrO_2 \rightarrow \beta ZrO_2 + L$ at 2300^0C reported by Shevchenko et al. [88], there is a great discrepancy with other experimental results [85, 89], possibly due to the experimental difficulties involved in measuring phase relations at such high temperatures. If the peritectic reaction reported by Shevchenko et al. [88] really exists, and the $TiO_2 - ZrO_2$ system were optimized taking this information into account, then the 'correct' ZrO_2 phase could be obtained.

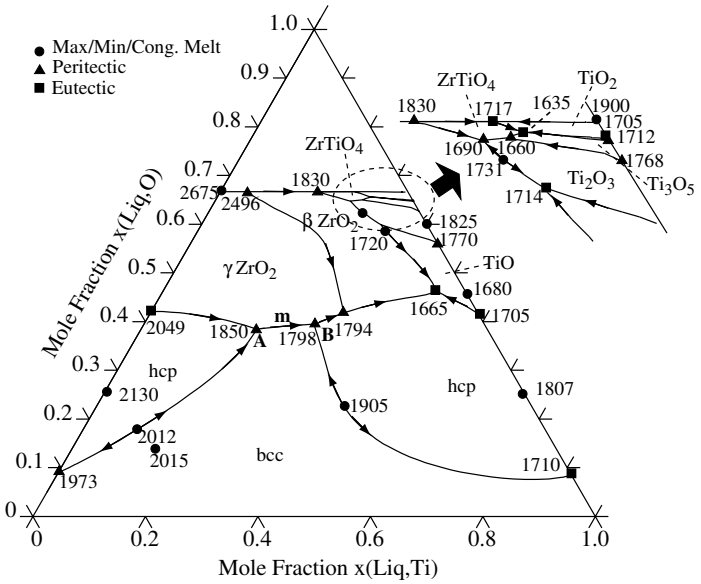

Figure 4-13: Calculated liquidus surface for the ternary system $Ti - O - Zr$.

In addition to discrepancies regarding the proper ZrO_2 involved in the first 2 invariant reactions presented in Table 4.7 ($L \rightarrow bcc + hcp + \beta ZrO_2$,$L \rightarrow bcc + hcp + \beta ZrO_2$), there is a discrepancy concerning the actual character of the reactions. Fig. 4-13 shows the calculated liquidus surface for the $Ti - Zr - O$ system. The eutectic reactions $L \rightarrow bcc + hcp + \beta ZrO_2$,$L \rightarrow bcc + hcp + \beta ZrO_2$ are marked with **A** and **B**. From this figure, it can be seen that, in order for these two reactions to

exhibit a eutectic character, it would be necessary for the monovariant line involving the $L, \gamma ZrO_2 and bcc$ (**m**) to exhibit a maximum. Using conventional optimization techniques [90], it is not currently possible to define the character of an invariant reaction as experimental information entered into the error minimization procedure. The character of the invariant reactions was therefore not considered in the model optimization.

At the very end of Table 4.7, it can be seen that there are three invariant reactions involving phases close to the $TiO_2 - ZrO_2$ pseudo-binary that cannot be calculated with the model parameters obtained with the optimization. In 4.5.4 a more detailed discussion of the discrepancies in this region of the liquidus surface is presented.

4.5.4 Optimization and Comparison to Experimental Data III: $TiO_2 - ZrO_2$ *pseudobinary section*

As mentioned in 4.5.2, [84] have already developed an assessment for the $TiO_2 - ZrO_2$ pseudobinary section of the $Ti - Zr - O$ system. Because of the pseudobinary character of this vertical section, this assessment can be used, in principle, independently of the rest of the $Ti - Zr - O$ system. The fact that the $TiO_2 - ZrO_2$ pseudobinary is virtually independent of the rest of the phase diagram can be best illustrated by observing the behavior of the liquid phase*. This can be best illustrated by examining the behavior of the liquid phase, from the metallic region of the compositional space, to the ionic oxide. Fig. 4-14 shows the site fraction of the different Ti charged species ($Ti^{+2}, Ti^{+3}, Ti^{+4}$) on the cationic sublattice (see A.2.4) for a constant titanium composition ($10\, at.\%$) and varying oxygen mole fraction. In the metallic region of the system, and up to high oxygen mole fractions ($x_O \sim 0.6$), the only titanium charged species is Ti^{+2}. This changes abruptly when the oxygen mole fraction reaches the $TiO_2 - ZrO_2$ section. At this point, Ti^{+4} is virtually the only titanium species in the melt. Since in the $TiO_2 - ZrO_2$ pseudobinary the only metallic cations are Ti^{+4} and Zr^{+4}, even the thermodynamic description of the liquid phase is independent of the rest of the assessment.

As has been noted above, the assessment for the $TiO_2 - ZrO_2$ system has been already published [84]. Since Park et al. [84] use their own description of the ZrO_2 system (which they do not reference in their work) a consistency problem with the rest of the database presented in this chapter (specially the one involving the $Zr - O$ binary) became evident as soon as the present model for the $Zr - O$ system was included. Although Park et al. [84] used the same description for the $Ti - O$ system [34] as the one used in this thesis, it was not possible to reproduce the correct $TiO_2 - ZrO_2$ section. The model for the $TiO_2 - ZrO_2$ system had therefore to be re-assessed.

Fig. 4-15 shows the calculated $TiO_2 - ZrO_2$ section with the experimental data points as compiled by [84]. As can be seen, except for the liquidus region, close to the

*Which uses the two-sublattice model for ionic liquids [80].

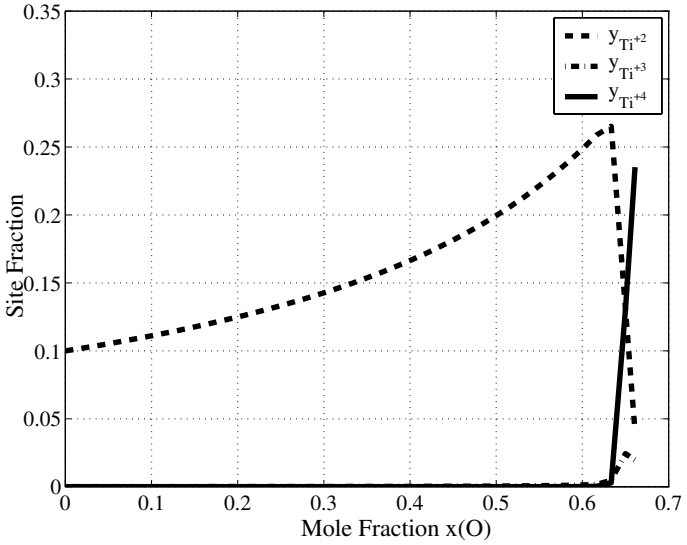

Figure 4-14: Site fraction of Ti ions in the cationic sublattice of the ionic liquid phase.

$x_{TiO_2} = x_{ZrO_2}$ composition, the agreement is good. Phase boundaries for the solid phases have been reproduced, as well as the temperatures and compositions for the invariant reactions relevant for this pseudobinary section.

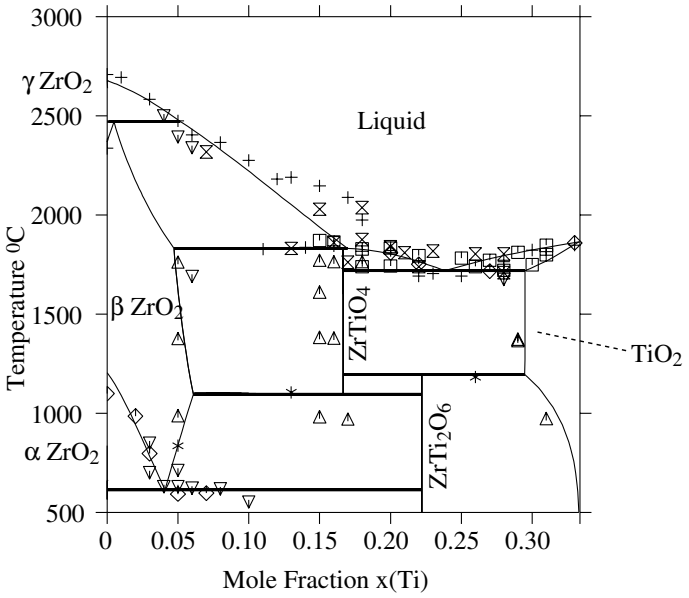

Figure 4-15: Comparison between calculated and experimental $TiO_2 - ZrO_2$ section. The experimental data points [85, 86, 88, 89, 91–93] were taken from the compilation by Park et al. [84].

The agreement between experiments and calculations does not rule out possible deficiencies in the model. In 4.5.3, it was shown that there are discrepancies in the calculated and experimental [87] liquidus surface. Although some of the discrep-

ancies can be attributed to deficiencies in the thermodynamic descriptions of the solid solution phases (*bcc*, *hcp*), many are likely to originate from discrepancies in the $TiO_2 - ZrO_2$ model. As was said in Section 4.5.3, the fact that the calculated and experimental invariant points in the metallic region of the system (see first four rows of Table 4.7) have the ZrO_2 phases inverted could be due to the fact that the present $TiO_2 - ZrO_2$ description does not consider the peritectic reaction as reported by Shevchenko et al. [88]. Because other works contradict this result [85, 92], it was not possible to assign a significant statistical weight to this data point.

4.5.5 Summary

Despite the discrepancies observed in the liquidus surface for the $Ti - Zr - O$ system, it can be considered that the present assessment constitutes a good approximation to the correct thermodynamic description for the $Ti - Zr - O$ ternary system, over a wide range of temperatures and composition. In the following chapters of this work, this description will be particularly useful to rationalize the interfacial interactions between zirconia-based ceramics and Ti.

Chapter 5

Application of Thermodynamics to the Study of Ceramic/Metal Interfaces

5.1 Introduction

In Chapter 3 and Chapter 4, thermodynamic models have been developed to describe several metallic and oxide systems that are of interest in ceramic/metal joining applications:

i) Using the thermodynamic descriptions of the $Ag-Cu-Ti$ and $Cu-Ti-Zr$ systems (see Section 3.2 and Section 3.3) it is possible to improve the design process for active brazing alloys. Important parameters in active brazing alloys, such as chemical activity of the reactive element and solidus/liquidus points as a function of alloy composition can be easily calculated for a great number of alloys without having to perform costly experimental runs.

ii) The thermodynamic description of the $Cu-Ti-O$ system (see Section 4.3) allows understanding of the reaction sequence observed in a great number of oxide/metal joining experiments that rely in the addition of Ti to otherwise non-reactive brazes.

iii) The main purpose of this thesis is to provide a methodology for the understanding, analysis and prediction of ceramic/metal interfacial interactions in a general manner. However, to illustrate the methodology, special attention has been placed to the understanding of the interactions between zirconia-based ceramics and active metals. Therefore, the thermodynamic models for the $Ti-Zr-O$ and $Cu-Zr-O$ (see Section 4.5 and Section 4.4) are essential to this work.

In the present chapter, the *CALPHAD* (or continuum) thermodynamic models developed in Chapter 3 and Chapter 4 will be used to analyze the available experimental evidence regarding the interfacial interactions between zirconia and active metals (principally titanium). By using metastable thermodynamic calculations and activity diagrams it will be shown that the reaction layer sequences observed under

several experimental conditions reported in the literature can be rationalized. Finally, experimental work on the joining of zirconia-based ceramics and Inconel ® superalloys will be presented and the results will be analyzed, using the techniques presented below.

5.2 Interfacial Interactions between Zirconia and Reactive Metals: Motivation and Fundamentals

As has been noted in Section 4.2, zirconia-based ceramics have several characteristics that make them attractive for a number of important industrial applications:

i) In Solid Oxide Fuel Cells, *SOFC*, for example, zirconia-based ceramics are used because of their ionic transport properties, as well as their high-temperature resistance [94]. Because of their transport properties, zirconia-based ceramics are also used as oxygen sensors in a variety of industries and for a variety of chemical conditions [95].

ii) Zirconia exhibits high strength and fracture toughness, particularly at temperatures below 600^0C [96]. This makes it the material of choice for high-temperature structural applications [97]. However, because of the great volume change undergone when this material transforms from the tetragonal polymorph to the monoclinic structure ($\triangle V \sim 4\,\%$), the use of pure zirconia is limited when the ceramic part is to be subjected to thermal cycling conditions. In order to make zirconia into a practical structural ceramic, different aliovalent dopants (Mg, Ca, Y) have been used to decrease the transformation temperature and retain either the cubic or tetragonal phases over a greater temperature range*. Provided the detrimental phase transformations are suppressed, zirconia-based ceramics constitute an excellent choice when a ceramic material is necessary for high-temperature, high-corrosion applications.

iii) Finally, because of their thermal, oxidation, corrosion and wear resistance, zirconia-based ceramics are the material of choice in thermal barrier coatings for turbine blades [98].

5.2.1 Motivation for the Study of Zirconia/Metal Interactions

In all the applications listed above, the understanding of the formation and evolution of ceramic/metal interfaces is key to their development and improvement:

In *SOFC* applications, the anode material is usually a Ni/YSZ cermet†. At the high operating temperatures of *SOFC*, the Ni in the cermet can act as an electronic conductor, while the YSZ is used to reduce the thermal mismatch between the electrode and the electrolyte. Although the use of these composite materials is promising,

*See Section 4.2.

†YSZ is zirconia stabilized with yttria.

the agglomeration of nickel particles due to sintering is a limiting characteristic in electrode performance of *SOFC* [99]. Since sintering is fundamentally a surface energy problem, understanding of the interfacial interactions and wetting characteristics of Ni/YSZ and Ni-Ti/YSZ systems is essential for the improvement of current *SOFC* designs.

As has been noted above, zirconia-based ceramics constitute the materials of choice for high-temperature structural applications in which the mechanical properties of metallic parts must be combined with the thermal resistance of ceramics [96]. As noted in Section 2.6, one of the most common ceramic/metal joining techniques is active brazing. Therefore, understanding of the thermochemistry of ceramic/active metal interfacial reactions is of fundamental importance for the design of strong and reliable ceramic/metal joints.

A limit to the application of zirconia-based ceramics as thermal barrier coatings for turbine blades is the spalling and de-bonding that occurs as the zirconia/metal interface is subjected to elevated temperatures for long times. One of the reasons for this de-bonding is the formation of what is known as a thermally grown layer [100]. This reaction layer is formed by the migration of oxygen, from the zirconia lattice into the metal and its subsequent reaction with active elements in the metal, such as Ti, Al and Cr. An understanding of active element migration, reaction layer formation and morphological evolution of such interfaces is fundamental for the improvement of current thermal coating technologies.

Although this work is mainly focused on application of thermodynamic and kinetic to the study of zirconia/active metal interactions (particularly for *C/M* joining applications), the proposed methodologies of analysis can be easily applied to other cases were zirconia/metal interactions play an important role. It is expected that the same approach can be applied to any case were interfaces between dissimilar materials are encountered.

5.2.2 Interactions between Zirconia and Active Elements

One of the most distinctive features of zirconia-based ceramics, is the relatively high degree of non-stoichiometry that they can withstand without decomposing. This is particularly true for the cubic phase, which can be reduced from oxygen/metal ratios of 2.0 to $\sim$ 1.9 (see Section 4.2)*. As has been noted above, to suppress thermal shock and improve the overall toughness of this ceramic material, aliovalent impurities † are added so the cubic phase is stabilized and the detrimental $c \rightarrow m$ or $t \rightarrow m$ transitions, with their large transformation volume are avoided. The introduction of aliovalent cations into the cubic lattice introduces vacancies to maintain the electroneutrality

*This degree if non-stoichiometry is greatly increased by doping zirconia with aliovalent impurities.

†Aliovalent impurities are those cations whose normal valence state is different from that of Zr^{+4}

condition. For example, when Y_2O_3 is added to ZrO_2, the electroneutrality condition would be given by [101]:

$$\left[Y'_{Zr}\right] = 4\left[V_O^{\bullet\bullet}\right]$$

According to a thermodynamic model developed for the $ZrO_2 - YO_{1.5}$ system by Hillert and Sakuma [102] and later refined by Katamura and Sakuma [103], the presence of oxygen vacancies, due to the introduction of aliovalent impurities, plays a dominant role in determining the stability of the cubic phase and the lowering of the $c \rightarrow t$ phase transition. To a first approximation, the solid solution formed when aliovalent impurities are added to the zirconia phase can be considered to be ideal.

Besides the extensive oxygen vacancy presence in stabilized zirconia due to the introduction of aliovalent cations, the stabilization of the cubic phase to lower temperatures will also allow the zirconia phase to withstand high degrees of non-stoichiometry, as is observed in the high-temperature, γZrO_{2-x} phase (see Section 4.2). Under localized reducing conditions, as those encountered when zirconia-based ceramics are put in contact with a highly reactive metal*, it is reasonable to expect that oxygen vacancies can be generated through the partial reduction of the Zr^{+4} cations.

Perhaps the most readily available evidence of the partial reduction of zirconia-based ceramics is the discoloration (blackening) of cubic zirconia ceramics subjected to strong chemical [51, 96] or electrochemical [104, 105] reduction conditions. To understand the partial reduction of zirconia, Janek and Korte [105] proposed several reactions schemes. In one of them, electrons are trapped at the oxygen vacancies created by the mass flow of oxygen ions towards the reducing surface of the crystal. These electrons in turn may be associated with the Zr^{+4} cations, reducing their overall valence to Zr^{+3}. The free charge carriers generated by this reduction reaction will interact with photons, giving the reduced zirconia its characteristic color.

In their analysis of the oxygen-deficient region of electrochemically reduced Y-PSZ, Kanda et al. [104] found, through *XPS* analysis, that the the reduced regions within the zirconia crystal exhibited larger peaks corresponding to the Zr^{+3} valence sate†. Moreover, after analyzing the bonding state of the $Y - O$ complexes within the zirconia lattice, they found that the Y^{+3} ions did not seem to be affected by the reduction of the Zr^{+4} ions, which is consistent with the fact that the $Y - O$ bonds are stronger than the $Zr - O$ bonds‡.

Regardless of the nature of the microscopic reduction conditions, the overall effect of the localized reduction of the zirconia lattice can be expressed in the following

*Such as titanium, zirconium, and so forth.

† Kanda et al. [104] also observed Zr^{+2} and Zr^{+1} peaks, but they interpreted them as ion-electron defect clusters, rather than an actual reduction of the Zr^{+4} ion.

‡The standard heat of formation, per mole of oxygen for ZrO_2 is $-545\,kJ/mol$, while that of Y_2O_3 is $-586\,kJ/mol$ [104].

equation [105]:

$$ZrO_2 + 2\delta e^{'} + \delta V_O^{\bullet\bullet} \leftrightarrow ZrO_{2-\delta} + \delta O_O^X$$

In the early stages of the localized reduction, a moving interface between the reduced and non-reduced regions within the zirconia crystal is expected to appear [105]. The movement of this interface is determined by the ionic and electronic conductivities within the material. Once a steady state is reached, a fixed oxygen chemical potential gradient may be imposed across the zirconia layer due to fixed chemical potentials at both extremes of the ceramic. Although the analysis presented above was applied to the electrochemical reduction of zirconia through the application of large electric fields, it is possible to relate these observations to the case in which the zirconia layer is subjected to an oxygen potential gradient, which is the case in zirconia/active-metal interactions.

Another important characteristic of zirconia-based ceramics is the difference in the diffusion rates for the ionic species observed in these materials. In their study of the diffusion mechanisms in YSZ, Solmon et al. [106] obtained the diffusion coefficients for the Zr^{+4}, Y^{+3} and O^{-2} ions within the zirconia lattice. These results are presented in Table 5.1.

Table 5.1: Ionic diffusion coefficients in YSZ crystals [106]. Note that $D = D_0 e^{\frac{-Q}{RT}}$

Ion	$\mathbf{D_0}$,$\mathbf{cm^2/s}$	**Q**,**kJ/mol**	**D at 1500 K**,$\mathbf{cm^2/s}$
Zr^{+4}	0.093	$+461 \pm 17$	8.21×10^{-18}
Y^{+3}	0.248	$+462 \pm 23$	2.37×10^{-17}
O^{-2}	0.001	$+86 \pm 2$	1.01×10^{-6}

As can be seen, the cationic diffusion coefficients are several order of magnitude lower than the oxygen diffusion coefficient. The implication of this experimental result is that it is possible to neglect the migration of cationic species towards the ceramic/metal interface, provided no $ZrO_2 \rightarrow (Zr) + \frac{1}{2}(O)$ decomposition reaction occurs.

In the following sections, thermodynamic models will be applied to the analysis of the ceramic/metal interactions occurring when zirconia substrates are put in contact with reactive elements. Before presenting the analysis, though, it may be useful to enumerate the assumptions made in the analysis, as well as their justification:

i) According to the thermodynamic models by Hillert and Sakuma [102] and Kata-

mura and Sakuma [103], the main effect of introducing aliovalent dopants in zirconia-based ceramics is the increase of the thermodynamic stability of the cubic phase (γZrO_{2-x}) due to the introduction of stabilizing oxygen vacancies. As a first approximation, the solid solution between ZrO_2 and its dopants can be consider as ideal. To analyze the thermodynamic interactions between zirconia solid solutions and active elements, it is possible to consider only the pure cubic zirconia phase, assuming that is stable (or metastable) at lower temperatures.

ii) Although most of the experimental work on the interactions between zirconia-based ceramics and active metals has been done with doped materials, it is possible to ignore the interaction between the dopants and the active metal. This assumption is justified by the findings by Kanda et al. [104]. As noted above, in YSZ, the Y^{+3} ions did not seem to change their oxidation state even under highly reducing conditions. This seems to be correlated with the stronger $Y-O$ bonding energy. The same can be expected to happen with zirconia-based ceramics stabilized with MgO and CaO, which have a more negative free energy of formation than ZrO_2.

iii) From the diffusion experiments performed by Solmon et al. [106], it is evident that, once subjected to a gradient in oxygen chemical potential, the only ions that will diffuse out of the zirconia lattice and into the zirconia/metal interface would be the oxygen ions, provided the zirconia phase itself does not decompose. Contrary to what could be expected with other ceramic systems that do not have large degrees of non-stoichiometry (i.e. Al_2O_3), the reaction between zirconia and the active element would not involve, at least during the first stages of the reaction, the full decomposition of the ceramic ($ZrO_2 \rightarrow (Zr) + 2\,(O)$) *.

5.3 Thermochemistry of Ceramic-Metal Interfaces: Previous Work

Several workers have used thermodynamics to gain a better understanding of the interfacial interactions between ceramic substrates and liquid (or solid) metals with active element additions. In this section, the evolution of the thermochemical methods of analysis of ceramic/metal interfacial interactions will be presented in chronological order. Although not all the relevant publications have been included in this review, the works selected represent an accurate picture of the evolution of the understanding of the basic thermochemistry of ceramic/metal reactions. Although considerable progress has been made in understanding this complex problem, several factors still limit the applicability of the analyses described in this section. As will be seen below, the main obstacle to a more generalized understanding of the nature of ceramic/metal interfaces is the lack of the proper thermodynamic descriptions for the relevant systems under study.

*This last assumption is only valid when the zirconia substrate is reacting with titanium in the solid state. In the liquid state, the dissolution reaction of the substrate may occur more rapidly than the partial reduction of the zirconia lattice

5.3.1 Thermochemistry of Active Metal Brazing Systems

Nicholas [15], examined the effect of adding titanium to several liquid metals, either pure ($Cu - Ti$, $Ni - Ti$) or alloyed ($Cu - Sn - Ti$), on the wetting characteristics of such liquids over alumina substrates. From simple thermodynamic calculations, Nicholas [15] concluded that in most cases, the activity coefficient of Ti in the pure metals was so low that the reaction products resulting from the alumina-liquid interfacial interaction were mostly oxides with O/Ti ratios greater than 1, corresponding to the non-metallic compounds Ti_3O_5, Ti_4O_7, etc. The contact angle between the liquid metals and these reaction products was not significantly different than that of the pure metal and the alumina substrate, which is in accord to the model by Li [9] described in Section 2.4. Based on this analysis, Nicholas [15] proposed the addition of solvents that increased the titanium activity (such as Sn and Ag), so wettable $Ti - O$ compounds (in general, with a O/Ti ration lower than 1) would form at the ceramic/metal interfaces.

Wang and Lannutti [107] concluded that the sole use of Ellingham diagrams to determine the reactivity of an active brazing alloy was inadequate. Using Miedema's semi-empirical model [40], they concluded that elements with a higher oxygen affinity than titanium (for example Zr, Hf) were not necessarily more effective as active additives to conventional brazing alloys. By comparing partial enthalpies of solution at infinite dilution for several reactive elements (Ti, Zr, Cr) with their respective oxygen affinity (measured by the Gibbs free energy of formation of the most stable oxide for each of the studied active metals), they attempted to predict the reactivity of different brazing alloys in contact with several ceramic substrates. A problem with their procedure, however, was that they did not consider the dissolution of the ceramic into the liquid. From their analysis, it followed that Ti additions to Cu and even Ag melts would not promote wetting on alumina substrates, since no reaction was expected. This is clearly contradicted by a wealth of experimental observations (see Kelkar et al. [72], for example).

5.3.2 Application of Chemical Potential and Phase Diagrams to the Study of Ceramic/Metal Interactions

A more sophisticated approach to the study of ceramic/metal interfacial reactions was presented by Inaba and Yokokawa [108]. Through the use of chemical potential diagrams [109, 110], the authors were able to determine the driving forces for interfacial reactions and possible reaction pathways for a number of dissimilar-materials diffusion couples. By using a chemical potential diagram for the $Al - Ti - O$ system, Inaba and Yokokawa [108] were able to successfully rationalize the layering of the reaction products resulting from Ti/Al_2O_3 couples. Although this approach is generally successful in determining likely reaction paths for dissimilar-materials interfaces, its application is usually limited to systems with three components as a maximum. The other limitation to this method is that extensive solubility of the components in one phase cannot be readily incorporated in the analysis.

Over the years, a number of researchers have proposed the use of thermodynamically consistent phase diagrams for the study of ceramic/metal interfacial interactions. Metselaar and Van Loo [111], for example, proposed the use of phase diagrams to study ceramic-metal interdiffusion. By relating the slopes of the tie-lines* with the relative diffusion rates of the interdiffusing species, they were able to rationalize the reaction layer sequence and even the morphology observed in different metal/carbide diffusion couples. Li et al. [112] performed a critical assessment of the thermodynamic information of the $Ti-Al-O$ system and used the calculated phase diagram, along with activity maps, to determine thermodynamically possible reaction paths in Ti/Al_2O_3 couples. Because of the interstitial nature of solid $Ti(O)$ solutions, and the extremely fast oxygen diffusion rates, Li et al. [112] established, as a condition for a thermodynamically allowed diffusion path, the continuous decrease of the oxygen chemical potential across the different reaction layers observed in the ceramic-metal diffusion couples studied.

5.3.3 Diffusion Simulations of Ti/Al_2O_3 Metastable Diffusion Couples

A more complete analysis of the Ti/Al_2O_3 system was proposed by Lee [50]. By using a one-dimensional simulation of the metastable $bcc-Ti(O,Al)/Al_2O_3$ diffusion couple, Lee [50] was able to determine the diffusion paths along the metastable $bcc-Ti(O,Al)/Al_2O_3$ phase boundary for different reaction times. Because of the much higher oxygen diffusion coefficient within the *bcc* phase†, the $bcc-Ti(O,Al)/Al_2O_3$ interface was initially enriched with Al, since alumina dissolution into the *bcc* phase required, due to mass conservation, that the $\frac{n(O)}{n(Al)}$ flux across the metastable interface to be constant at all times. By calculating the driving forces for phase precipitation (see Appendix D) at very short times after the diffusion reaction began, Lee [50] was able to successfully predict the reaction layer sequence observed in Ti/Al_2O_3 diffusion couple experiments. The predicted sequences also agreed with the analysis performed by Li et al. [112].

5.3.4 Use of Activity Diagrams: A More General Approach

Although the methods presented above can be used to describe ceramic/metal reaction experiments in three-component systems, this analysis, becomes almost intractable for higher-order systems. By incorporating more elements to the system under study, increasingly more information is required regarding the different diffusion rates and stable (or metastable) phase relations between all the possible reaction products that could form under different thermal and chemical conditions. An example of this limitation can be readily seen in the study of $Ag-Cu-Ti/Al_2O_3$ interfacial reactions. As has been shown in Section 3.2, due to the highly positive

*Indicating thermodynamic equilibrium between two phase fields

†Oxygen is an interstitial solute in *bcc* titanium, while aluminum is substitutional.

$Ag-Ti$ interaction, the liquid phase in the $Ag-Cu-Ti$ system presents a miscibility gap in most of the Gibbs compositional triangle at temperatures not much higher than the eutectic in the $Ag-Cu$ system. This phase separation in the liquid, coupled with the fact that there are five components in this system, makes it almost impossible to use the techniques outlined above.

In order to simplify the analysis of the $Ag-Cu-Ti/Al_2O_3$ system, Kelkar et al. [72] proposed the use of activity diagrams for the $Cu-Ti-O$ system to rationalize the reaction layers observed during alumina-ceramic active brazing operations. By using a methodology similar to that outlined in 4.3.3, the thermodynamic properties of the M_6X compounds Ti_4Cu_2O and Ti_3Cu_3O were coupled to the existing thermodynamic descriptions for the $Ti-O$ and $Cu-Ti$ systems to develop thermodynamically consistent two-dimensional activity diagrams for Ti and O components in the $Cu-Ti-O$ ternary. By using the criterion of a continuous decrease in the chemical potential of the reacting components Inaba and Yokokawa [108], Kelkar et al. [72] were able to explain the different interfacial layering in several $Ag-Cu-Ti/Al_2O_3$ diffusion couples. Because of lack of thermodynamic models for the incorporation of Al in the M_6X compounds (see 4.3.5), Kelkar et al. [72] did not consider the stabilizing effect of Al in these compounds and therefore they were unable to predict the Al content in the Ti_3Cu_3O and Ti_4Cu_2O layers observed.

5.3.5 Limitations and Application to Zirconia/Metal Interactions

One of the main difficulties encountered when trying to understand the nature of ceramic/metal interfacial interactions lies in the fact that, up until recently, the thermodynamic models describing the systems under study were not available. For example, thermodynamic descriptions for $metal-metal-oxygen$ systems have been limited to a few systems (for example, $Ti-Al-O$ [113], $Ag-Cu-O$ [81]). In the particular active brazing of ceramic materials, even the widely used $Ag-Cu-Ti$ alloy system has not been critically assessed until the present work (see Section 3.2). The problem becomes even more evident when one considers the available thermodynamic assessments for the $Cu-Ti-O$ system, which is of fundamental importance if one is to understand the nature of ceramic oxides-active brazing interfacial interactions, as most of the reaction products observed in these systems belong to the $Cu-Ti-O$ ternary*.

As has been noted in Section 5.2, there are several industrially important applications where the understanding of zirconia/metal interactions under high-temperature conditions is essential to the development and reliability assessment of critical components of such technologies. To the best of this author's knowledge, although there have been some experimental studies on the nature of zirconia/metal interactions,

* Kelkar et al. [72] obtained the thermodynamic properties for the M_6X $Cu-Ti-O$ compounds at one temperature ($\sim 945^0C$), and the relative thermodynamic stability of such compounds at different temperatures was not assessed until this work.

no thermodynamic analysis of such systems has been developed. In the remaining sections of this chapter, several examples of zirconia/metal interactions will be investigated and rationalized using the thermodynamic models described in Chapter 3 and Chapter 4. The thermodynamic models developed for the active brazing alloys will be used to determine the thermochemical conditions at the very early stages of the zirconia/braze interdiffusion processes. By using metastable thermodynamic calculations, coupled with simple assumptions regarding the likely thermodynamic behavior of the ceramic/metal couples, it will be shown that a wide variety of experimental conditions can be readily explained. Moreover, by combining the results of this chapter with the analysis of the metal substrate effects on the thermochemistry of active metal brazes presented in Chapter 6, a methodology for an improved design of ceramic/metal joining procedures will be presented.

5.4 Application of Thermodynamic Models to the Study of Zirconia/Ti Interactions

Over the years, several researchers have performed experiments to understand the nature of interfacial interactions between zirconia-based ceramics and *pure* titanium, both in the liquid and solid states [114–117]. Understanding liquid Ti/zirconia interactions is important in Ti-processing technologies [117] and the development of metal-matrix composites via the liquid route [116], while the understanding of solid Ti/zirconia interfacial reactions is essential to the development of C/M joining applications [51]. In this section, the thermodynamic model for the $Ti-Zr-O$ system presented in Section 4.5 is used to rationalize the interfacial reactions occurring in this system.

5.4.1 Interfacial Reactions between Liquid Ti and ZrO_2

5.4.1.1 Experimental Evidence on Liquid Ti/ZrO_2 Interactions

Zhu et al. [116] studied the wettability and reactivity of molten titanium on YSZ zirconia substrates. By using the sessile drop experimental technique, they measured the contact angle between titanium and zirconia at 1700^0C under a highly purified argon atmosphere. The oxygen partial pressure throughout the experiments was kept below $10^{-22}\,atm.$. From their experiments, Zhu et al. [116] observed the formation of a thin film of TiC on the molten titanium surface, due to adsorption of C from the heating elements. The formation of this film occurred about $8\,min.$ after the titanium was melted. The duration of the wetting experiments were later reduced to $8\,min.$. Zhu et al. [116] used *EPMA*, *AES* and *EDS* to study the interfacial structure formed due to the interaction between molten titanium and zirconia. The main results are outlined below:

i) A gradual discoloration of the zirconia substrate towards the Ti/ZrO_2 interface was observed.

ii) The affected region of the zirconia substrate presented evidence of decomposition of the ceramic into ZrO_2 and $hcp - Zr(O)$.

iii) Small quantities of Ti were observed to be dissolved in the ZrO_2 sublattice (less than $1.5\,at.\%$).

iv) On the titanium side of the interface, a region of $hcp - Ti(O)$ was observed, with Zr dissolved substitutionary in the Ti matrix.

v) The penetration of Zr within the $hcp - Ti(O)$ phase was negligible compared to that of O.

vi) A phase with compositions close to the stoichiometry Ti_2ZrO was observed near the ZrO_2/Ti interface.

vii) Through the use of x-ray line scanning, it was determined that the Y_2O_3 in solution with cubic ZrO_2 remained virtually inert, with negligible diffusion into the liquid Ti.

In similar experiments, Lin and Lin [117] and Lin and Lin [118] studied the interfacial reactions between molten titanium and CaO-stabilized and Y_2O_3-stabilized zirconia, respectively. The experiments were performed under a high-purity argon atmosphere. The titanium/zirconia wetting couple was held at 1750^0C for $7\,min.$ and then cooled at a rate of $40\,^0C/min$ to 0100^0C. The specimen was then cooled to room temperature inside the furnace. The resulting interfacial structure was prepared and analyzed using an analytical *TEM* and *SEM*. The results are summarized as follows:

i) The region within the zirconia substrate in direct contact with Ti was observed to be non-stoichiometric zirconia,(ZrO_{2-x}), with non-stoichiometry coefficient $x \sim 0.3$.

ii) Secondary $hcp - Zr(O)$ spherical particles and ZrO_{2-x} nano-crystallites with $x \sim 0.1$ within the zirconia substrate were observed.

iii) $hcp - Ti(O, Zr)$ was observed between the TiO_2 and Ti layers.

iv) Lin and Lin [117] observed Ti_2ZrO precipitates within the saturated $hcp - Ti(O, Zr)$ matrix.

v) CaO and Y_2O_3 remained in the zirconia layer, without dissolving in the liquid Ti.

vi) Upon cooling, interstitial ordered phases, with stoichiometric compositions Ti_2O and Ti_3O precipitated out of the $hcp - Ti(O)$ layer.

Lin and Lin [119] studied the interfacial reactions between a porous zirconia mold and a $Ti - 6Al - 4V$ alloy during centrifugal casting. Due to the porosity of the zirconia substrate, the molten titanium was able to infiltrate the mold through capillary and centrifugal forces. Once a zirconia particle was surrounded by the liquid

titanium alloy, it was rapidly dissolved. Oxygen-saturated $hcp - Ti(O)$ was observed up to $100\,\mu m$ within the Ti alloy.

Lin and Lin [117] reported the presence of small quantities of TiO_2 at the calcia-stabilized zirconia/titanium interface. This was not reported in a later investigation by Lin and Lin [118] on the yttria-stabilized zirconia/titanium interfacial interactions. Lin and Lin [119] and Zhu et al. [116] do not report the presence of the rutile, TiO_2 phase at the zirconia/metal interface. It is important to note that the three cases [116, 118, 119] that do not report the presence of TiO_2 at the ceramic/metal interface studied the interaction between yttria-stabilized zirconia and molten titanium. From these experimental results, it may be possible that the aliovalent dopant in zirconia-based ceramics determines whether TiO_2 precipitates at zirconia/liquid titanium interfaces.

5.4.1.2 Thermodynamic Analysis of Liquid Ti/ZrO_2 Interactions

In this section it will be shown that by using the thermodynamic models developed in Section 4.2 and Section 4.5 it is possible to rationalize the experimental results on the interfacial interactions between liquid titanium and zirconia substrates.

A result common to all reaction experiments presented in 5.4.1 was the fact that the stabilizing aliovalent dopant (in this case, either Y_2O_3 or CaO) did not interact with liquid titanium. This is compatible with the results described in 5.2.2. Due to this non-interaction, it is possible to analyze the Ti/ZrO_2 system independently of the stabilizing dopant. Thus, the analysis becomes greatly simplified.

Fig. 5-1 presents the calculated $Ti - Zr - O$ isothermal section at 1700^0C. Although some of the experiments reported were done at $1,750^C$ [117, 118], rather than 1700^0C [116], it is expected that the results would not be much different. The main features of the isothermal section presented in Fig. 5-1 can be summarized as follows:

i) The liquid phase is stable in two non-connected regions. From the $Ti - O$ phase diagram presented in Fig. 7-2, it is evident that the two regions correspond to melting of the $bcc - Ti$ and TiO_{1-x} phases.

ii) The *bcc* phase remains stable around the central region of the isothermal section, at oxygen concentrations below $30\,at.\%$.

iii) The *hcp* phase is stable in the regions corresponding to high Ti and Zr, with a maximum oxygen solubility of about $30\,at.\%$.

iv) The cubic γZrO_{2-x} phase is at equilibrium with both the *bcc* and *hcp* solid solution phases and with the oxides $TiZrO_4$, Ti_2O_3, Ti_3O_5 and TiO_2.

As can be seen in Fig. 5-1, the 1700^0C isothermal section is complex, since a great number of phases are thermodynamically stable at this temperature. To try to

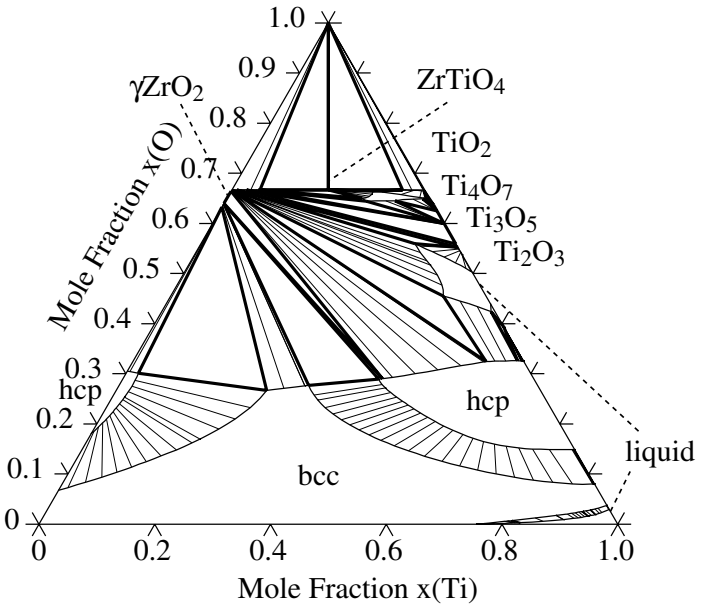

Figure 5-1: Calculated 1700^0C isothermal section of the $Ti - Zr - O$ system.

rationalize plausible diffusion paths across the Ti/ZrO_2 diffusion couple, it is possible to use metastable equilibrium calculations, coupled with simple assumptions regarding the kinetic behavior of the system [120]. Appendix D presents an example of the methodology developed by Lee et al. [120], applied to the $Ag - Cu/Ti$ diffusion couple, relevant to many ceramic/metal active brazing applications. In this section, the same methodology is used to analyze the reaction sequence observed in Ti/ZrO_2 couples, both in the liquid and the solid states.

At the very early stages of the interfacial interaction between molten titanium and a solid substrate of the cubic γZrO_{2-x} phase, it is expected that a *metastable* equilibrium will be established between the two phases. Fig. 5-2 presents the *metastable* 1700^0C section of the $Ti - Zr - O$ system, considering *liquid* and γZrO_{2-x} as the only stable phases. In principle, there are an infinite number of thermodynamically consistent paths that the Ti/ZrO_2 diffusion couple can follow. To find a plausible diffusion path, it is necessary first to determine the compositions at the interface between the solid γZrO_{2-x} and the liquid Ti phases. Using the local equilibrium assumption, which is reasonable at this high temperature, it can be postulated that the compositions at the solid/liquid interface will lie somewhere along the $\gamma ZrO_{2-x}/(ZrO_{2-x} + liquid)$ and the $(ZrO_{2-x} + liquid)/liquid$ *metastable* phase boundaries.

At these high temperatures, it is reasonable to assume that the rate of solid dissolution into the liquid is much faster than the rate of diffusion of the ions within the γZrO_2 phase. Table 5.3 presents the diffusion coefficients for Ti, Zr and O, based on the diffusivities in Table 5.1 and Table 5.2. As can be seen, the rates of diffusion within the liquid are much higher than those in all the solid phases. Moreover,

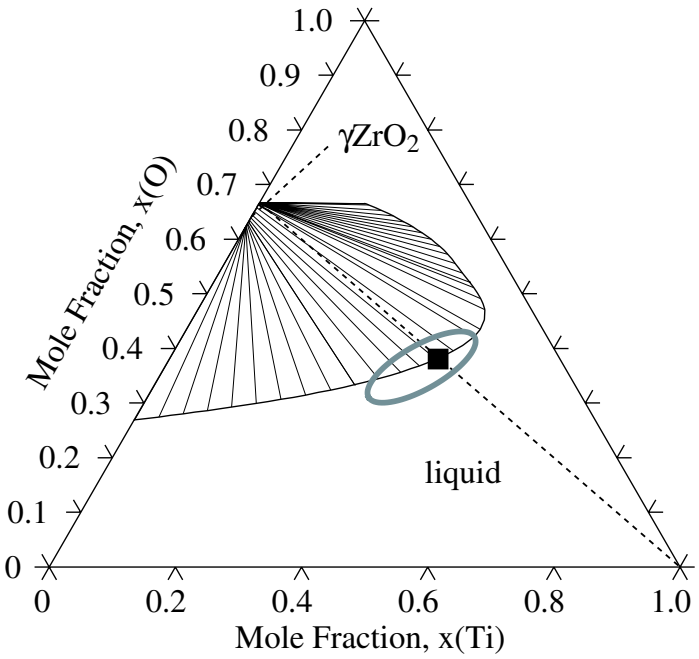

Figure 5-2: Calculated metastable 1700^0C isothermal section of the $Ti - Zr - O$ system.

dissolution of the solid in the liquid implies that the flux of oxygen and zirconium atoms from the solid to the liquid phase should approximately* maintain the stoichiometry corresponding to ZrO_2. The composition of the liquid at the metastable solid/liquid interface should therefore correspond to the point at which the metastable $(ZrO_{2-x} + liquid)/liquid$ phase boundary is intersected by the line connecting pure titanium to pure zirconia [120]. This point is indicated by the solid square in Fig. 5-2.

Table 5.2: Diffusion coefficients in *bcc* and *hcp* $Ti - Zr - O$ solutions from [121, chapter 13] and extrapolations. Note that $D = D_0 e^{\frac{-Q}{RT}}$.

Diffusion Coefficient	**bcc**		**hcp**	
	$\mathbf{D_0}$,$\mathbf{cm^2/s}$	**Q**,**kJ**/mol	$\mathbf{D_0}$, $\mathbf{cm^2/s}$	**Q**,**kJ/mol**
D_{Ti}^{Ti}	3.58×10^{-4}	$130,600$	6.6×10^{-5}	$169,100$
D_{Zr}^{Zr}	8.5×10^{-5}	$115,970$	9.713×10^{-2}	$256,686$
D_{O}^{Ti}	8.56×10^{-2}	$138,200$	7.78×10^{-1}	$203,478$
D_{O}^{Zr}	9.77×10^{-1}	$171,700$	1.32×10^{0}	$201,800$

*Due to the much higher oxygen diffusion within the ZrO_{2-x} phase, it is expected that an additional flux of oxygen atoms will come from within the ceramic itself.

Table 5.3: Calculated/estimated diffusion coefficients (cm^2/s) for phases in the $Ti-Zr-O$ system, at 1700^0C. For the liquid phase, the estimation $D \sim 1 \times 10^{-8} \cdot T^{3/2}\, cm^2/s$ by Kirkarldy and Young [122, page 93] was used.

element	**liquid**	**$\gamma ZrO_{2\ x}$**	**bcc**	**hcp**
Ti	8.8×10^{-4}	N/A	6.5×10^{-7}	2.2×10^{-9}
Zr	8.8×10^{-4}	5.8×10^{-14}	7.3×10^{-8}	1.6×10^{-8}
O	8.8×10^{-4}	5.3×10^{-6}	$1.9 \times 10{-}5$	3.2×10^{-6}

Once the equilibrium compositions at the metastable solid/liquid interface have been determined through the procedure outlined above, it is possible to determine whether another phase can precipitate under these conditions. To establish which phase precipitates first, one can calculate the driving force for precipitation for all the possible phases in the system. Ignoring surface effects, the phase that precipitates first is the one with the largest driving force for precipitation [120]. When a metastable equilibrium between two phases, α and β is established, this driving force can be calculated using (see Fig. D-1 in Appendix D):

$$\triangle G_P^{A_aB_b} = a\mu\left(A\right) + b\mu\left(B\right) - G_f^{A_aB_b} \tag{5.1}$$

where $\mu\left(A\right)$ and $\mu\left(B\right)$ are the chemical potentials of elements A and B when the phases α and β are at *metastable* equilibrium, $G_f^{A_aB_b}$ is the Gibbs free energy of formation of phase A_aB_b and $\triangle G_P^{A_aB_b}$ is the driving force. Only phases with positive driving forces for precipitation will precipitate.

Fig. 5-3 shows the calculated *normalized* driving forces for precipitation for several phases along the $(\gamma ZrO_{2-x} + liquid)/liquid$ metastable phase boundary. The region enclosed with the oval corresponds to the region enclosed within the oval in Fig. 5-2. As can be seen from Fig. 5-3, there are only two phases (*bcc* and *hcp*) that have positive driving forces for precipitation within the compositional range of the metastable solid/liquid interface. Of these two phases, *hcp* always has the greatest driving force for precipitation, except for a narrow region close to the central region of the phase diagram. The *bcc* phase becomes unstable with respect to precipitation when the oxygen content of the liquid phase is $x_O \sim 0.1$. Note that the driving forces for precipitation for the TiO and Ti_2O_3 phases become less negative, as the oxygen content in the liquid phase increases.

Based on the calculations depicted in Fig. 5-3, it is possible to calculate the metastable $Ti - Zr - O$ isothermal section at 1700^0C, considering only the phases γZrO_{2-x}, *hcp* and *liquid*. Fig. 5-4 presents this isothermal section.

Before discussing the possible diffusion paths of the system in which the phase

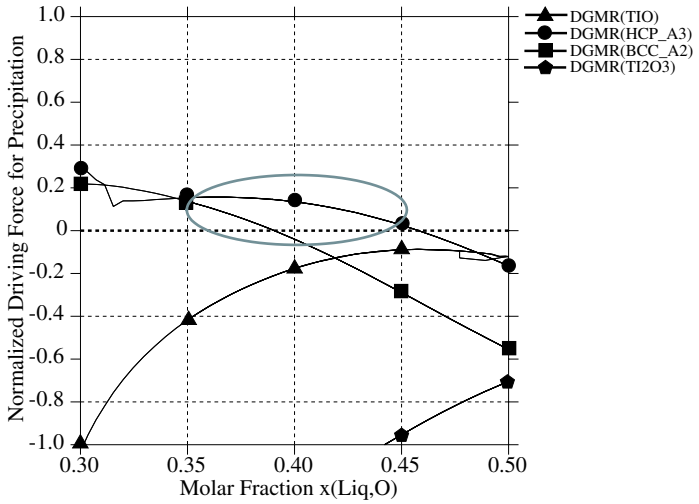

Figure 5-3: Normalized $\left(\frac{\Delta G_P^{A_a B_b}}{RT}\right)$ driving forces for precipitation for several phases along the metastable (solid+liquid)/liquid phase boundary in the metastable 1700^0C isothermal section in the $Ti - Zr - O$ system.

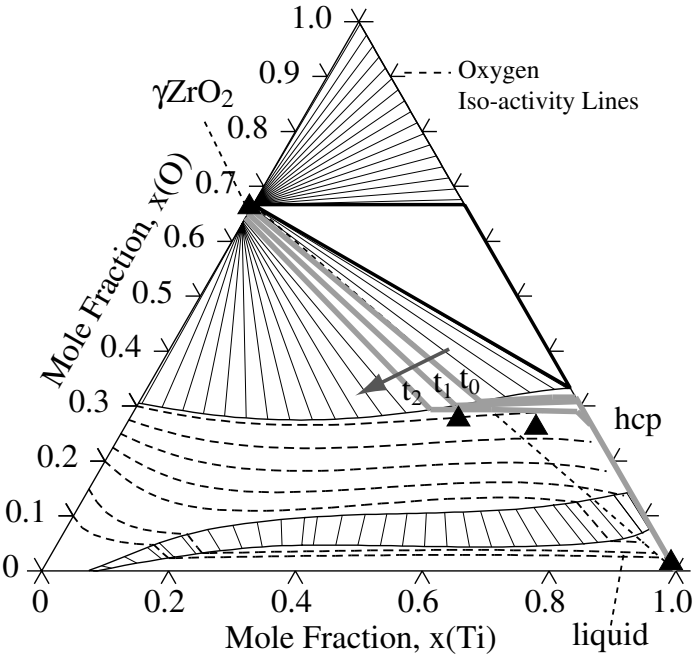

Figure 5-4: Calculated metastable 1700^0C ternary section for the $Ti - Zr - O$ system considering the γZrO_{2-x}, *hcp* and *liquid* phases.

sequence is $\gamma ZrO_2 2 - x/hcp/liquid$, it is worth examining the possibility of any other further precipitation across the new interfaces created by the formation of the *hcp* phase. Fig. 5-5 shows the calculated *normalized* driving forces for precipitation for two phases *bcc* and βZrO_2 along the $(\gamma ZrO_{2-x} + hcp)/hcp$ phase boundary. As can be seen in this figure, the maximum normalized driving force for precipitation observed at this metastable phase boundary is ~ 0.08, which is considerably less than

the driving force for precipitation of the *bcc* phase at the metastable solid/liquid interface ($\triangle G_P^{hcp} \sim 0.2$). Note that the *bcc* phase becomes unstable with respect to precipitation as soon as the titanium content in the hcp phase reaches $x_{Ti} \sim 0.5$. The βZrO_2 phase becomes slightly stable with respect to precipitation at titanium contents $x_{Ti} > 0.5$. The possible precipitation of βZrO_2 calculated in this figure may be corroborated by the fact that ZrO_2 crystallites have been observed to precipitate at the zirconia/titanium interface [118], although it is more likely that these crystallites precipitated from the eutectoid decomposition $\gamma ZrO_{2-x} \rightarrow hcp - Zr(O) + \beta ZrO_{2-x}$ (see below).

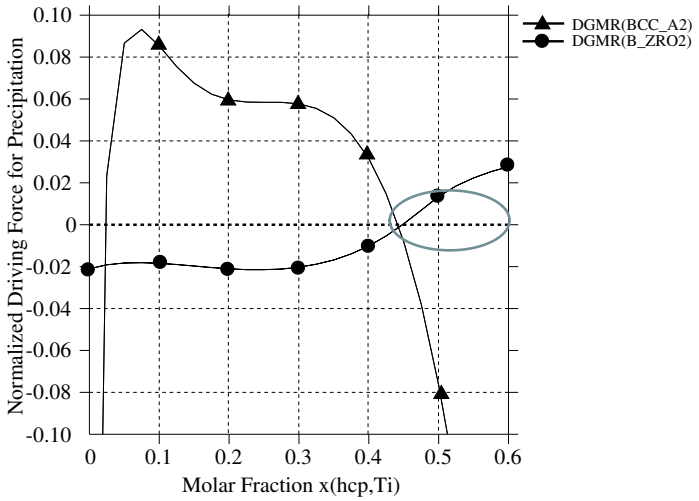

Figure 5-5: Normalized $\left(\frac{\Delta G_P^{A_a B_b}}{RT}\right)$ driving forces for precipitation along the $(\gamma ZrO_{2-x} + hcp)/hcp$ phase boundary at $1700^0 C$.

To try to predict the possible diffusion path once the interaction between molten titanium and cubic zirconia γZrO_{2-x} has led to the precipitation of an $hcp{-}Ti(O, Zr)$ phase, it is possible to use the metastable ternary section presented in Fig. 5-4. To simplify the analysis, the composition at the metastable $(\gamma ZrO_{2-x} + hcp)\,/hcp$ phase boundary was considered to be located at the intersection of this phase boundary and the line connecting the $ZrO_2 - Ti$ initial compositions of the diffusion couple.

A likely diffusion path at the early stages of the ceramic/metal interfacial reaction is indicated by the thick gray line labelled as t_0. Due to the low diffusivity of zirconium in the *hcp* phase, it is expected that the $hcp - Ti(O, Zr)$ layer adjacent to the zirconia surface will be highly enriched with zirconium, compared to regions within the $hcp - Ti(O, Zr)$ phase away from the interface. The flux of oxygen atoms from the zirconia phase into the interface will be much greater than that of zirconium due to the great difference in diffusion rates within the oxide (see Table 5.3). Since cubic zirconia can withstand considerable ranges of non-stoichiometry (see Fig. 4-4), it is possible for this phase to supply the interface with a continuous flux of oxygen atoms, without having to maintain the flux ratio between zirconium and oxygen ac-

cording to the stoichiometry of ZrO_2. Because the diffusion rate of oxygen within the *hcp* phase is at least two orders of magnitude greater than that of zirconium, it is expected that the diffusion path at the early stages of the reaction will follow the oxygen iso-potentials [50], indicated in Fig. 5-4 as back dashed lines. Regions far away from the ceramic/metal interface will not have any zirconium, and is expected that the diffusion path in these regions will follow the $Ti-O$ boundary in the Gibbs compositional triangle for the $Ti-Zr-O$ system.

As time progresses, considerably higher degrees of non-stoichiometry will be reached at the zirconia side of the zirconia/titanium interface. The region adjacent to the $hcp-Ti(O,Zr)$ interface may even decompose trough the reaction $ZrO_2 \rightarrow Zr+\frac{1}{2}O$. The equilibrium tie-line will then be shifted towards higher oxygen non-stoichiometries and higher zirconium contents at the $(\gamma ZrO_{2-x}+hcp)/hcp$ phase boundary. This is indicated by diffusion paths t_1 and t_2 (thick gray lines in Fig. 5-4), the direction of the diffusion paths is indicated by the dark gray arrow in Fig. 5-4. Because of the shifting in the tie-lines, the iso-potentials along which oxygen will diffuse within the *hcp* phase will also be shifted downwards.

Once the diffusion couples reacted at high temperatures for $\sim 10min$, they were cooled to 1000^0C at a rate of about $50^0C/hr$. On the zirconia side of the ceramic/metal interface, as temperature decreases, the maximum possible oxygen non-stoichiometry also decreases until, at 1540^0C the highly reduced region within ZrO_{2-x} is expected to undergo the eutectoid transformation $\gamma ZrO_{2-x} \rightarrow \beta ZrO_{2-x}+hcp-Zr(O)$, as shown in Fig. 5-6. According to this transformation, it is expected to observe precipitation of saturated $hcp-Zr(O)$ particles, as well as secondary ZrO_{2-x} crystallites, with lower non-stoichiometries, x, than the parent material. Although Fig. 5-6 indicates that the cubic phase undergoes the $c \rightarrow t \rightarrow m$ transformation sequence, the ZrO_{2-x} nano-crystallites observed in Lin and Lin [117] and Lin and Lin [118] preserved the cubic structure due to strain energy effects*.

From the results above, it can be seen that metastable thermodynamic calculations for the $Ti-Zr-O$ system can account, at least on a qualitative manner, for most of the experimental results reported in the literature [116–119]. Moreover, the compositional measurements by Zhu et al. [116] (solid squares in Fig. 5-4) agree well with the proposed diffusion paths. However, the reported presence of TiO_2 during calcia-stabilized zirconia/titanium interactions reported by Lin and Lin [117] cannot be accounted for in this analysis. Although it is possible that some oxygen could have been leached out from the zirconia substrate before the whole substrate was dissolved in the molten metal, driving the metastable solid/liquid interface towards lower contents of zirconium and thus, higher probability for the precipitation of TiO_2, it is unclear how these TiO_2 precipitates could remain stable with respect to re-dissolution into liquid titanium. The other three experiments reviewed here [116, 118, 119] do

*The nano-crystallites did not reach the critical volume to make the $c \rightarrow t$ transformation thermodynamically possible

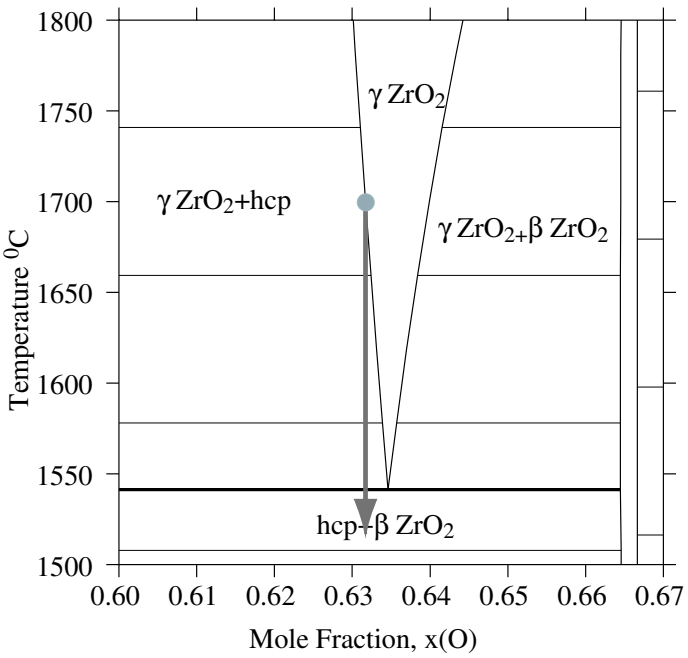

Figure 5-6: $Zr - O$ phase diagram, ZrO_2 region.

not report the presence of TiO_2, despite being done at similar temperatures and for similar times, The only difference between these experiments and the one reported by Lin and Lin [117] seems to be the dopant used to stabilize the cubic zirconia phase. It is unclear, however, how a dopant that remains relatively inert with respect to reduction (see 5.2.2) could affect whether TiO_2 would precipitate or not under these experimental conditions.

5.4.2 Interfacial Reactions between Solid Ti and ZrO_2

5.4.2.1 Experimental Evidence on Solid Ti/ZrO_2 Interactions

In order to study the possible use of partially stabilized zirconia, PSZ, for structural applications, Suganuma et al. [123] performed solid state diffusion bonding experiments between PSZ and steel, using a titanium interlayer. In their experiments, Suganuma et al. [123] used YSZ and AISI Type 405 stainless steel and assembled sandwich structures consisting of steel/titianium/PSZ/titianium/steel. The arrangements were subjected to hot isostatic pressing, *HIP*, for $15 - 30\,\text{min}$. at 1000^0C, under a pressure of $100\,MPa$. After the diffusion bond, some of the samples were analyzed using *EPMA*, *SEM* and *XRD* to determine the interfacial microstructure. Their findings can be summarized as follows:

i) From the *XRD* analysis, it was determined that there were no titanium oxides present at the ceramic/metal interface.

ii) The *EPMA* showed that zirconium had not diffused into the titanium phase.

iii) Oxygen diffused into the $hcp-Ti(O)$ phase, up to a depth of $30\,\mu m$ after $30\,min.$ at 1000^0C.

iv) The zirconia substrate presented the characteristic discoloration (blackening).

In a more recent experiment, Correia et al. [124] studied the interfacial interactions between ytttria-stabilized zirconia and a titanium in its pure state or alloyed $(Ti-6Al-4V)$. $1\,mm$ thick Ti sheets were place between zirconia pieces (with a thickness of $5\,mm$) in a sandwich structure. The $YTZ/Ti/YTZ$ arrangements were joined at 1162, 1245, 1328 and 1494^0C, under an axial pressure of $5\,MPa$ for $15-180\,min.$, under a highly purified argon atmosphere. Their results for the sample joined at 1494^0C, are summarized as follows:

i) The zirconia pieces exhibited extensive blackening.

ii) In the region within the zirconia piece, adjacent to the zirconia/titanium interface, *EPMA* measurements revealed extensive oxygen depletion, where the $\frac{x_O}{x_{Zr}}$ decreased from 2 to 1.6.

iii) The *SEM* micrograph of this joint exhibited considerable decomposition of the zirconia substrate.

iv) From the concentration profiles, obtained through *WDS*, it was determined that there were two distinct layers present on the titanium side of the zirconia/titanium interface. The first layer, about $20\mu m$ thick, presents significant amounts of zirconium dissolved, with complete oxygen saturation of the $hcp-Ti(O)$ phase. On this layer, the $\frac{x_{Zr})}{x_{Ti}}$ ratio decreased, from ~ 0.5 to 0.

v) From the *WDS* analysis, it was concluded that, in the region where Zr was present in significant amounts, the solubility of O in the metal decreased, compared to the saturation concentration observed in the $hcp-Ti(O)$ phase.

vi) The second layer presented a uniform oxygen atomic concentration of about $30\,at.\%$.

5.4.2.2 Thermodynamic Analysis of Solid Ti/ZrO_2 Interactions

As can be seen in Fig. 5-7, the ternary sections for the $Ti-Zr-O$ system at 1000 and 1494^0C are very similar. The *bcc* phase is stable at the central portions of the metal-rich section of the phase diagram and the zirconia phases (αZrO_2 at 1000^C and βZrO_2 at 1494^0C) are in equilibrium with most of the stable phases at these temperatures. The main difference in these ternary sections lies on the stability range of the *hcp* phase on the titanium and zirconium-rich sides of the phase diagram. As can be seen in Fig. 5-7, as the temperature decreases, the *hcp* stability range, especially in the Ti-rich region, narrows. At higher temperatures, however, the Ti-rich *hcp* phase becomes stable over a wide compositional range. The Zr-rich *hcp* phase, however, does not seem to be as stable. The reason for this asymmetry in the stability ranges for the two *hcp* phase fields is the asymmetry of the *bcc* field itself. As has been noted

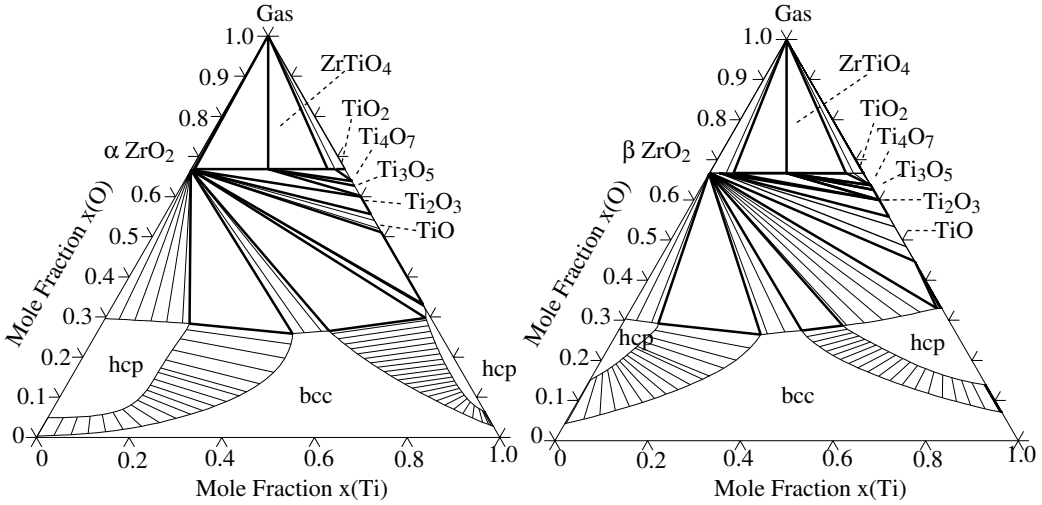

(a) Calculated $Ti - Zr - O$ ternary section at 1000^0C

(b) Calculated $Ti - Zr - O$ ternary section at 1494^0C

Figure 5-7: Analysis of zirconia/solid titanium interactions. Calculated equilibrium ternary sections of the $Ti - Zr - O$ system.

in Section 4.5, the *bcc* phase congruently melts at the Zr-rich side of the metallic region of the $Ti - Zr - O$ phase diagram.

Despite the differences between the 1000^0C and 1494^0C ternary sections of the $Ti - Zr - O$ system, the solid-state diffusion results reported by Suganuma et al. [123] and Correia et al. [124] could be rationalized using only one of these phase diagrams, taking into account the differences in diffusion rates, as well as the stability ranges of the *bcc* phase. Although under these conditions the βZrO_{2-x} allotrope of ZrO_2 is the stable phase, the presence of Y_2O_3 in the zirconia lattice stabilizes the cubic form, γZrO_2 and allows a much greater degree of non-stoichiometry. In the following analysis, the effect of aliovalent additions will be included by requiring that the γZrO_2 be stable at these temperatures. In order analyze the diffusion path in the solid Ti/ZrO_2 system, the procedure described in 5.4.1.2 can be used.

Above 1000^0C, the stable phase is in the $Ti - Zr$ system is *bcc* *. Therefore, at the very early stages of the inter-diffusion process between solid titanium and zirconia, it is expected that a *metastable* thermodynamic equilibrium will be established between $bcc - Ti$ and βZrO_{2-x}. Fig. 5-8 presents a metastable thermodynamic calculation for the $Ti - Zr - O$ system, at 1494^0C, considering only the *bcc* and γZrO_{2-x} phases. Based on the fact that ZrO_{2-x} can withstand considerable ranges of non-stoichiometry before undergoing the $ZrO_2 \rightarrow (Zr) + \frac{1}{2}(O)$ decomposition reaction, the initial composition of the zirconia/titanium interface is expected to lie around the region marked with the black oval in Fig. 5-8. In Fig. 5-8(b), the normalized driving

*See Fig. 4-11(a) in Section 3.3.

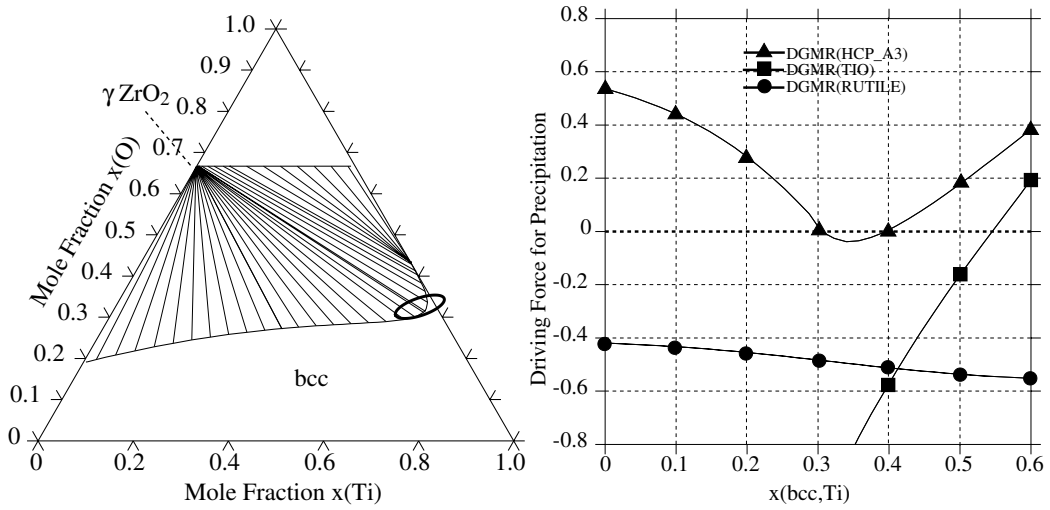

(a) Metastable 1494^0C section of the $Ti-Zr-O$ system considering only the βZrO_2 and *bcc* phases.

(b) *Normalized* driving forces for precipitation of several phases along the $(\gamma ZrO_{2-x} + bcc)\,/bcc$ phase boundary.

Figure 5-8: Metastable thermodynamic calculation for the $Ti-Zr-O$ system at 1494^0C, considering only the γZrO_{2-x} and *bcc* phases.

forces for precipitation of *hcp*, TiO and Ti_2O_3 were calculated along the metastable $(\gamma ZrO_{2-x} + bcc)\,/bcc$ phase boundary. As expected, the *hcp* phase has a *positive* driving force for precipitation at both the Ti and Zr-rich regions of the phase boundary. This phase, however, becomes unstable with respect to precipitation at the central region of the phase diagram, where *bcc* is the most stable phase(see Fig. 5-7). At the Ti-rich region of the phase boundary, the $fcc\ TiO_{1-x}$ phase starts to become stable, although its precipitation driving force never exceeds that of *hcp*. It is expected that the first phase to precipitate at the metastable bcc/ZrO_{2-x} interface is *hcp*.

Fig. 5-9(a) presents a qualitative depiction of likely diffusion paths in the solid Ti/ZrO_2 system. The basic sequences can be summarized as follows:

i) At the early stages of the diffusional reaction between γZrO_{2-x} and solid $bcc-Ti(O)$, it is expected that oxygen saturation of this phase will lead to the precipitation of $hcp-Ti(O)$, with the same oxygen saturation content. This initial interfacial composition is indicated in Fig. 5-9(a) as point *c*.

ii) Due to the fact that γZrO_{2-x} can withstand high degrees of non-stoichiometry without decomposing, the ratio between the oxygen and zirconium fluxes across the ceramic/metal interface do not have to satisfy the stoichiometric condition ZrO_2.

iii) As oxygen continues to diffuse through the $hcp-Ti(O)$ phase, and into the $bcc{-}Ti(O)$ (point *a* in Fig. 5-9(a)), the $bcc{-}Ti(O)$ phase will become increasingly

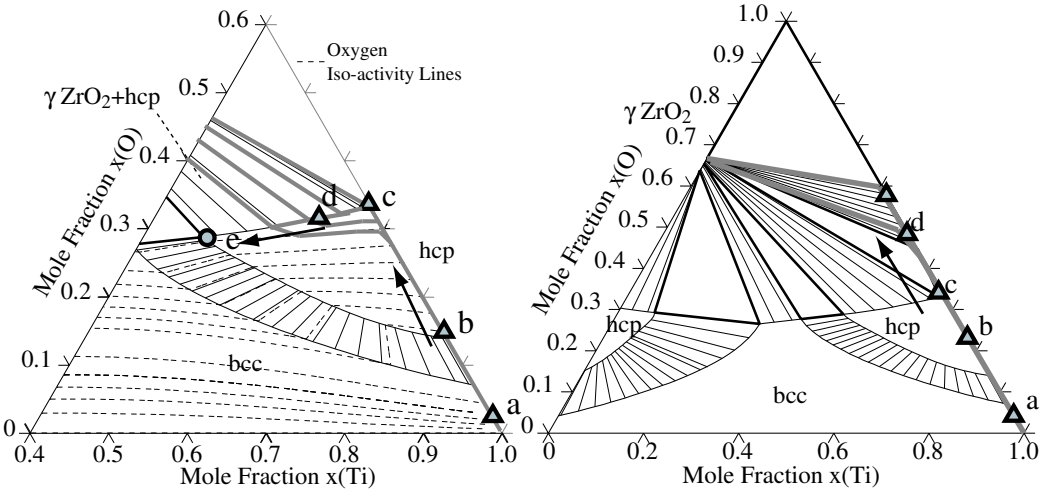

(a) Qualitative diffusion paths in the solid Ti/ZrO_2 system. The ratio between the thicknesses (scaled by the relative molar volumes of the substrates) of the titanium and zirconium samples is $\frac{ZrO_2}{Ti} \sim 1$.

(b) Qualitative diffusion path for the solid Ti/ZrO_2 system for the case where the ratio between the thicknesses of the titanium and zirconia substrates is $\frac{ZrO_2}{Ti} \sim \infty$..

Figure 5-9: Diffusion paths in the solid Ti/ZrO_2 system. Metastable thermodynamic calculations in the $Ti - Zr - O$ system at 1494^0C.

saturated with oxygen. This early stage of the diffusion process corresponds to the experiments reported by Suganuma et al. [123], which observed an oxygen saturated $hcp - Ti(O)$ layer directly at the ceramic/metal interface, while the oxygen penetration into the rest of the titanium substrate only reached $40\mu m$. Because the *bcc* phase transforms to *hcp* at temperatures below 1000^0C, this phase was not observed in the study by Suganuma et al. [123].

iv) Once the *bcc* phase saturates, the *hcp*/*bcc* interface will move towards the titanium rich side of the metal substrate, until the remaining *bcc* phase completely transforms into *hcp*. This is indicated by point *b* in Fig. 5-9(a).

v) Since zirconia can still provide oxygen to the zirconia/metal interface without having to undergo the $ZrO_2 \rightarrow (Zr)+(O)$ decomposition reaction, the zirconium content on the titanium side of the interface is still zero, as has been observed by Suganuma et al. [123].

vi) Once the $bcc \rightarrow hcp$ transformation has been completed, $hcp-Ti(O)$ will rapidly saturate with oxygen.

vii) If the relative sizes of the zirconia and titanium substrates are such that further oxygen dissolution into the $hcp - Ti(O)$ phase involves the decomposition of ZrO_2, zirconium will start to accumulate at the ceramic/metal interface (point *d* in Fig. 5-9(a)). The fact that Zr does not rapidly diffuse into the $hcp-Ti(O)$

phase has to do with its relatively low diffusion coefficient, compared to that of oxygen*.

viii) Correia et al. [124] observed that this was the case: while the titanium metal away from the interface seemed to be completely saturated with oxygen (at least up to a distance of $100\mu m$ away from the C/M interface), Zr was heavily concentrated in a region within $10\mu m$ from the C/M interface.

ix) Further decomposition of ZrO_2 will eventually lead to a displacement of the composition of the ceramic/metal interface composition towards the Zr rich side of the phase diagram, along the $(\beta ZrO_{2-x} + hcp)/hcp$ phase boundary. This is indicated by point e in Fig. 5-9(a).

x) From Fig. 5-9(a) it is observed that further zirconium enrichment of the C/M interface implies a lower oxygen concentration on the metal side of the interface. This is also consistent with the experimental results reported by Correia et al. [124].

xi) A simple calculation considering the initial thicknesses of the titanium and zirconium samples and the moral volumes of the substrates indicates that the *final* equilibrium state of the system corresponds to point e in Fig. 5-9(a).

The diffusion path and reaction sequence described above corresponds to the case where the relative thicknesses of the zirconia and titanium substrates are of the same order of magnitude, once they are scaled using the differences in molar volumes of the substrates. A different behavior is to be expected when the ratio of thicknesses between the zirconia and titanium systems, $\frac{ZrO_2}{Ti}$, approaches infinity. Under these conditions, it is unlikely that the zirconia substrate will undergo the $ZrO_2 \rightarrow (Zr) + (O)$ decomposition. In this case, no zirconium is expected to be observed on the titanium side of the C/M interface. Fig. 5-9(b) indicates the expected diffusion path in this case:

i) As before, it is expected that the initial *bcc* phase will eventually transform to $hcp - Ti(O)$.

ii) If there is still oxygen available from the zirconia lattice, complete saturation of the $hcp - Ti(O)$ phase is to be expected. This is indicated by point c in Fig. 5-9(b).

iii) Further dissolution of oxygen into the $hcp - Ti(O)$ layer will promote the $hcp \rightarrow TiO_{1-x}$ transformation, as indicated in point d in Fig. 5-9(b).

iv) Eventually, it is expected that the titanium layer will further oxidize to oxides with higher $\frac{x_O}{x_{Ti}}$ ratios.

*As a manner of comparison, Table 5.3 can be examined.

An example of this behavior was observed by Arroyave [51], when developing a ceramic/metal joining technique for zirconia/Ni-based super alloys composites with operating temperatures higher than joints using $Cu-based$ brazing alloys. In this case, a $5\mu m$ thick titanium layer was sputtered on a zirconia substrate. A ni-based brazing alloy belonging to the $BNi-5$ classification* was placed between the Ti-coated zirconia and the Ni-super alloy substrates. The formation of a *wettable* $Ti-O$ coating promoted the formation of a sound zirconia/Ni joint. Fig. 5-10 shows an *SEM* back-scattered micrograph of this experiment. Using *EDS* it was determined that the composition of the layer closely corresponded to TiO_{1-x} [51].

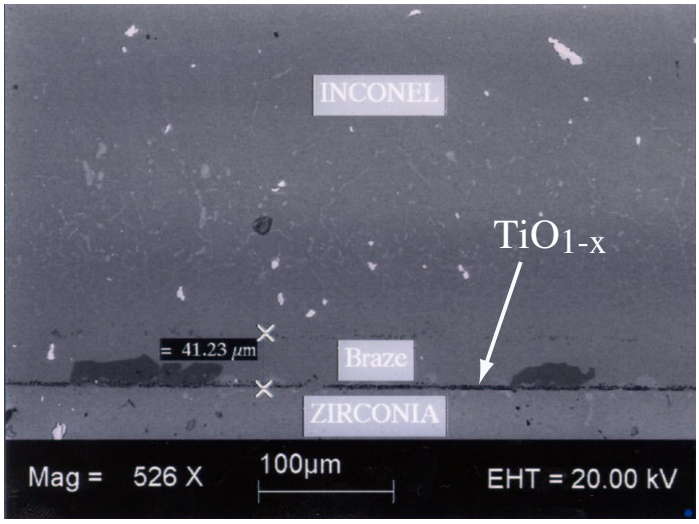

Figure 5-10: Zirconia/Ni-based super alloy joint using Ti thin film and Ni-based brazing alloy. Joint created at 1100^0C for $15\,min$.

5.4.3 Comparison with Al_2O_3/Ti Interactions

To illustrate the effect that the wide range of non-stoichiometry of γZrO_{2-x} has on the nature of its interfacial reaction with Ti, it is worth comparing the diffusion paths described above with that of a very similar and much more studied ceramic/metal system. Fig. 5-11 shows the qualitative diffusion paths expected in the Al_2O_3/Ti system, based on the analysis by Lee [50]. Alumina does not withstand its partial reduction, i.e. the formation of oxygen vacancies, without decomposing. When this ceramic material is subjected to reducing conditions, it undergoes the $Al_2O_3 \rightarrow 2\underline{Al} + 3\underline{O}$ decomposition reaction. This is the case when alumina is put in contact with Ti at high temperatures.

In this case, due to mass conservation, the fluxes of aluminum and oxygen into

*These alloys belong to the $Ni-Si-B$ system and have melting ranges around 1100^0C. Since B is a fast diffuser in Ni-based alloys, it can diffuse out of the braze and into the base metal, increasing the re-melting temperature of the joint.

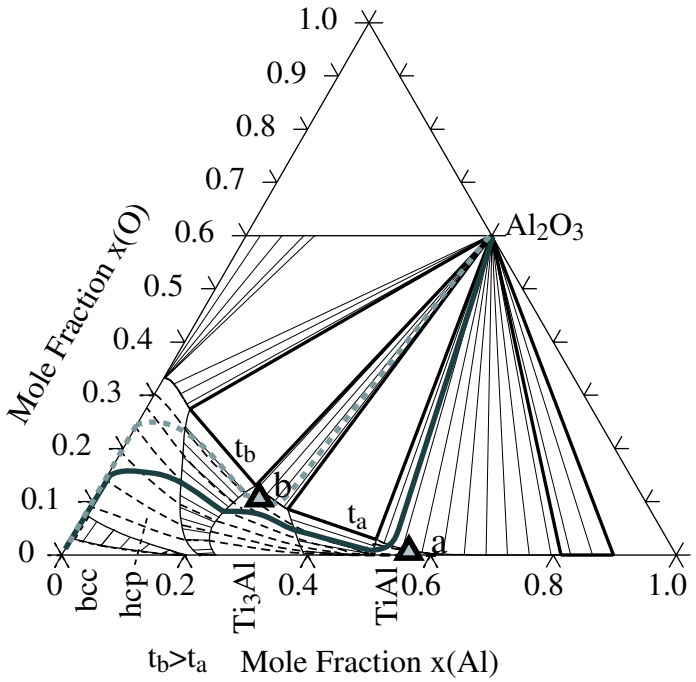

Figure 5-11: Qualitative diffusion path in the Al_2O_3/Ti system at $T \sim 1100^0C$. Based on the analysis by Lee [50].

the ceramic/metal interface must maintain the stoichiometric ratio corresponding to Al_2O_3. Since the diffusion rate of oxygen in $bcc - Ti$ or $hcp - Ti$ is much higher than that of aluminum, the metal side of the C/M interface is initially enriched with Al. By using similar arguments to those used in this section, it is found that, under this conditions, the $TiAl$ phase has the highest driving force for precipitation and will be the first phase to precipitate. This is indicated by point a in Fig. 5-11. As the reaction progresses, more aluminum will diffuse, through the $TiAl$ layer, into the remaining $hcp - Ti$ phase. As the interface becomes depleted of Al, the driving force for the precipitation of Ti_3Al becomes thermodynamically possible and it will precipitate between the $hcp - Ti$ and $TiAl$ layers, as is indicated by point b in Fig. 5-11. As in the case for ZrO_2/Ti interactions, the diffusion path will lie parallel to oxygen iso-activity lines within the $hcp - Ti$ phase. This is due to the much higher oxygen diffusion rates. As can be seen, in this case no $Ti - O$ phase is likely to be in equilibrium with the ceramic oxide. The reason for this is the different nature of the reduction/decomposition process of the ceramic oxide.

5.5 Thermodynamic Study of the Interactions between Zirconia and $Ag - Cu - Ti$ Brazing Alloys for Ceramic/Metal Joining Applications

As has been mentioned in Section 2.4, due to the difference in electronic structure of ceramic substrates and liquid metals, wetting angles in these systems tend to be greater than 90^0. This makes the application of conventional brazing techniques to C/M joining impossible. For example, Shinozaki et al. [125] studied the contact an-

gle between molten zinc and zirconia and found it to be greater than 150^0. As noted in 2.3.2 and Section 2.6, the addition of reactive elements, such as Ti, Hf, Zr can promote wetting of an otherwise non-reactive molten metal on a ceramic substrate, mainly because of the formation of a *wettable* reaction product. In the particular case of wettability of molten metals over zirconia substrates, for example, Xue et al. [126] found that the wetting angle of silver-indium-titanium alloys over zirconia substrates decreased to less than 10 degrees due to the formation of wettable precipitates.

As mentioned in Section 2.6, active brazing is one of the preferred techniques for joining ceramics to metals. Active brazes based on the $Ag-Cu-Ti$ system are the alloys of choice when the ceramic in question is an oxide. In this section, the thermodynamic models developed for the $Ag-Cu-Ti$ (see Section 3.2) and $Cu-Ti-O$ (see Section 4.3) systems are used to understand the available literature regarding the interfacial reactions observed in zirconia/$Ag-Cu-Ti$/metal systems.

5.5.1 Thermochemistry of $Ag-Cu-Ti$ Alloys

The thermodynamic model for the $Ag-Cu-Ti$ system was developed in Section 3.2. As was mentioned in that section, experimental investigations of this system suggest the presence of an extensive miscibility gap in the central region of the liquidus surface of the ternary. This miscibility gap is an indicator of a strongly positive chemical interaction between Ag and Ti. When liquids belonging to this system are put in contact with ceramic oxides, the high chemical activity of Ti promotes the ceramic decomposition and the further precipitation of $Ti-O$-based reaction products.

Fig. 5-12 shows the calculated chemical activity of titanium as a function of Ag molar fraction for a $Ag-Cu-Ti$ alloy with fixed Ti molar fraction $x_{Ti}=0.05$. As can be seen, the presence of Ag increases the Ti activity to levels up to $a_{Ti}^{bcc}=0.55$ when the copper/silver fraction reaches $\frac{x_{Cu}}{x_{Ag}}=0$.

In brazing applications, one of the most important parameters to control is the temperature at which the brazing procedure takes place. In order to design proper brazing procedures, knowledge of the solidus and liquidus points is essential. Providing the thermodynamic models are accurate, it is possible to use computational thermodynamics tools to design brazing alloys suitable for specific applications as well as their corresponding brazing temperature schedules. As a manner of example, the phase fraction calculation for a commonly used $Ag-Cu-Ti$ brazing alloy ($Cu-40Ag-5Ti\,wt.\%$) is presented in Fig. 5-13. In their study on the active brazing of zirconia to titanium alloys, Peytour et al. [75] verified the liquidus point for the $Cu-40Ag-5Ti\,wt.\%$ active brazing alloy to be about 850^0C, which agrees well with the phase fraction calculation presented in Fig. 5-13.

As has been noted in Section 2.3.2, the addition of reactive elements to otherwise non-reactive liquid metals can promote the decomposition of a ceramic substrate

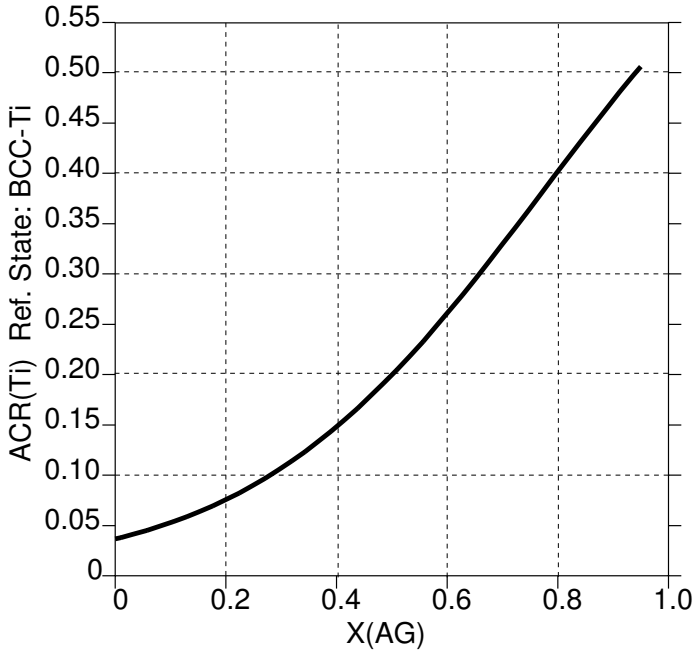

Figure 5-12: Chemical activity of Ti in an $Ag-Cu-Ti$ alloy at 1100^0C with the composition constraint $x_{Ag} + x_{Cu} = 0.95$.

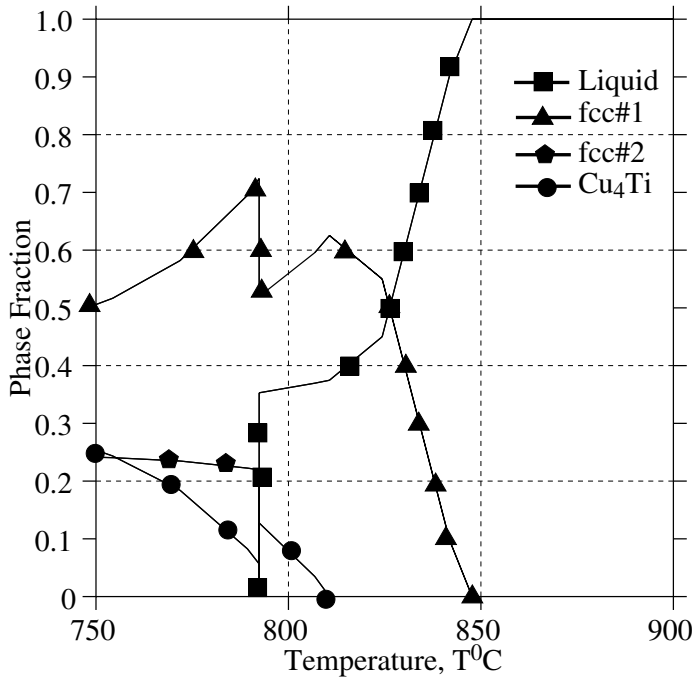

Figure 5-13: Phase fraction calculation for $Cu - 40Ag - 5Ti\,wt.\%$ active brazing alloy.

in contact with it, provided there is a highly negative interaction energy between the active element and the anion in the ceramic. To illustrate the increase in reactivity of brazing alloys through the addition of titanium, the equilibrium between γZrO_{2-x} and $Ag - Cu$ alloys was calculated, considering the dissolution reaction

$ZrO_2 \rightarrow (Zr) + 2(O)$. Fig. 5-14 presents equilibrium calculations of the interaction between zirconia and silver-copper brazing alloys. In 'Fig. 5-14(a) the oxygen dissolution in a $Cu - 40Ag\,wt.\%$ braze is shown as a function of titanium content in the braze. As can be seen, the degree of dissolution increases as Ti increases, due to the strongly negative $Ti - O$ interaction. As a manner of comparison, the same calculation was performed for a brazing alloy with no titanium but with varying amounts of copper and silver.

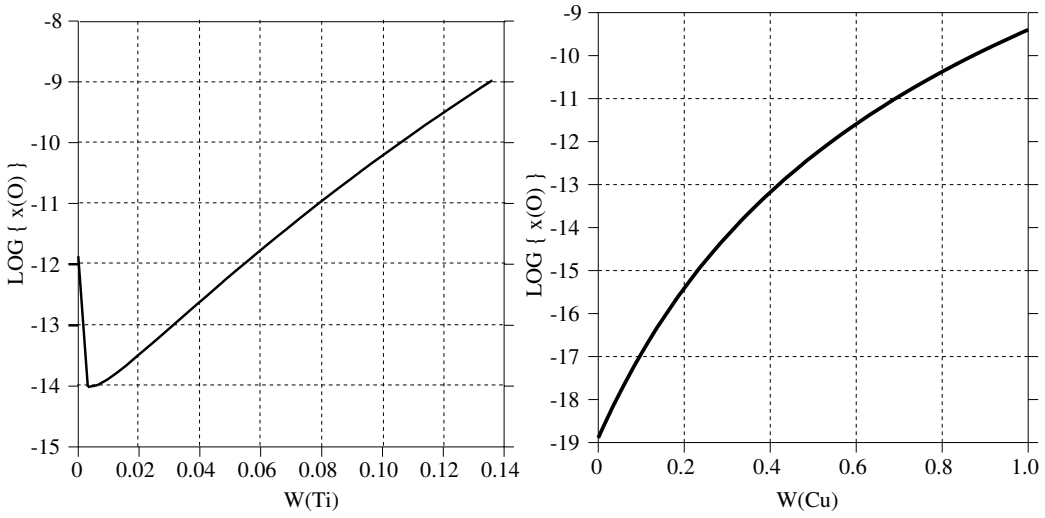

(a) Oxygen dissolution in liquid $Ag - Cu - Ti$ brazing alloy when it reacts with γZrO_2 as a function of titanium content. Base alloy was $Cu - 40Ag\,wt.\%$.

(b) Oxygen dissolution in liquid $Ag - Cu$ brazing alloy when it reacts with γZrO_2 as a function of copper content.

Figure 5-14: $\gamma ZrO_2 \rightarrow (Zr) + 2(O)$ dissolution in $Ag - Cu - Ti$ brazing alloys at 1100^0C. The thermodynamic models developed in this work were coupled with the thermodynamic assessment of the $Ag - Cu - O$ system by Assal et al. [81].

5.5.2 Interfacial Reactions Occurring during $Ag - Cu - Ti$ Brazing of Zirconia

Peytour et al. [127] and Peytour et al. [75] examined the use of $Ag - Cu - Ti$ brazing alloys in the brazing of zirconia-based ceramics (YSZ) to titanium alloys ($Ti - 6Al - 4V$). A sandwich structure $YSZ/Ag - Cu - Ti/Ti$ was assembled and brazed in a vacuum furnace ($1 \times 10^{-5}\,torr$) at 870^0C for $5\,min.$ and cooled to room temperature in $3 - 4\,h.$. The brazed alloy used during these experiments had the composition $Cu - 40Ag - 5Ti\,wt.\%$. The samples were then cross-sectioned and analyzed using *EPMA*, *TEM* and *XRD*. The results from their experiments are summarized as follows:

i) The region of the zirconia piece adjacent to the ceramic/metal interface presented significant discoloration, indicating migration of oxygen atoms from the zirconia

lattice towards the interface.

ii) Zirconium did not diffuse through the interface, therefore, no decomposition of zirconia took place during the brazing operation.

iii) A $2-4\mu m$ reaction layer was observed at the zirconia/braze interface. Through *TEM* and *EPMA* analyses, it was concluded that this phase was an M_6x compound with the stoichiometric composition corresponding to Ti_4Cu_2O.

iv) Small amounts of aluminum from the titanium alloy were observed dissolved in this phase ($x_{Al} < 2\,at.\%$).

v) The sequence $Ag-Cu-Ti/\left(Cu,Al\right)_4 Ti/Cu_4Ti_3/CuTi/CuTi_2/hcp-Ti$ was observed on the metal side of the interface. This sequence correlates well with the equilibrium $Cu-Ti$ phase diagram (see Fig. 3-3(b)).

Yamazaki and Suzumura [128] studied the segregation and reaction layer formation phenomena when zirconia-based ceramics are brazed to themselves using $Ag-Cu-Ti$ brazing alloys. In their experiments, Yamazaki and Suzumura [128] used a brazing filler metal based on the eutectic of the $Ag-Cu$ system with a composition $Ag-26.7Cu-4.5Ti\,wt.\%$. The joints were brazed in a vacuum furnace with a pressure $P < 6\times10^{-2}\,Pa$. The sample was heated to 816^0C, held at this temperature for $5\,min.$ and then cooled to 396^0C in less than $5\,\mathrm{min}$.. The samples were then cross-sectioned and analyzed using *SEM* and *EDX* analysis. From their analysis, it was found that there were two reaction layers adjacent to the zirconia surface. The first one had a composition close to the γTiO phase. The next layer was a $Cu-Ti-O$ compound, with a copper-titanium ratio close to $\frac{x_{Cu}}{x_{Ti}}\sim 1$. The exact composition of this interface could not be determined.

Emiliano et al. [115] studied the brazing of zirconia, TZP, to Ti and to itself using a $Ag-Cu-Ti$ brazing alloy with the nominal composition $Ag-35Cu-1.65Ti$. The samples were heated to 900^0C for up to $30\,min.$ The resulting joints were cross-sectioned and analyzed using conventional analytical techniques (*EPMA*, *EDS*, *SEM*). The results from this study can be summarized as follows:

i) In all cases, the zirconia substrate exhibited significant discoloration close to the ceramic/metal interface.

ii) In the case of TZP/TZP joints, it was observed that the only reaction product formed at the zirconia/braze interface corresponded to TiO.

iii) The TZP/Ti joints exhibited a more complex microstructure. In this case, the first reaction layer observed at the zirconia/braze interface was Ti_2O, followed by a sequence of complex $Cu-Ti-O$ intermetallic compounds belonging to the stoichiometries Ti_3Cu_3O and Ti_4Cu_2O.

iv) On the metallic side of the interface, the phase sequence observed was $Ag-Cu-Ti/Cu4Ti/Cu4Ti_3/CuTi/CuTi_2/Ti$.

Chuang et al. [129] studied the interfacial phenomena during active metal brazing of PSZ to itself using a $Ag - 27Cu - 3Ti\,wt.\%$ alloy. The joints were brazed at 900^0C for $10\,min.$ under a vacuum atmosphere of $10^{-4}\,torr$. Their results were similar to those of Emiliano et al. [115] and the only reaction layer observed at the ceramic/braze interface was TiO.

5.5.3 Thermodynamic Analysis of $ZrO_2/Ag - Cu - Ti/Ti$ Brazed Joints

As has been seen above, the nature of the interfacial reactions at zirconia/metal interfaces become increasingly complicated when the number of components in the molten alloy increases. In principle, a diffusion path analysis similar to the one presented in Section 5.4 may be possible, providing there is a precise knowledge of the thermochemical conditions of the braze alloy and the relative diffusivities of all the elements involved in such reactions are known, at least qualitatively. In the particular case of the interfacial interactions occurring in the $ZrO_2/Ag - Cu - Ti/Ti$ system, very little is known about the properties of the observed reaction products, especially with regard to the M_6X compounds. Despite the lack of knowledge of the properties of this system, it is still possible to examine and rationalize the interfacial reactions observed, provided an accurate thermodynamic description of the system is available.

Kelkar et al. [72] estimated the thermodynamic properties of the $Cu - Ti - O$ system at 945^0C based on the phase diagram determination of the ternary section, coupled with simple thermodynamic calculations considering the phases observed to be at equilibrium with the M_6X compounds Ti_4Cu_2O and Ti_3Cu_3O. From this analysis, they calculated the ternary activity map (described below) for this system. Assuming that at these high-temperatures local equilibrium could be achieved and that the reaction path observed in the $Al_2O_3/Ag - Cu - Ti/Ti$ system should be such that the chemical activities of the reacting components decreased monotonically, Kelkar et al. [72] were able to rationalize the reaction layer sequences observed in alumina/titanium active brazing experiments. The applicability of the analysis by Kelkar et al. [72] is limited due to the fact that the analysis of the $Cu-Ti-O$ system was performed at only one temperature.

In Section 4.3, the $Cu-Ti-O$ system was thermodynamically assessed taking into account the most recent thermodynamic descriptions for the $Cu-Ti$ [30], $Cu-O$ [71] and $Ti - O$ [34] systems, the experimental results on the thermal stability limits of the M_6X compounds [23], and the phase diagram determination of the $Cu - Ti - O$ system [72]. By using the model for the $Cu - Ti - O$ system developed in this work, it is possible to rationalize the interfacial interactions between zirconia and active brazing alloys at arbitrary brazing temperatures.

Fig. 5-15 presents the calculated activity diagram for the $Cu - Ti - O$ system at 900^0C. In a ternary activity diagram, the phase-state of the system is determined by the activity of one element, plus the relative compositions of the remaining two

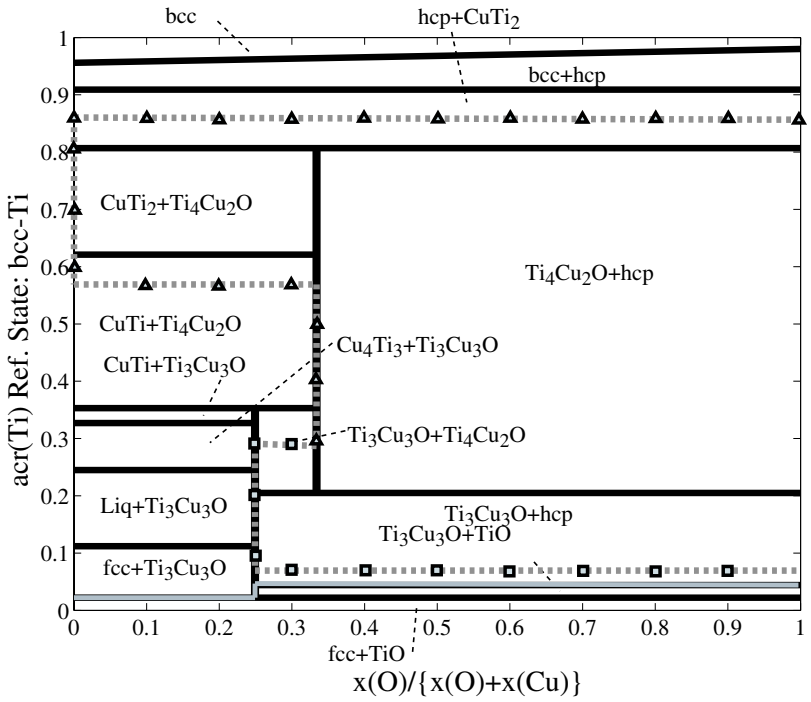

Figure 5-15: Activity diagram for the $Cu - Ti - O$ system at 900^0C

components of the system. In this diagram, horizontal lines represent the activity at which three phases are at equilibrium.

In principle, the activity of an element should show a monotonic variation across a thermodynamically stable reaction zone *. Based on this constraint, it is possible to restrict the possible diffusion paths and reaction layer sequences in any given diffusion couple. The monotonic variation of the activity of a reacting element implies that the reaction path observed in an activity diagram should always follow a direction towards decreasing chemical activity.

The reaction sequence observed by Peytour et al. [75, 127] is depicted in Fig. 5-15 as the dashed gray line with triangles as the markers. From this diagram, it can be seen that the titanium substrate acts as a continuous source of titanium, maintaining always the saturation composition in the liquid. The titanium activity decreases monotonically towards the reaction product with the lowest Ti activity, Ti_4Cu_2O. Even though the samples were held at the brazing temperature for only $5\,min.$, the reaction products observed satisfy the local equilibrium condition.

The reaction sequence observed by Peytour et al. [75, 127], however, does not contemplate the formation of Ti_3Cu_3O and Ti_2O at the zirconia/braze interface, as was observed by Emiliano et al. [115]. This latter reaction sequence is also depicted

*This requirement, however, does not hold when this element is forced to diffuse uphill due to the diffusion of other elements [72]

by the dashed gray line with triangles, plus the dashed line with squares. It is important to note that in the brazing experiments by Emiliano et al. [115], the samples were held at the brazing temperature for $30\,min.$. The formation of the Ti_2O and Ti_3Cu_3O phases seems to be limited by kinetic (i.e. nucleation) factors.

It is important to note that the $Cu4Ti$ reaction product observed in Peytour et al. [75], Emiliano et al. [115], Peytour et al. [127] is not stable at 900^0C. Its formation, therefore, must have occurred upon cooling of the sample.

5.5.4 Thermodynamic Analysis of $ZrO_2/Ag-Cu-Ti/ZrO_2$ Brazed Joints

Contrary to the experiments on ZrO_2/Ti brazing, when zirconia was brazed to itself the only reaction products observed where Ti_3Cu_3O and TiO [115, 128, 129]. The reason for this is that the maximum Ti activity in the system corresponds to the initial thermochemical condition of the brazing alloy, since there is no external titanium source. Table 5.4 shows the calculated initial activities for the three different brazing alloys used by Emiliano et al. [115], Yamazaki and Suzumura [128], Chuang et al. [129]. Comparing these Ti activities to the activity map in Fig. 5-15, it is evident that the maximum activity of these alloys lie below the minimum stability range of the Ti_4Cu_2O. This reaction layer is not expected to form at the zirconia/braze interface during *Zirconia/Zirconia* active brazing.

Table 5.4: Titanium activities of $Ag-Cu-Ti$ Brazing Alloys.

Alloy Composition	**Brazing Temperature**	**Ti Activity. Ref: Ti-bcc**
$Ag-26.7Cu-4.5Ti\,wt.\%$ [128]	816^0C	0.20
$Ag-35Cu-1.65Ti\,wt.\%$ [115]	900^0C	0.15
$Ag-27Cu-3Ti\,wt.\%$ [129]	900^0C	0.19

At the early stages of the zirconia/braze interaction, oxygen will diffuse out of the zirconia lattice. Due to the strong $Ti-O$ interaction, Ti will segregate to the zirconia/braze interface [5, 72]. Since in all these brazing experiments the braze interlayer was a thin foil of about $100\mu m$, it is expected that this titanium segregation will cause the titanium content in the brazing alloy to decrease as the interfacial reaction progresses. Yamazaki and Suzumura [128], Chuang et al. [129] report that, according to *EDS* measurements, the active braze interlayer was effectively depleted of titanium after the brazing process was completed. Since most of the titanium will be present in the reaction layers at the zirconia/braze interface, a diffusion path in this case will be-

gin with the highest activity of titanium in the reaction layer immediately adjacent to the zirconia surface. This diffusion path is indicated in Fig. 5-15 as a solid gray line, beginning in the TiO phase field, through the Ti_3Cu_3O phase, towards the fcc phase.

In order to determine the first phase to precipitate under these experimental conditions, a metastable thermodynamic equilibrium calculation between γZrO_{2-x} and three $Ag-Cu-Ti$ liquid alloys with compositions indicated in Table 5.4 was performed. From these calculations (see Table 5.5), it was evident that both TiO and Ti_3Cu_3O will precipitate, provided there was enough time for the phases to nucleate. In all cases, the phase with the highest driving force for precipitation was TiO and it is therefore expected that this phase will be found adjacent to the zirconia surface. Contrary to what would be expected, however, there is only one instance [128] in which Ti_3Cu_3O is also present in the reaction zone close to the zirconia/braze interface. The reason for this remains unclear, although it could be related to a lower stability of the Ti_3Cu_3O phase as the temperature increases. The melting point of this compound was found by Kelkar and Carim [23] to be about 1120^0C.

Table 5.5: Normalized driving forces for precipitation at a metastable $\gamma ZrO_2/Ag-Cu-Ti$ interface.

Alloy Composition	**Driving Force TiO**	**Driving Force Ti_3Cu_3O**
$Ag-26.7Cu-4.5Ti\,wt.\%$ [128]	2.81	1.6
$Ag-35Cu-1.65Ti\,wt.\%$ [115]	2.54	1.28
$Ag-27Cu-3Ti\,wt.\%$ [129]	2.73	1.49

5.6 Interfacial Reactions in the Zirconia/Cu-Ti-Al/Ni System

Although conventional active brazing alloys based on the $Ag-Cu-Ti$ have been proven effective in zirconia/metal applications, their applicability is somewhat limited due to their relatively low melting range ($800-850^0C$). In many technologies were zirconia-based ceramics play an important role, it is necessary to develop ceramic/metal joining techniques capable of producing joints with higher operating temperatures. To this effect, brazing alloys based on the $Cu-Ti$ system were examined.

Partially stabilized zirconia and Inconel 718® discs ($10\,mm\,diameter \times 5\,mm\,height$

were cut and polished to a $1\,\mu m$ surface finish. Ti, Cu and Al powders were premixed and then ball milled for 2 hours to achieve uniform particle size. The resulting mixtures were cold-pressed in a die to make preforms with dimensions $10\,mmdia \times 1\,mmh$. The zirconia, nickel and brazing preforms were assembled into a sandwich structure and placed inside a vacuum furnace (see Appendix F). A constant axial load was applied to the samples*.

5.6.1 Experimental Results

In Arroyave [51], a complete description of the active brazing experiments using several braze compositions and temperatures is presented. For the purpose of this work, and to illustrate the use of thermodynamic tools to rationalize just some selected experimental results are presented. Note that all the brazing experiments presented here had holding times of about $1\,hr$ at the brazing temperature.

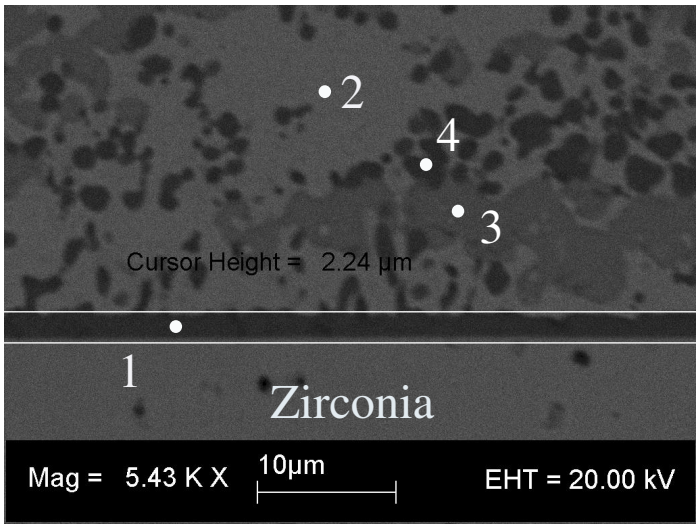

Figure 5-16: Zirconia/Metal brazing using $Cu - 10\,wt.\%$ at 1025^0C.

Fig. 5-16 shows the zirconia/braze interface of a zirconia/Inconel® joint using a $Cu - 10\,wt.\%$ brazed at 1025^0C. This interface is representative of all the other joints using this composition and brazing temperatures within the $1025 - 1050^0C$ range. The reaction product adjacent to the zirconia surface was found to have a composition corresponding to Ti_2O_3. At these high temperatures, significant dissolution of Ni into the liquid braze was observed (point 3 in Fig. 5-16).

In order to reduce the Ni dissolution and to develop brazing alloys with a higher solidus-liquidus range, brazing alloys with a composition $Cu - 5\,wt.\%$ were used in zirconia/Inconel® joining experiments. Fig. 5-17 shows two micrographs corresponding to joints brazed at 950^0C and 1025^0C. Note that the reaction products at

*For details regarding the experiment, refer to Arroyave [51]

Table 5.6: Compositions of points indicated in Fig. 5-16, $at.\%$

	1	**2**	**3**	**4**
Cu	2.2	21	14.6	97
Ni	0	0	18	0.6
Ti	37	79	59	1.2
Cr	0	0	3.2	0.4
Fe	0	0	3.2	0.3
O	60.8	0	0	0

the zirconia/braze interface have different stoichiometry. At 950^0C the $Ti-O$ oxide can be identified as TiO, while the reaction layer at the higher temperature has a composition close to that of Ti_2O_3. In the joint at 1025^0C incipient dissolution of the nickel super alloy can be observed (point 5 in Fig. 5-17(b)).

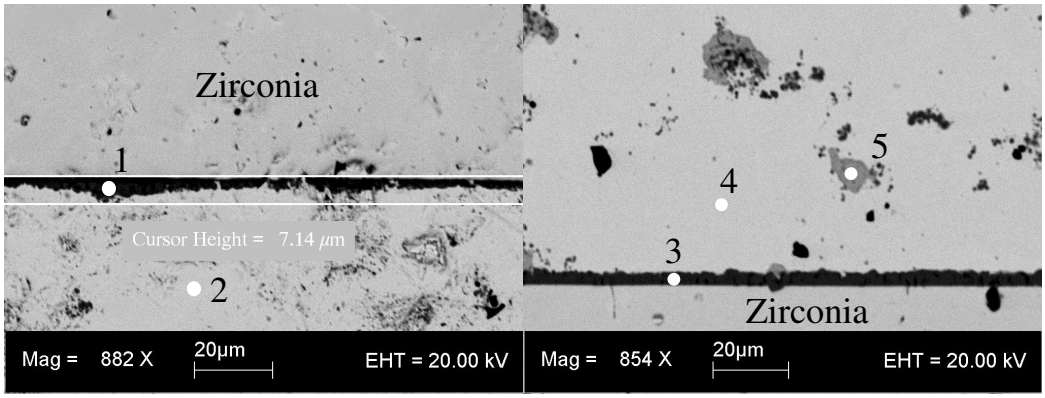

(a) Zirconia/Inconel® joint. $Cu-5\,wt.\%$ Braze at 950^0C.

(b) Zirconia/Inconel®joint. $Cu-5\,wt.\%$ Braze at 1025^0C.

Figure 5-17: Brazing experiments using $Cu-5\,wt.\%$ brazing alloys.

One of the main limitations of active metal brazing alloys based on the $Ag-Cu-Ti$ system is their poor oxidation resistance [130]. In order to increase the oxidation resistance of active brazing alloys, Kapoor and Eagar [131] proposed the addition of aluminum to $Cu-Ti$ and $Sn-Ti$ conventional active brazing alloys. In their experiments, Kapoor and Eagar [131] determined that Al effectively reduced the oxidation rates of these active alloy. Through wetting experiments, it was also shown that the addition of Al did not affect the reactivity and wettability of the brazing alloys when they were put in contact with a Al_2O_3 substrate. Based on these results, an investigation on the use of $Cu-Ti-Al$ alloys for zirconia/metal brazing applications was

Table 5.7: Compositions of points indicated in Fig. 5-17, $at.\%$

	1	**2**	**3**	**4**	**5**
Cu	0	96	0	96.6	8.6
Ni	0	0	0	1.0	6.9
Ti	46.8	3.8	38	1.6	57.4
Cr	0	0	0	0.4	6.9
Fe	0	0	0	0.3	7.8
O	53.3	0	62	0	0

performed.

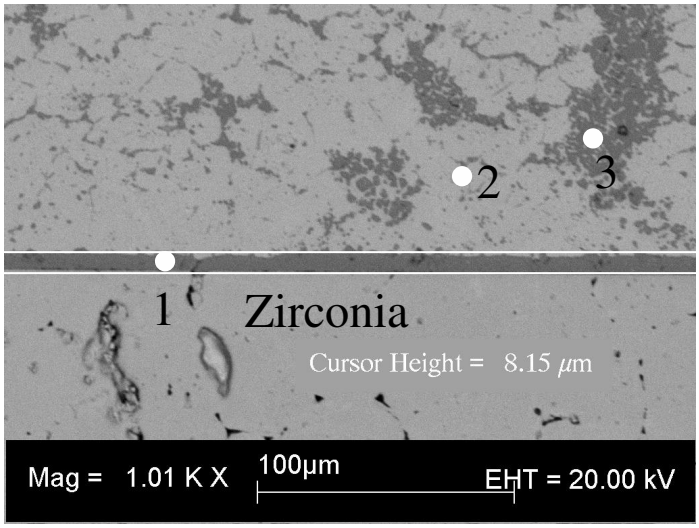

Figure 5-18: Zirconia/Inconel® joint. $Cu-10Ti-5Al\,wt.\%$ braze at 975^0C.

Fig. 5-18 shows a micrograph of the zirconia/braze interface resulting when the ceramic/metal joint is created using a $Cu-10Ti-5Al\,wt.\%$ brazing alloy. According to Table 5.8, the composition of the reaction layer adjacent to the zirconia substrate has a composition corresponding to $Ti_3(Cu,Al)_3O$. Extensive dissolution can be observed (point 3 in Fig. 5-18). Fig. 5-19 shows a higher magnification micrograph of the interface shown in Fig. 5-18. From this figure, it is evident that a third phase has precipitated at the ZrO_2/Ti_3Cu_3O interface. Although the analytical techniques used in this work do not allow the identification of these small precipitates, it may be possible that they are TiO particles.

Table 5.8: Compositions of points indicated in Fig. 5-18, *at.*%

	1	**2**	**3**
Cu	36.8	93.7	30.1
Al	7.4	3.5	8.2
Ni	2.7	0.2	15.1
Ti	38.2	2.7	43.8
Cr	0	0	1
Fe	0	0	1.8
O	14.9	0	0

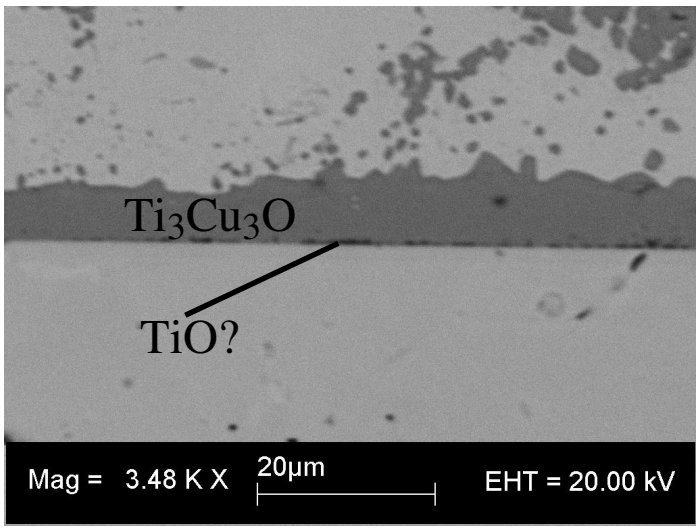

Figure 5-19: High magnification of zirconia/$Cu - Ti - Al$ interface.

5.6.2 Analysis of Experimental Results

The results presented above can be summarized as follows:

i) When the $Cu - 10\,wt.\%$ brazing alloy is used at high temperatures, extensive dissolution of the nickel based substrate occurs. Under these conditions, the reaction product observed is Ti_2O_3

ii) In the case of the $Cu - 5\,wt.\%$ brazing alloy, at the lower brazing temperature, 950^0C, TiO is observed to form at the zirconia/braze interface. When the brazing temperature is 1025^0C, incipient dissolution of the metal substrate leads to Ti scavenging and the resulting reaction product is Ti_2O_3.

iii) When the $Cu - 10Ti - 5Al$ brazing alloy is used, although significant titanium scavenging occurs, the reaction product at the zirconia/braze interface seems to

be $Ti_3(Cu, Al)_3O$.

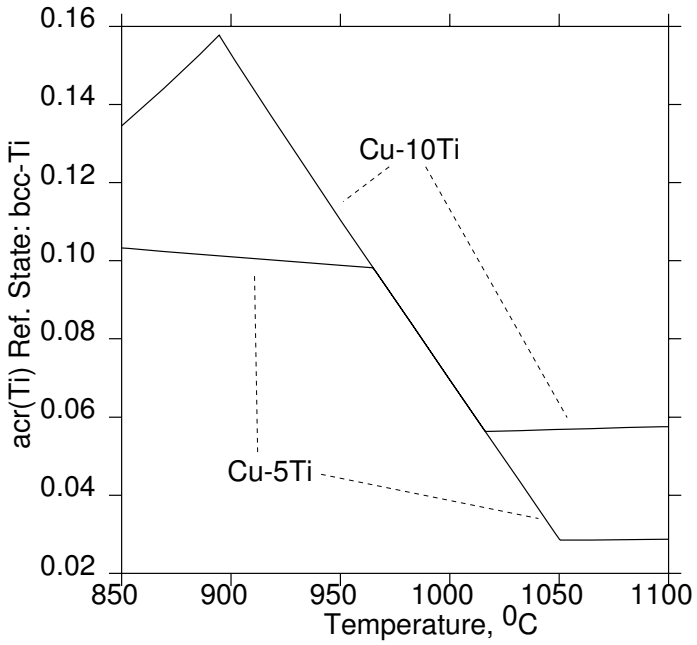

Figure 5-20: Ti activities of the $Cu-10$ and $Cu-5$ brazing alloys as a function of temperature.

Fig. 5-20 shows the Ti chemical activity for the $Cu-10\,wt.\%$ and $Cu-5\,wt.\%$ brazing alloys as a function of temperature. As can be seen, when the brazing alloy lies within the $fcc+liquid$ two phase field, the chemical activity of titanium increases. At higher temperatures, the chemical activity is about 0.03 for the $Cu-5\,wt.\%$ alloy and 0.06 for the $Cu-10\,wt.\%$ braze.

By examining the activity diagram for the $Cu-Ti-O$ system at 1000^C in Fig. 5-21, and using the chemical activities for the two brazing alloys in Fig. 5-20, it is evident that both Ti_3Cu_3O and TiO should be observed at zirconia/braze interfaces when the $Cu-10\,wt.\%$ is used. For the case of the $Cu-5Ti\,wt.\%$ alloy, the expected reaction layer is TiO. According to the results presented above, the only instance where the reaction product observed at the ceramic/metal interface corresponds to what should be expected is when the $Cu-5Ti\,wt.\%$ alloy is used at 950^0C. In the experiments corresponding to this case, it was observed that no metal substrate dissolution into the braze.

In Chapter 6, it is shown that the nature of the metal substrate to be joined to a ceramic may determine to a great extent the thermochemistry of the brazing alloy. According to the analysis in that chapter, the large solubility of Ni in Cu, coupled to the highly negative interaction energy between Ni and Ti may result in a dramatic decrease in the chemical reactivity of the brazing alloy. Because of the high diffusion rates within the liquid, the chemical activity of Ti in the braze my be

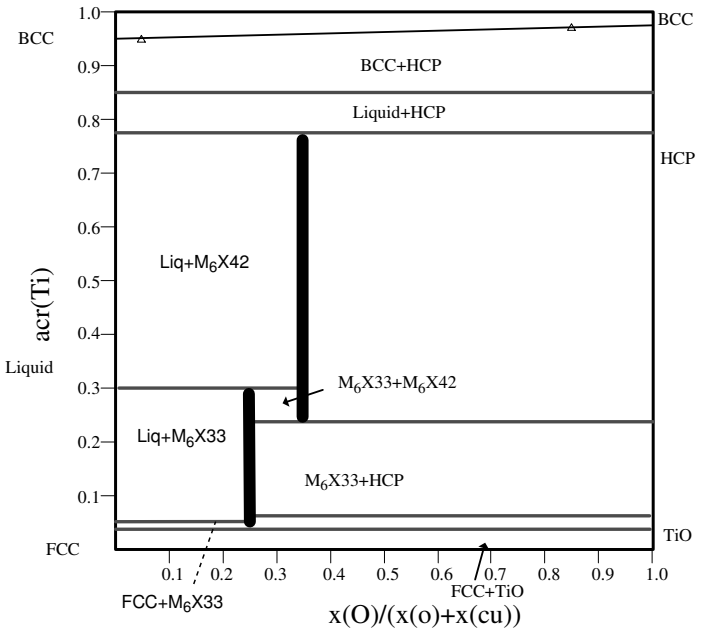

Figure 5-21: Activity diagram for the $Cu - Ti - O$ system at 1000^0C.

reduced by a factor of 5 within $100\,s$ from the start of the interdiffusion reaction. In the experiments presented above, the only case where the reaction product observed at the ceramic/metal interface corresponded to what was expected was the brazing experiment at 950^C. According to the $Cu - Ti$ phase diagram, at this temperature and with the $Cu - 5\,wt.\%$ brazing alloy, the liquid fraction at the interlayer is less than 50%. Under these conditions, the dissolution reaction is limited, and Ni cannot scavenge Ti from the braze. At higher temperatures, however, Ni dissolution occurs and the chemical activity of Ti in the braze is reduced below the stability range of TiO. According to thermodynamic calculations in the $Cu - Ti - O$ system, in order to observe Ti_2O_3 at the zirconia/braze interface, the chemical activity in the liquid must decrease to values below 0.005. It is expected that when the ceramic/metal joint is held at the brazing temperature for about an hour and the liquid fraction in the interlayer is higher than 50% the chemical activity of Ti should decrease to 0.005 or less. These observations have been confirmed in a related experimental work:

Sciti et al. [132] studied the brazing of YSZ zirconia to Ni-based super alloys. In their experiments, small pieces of zirconia and Ni-based super-alloy (thickness $\sim 2\,mm$) were assembled in a sandwich structure with a $Ag - 35.25Cu - 1.75Ti\,wt.\%$ brazing foil as an interlayer. The samples were brazed at $820 - 950^0C$ for $20\,min.$ and then cooled to room temperature. Their results are summarized below:

i) The reaction layer observed at the zirconia/braze interface was a TiO_x oxide. The exact stoichiometry was not determined, but it was established that the composition of this phase was within the $Ti_2O_3 < TiO_2$ range. This layer had a thickness of about $1.2\mu m$.

ii) Immediately adjacent to this reaction product, a layer composed of Ni, Ti and Cu was observed.

iii) It was also observed that both Ti and Cu diffused into the $Ni-based$ super alloy.

In the case of the brazing experiments with the $Cu-10Ti-5Al$ brazing alloy, there was significant Ti scavenging. However, the observed reaction product at the ceramic/metal interface was Ti_3Cu_3O. To explain this, it is necessary to determine the effect of Al on both the thermochemistry of the brazing alloy, and on the stability of the $Ti_3(Cu,Al)_3O$ compound. In Section 4.3, a model was proposed to describe the dissolution of aluminum in the Ti_3Cu_3O M_6X compound. According to the calculations presented in that section, aluminum stabilized the M_6X structure and dissolved in significant amounts. Fig. 5-22(a) shows the effect of aluminum additions on the stability of the Ti_3Cu_3O compound. As can be seen, the minimum activity for which this phase is stable decreases as the aluminum content in the braze increases. This effect is coupled to the *slight* increase on the chemical activity of Ti in $Cu-Ti-Al$ alloys as the aluminum content increases (note that there is a maximum in the chemical activity of titanium as a function of aluminum content). Using these results, the presence of Ti_3Cu_3O at the zirconia/braze interface can be easily explained.

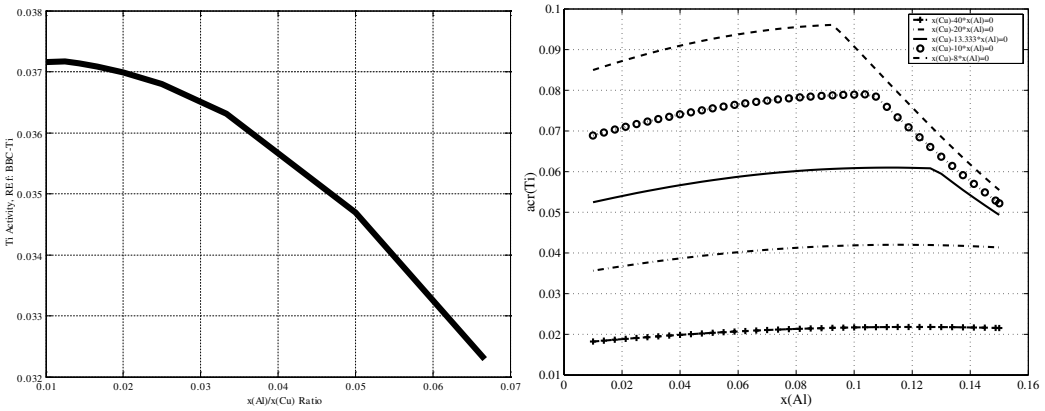

(a) Minimum Ti activity to observe Ti_3Cu_3O precipitation at ceramic/braze interfaces as a function of aluminum content.

(b) Effect of aluminum on the activity of Ti in $Cu-Ti$ brazing alloys for different $Cu-Ti$ ratios.

Figure 5-22: Aluminum effect on the thermochemistry of zirconia/$Cu-Ti-Al$ interactions.

It is important to note that further evidence for the stabilizing effect of Al on the Ti_3Cu_3O phase comes from the experimental results on the active brazing of alumina using $Ag-Cu-Ti$-based brazing alloys. According to Kelkar et al. [72], in all the experiments where alumina was joined to itself using $Ag-Cu-Ti$ brazes, the sequence $TiO/Ti_3(Cu,al)_3O$ was observed at the alumina/braze interface. The

presence of aluminum, dissolved from the ceramic substrate, stabilized and promoted the formation of the $Ti_3(Cu, al)_3O$ compound, in agreement with the $Cu - Ti - O$ ternary activity map.

5.7 Interaction between $Cu - Zr$ melts and Zirconia

In all the experimental results described above, the reaction products observed at the zirconia/liquid-metal interface formed a layered, approximately planar structure, irrespective of the complexity of the reaction sequence. Once the reaction product precipitated on the zirconia surface, the diffusion of oxygen atoms across the reaction products constituted a limiting factor. An entirely different interfacial structure could be observed, however, if no solid phase precipitates on the zirconia surface and the dissolution of the zirconia substrate is thermodynamically favorable. Such an interface is observed when $Cu-Zr$ brazes react with zirconia substrates, as shown in Fig. 5-23.

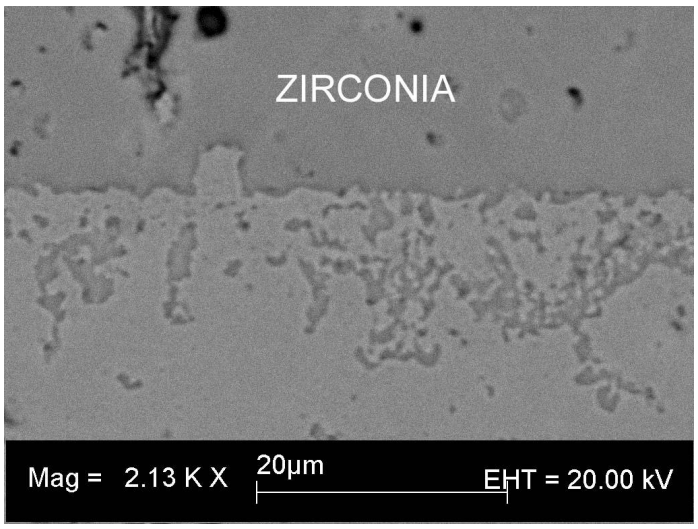

Figure 5-23: $Cu - 5\,wt.\%$ braze/zirconia interface, at 1050^0C. Held at brazing temperature for $1\,hr$.

The zirconia samples brazed in these experiments showed the typical blackening observed in other experiments on zirconia/active metal interactions, indicating the partial reduction of the zirconia lattice and the subsequent formation of oxygen vacancies and free charge carriers. From Fig. 5-23, it is evident that the $Cu - Zr$ braze not only drives oxygen atoms from the zirconia lattice into the braze, but also attacks the zirconia substrate. The irregular zirconia/braze interface clearly shows that some zirconia particles partially detach from the bulk. In some cases, this detachment is complete and zirconia particles can be observed to completely separated from the zirconia surface. Unfortunately, there is almost no experimental information regarding the thermodynamics of the $Cu - Zr - O$ (see Section 4.4), and the approaches outlined above cannot be used. Despite this, it is possible to calculate whether, under

these thermal and chemical conditions, extensive zirconia dissolution in the melt can be expected. To do this, the approach outlined in Section 2.3 can be followed.

The dissolution of ZrO_2 into a $Cu - Zr$ melt ($ZrO_2 \rightarrow (Zr) + 2(O)$) can be studied using Eq. 2.6 in 2.3.1:

$$\begin{aligned} a_{Zr}a_O^2 &= \exp\left(\frac{\Delta G_f^{Zr}}{RT}\right) \\ x_{Zr}\gamma_{Zr}\left(x_O\gamma_O\right)^2 &= \exp\left(\frac{\Delta G_f^{Zr}}{RT}\right) \end{aligned} \tag{5.2}$$

where

$$\begin{aligned} \ln\left(\gamma_{Zr}\right) &= \ln\left(\gamma_{Zr}^{\infty}\right) + \varepsilon_{Zr}^{Zr}x_{Zr} + \varepsilon_o^{Zr}x_O \\ \ln\left(\gamma_O\right) &= \ln\left(\gamma_O^{\infty}\right) + \varepsilon_O^{O}x_O + \varepsilon_o^{Zr}x_{Zr} \end{aligned}$$

Assuming that $\varepsilon_{Zr}^{Zr}x_Zr$ and $\varepsilon_O^{Zr} << ln\gamma_Z r^{\infty}$ and $\varepsilon_O^{O}x_O \sim 0$ (see Table 5.9):

$$x_{Zr}\left(x_O\right)^2\exp\left(2\varepsilon_O^{Zr}\cdot x_{Zr}\right) = \exp\left(\frac{\Delta G_f^{ZrO_2}}{RT}\right)\cdot\frac{1}{\gamma_{Zr}^{\infty}\left(\gamma_O^{\infty}\right)^2}$$

If there is no Zr initially in the melt, it is possible to use the relationship $x_{Zr} = \frac{x_O}{2}$ and we have (since $x_{Zr} \sim 0$):

$$x_O^a \approx \left\{2\exp\left(\frac{\Delta G_f^{ZrO_2}}{RT}\right)\cdot\frac{1}{\gamma_{Zr}^{\infty}\left(\gamma_O^{\infty}\right)^2}\right\}^{1/3} \tag{5.3}$$

When there is already Zr in the melt, $x_{Zr} >> z_O$, and therefore

$$x_O^b \approx \left\{\exp\left(\frac{\Delta G_f^{ZrO_2}}{RT}\right)\cdot\frac{1}{\gamma_{Zr}^{\infty}\left(\gamma_O^{\infty}\right)^2}\cdot\frac{1}{x_{Zr}\exp\left(2\varepsilon_O^{Zr}\cdot x_{Zr}\right)}\right\}^{1/2} \tag{5.4}$$

Using the thermochemical values for $Cu - Zr - O$ melts at 1100^0C in Table 5.9, it is possible to calculate the two different cases presented in Eq. 5.3 and Eq. 5.4, considering an initial zirconium concentration for the second case of $x_{Cu} = 0.05$. The calculations yield $x_O^a = 4 \times 10^{-10}$ and $x_O^b = 9 \times 10^{-12}$. As expected, $x_O^a >> x_O^b$.

Based on the analysis presented above, one would expect the dissolution of ZrO_2 into Cu alloys to be significantly decreased when Zr is added to the melts. Obviously, this is not what has been observed in the experimental results, exemplified by Fig. 5-23. This discrepancy between theory and experiments shows that there is a limit to the simplified analyses presented in this work. In this particular case, the observed interfacial structure cannot be explained using the bulk thermodynamic properties of the phases involved. Although explaining the nature of this interfacial reaction lies

Table 5.9: Thermochemistry of $Cu-Zr-O$ melts at 1100^0C in the Cu-rich region.

$\Delta G_f^{ZrO_2}$	$-836,971\ J/mol(ZrO_2)$
$ln\,(\gamma_O^{\infty})$	-2.03
$ln\,(\gamma_{Cu}^{\infty})$	-3.7
ϵ_O^O	-8.57
ϵ_{Zr}^{Zr}	0.6
ϵ_O^{Zr}	-118
ϵ_{Zr}^{O}	-118

beyond the scope of this work, it may be possible to present a hypothesis regarding the apparent attack of the zirconia substrate by $Cu-Zr$ melts.

In general, defects (one or two-dimensional) constitute highly energetic and chemically active regions within a phase. It is likely then that defects within the zirconia substrate, such as grain boundaries, were selectively attacked by the $Cu-Zr$ melt. Initial depletion of oxygen within these grain boundaries may have made them unstable with respect to further decomposition and dissolution into the attacking liquid. This attack may have been aided by liquid permeation through the porous zirconia structure. Once the grain boundaries were selectively attacked, grains or particles of the zirconia substrate could be easily detached from the bulk.

This hypothesis, however, is highly speculative, and further analysis of the interfacial structure is required. Furthermore, in order to rationalize the formation of this interface requires a much more sophisticated theory, which is definitely beyond the scope and objectives of this thesis.

5.8 Application of Thermodynamics to the Study of Zirconia/Metal Interfaces: Conclusion

In this chapter, the thermodynamic models developed in Chapter 3 and Chapter 4 have been used to rationalize several interesting interfacial phenomena occurring when zirconia-based ceramics are put in contact with reactive metals. In the case of ZrO_2/Ti interactions, it was shown how the use of metastable thermodynamic calculations allow the prediction of reaction paths that are in good agreement, at least qualitatively, with reported experiments. According to the analysis presented in this chapter, the relative size of the zirconia and titanium subsystems influences the reaction path observed. The interactions between active brazing alloys and zirconia substrates were analyzed using chemical activity diagrams and simple thermodynamic calculations. From these analyses, it was concluded that in the majority of the cases

the reaction layers formed at the interface satisfied the local equilibrium condition, despite the relatively short brazing times in some ceramic/metal joining experiments.

Chapter 6

Metal Substrate Effects on the Thermochemistry of Active Brazing Interfaces

6.1 Introduction

In most cases, ceramics are not wetted by molten metals [9]. The reason for this is the relatively high stability of ceramic surfaces: a ceramic/vapor interface is more stable than a ceramic/liquid interface. Therefore, in ceramic/metal (C/M) joining applications using a liquid interlayer between the ceramic and metal parts (i.e. brazing), the melt usually has to be chemically modified to promote wetting. Adding chemically active elements to the melt improves the wettability of molten metals over ceramic substrates for two reasons (see Section 2.6):

i) The active element can promote a greater ceramic dilution. Dissolved oxygen reduces the *Solid/Liquid* interfacial energy and increases the work of adhesion of the C/M system.

ii) If the interaction between the active element and the anion is strong, the precipitation of a reaction layer can be promoted. If this reaction layer has the appropriate electronic properties* wetting is further promoted and the work of adhesion increases to levels that make C/M interfaces practical.

Much of the literature on C/M active brazing has been focused on the nature of the interactions between the ceramic substrate and active brazing alloys (see for example Eustathopoulos and Drevet [16]). Almost nothing, however, has been published on the analysis of the effects of using different metal substrates on the thermochemistry of the brazing alloys themselves. It will be shown in this work that the metal substrate can have a significant effect on the thermochemical behavior of the brazing alloy.

*i.e. metallic in character.

The chemical activity of the active element used in the brazing alloy determines the extent and character of interfacial reaction at the C/M interface*. Therefore, studying the changes in the reactivity of the brazing alloy as it interacts with the metal substrate is of great importance when designing and analyzing C/M active brazing processes. In this chapter, the work by Arroyave and Eagar [133] on the metal substrate effects on the thermochemistry of brazing alloys will be presented and complemented with some experimental results by Arroyave [51].

6.2 Previous Experimental Evidence

There are a number of experimental results available in the literature that illustrate the effects of using a particular substrate material on the thermochemistry of active brazing alloys. Through their work on alumina/metal joining processes, Barry and Leatherman [134] found that the brazing temperature had a noticeable effect on the final tensile strength of alumina/(Fe-29Ni-17Cu) joints. Using three different Cu-based active brazing alloys they found that by brazing at temperatures much higher than the alloy liquidus, the strength of the joint was greatly decreased. As the temperature increased, a larger Ni content was observed and this correlated with a lower tensile strength.

Stephens et al. [135] found that when brazing alumina to Kovar® with $Ag-Cu-Ti$ alloys the Ti active element was scavenged from the brazing alloy and $Ni-Ti$ intermetallic compounds were formed (Ni_3Ti was the most usual intermetallic phase observed). The scavenging prevented the formation of a continuous Ti_xO layer at the alumina/braze interface. It was found that the joints with discontinuous reaction layers offered poor hermeticity. By using a Mo-based diffusion barrier, it was found that dissolution of the Kovar® substrate was decreased and a continuous Ti_xO layer was observed at the alumina/braze interface. The performance of the joints using this diffusion barrier was noticeably better that those without it.

The detrimental effect of Ni dissolution into the braze alloy is not limited to ceramic oxide/metal joining applications. Kim et al. [136] investigated silicon nitride/steel joints using Ni-based interlayer materials and Ti-based active brazing alloys. In their work, Kim et al. [136] found that the Ni interlayer dissolved into the brazing alloy. As this dissolution increased, the joint strength decreased due to the formation of a brittle $Ni-Ti$ compound and a decreased reactivity of the braze at the interface with the ceramic. Due to the decreased reactivity of the brazing alloy, the active brazing alloy did not wet the ceramic substrate.

Using the same type of active brazing alloys used in the experiments previously described, Bucklow [137] studied zirconia/cast iron joints. In this case, no detrimental excessive dissolution reactions between the substrate metal and the brazing alloy were reported.

*Determining, for example, the interfacial reaction product.

Based on the experimental evidence above, complemented by the experiments described in Section 5.6 it is possible to conclude that:

- At temperatures much higher than the liquidus of the $Cu-Ti$ brazing alloys, the reaction between the brazing alloy and the ceramic is negligible or non-existent when the metal substrate has a high Ni content.
- The same effect is less pronounced when the alloy's main component is Fe.
- In brazing experiments with Ni-based metal substrates, considerable Ni dissolution in the brazing alloy is observed. Moreover, when Ni is dissolved in great amounts, brittle $Ni-Ti$ precipitates have also been observed.

6.3 Substrate-Brazing Alloy Interaction: Simplified Analysis

Table 6.1: Enthalpies of infinite dilution of Ti in melts.

Solvent	**Enthalpy of Dilution, J/mol**
Cu	$-10,000$ [30]
Fe	$-54,000$ [138]
Ni	$-187,000$ [139]

Table 6.1 shows the calculated partial enthalpies at infinite dilution for Ti in different liquid solvents. As can be seen, the infinite dilution enthalpy for Ti in Ni is very negative* and therefore it should be expected that the chemical activity of Ti in Ni melts has very large negative deviations from ideality †.

At $1300\,^0C$, and using the thermodynamic description for the $Ni-Ti$ binary system according to Kaufman [139]:

$$RT\ln\left(\gamma_{Ti}^{0}\right) = -102,000\,J/mol \tag{6.1}$$

Therefore, $\gamma_{Ti}^{Ni} \sim 4\times10^{-4}$. Thus, at infinite dilution the activity of Ti is greatly reduced if Ni is present in significant amounts. In the case when Ti is dissolved into Fe, under the same dilution and temperature conditions and using the thermodynamic description given by Jonsson [138], $\gamma_{Ti}^{Fe} \sim 10^{-2}$. Thus, the effect of Fe on the chemical activity of Ti should be, based on these simple calculations, much smaller than that of Ni.

*i.e. large negative interaction energies

†$\gamma << 1$

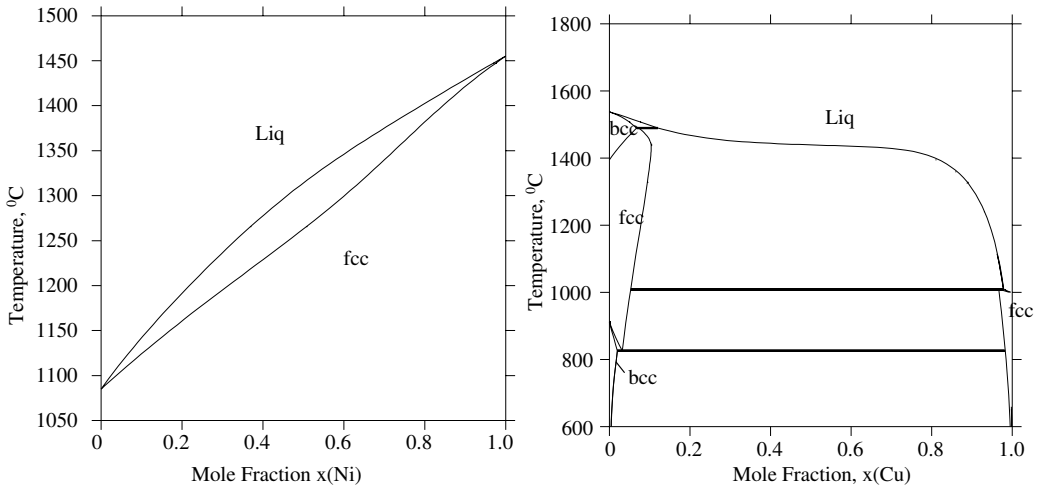

(a) $Cu - Ni$ phase diagram.

(b) $Cu - Fe$ phase diagram.

Figure 6-1: Calculated $Cu - Ni$ and $Cu - Fe$ phase diagrams.

Using thermodynamic arguments, it is also be possible to examine the nature of the interactions between Cu and the metal substrates Ni and Fe.

The lenticular shape of the $Cu - Ni$ phase diagram in Fig. 6-1(a) shows that the system is nearly ideal. The system exhibits complete solubility in both the solid (fcc) and the liquid phases. It is therefore reasonable to expect that, when in contact with a Cu-rich liquid, significant amounts of Ni will be dissolved in the melt. The $Cu-Fe$ phase diagram (Fig. 6-1(b)), on the other hand, exhibits very little solubility of Fe into Cu-based liquid solutions, so the degree of dissolution of an Fe-rich metal substrate into a Cu-based brazing alloy should be significantly less.

From this analysis, it follows that Ni will have a much larger effect than Fe on the chemical activity of Ti in Cu melts due to two factors:

- There is a very strong affinity between Ni and Ti (see Table 6.1).
- Ni dissolves extensively in Cu melts (see Fig. 6-1(a)).

6.4 Thermochemical Analysis of Metastable Interfacial Systems

To verify the analysis presented above, numerical simulations of the thermochemical interactions between the two different metal substrates and Cu-based active brazing alloys were performed. For simplicity, the analysis was focused on two commonly used metal substrates (Ni and Fe) and a simple active brazing alloy belonging to the $Cu - Ti$ system ($95\,at.\,\%Cu$). This analysis, however, can be applied to other active brazing/metal substrate combinations that are important in ceramic/metal joining applications. Thanks to recent developments in computational thermodynamics, it is now possible to perform complex stable and metastable thermodynamic calculations

involving large numbers of species and phases [21]. These calculations involve the use of suitable thermodynamic models for each of the phases participating in the calculated equilibria. In this work, *CALPHAD* thermodynamic descriptions for the $Cu-Ni-Ti$ and $Cu-Fe-Ti$ systems were used to analyze the nature of the metal substrate/braze interactions.

By integrating previously assessed thermodynamic data [30, 138–141] with readily available experimental diffusion coefficient measurements [121] it was possible to simulate the diffusional reactions taking place at the metal-substrate/brazing alloy interface just after it is assembled and subjected to elevated temperatures. These simulations involved the calculation of a (one-dimensional) moving boundary-type problem with a metastable solid/liquid interface so it was necessary to use metastable thermodynamic extrapolations for the systems of interest. The thermodynamic calculations in this work were performed using Thermo-Calc® [142].

Within the explored temperature range ($1000\,^0C-1300\,^0C$) both Ni and Fe in the pure state exist in the fcc crystal structure. Therefore, all the calculations necessary to compare the effect of these two elements on the chemistry of active brazing alloys involved only the fcc and *liquid* phases. In the present analysis, it was additionally assumed that the kinetics for the precipitation of binary and/or ternary intermetallic compounds is very sluggish compared to the diffusion rates of the elements at the S/L interface. Effectively, this excluded the precipitation of such phases from the analysis, which is a reasonable assumption for calculations involving the very first stages of the dissolution of the metal substrate into the brazing alloy*.

6.5 Kinetic Analysis of $liquid/fcc$ Moving Boundary.

The diffusion in a multicomponent system can be expressed by the Fick-Onsager law:

$$J_k = -\sum_{j=1}^{n-1} D_{kj}^{n} \nabla C_j \tag{6.2}$$

where J_k is the diffusional flux of species k and C_j is the concentration (in $^{moles}/_{m^3}$), while D_{kj}^{n} is the diffusion coefficient in the $(n-1)$ by $(n-1)$ diffusion matrix [143].

When there is a diffusional reaction between two phases, say α and β, the velocity v_ξ of the moving boundary can be calculated using the flux balance equation:

$$v_\xi = \frac{J_k^{\xi\alpha} - J_k^{\xi\beta}}{C_k^{\xi\alpha} - C_k^{\xi\beta}} \qquad \text{for } k = 1 \ldots n-1 \tag{6.3}$$

where $J_k^{\xi\alpha}$ and $J_k^{\xi\beta}$ are the mass fluxes in the α and β phases at the interface ξ, and

*After long periods of time, it can be expected that those phases with positive driving forces for precipitation would start nucleating.

$C_k^{\xi\alpha}$ and $C_k^{\xi\beta}$ are the corresponding interfacial concentrations.

A two-phase equilibrium in an n-component system has $n-2$ degrees of freedom at a fixed temperature and pressure. Therefore the same number of constraint equations should be found in order to determine the tie-line, i.e. the iso-activity line linking the two equilibrium compositional coordinates at each side of a two-phase field. The tie-line defines the interface compositions used in Eq. 6.3. This equation can be applied to any of the solute components. In a ternary system there are two solute components and therefore there are 2 equations of the type of Eq. 6.3. The interfacial velocity must be the same no matter which solute component is chosen and therefore:

$$\frac{J_1^{\xi\alpha} - J_1^{\xi\beta}}{C_1^{\xi\alpha} - C_1^{\xi\beta}} = \frac{J_2^{\xi\alpha} - J_2^{\xi\beta}}{C_2^{\xi\alpha} - C_2^{\xi\beta}} \tag{6.4}$$

In a ternary system, it is necessary to solve one non-linear differential equation (Eq. 6.4) in order to find the correct tie-line, i.e., the interfacial composition of the two phases. Once the interfacial compositions are known by finding the appropriate tie-line through the mass conservation equation (Eq. 6.4), Fick's second law can be solved for each of the regions in the simulation:

$$\frac{\partial C_i^{\phi}}{\partial t} = -\nabla J_i^{\phi} \tag{6.5}$$

The interfacial compositions obtained from solving Eq. 6.4 become the boundary conditions necessary for solving Eq. 6.5.

The simulations were performed in the commercial software DICTRA® [144], which is capable of performing local equilibrium calculations and diffusion simulations for moving boundary problems. The kinetic data were taken from Smithells [121]. Whenever there was no data for the impurity diffusion coefficient of one of the elements into another, the self-diffusion coefficient of the element acting as the solvent was used as a first approximation. For the case in which Ti had to be treated as the solvent element in the (metastable) fcc phase , the diffusion coefficients were taken from the data measured for the *hcp* phase, given the fact that both phases are closed packed and therefore would present a similar kinetic behavior*. The values for the diffusion coefficients of all the elements in the liquid phase were set to be $\sim 1 \times 10^{-9}\ \frac{m^2}{s}$, according to criteria set by Kirkarldy and Young [122] .

6.6 Simulation

To analyze the thermochemical interactions occurring at metal-substrate/brazing alloy interfaces the simulation was constrained to a simple one-dimensional geometry.

*Since the mobility for the *hcp* is non-isotropic an "average" value considering the mobility values parallel and perpendicular to the basal plane was used.

The simulation domain was composed of two distinct regions. The region on the left-hand side was defined as a *liquid* phase ($Cu-Ti$ brazing alloys) and a width of $100\,\mu$. The right-hand side was defined as an fcc phase (either pure Fe or Ni) and a width of $1,000\,\mu$:

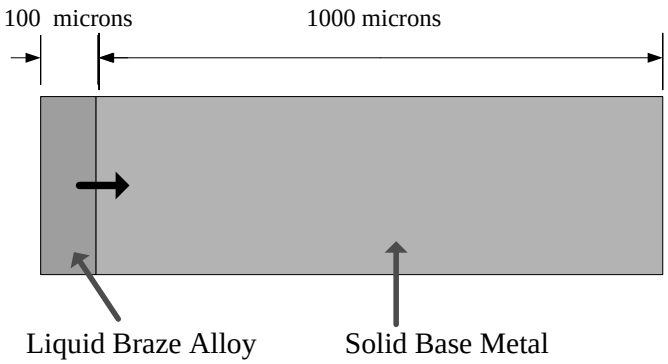

Figure 6-2: Schematics of the simulation domain.

The number of grid points in each computational region were allowed to be varied as the simulation progressed. A higher density of grid points was used on both sides of the S/L interface.

Zero flux conditions * were used on the left and right boundaries of the computational domain and the simulated time for all the cases explored was $100\,s$, although simulations for much longer times ($t > 10^6\,s$) were performed to verify that the system reached the expected equilibrium state. The initial conditions for the liquid region are the same for both the $Cu-Ni-Ti$ and $Cu-Fe-Ti$ subsystems ($5\,at.\%Ti$,Cu-balance.) The initial conditions for the solid regions were either pure Fe or pure Ni in the fcc structure.

To determine the final state of the *closed* system for the given initial conditions, metastable equilibrium calculations were run and it was found that the metastable final state is fcc in all of the cases. To verify that the systems studied reached the equilibrium state, the diffusion simulations were run for times in excess of $10^6\,s$ for both the $Cu-Fe-Ti$ and $Cu-Ni-Ti$ cases. In Fig. 6-3 it is possible to see the simulation results for long times for both the $Ni/(Cu-Ti)$ and $Fe/(Cu-Ti)$ systems†. Note that these calculations are not really applicable for long times after the diffusion reaction begins, as some of the phases whose precipitation is limited by kinetic factors would then have plenty of time to nucleate and grow.

From these simulations, it is possible to extract the following results:

*The system was closed.

†The simulations for the $Cu-Fe-Ti$ system at 1100^0C and 1200^0C were so sluggish that the equilibrium state was not reached until $t > 10^{10}\,s$.

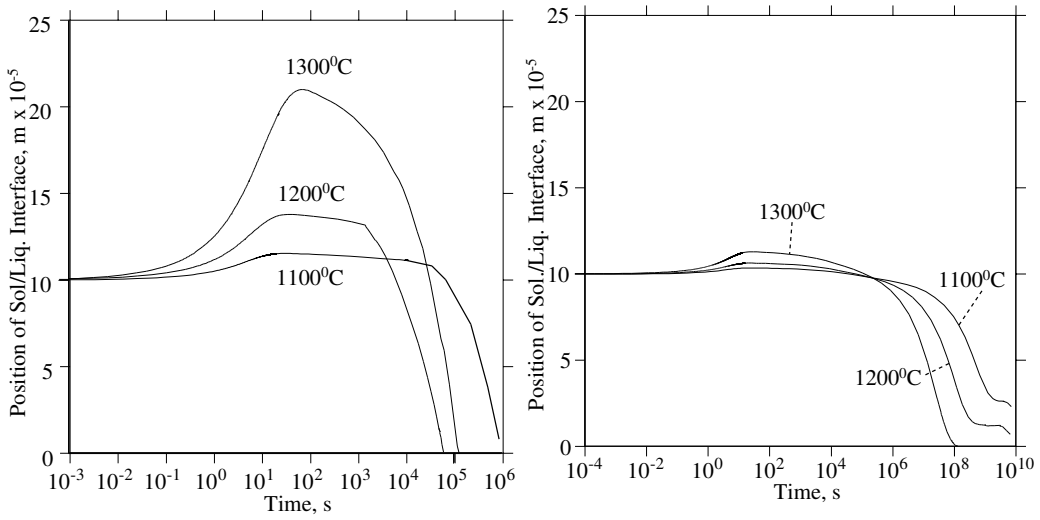

(a) S/L interface position calculations for the $Cu - Ni - Ti$ system.

(b) S/L interface position calculations for the $Cu - Fe - Ti$ system.

Figure 6-3: S/L interface position calculations.

- At the first stages of the dissolution reaction, the solid region begins to dissolve into the liquid. The extent of this dissolution is greatest in the case of the $Ni/(Cu - Ti)$ interaction, due to the much greater solubility of Ni into Cu melts.

- After the initial enlargement of the liquid region (larger when the metal substrate is Ni-based), diffusion of both Cu and Ti into the solid fcc phase takes place and the liquid layer starts to shrink

- If these metastable inter-diffusion reactions were to continue indefinitely, the layer would solidify isothermally, provided that the other intermetallic compounds did not overcome the kinetic barriers for nucleation and subsequent growth.

- From Fig. 6-3 it is evident that it takes at least two orders of magnitude longer for the liquid in the $Fe/(Cu - Ti)$ diffusion reaction to disappear.

- For both system, the enlargement of the liquid layer reaches a maximum at around $100\,s$.

In order to make a proper comparison between the effects of Ni and Fe on the thermochemistry of brazing alloys it was necessary to find a proper time at which both systems were in equivalent states. As seen in Fig. 6-3 the Ni and Fe cases reach equilibrium, meaning disappearance of the liquid layer, at very different times *. It is worth noting that once Ti and Cu start to diffuse into the substrate metal, the

*A difference greater than two orders of magnitude

chemical activity of Ti not only decreases because of the chemical interaction with either Ni and Fe in the liquid layer, but because the actual amount of Ti in the liquid layer decreases as well. Additionally after very long times, it is likely that phases with positive driving forces for precipitation would start to nucleate and grow. These phases would necessarily be different in the two cases. Thus, the equilibrium states of the systems do not constitute a proper common ground for making the comparison. From Fig. 6-3 it is seen that maximum dissolution* is reached in both systems at similar times ($\sim 100\,s$). The point of maximum dissolution was therefore selected as the common state at which a comparison between both systems was meaningful.

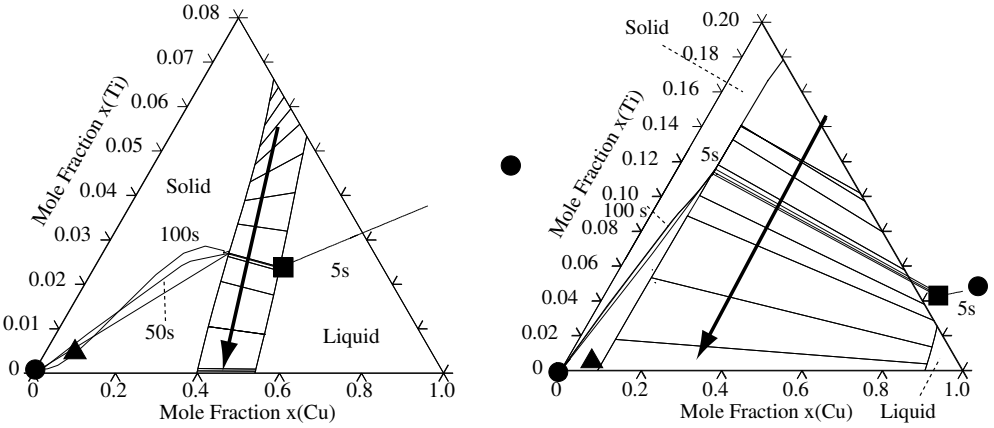

(a) Diffusion paths for the $Cu-Ni-Ti$ system.

(b) Diffusion paths for the $Cu-Fe-Ti$ system.

Figure 6-4: Diffusion path calculations.

Fig. 6-4 shows the calculated diffusion paths for both the $Cu-Ni-Ti$ and $Cu-Fe-Ti$ systems (at 1300^0C) for very short times after the inter-diffusion reactions begin. The diffusion paths are superimposed over the calculated metastable ternary phase diagrams at the same temperature. At very low Ti contents, it is expected that both ternary systems exhibit behaviors similar to those of the dominant binary systems, $Cu-Ni$ (see Fig. 6-1(a)) and $Cu-Fe$ (see Fig. 6-1(b)). Fig. 6-4(a) and Fig. 6-4(b) show that the $Cu-Ni-Ti$ ternary system exhibits a much wider range of solubility for both the *liquid* and fcc phases than the $Cu-Fe-Ti$ ternary.

The diffusion paths shown in Fig. 6-4 show that after very short times ($t < 50\,s$) the composition of the entire liquid region approaches the composition given by the tie-line corresponding to the metastable $fcc/liquid$ equilibrium condition at any given time. This liquid composition is indicated by the filled square in both diagrams. Because the diffusion rates at the S/L are slow compared to the diffusion rates in the liquid phase, it can be expected that the liquid composition will always be homoge-

*The point at which the enlargement of the liquid layer reaches a maximum

neous after the first $\sim 100\,s$ of the reaction and the composition of the liquid will thus follow the *liquid/(fcc+liquid)* phase boundary.

In both systems, the Ti and Cu content of the liquid phase will start to decrease as the diffusion reaction progresses (this is seen more clearly in Fig. 6-4(b)). The diffusion paths will thus follow decreasing Ti activity tie-lines (in the direction of the arrow) until the liquid phase disappears and the final composition in the sample is the one given by the initial conditions of the simulation ($x_{Cu} \sim 0.08$ and $x_{Ti} \sim 0.005$). It can be seen in Fig. 6-4(a) that for both systems, the final composition (at 1300^0C) indicates that the liquid should disappear entirely (the final state of the system is indicated by a triangle), as can also be seen in Fig. 6-3.

Fig. 6-5 show the metal substrate mole fraction ($at.\%$) profiles for both simulated systems at different temperature conditions and at different times. It is evident that in all cases, after relatively short times ($50\,s$) the molar concentration profiles for the metal substrate become flat in both regions (solid and liquid) of the simulation domain.

In the liquid region, the diffusional processes are so fast that once the system reaches a tie-line* the composition of the liquid is more or less uniform and equal to the composition at the metastable solid/liquid interface throughout the region (see also Fig. 6-4). Although the liquid composition is uniform throughout the entire liquid layer, this does not mean that the composition remains constant during the entire reaction. Slow, not fast, diffusion rates are the main cause for the relative flatness of the substrate metal (Ni or Fe) composition profile in the solid region: the diffusion of both Cu and Ti into the metal substrates is so slow that at short times there is virtually no diffusion whatsoever. Thus, just after the diffusional reaction begins,the mass flux direction across the S/L interface is from the substrate metal towards the melt. After long enough times, diffusion across the solid region becomes important and the liquid starts to disappear as both Cu and Ti diffuse out of the liquid and into the substrate metal.

From Fig. 6-5(a) it is seen that at 1300^0C the dissolution of the Ni metal substrate is extensive and the molar concentration of Ni in the $Cu-Ti$ brazing alloy at the point of maximum dissolution is relatively high ($\sim 50\,at.\%$). At the same temperature conditions, the dissolution of Fe into the $Cu-Ti$ brazing alloy is 5 times lower (see Fig. 6-5(b)).

From these results and the values for the $Ni-Ti$ and $Fe-Ti$ chemical interaction energies given in Table 6.1, it may be expected that the final chemical activity of Ti in the Cu liquid brazing alloy after $100\,s$ will depend on the nature of the metal substrate.

*That is, a two-phase local equilibrium condition at the *solid/liquid* interface.

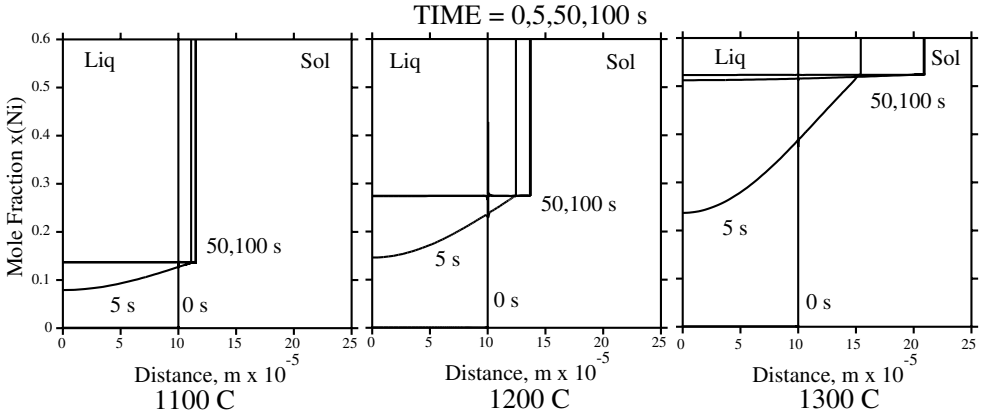

(a) x_{Ni} profile for the $Cu - Ni - Ti$ system.

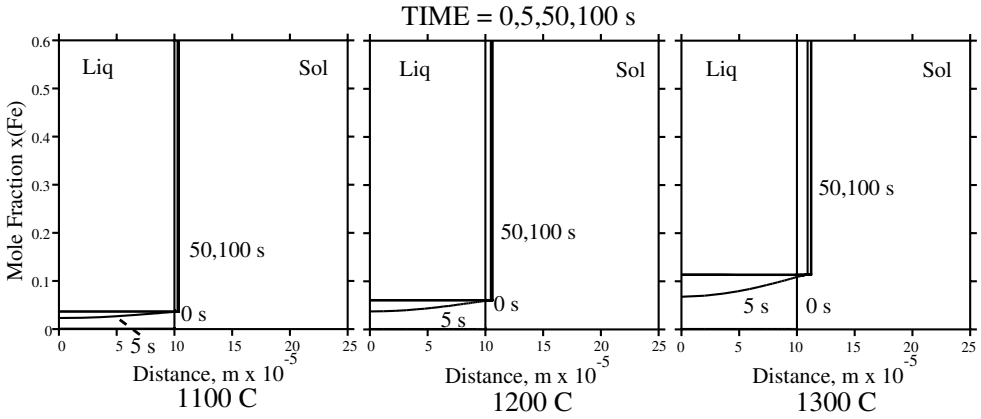

(b) x_{Fe} profile for the $Cu - Fe - Ti$ system.

Figure 6-5: Molar fraction profile for the diffusion couple calculations.

Fig. 6-6 shows the chemical activity* of Ti $100\,s$ after the substrate/braze reaction begins for three different temperature conditions and for Fe and Ni-based substrates. Because of the greater solubility of Ni in Cu and the strongly negative chemical interaction between Ti and Ni the effect of Ni on the thermochemistry of the braze is greater than that of Fe. When Fe dissolves into the braze (after $100\,s$), the activity of Ti decreases to 70% of the level it had at $t = 0\,s$ and $T = 1100^0C$. At the same temperature and with the same elapsed time, Ni causes the Ti chemical activity to decrease to 20% of the initial value. The effect becomes even more noticeable when comparing both cases at 1300^0C: while the Ti activity levels in the $Cu - Fe - Ti$ system have decreased to 40% of the original value, the Ti activity in the $Cu-Ni-Ti$ system is so low ($< 1\%$) that the brazing alloy ceases to be 'active' in the strict sense of the word.

*The chemical activity is normalized with respect to that found in the braze at $t = 0$ and $T = 1300^0C$.

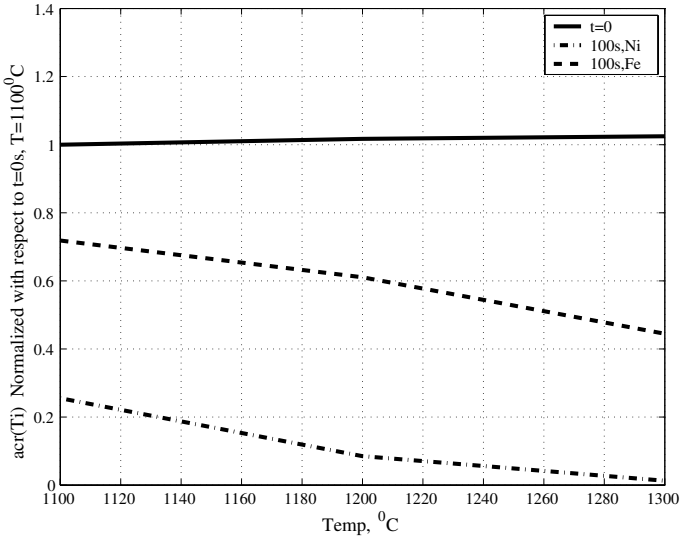

Figure 6-6: Normalized chemical activities of Ti at $t = 0$ and $t = 100\,s$ for the Ni and Fe cases. The activities are normalized with respect to the chemical activity of Ti in the $Cu - Ti$ braze at $t = 0$ and $T = 100^0C$

As noted in Section 6.2, several authors have found that one of the results of an excessive reaction between the braze alloy and a Ni-rich metal substrate is the formation of brittle $Ni - T$i compounds [135, 136]. Using the calculated liquid composition obtained after $100\,s$ for the *Cu-Ni-Ti* case at 1200^0C (see Fig. 6-5(a)) the equilibrium phase fraction as a function of temperature was calculated. According to this calculation, shown in Fig. 6-7, the $Ni - Ti$ intermetallic compound that is likely to form (scavenging significant amounts of Ti from the brazing alloy) is Ni_3Ti, as reported by Stephens et al. [135].

6.7 Experimental Verification: Zirconia/Cu-Ti/Ni Interactions

As has been noted in Section 6.2, sometimes the reactions observed in ceramic/metal joining operations do not correspond to what could be expected when the analysis only incorporates the thermodynamics of the brazing alloy and the ceramic. The discrepancies between experiment and prediction can often be attributed to the effect of the metallic substrate on the thermochemistry of the brazing alloy used in the C/M joining operation. As has been seen in this section, metal substrates rich in Ni can have specially strong effects on the thermochemistry of Cu-based brazing alloys. Because of the strong $Ni - Ti$ chemical interaction, if Ni is substantially dissolved in the Cu-based alloy, the Ti chemical activity will be decreased. This effect is dramatically increased as the temperature at which the brazing operation is performed increases.

Arroyave [51] studied the interfacial reactions occurring at zirconia/braze interfaces when the ceramic was joined to a Ni-based (Inconel 718 ®) super alloy, using

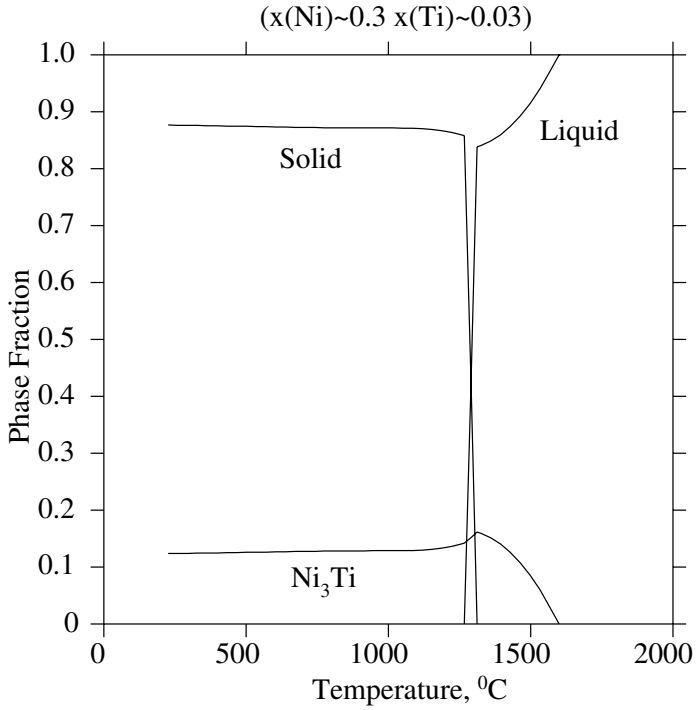

Figure 6-7: Phase fraction calculation for $Cu-Ni-Ti$ case, after $t = 100\,s$ and $T = 1200^0C$.

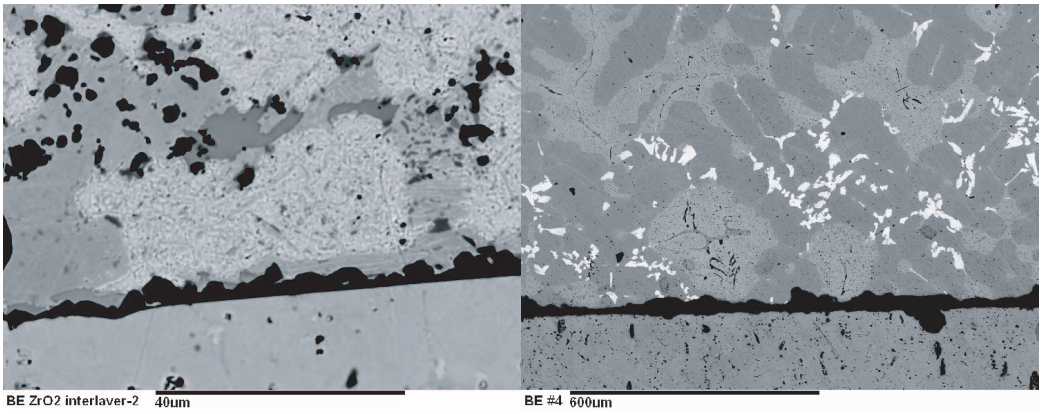

(a) $ZrO_2/Cu-Ti$/Inconel 718® joint created at 1050^0C and held at that temperature for $1\,hr$

(b) $ZrO_2/Cu-Ti$/Inconel 718® *failed* joint created at 1150^0C and held at that temperature for $1\,hr$

Figure 6-8: $ZrO_2/Cu-Ti$/Inconel 718® joints brazed at two different temperatures [51]. Zirconia substrate is at the bottom of both micrographs.

Cu-based active brazing alloys. According to the model developed in this section, a noticeable effect should be observed in the nature of the interfacial reactions occurring at the zirconia/braze interface. In fact, if the temperature is increased many degrees above the liquidus line, Ni dissolution from the metal substrate into the liquid active brazing alloy should be so extensive, that the brazing alloy could be rendered chemi-

cally inactive, at least for practical purposes.

Fig. 6-8 presents a dramatic verification of the model presented in this section:

Fig. 6-8(a) presents a micrograph of a zirconia/$Cu-10\,wt.\%Ti$/Inconel® joint created at $1,050^0C$. As can be seen in the figure, a reaction layer of TiO_x composition is present at the zirconia/braze interface. The titanium activity was thus high enough to drive oxygen ions from the zirconia lattice through the zirconia/braze interface. Oxygen then reacted with the titanium dissolved in the braze. The reaction layer thus formed was then wetted by the liquid braze and a continuous ceramic/metal interface was created.

When the same zirconia/$Cu-10\,wt.\%Ti$/Inconel® arrangement is brought up to increasingly high temperatures, nickel migration from the Inconel® substrate increases, as has been shown in Section 6.6. Fig. 6-8(b) shows an extreme case of dissolution. This sample was heated to $1,150^0C$ and, as can be seen from the micrograph, the braze almost completely dissolved the Inconel® substrate. The titanium activity was therefore reduced to levels at which no reaction layer was formed at the ceramic/braze interface and no continuous ceramic/metal interface was therefore formed. According to the model presented in this section, maximum dissolution should take place in the order of $1,000\,s$. The sample was held at $1,150^0C$ for $3,600\,s$ and the model has been validated.

Even at the relatively low temperature at which the joint shown in Fig. 6-8(a) was created, there should be some nickel dissolution. Due to the high chemical interaction between nickel and titanium, even such reduced amounts of nickel should be enough to effectively scavenge some of the titanium that otherwise would be available to react with the oxygen driven from the zirconia lattice. Fig. 6-9 shows an enhanced* x-ray map of the sample shown in Fig. 6-8(a). As can be seen, the regions rich in nickel and titanium almost overlap completely. This provides additional verification of the scavenging effects explained in this section.

6.8 Metal Substrate Effects in Ceramic-Metal Joining: Concluding Remarks

In the present section the nature of the thermochemical interactions between a metal substrate (Fe and Ni) and an active brazing alloy ($Cu-Ti$) at short times at high temperatures have been investigated. Based only on the enthalpies for infinite dilution of Ti in Fe and Ni it was concluded that Ni would have a much stronger effect than Fe when they were in solution in a Ti-containing Cu brazing alloy. From phase diagram calculations it was evident that Ni is much more soluble than Fe in Cu melts.

To gain a deeper understanding of these effects, we proceeded to analyze the na-

*The sample was digitally processed and the color codes were enhanced to make the titanium scavenging by nickel more evident.

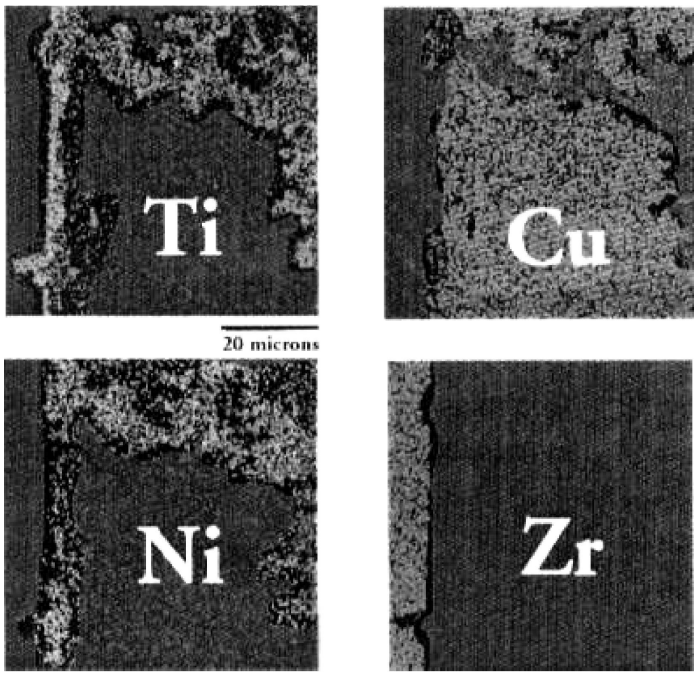

Figure 6-9: X-Ray mapping of $ZrO_2/Cu-Ti$ sample. Sample held at 1050^0C for $1\,hr$ [51].

ture of the thermochemical interactions occurring in the brazing alloy/metal system. In order to do so, metastable extrapolations for the assessed systems were used to simulate a moving-boundary problem in an $fcc/liquid$ system. The dissolution of the metal substrates (Fe and Ni) in the brazing alloy was calculated and resulting effect on the chemical activity of Ti in the melt was determined for several times and temperatures. Through this analysis it was found that both metal substrates decrease the chemical activity of Ti in the melt. However, the effect is much more intense when the metal substrate is Ni-based.

The nature of the reaction products and extent of the ceramic/metal reaction can be modified by changing the Ti chemical activity of the brazing alloy. It has been proven in this section that the metal substrate in a C/M joint can have a great effect of the reactivity of the brazing alloy. Thus, the metal used in a C/M joint and the actual joining temperatures are factors that need to be considered when designing a C/M active brazing procedure.

Chapter 7

Using Phase Field Techniques to Model Coupled Oxide Growth during Active Brazing of Ceramic Oxides

7.1 Introduction

As noted in Section 2.6, several industrial applications have required the use of novel ceramic/metal C/M composite parts. In order to obtain reliable C/M joints, several techniques for joining these materials have been developed [see 1]. One of the most commonly used techniques for joining ceramic oxides (such as ZrO_2, Al_2O_3) and metals is reactive brazing, which relies on the use of conventional brazing materials (such as $Cu - Ag$ alloys) with active additions (such as Ti) to promote an exchange reaction in which the reactive element is oxidized by the oxygen present in the oxide (see Section 2.6). As time proceeds, the interfacial products formed at the C/M interface evolve and grow, affecting the reliability and long-term behavior of the joints created. It is therefore important to develop reliable models that describe the formation and growth of reaction products during C/M bonding applications.

The modelling of C/M joining processes requires a thorough knowledge of the thermodynamic and kinetic behavior of the elements and phases involved. Several models have been proposed for different C/M systems. In a few cases, the models describe describe the growth of only a single transformation product*. Thus, relatively simple one-phase, one-mechanism diffusion models can be used. Unfortunately, for the majority of the cases relevant to practical applications, the reaction at C/M interfaces involves the formation and subsequent growth of a series of reaction products [146], whose layering and morphology is determined by both thermodynamics and kinetics. In most cases, the usual approach to analyze these interfacial reactions consists of splitting the various possible diffusional transformations into individual

*For example, in the study of the reaction between liquid silicon and carbon studied by Zhou and Singh [145], the only reaction product considered is SiC.

stages, which are then separately analyzed and then coupled in such a way that equilibrium and conservation conditions (both local and global) are satisfied.

In this chapter, a model based on the *Cahn-Hilliard* equation [147, 148] for the description of the kinetic evolution of a heterogeneous system with diffuse interfaces is described. The particular problem that will be addressed is the oxide layering and growth occurring when zirconia-based ceramics are reactively brazed to a metal using Ti-containing brazing alloys. Thermodynamic and kinetic factors will be discussed and the details of the numerical model will be commented.

7.2 Interactions between Zirconias Ceramics and Ti-containing Brazes

As has been noted above, zirconias (ZrO_2) constitute a very important family of ceramic oxides used in several industrial applications because of their great thermal stability, low thermal conduction, ionic transport properties, and so forth. In many of this cases, the joining of these ceramic to metals is essential for the proper functioning of the particular application. In order to create these ceramic/metal, *C/M*, composite parts using liquid-based joining approaches*, it is necessary to incorporate active element additives (such as Ti) to promote wetting on the otherwise non-wettable zirconia surfaces†. As noted in Eustathopoulos et al. [5, chap. 6], wetting of ceramic substrates by molten metals is promoted by active additions due to either the formation of a wettable reaction product, the reduction of the *C/M* interfacial energy due to surface co-segregation‡ of the active element (Ti, for example) and the anion (O in this case). As zirconia reacts with Ti§, a pattern of temper colors (blackening) develops in the zirconia ceramic. This pattern begins to be observed at the zirconia/titanium interface and, as the reaction progresses, the blackened region expands, sometimes covering the entire thickness of the ceramic substrate [51]. The blackening, as has been observed by Park and Blumenthal [101], Janek and Korte [105] is a qualitative indication of an increased interaction between photons and free carriers, whose formation can be explained by the reaction:

$$2Zr_{Zr}^{X} + O_{O}^{X} \rightarrow 2 \cdot Zr_{Zr}^{'} + V_{O}^{\bullet\bullet} + \frac{1}{2}O_2\,(g) \tag{7.1}$$

where $V_{O}^{\bullet\bullet}$ represents a doubly-ionized oxygen vacancy (or free electrons within the vacancy).

*For example brazing, transient liquid phase diffusion bonding, etc.

†As has been noted by Li [9], a high thermodynamic stability of the ceramic substrate is related to a very low work of adhesion for the interface between a non-reactive liquid metal and the ceramic itself.

‡The reason for this segregation is that the perturbations in the structure and energy of bulk metals due to the presence of electronegative elements such as oxygen can be better relaxed in 2D geometries [5]. Due to the high chemical affinity between the active element and oxygen, it is reasonable to expect that the active element will co-segregate to the free surface.

§Either present as a thin film or dissolved in the liquid braze.

Because of the high chemical affinity between O and Ti*, a large oxygen chemical potential gradient is created across the C/M interface as soon as the ceramic is put in contact with the titanium layer. This gradient constitutes the driving force necessary to carry out Eq. 7.1. As oxygen vacancies are created, oxygen atoms diffuse towards the zirconia/Ti interface. As zirconia reacts with Ti, a sequence of titanium oxides (see Fig. 7-1) is formed at the interface and the complex layering grows with time until thermodynamic equilibrium is reached.

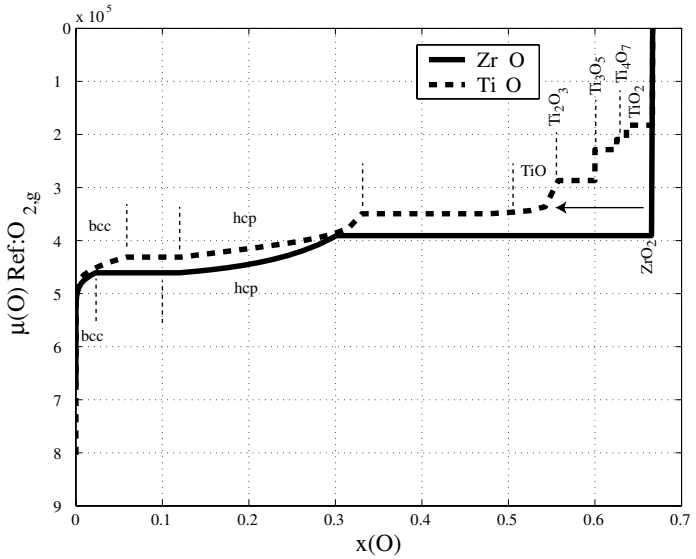

Figure 7-1: $\mu(O)$ vs. x_O for the $Zr{-}O$ and $Ti{-}O$ systems. Calculated using thermodynamic models by Arroyave et al. [52] and Lee [34].

According to experimental results [51, 149] the titanium reaction layer often found at zirconia/Ti interfaces is TiO_{1-x}[†]. The nature of the first-forming titanium-oxygen compound at the C/M interface is determined by the interfacial oxygen chemical potential[‡], which can be fixed by additional chemical reactions occurring in the system. For example, the titanium oxide present at zirconia-toughened alumina/Ti interfaces is TiO [149]. The region in the oxygen chemical potential diagram (Fig. 7-1) where this phase is stable corresponds to the oxygen chemical potential (indicated by the arrow in Fig. 7-1) at which the decomposition reaction $Al_2O_3 \Leftrightarrow 2\underline{Al} + 3\underline{O}$ occurs.

In general, for zirconia/Ti interfacial reaction processes involving active metal brazing[§], it can be assumed [see 149] that:

*This is indicated by a very negative heat of solution of oxygen in both $bcc - Ti(O)$ and $hcp - Ti(O)$.

†A rock-salt structure with oxygen and titanium atoms located in interpenetrating fcc lattices [34].

‡Provided there are no kinetic barriers to the precipitation of the thermodynamically stable phase.

§It is possible to make similar assertions with regard to other zirconia/Ti interaction systems, such as those described by Arroyave [51]

i) Because of the high mobility of solutes in liquid alloys *, Ti dissolved in the brazing alloy is expected to diffuse very rapidly towards the interface with zirconia, where it will react with the oxygen diffusing out of the zirconia lattice. To ensure charge neutrality, it is assumed that the proper charge transfer mechanism occurs at the interface and that the oxygen vacancies formed are always charged-compensated.

ii) As oxygen diffuses out of the zirconia lattice, unsaturated $bcc - Ti(O)$ forms. As oxygen continues to flow across the zirconia/Ti interface a second phase, $hcp - Ti(O)$, precipitates and becomes increasingly saturated with oxygen until it reaches the saturation composition with a stoichiometry corresponding to Ti_2O. If the oxygen chemical potential at the interface is fixed at a suitable value, the TiO_{1-x} phase can precipitate (see Fig. 7-2, horizontal arrow).

iii) When cooling the sample, solid-state transformations can take place, by which the reaction layer is transformed to oxide phases stable (Ti_2O_3, for example) at low temperatures (see Fig. 7-2, vertical arrow)†.

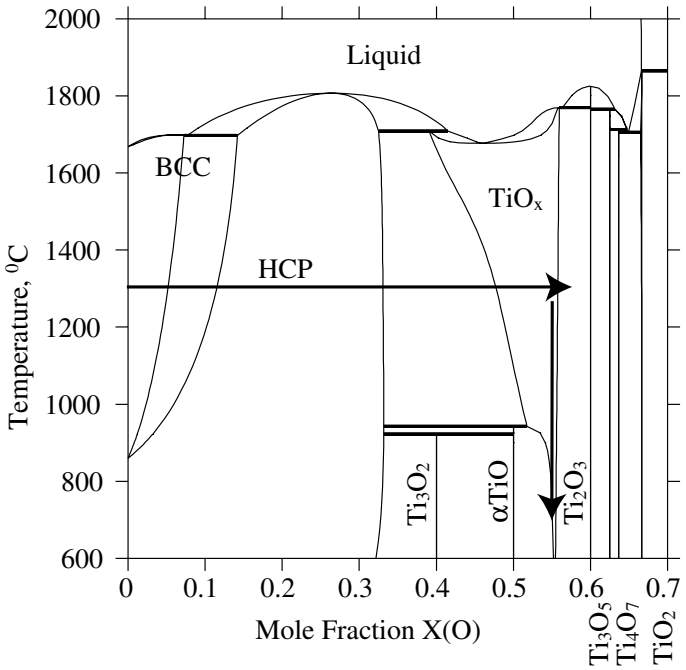

Figure 7-2: Calculated $Ti - O$ phase diagram, calculated from the model by Lee [34]

*According to Kirkaldy and Young [122], a typical value for the diffusion coefficient in liquid metals is $\sim 1 \times 10^{-9}\, m^2/s$

†Ti_2O_3, for example.

7.3 Current Modelling of Coupled-Oxide Growth

As mentioned in the section above, due to the large gradient in the oxygen chemical potential* across the zirconia/Ti interface, a complex set of coupled phases are likely to form. Multiple interfaces are thus created, whose temporal evolution is determined by both kinetic and thermodynamic properties of the phases involved. In order to understand the basic phenomena underlying these complex interfacial reactions, increasingly-sophisticated diffusion models have been developed over the years [149]. As mentioned in Section 7.1, the present chapter deals with the development of a model that combines the solution of a Cahn-Hilliard(or, in modern terms, *Phase-Field*†)-type problem with assessed thermodynamic data obtained through CALPHAD methods in order to model the coupled oxide growth of $Ti-O$ phases during zirconia/metal active brazing operations. Before the Phase-Field model is developed, it is necessary to analyze the approaches currently used to model coupled-oxide growth occurring during zirconia/metal joining processes.

The model developed by Torvund et al. [149] is a good example of current models and it describes the behavior of zirconia-alumina ceramics, as they react with Ti-rich metals. In their model, Torvund et al. [149] considered that, because of the extremely fast diffusion rates in the liquid braze, there is always a Ti-rich layer in contact with the ceramic substrate. Once it is established that a Ti layer is always in contact with the zirconia surface, the process of interfacial layering was divided into three independent stages:

i) *Stage I.* This stage corresponded to the rapid formation of unsaturated $hcp-Ti(O)$, followed by a gradual oxidation to Ti_2O‡ (see Fig. 7-2) through diffusion of oxygen. Note that this implied the complete transformation of $bcc-Ti(O)$ into $hcp-Ti(O)$ due to fast oxygen diffusion§ through the Ti layer. In their

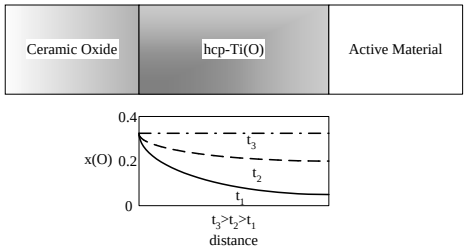

Figure 7-3: Stage I. of model by Torvund et al. [149].

model, Torvund et al. [149] considered that the diffusion of oxygen through the

*This is due to the large chemical affinity between Ti and O.

†The model presented in this work does not include an explicit description of a variable indicating the phase state of the system. However, the authors consider the model to belong in the Phase-Field category since the phase state of the system is implicitly defined through its local composition.

‡Ti_2O is the $hcp-Ti(O)$ solid solution completely saturated with oxygen.

§Since oxygen behaves as an interstitial atom in both the $bcc-Ti(O)$ and $hcp-Ti(O)$ phases, it is expected that its diffusion rate is very fast, compared to that of the oxide phases (i.e. TiO_{1-x}).

$hcp - Ti(O)$ was the rate controlling step. By setting a constant diffusion coefficient, they were able to obtain a mathematical expression for the concentration of oxygen as a function of time in the form of a convergent series.

ii) *Stage II.* The second stage of the process considered that the already formed Ti_2O phase was further oxidized to TiO_{1-x}. In this case, the problem was solved by considering s Stefan-like problem in which the velocity of the moving interface (Ti_2O/TiO_{1-x}) is controlled by the mass conservation condition

$$J_L = J_R. \tag{7.2}$$

where J_L and J_R correspond to the flux entering through the left-hand side and exiting through the right-hand side of the interface, respectively.

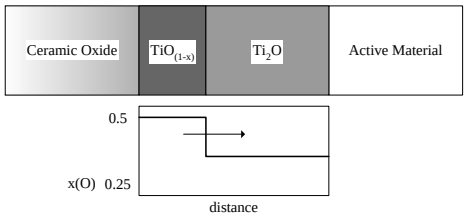

Figure 7-4: Stage II. of model by Torvund et al. [149].

iii) *Stage III.* This last stage involved the solid-state transformation of the high-temperature TiO_{1-x} phase into phases stable at lower temperatures, such as TiO orTi_2O_3.

Despite the simplicity of the model described above and its ability of represent the growth of a sequence of oxide layers in zirconia-Ti interfacial reactions, there are serious shortcomings that need to be addressed:

i) Due to the complexity of the diffusion phenomena involved, the model described above did not consider the diffusion of oxygen into the high-temperature $bcc - Ti(O)$ phase, which is expected to be observed at the very early stages of the zirconia/Ti reactions.

ii) The model is unrealistic in that it separates the formation process of new phases into arbitrarily defined stages. Consequently, different diffusional models are applied depending on the particular stage of the process. A unifying transformation mechanism cannot therefore be proposed for a more general analysis of such a complex system.

iii) For the actual simulation of the growth process, it is necessary to rely on the sharp-interface moving-boundary problem to represent all the moving interfaces considered. From a computational point of view, the tracking of all the moving interfaces requires the establishing of mass-conservation conditions across all interfaces. This is complicated when the transport properties of the phases differ greatly: As has been noted by Lee and Oh [150] and others, the solution of moving interface problems are usually accompanied by mass conservation errors that need to be corrected using global mass balance conditions throughout the entire system. As the number of simultaneously moving interfaces increases, the uncertainty with regard to where to apply such corrections increases accordingly.

iv) Because of the complexities involved in the modelling of multiple moving-boundary problems, the simulation of simultaneous diffusional reactions taking place in $2-D$ systems, for example, is extremely expensive, from the computational point of view

Given the limitations outlined above, it is necessary to develop a model capable of describing the complex simultaneous diffusional reactions occurring in multiple moving boundary processes such as those occurring during ceramic/metal interfacial reactions. In the following sections, it will be seen that by applying the *Phase-Field* methodology, coupled with *CALPHAD* descriptions of the thermodynamic behavior of the system it is possible to model, in a qualitative manner, these complex phenomena.

7.4 Thermodynamics and Kinetics of Heterogeneous Systems

In their paper on the thermodynamics of heterogeneous systems*, Cahn and Hilliard [147] established that the local free energy per molecule, f, in a region of space where an intensive variable (such as composition) is non-uniform depends on both the local value of the variable and on the value that the variable takes in the surrounding environment. As a concrete example, it is possible to consider a binary system, in which the only variable that changes its value across space is composition. For this particular example, the free energy of the system at any given point in space, as a function of the local composition and the environment†, will be given by:

$$f\left(c, \nabla c, \nabla^2 c, (\nabla c)^2, \ldots\right) = f_0(c) + k_0 \cdot \nabla c + k_1 \cdot \nabla^2 c + k_2 \cdot (\nabla c)^2 \qquad (7.3)$$

where f is the free energy of the system (in J/mol)‡, c is the mole fraction of component B, f_0 corresponds to the free energy as a function of concentration c in a

*A heterogeneous system is defined as having a spatial variation in one or more of its intensive scalar properties, such as composition, density, order parameter, and so forth.

†The environment, in this sense, is given by the spatial derivatives of the concentration field.

‡Note that f in theory corresponds to a constant-volume free energy, i.e. Helmholtz'. However, since in condensed phases the compressibility $\frac{\partial V}{\partial P}$ is so small, the effect of pressure can be neglected and the Gibbs free energy can be used instead.

homogeneous system and k_0, k_1, k_2 are constants relating particular spatial derivatives of the concentration field to the total energy of the system*.

Eq. 7.3 indicates that in a heterogeneous system, the free energy of the system will be a function of both the local value of the intensive variable and the spatial variation of such variable. Since composition is a scalar material property, the free energy of the system must be invariant with respect to its gradient †, and therefore, $k_0 = 0$.

The total energy (F, in J) over a spatial volume V would be given by:

$$F = \frac{1}{\Omega} \int_V \left[f_0(c) + k_1 \cdot \nabla^2 c + k_2 \cdot (\nabla c)^2 \right] \cdot dV \tag{7.4}$$

where Ω is the molar volume of the system‡.

By using the divergence theorem [see 147] we obtain:

$$\int_S (k_1 \nabla c \cdot n)\, dS = \int_V \nabla (k_1 \nabla c)\, dV = \int_V \left(\frac{dk_1}{dc} (\nabla c)^2 + k_1 \nabla^2 c \right) dV \tag{7.5}$$

Since the external boundaries of the system enclosed within the volume V are of no consequence§, it is possible to make $\nabla c \cdot n = 0$ and therefore we have that:

$$-\frac{dk_1}{dc} (\nabla c)^2 = k_1 \nabla^2 c \tag{7.6}$$

so Eq. 7.4 can be simplified into

$$F = \frac{1}{\Omega} \int_V \left[f_0(c) + \left\{ k_2 - \frac{dk_1}{dc} \right\} (\nabla c)^2 \right] \tag{7.7}$$

In the general case, it can be safely assumed that $\frac{dk_1}{dc} = 0$¶. k_2 is usually called the gradient energy coefficient and relates the absolute value of the local gradient of composition to the total value of the free energy of the system at any given point‖. At regions of relative homogeneity, this parameter has no influence whatsoever. At

*In principle, k_0, k_1, k_2 can be, in turn, functions of composition or other intensive variables, but given the current lack of experimental information, they can be considered as constants.

†A mirror symmetry operation performed on the system must not change the value of the energy due to inhomogeneities in a scalar property.

‡Note that this requires that there is no change in molar volume with composition.

§It is possible to assume that the system is so large that surface interactions with the outside world are irrelevant.

¶Although this assumption is arbitrary, ignorance on the actual values for the gradient energy coefficient for real materials interfaces, makes it reasonable enough.

‖This parameter has units of $\frac{J \cdot m^2}{mol}$

interfaces, however, where composition changes abruptly*, the term containing k_2 becomes dominant. The gradient energy coefficient can therefore be conceptualized as a proportionality constant that determines the energy that the system has to expend in order to create an interface across which ∇c has a finite value.

If the system is constrained to one dimension and it is further assumed that the system is composed of two homogeneous phases joined through a diffuse interfacial area, a specific surface energy can be defined† as [147]:

$$\sigma = \frac{1}{\Omega} \int_{-\infty}^{+\infty} \left[\Delta f(c) + k_2 \left(\frac{dc}{dx} \right)^2 \right] dx \tag{7.8}$$

where $\Delta f(c)$ corresponds to the non-equilibrium free energy of material located at the interface.

As the system approaches equilibrium, it follows that the surface energy must be a minimum. By looking at the integrand in Eq. 7.8, it is obvious that the free energy is minimized as $\frac{dc}{dc} \to 0$, that is, as the interface becomes more diffuse. In order to make the interface more diffuse, it is necessary then to add more material into the interface itself, increasing the $\Delta f(c)$ term. A minimization problem thus results: by using Euler's equation‡ it is possible to find that $\Delta f(c) = k_2 \left({}^{dc}/_{dx} \right)^2$, and finally the interfacial energy of the system can be expressed as:

$$\sigma = \frac{2}{\Omega} \int_{c_\alpha}^{c_\beta} \left[k_2 \Delta f(c) \right]^{1/2} dx \tag{7.9}$$

An important result of this analysis is that, if the concentration or compositional profile across the interface is the optimum so the surface energy of the system is minimized, the interface thickness is related to the gradient energy term, k_2 or simply k, through the relation $\delta \propto k^{1/2}$.

It is possible to consider a system, whose energy is given by Eq. 7.7, which is initially in a non-equilibrium state. In order for the system to reach equilibrium, its *local* properties (i.e. c) must change. It can be assumed that the system will evolve towards equilibrium through the fastest path possible§ and the kinetics of the system

*In real interfaces, the change occurs within a few monolayers-width.

†This surface or interfacial energy is the difference, per unit area between the actual energy of the system and that which it would have if the interface was neglected

‡If the integrand in Eq. 7.8 is identified as I, the equation $I - \left({}^{dc}/_{dx} \right) \left[{}^{\partial I}/_{\partial \left({}^{dc}/_{dx} \right)} \right] = 0$ must be satisfied in order to make σ a minimum.

§This assumption is based on pure variational arguments and it is assumed to be valid for any

can, using variational arguments, therefore be related to the first variational derivative of its free energy [see 151]*:

$$\delta F = \frac{1}{\Omega}\left(\frac{\partial f}{\partial c} - 2k\nabla^2 c\right)\delta c(x) \tag{7.10}$$

By using linear kinetic theory, it is possible to assume that the local flux of mass occurring in any region of a non-uniform system evolving towards equilibrium will be given by†:

$$J = -M\nabla\delta F = -\frac{1}{\Omega}M\nabla\left(\frac{\partial f}{\partial c} - 2k\nabla^2 c(x)\right) \tag{7.11}$$

where M is the atomic mobility given by:

$$M = \frac{D}{RT} \tag{7.12}$$

with D being the diffusion coefficient, R, the universal gas constant and T the temperature.

Since c is a conserved parameter, the rate of change of c with respect to t, dc/dt must be equal to minus the divergence of a flux, and therefore‡:

$$\begin{aligned}\frac{dc}{dt} &= -\nabla\cdot M\cdot\nabla\left(\frac{\partial f}{\partial c} - 2k\nabla^2 c(x)\right)\\ &= M\left(\nabla^2\left(\frac{\partial f}{\partial c}\right) - 2k\nabla^4 c(x)\right)\end{aligned} \tag{7.13}$$

Note that the first term in Eq. 7.13 (*Cahn-Hilliard* equation) corresponds to *Ficks' Second Law*, with $\frac{\partial f}{\partial c}$ corresponding to the chemical potential of c, $\mu(c)$. The second term in Eq. 7.13 is related to the excess energy resulting from the creation of interfaces.

Originally, the *Cahn-Hilliard* equation was developed to describe the kinetics of spinodal decomposition [148], which is a nucleation-free phase separation process occurring when a system, having a free energy vs. composition as described in Fig. 7-5, has a composition within the spinodal (defined as the region enclosed by the condition $\frac{\partial^2 G}{\partial c^2} < 0$). Within the spinodal, the system is unstable with respect to any variation

physical system.

*For a general functional $P(y) = \int_V Q(y(x), \nabla y)\, dV$, the variational derivative of P [151, chap. 22] is given by $\frac{\partial Q}{\partial y} - \nabla\frac{\partial Q}{\partial \nabla y}$, which is basically Euler's Equation Collins [152, chap. 12]. According to variational principles, when the variational derivative vanishes, $y(x)$ is a extremal function.

†Note that with M having units of $\frac{m^2\cdot mol}{s\cdot J}$, the flux, J, has the correct units of $\frac{mol}{m^2 s}$

‡Note that the factor $\frac{1}{\Omega}$ must be dropped, as c represents local composition (non-dimensional), and not concentration (moles per volume).

in composition and therefore it will minimize its energy by separating into two phases (of the same crystalline structure) with compositions indicated in Fig. 7-5 by c_A and c_B. In principle, the system will try to form as many interfaces as possible, however, the surface energy that must be expended* in order to create those interfaces will limit the total interfacial area of the system.

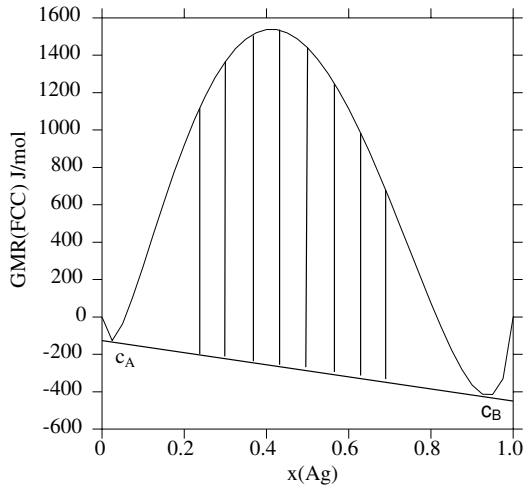

Figure 7-5: Free energy v.s composition diagram for the $Ag - Cu$ fcc system at $900\,K$.

7.5 Gibbs Energy Expression to model Coupled Growth System

The *Cahn-Hilliard* equation has been successfully used to describe complex processes such as spinodal decomposition. It is therefore valid to inquire wether similar models can be used to describe other similarly complex phenomena, such as the coupled growth of multiple reaction layers occurring due to interfacial reactions between a ceramic and an active material. At first glance, however, there is one issue regarding the implementation of *Cahn-Hilliard*-type models to describe diffusional massive transformations (such as the one described in Section 7.3) that needs to be considered: the issue in question regards the mathematical representation of the Gibbs free energy of the system. In the case of spinodal decomposition, a single expression for the free energy can be used to describe the thermodynamics of the system in its entirety, since it is comprised of a single phase†. When attempting to model diffusional transformations in a system of several phases which can also vary in composition, the (Gibbs) free energy of the system (at a given T and P), as whole, must be necessarily expressed as both a function of the local composition, c, and another, non-conserved property, that reflects the change in the local arrangement of the atoms belonging to

*The area enclosed by the free energy curve and the common tangent linking the equilibrium compositions c_A and c_B represents the non-equilibrium free-energy $\triangle f(c)$ appearing in Eq. 7.8.

†Which can exist at two different equilibrium compositions

different crystalline phases (see Fig. 7-6(a)):

$$G^{System} = G\left(c, \eta, T, P\right) \tag{7.14}$$

That is, for any given phase, ϕ, having a particular crystalline structure, it must be possible to represent its Gibbs free energy as a function of composition. Furthermore, at any given composition, the Gibbs free energy of the system must also be expressed as a function of an 'order parameter', η, which is directly dependent on the specific crystalline structure of the phase ϕ. For the system to undergo a phase transformation (in Fig. 7-6(a), from $bcc - Ti(O)$ to $fcc - Ti(O)$, for example) at a composition c, it is necessary to overcome an energy barrier, whose magnitude is determined by the energetics of the atomic-rearrangements necessary for the transformation to take place. As can be seen in Fig. 7-6(a), the *local* minima along the η axis of the Gibbs free energy *surface* corresponds to the (*metastable* or *unstable*) equilibrium functions for the Gibbs free energy of each phase as a function of composition.

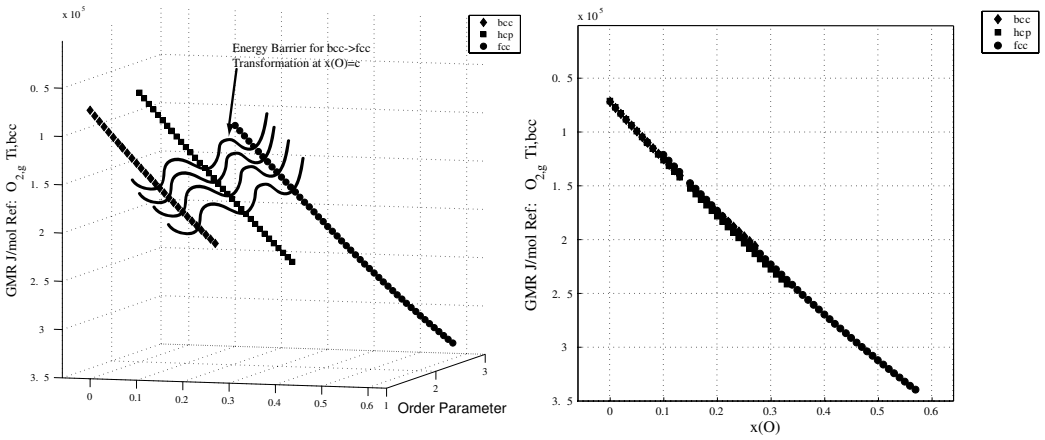

(a) Gibbs free energy vs. x_O and order parameter η.

(b) Gibbs free energy vs. x_O

Figure 7-6: Gibbs free energy for the phases $bcc-Ti(O)$, $hcp-Ti(O)$, $fcc-Ti(O)$ (TiO_{1-x}) at 1200^0C, for the system $Ti - O$ after assessment by Fischer [153].

In many applications of phase-field models [e.g. 154] describing diffusional transformations, the parameter η is explicitly used to represent the phase-state of the system at any given point in space. In these models, it is essential to find the equilibrium compositions at both sides of the interface and the concentration profile within the interface itself. In order to do this, it is necessary to perform Gibbs free energy minimization calculations at every single point of the simulation domain. Once the

equilibrium compositions and the phase state of the system are defined, the time-evolution of the system is then determined by solving two types of coupled equations: the *Cahn-Hilliard* equation for the conserved variables and the *Allen-Cahn* equation (for a more detailed explanation please refer to Allen and Cahn [155].) for the non-conserved parameter. In addition to providing the proper thermodynamic models for each of the phases involved and realistic values for the atomic mobilities of the components comprising the system, mobilities for each of the interfaces involved in the simulation must be provided. If the system is known not to be limited by surface attachment kinetics, the interface mobilities must be chosen in such a way that the time-evolution of the phase order parameter, η, does not affect the kinetics of the phase transformation.

Although there is a physical argument for the existence of an order parameter η, most of the current phase-field models use arbitrary mathematical expressions to describe the Gibbs energy dependence on the value of this parameter. If the system to be modelled is known to be controlled by bulk-diffusion mechanisms, rather than by surface attachment limited kinetics, it may be possible to avoid the use of the η parameter (and therefore of *Allen-Cahn*-type equations describing the kinetics of non-conserved variables) and instead consider the phase-state of the system in an implicit manner. In this case, the concentration, c, acts as an indicator of both the thermodynamic and phase-state of the system:

$$G^{System} = G\left(c, T, P\right) \tag{7.15}$$

This is equivalent to collapsing the Gibbs free energy surface in Fig. 7-6(a) across the η axis, as shown in Fig. 7-6(b). In order to justify this procedure, it can be supposed that the energy barrier for a phase transformation (at a given composition c) is small enough so it can be neglected. Thus, the system will always be in a state for which the local Gibbs energy is a *global* minimum at a given composition c, changing its crystalline structure (i.e. the value of the parameter η). In a mathematical sense, this last assertion is equivalent to assuming that the Gibbs energy of the whole system will be given by the envelope of the Gibbs free energy functions for the different phases comprising it, along the η axis projection.

$$G^{System} = \min\left(G^{bcc-Ti(O)}, G^{hcp-Ti(O)}, G^{fcc-Ti(O)}\right) \forall \left\{x_O\right\} \tag{7.16}$$

Fig. 7-7 shows the Gibbs free energy of the system $bcc - hcp - fcc$ in the $Ti - O$ binary after the operation in Eq. 7.16 was performed on the projection of the Gibbs free energy of the phases $bcc - Ti(O)$, $hcp - Ti(O)$ and $fcc - Ti(O)$ along the η axis, as shown in Fig. 7-6(b). The insert in Fig. 7-7 illustrates a schematics of the process. Note that, in this operation, the points at which the common tangent (equilibrium between phases α and β) touches the Gibbs free energy curve remain the same, that is, the equilibrium compositions of the two-phase field do not change. Since the slope of the common tangent is also the same, the chemical potential at which both phases are at equilibrium remains invariant. The shaded area in Fig. 7-7, between the com-

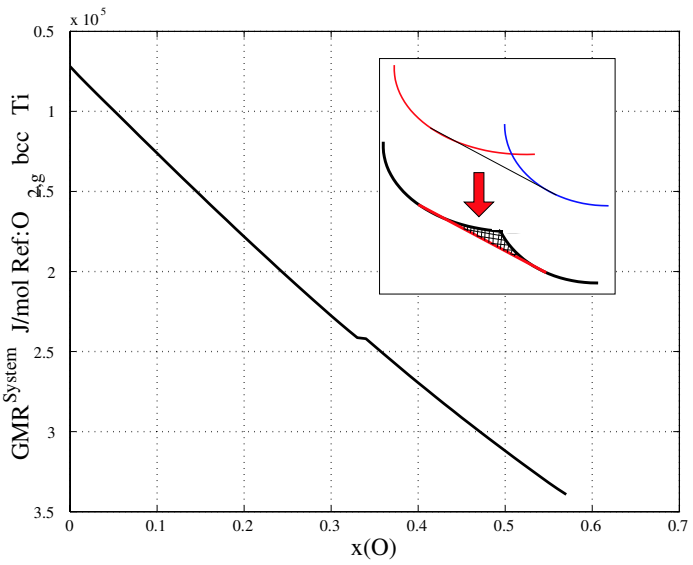

Figure 7-7: $\min\left(G^{bcc-Ti(O)}, G^{hcp-Ti(O)}, fcc-Ti(O)\right)$ at 1200^0C.

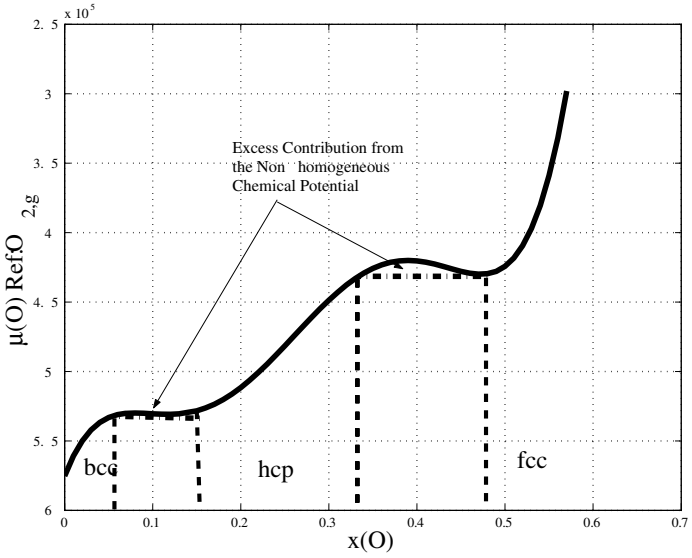

Figure 7-8: Oxygen chemical potential $\mu(O)$ as a function of mole fraction of oxygen x_O.

mon tangent and the envelope of the Gibbs free energy, corresponds to the excess energy of the material within the interface, or $\triangle f(c)$ in Eq. 7.8. Note that $\frac{\partial f}{\partial c}$ in Eq. 7.13 can be considered to be equivalent to a chemical potential *.

The oxygen chemical potential, $\mu(O)$ depicted in Fig. 7-8 was obtained through the numerical fitting of the function represented by Fig. 7-7† and it is therefore an

*$\mu = \left(\frac{\partial G}{\partial n_i}\right)_{n_k,T,P}$

†The oxygen chemical potential was represented through a polynomial of order $N+1$. $\overrightarrow{P} = 1\times10^8\,[1.9124, -2.5315, 1.1574, -0.2117, 0.0164, -0.0058]$ represents the vector with the coefficients of the polynomial given by $\mu(c) = P(1)\cdot c^N + \cdots + P(N+1)$, where c corresponds to the oxygen

approximation to the 'real' values obtained through the use of the thermodynamic models for the $bcc-Ti(O)$, $hcp-Ti(O)$ and $fcc-Ti(O)$ phases as developed by Fischer [153]*. Comparison with the oxygen chemical potential plotted in Fig. 7-1, the agreement is good.

7.6 1D Simulation Results

In order to simulate the coupled oxide growth process described in Section 7.3, the *Cahn-Hilliard* equation (Eq. 7.13 in Section 7.4) was solved using the numerical methods briefly described in Appendix E. The thermodynamic properties for the $Ti-O$ phases† were obtained from the CALPHAD model developed by Fischer [153] and were later modified (see Section 7.5) so the Gibbs free energy of the system‡ could be described with a single mathematical expression. The boundary conditions for all the simulations described in this section were: fixed chemical potential on the left-hand side of the simulation domain, and closed boundary (i.e. zero flux) on the right-hand side.

In order to analyze the ability of Phase-Field methods to describe complex multiple moving boundary diffusion problems, a series of numerical experiments were performed using the 'real' thermodynamic descriptions and somewhat 'simplified' kinetic parameters. For the simulations presented in this section, the mobility appearing in Eq. 7.13 was given by§:

$$\frac{M}{\Omega} = \frac{D}{RT} \tag{7.17}$$

Note these simulations, mobility, M is a constant and is the same for the three phases involved¶. Although this assumption may hold for the cases of the $bcc-Ti(O)$ and $hcp-Ti(O)$, it is not clear that the assumption is valid for the $fcc-Ti(O)$. This simplification of the model can be easily removed by allowing the mobility to be a function of composition, but for the purposes of illustrating the applicability of Phase-Field methods in these kind of diffusional problems, its removal is not essential.

As is noted in Appendix E, the gradient energy coefficient k in the *Cahn-Hilliard* equation is a fundamental physical parameter of real interfaces whose value determines their width and basic properties. In principle, the smaller the value for k, the smaller the actual with of the interface, since, as noted in Section 7.4,

$$\delta \propto k^{1/2} \tag{7.18}$$

---

mole fraction, or x_O.

*Note that in principle, $\mu(O)$ must approach $-\infty$ as $x_O \to 0$

†$bcc-Ti(O)$, $hcp-Ti(O)$ and $fcc-Ti(O)$.

‡The entire compositional range examined.

§This basically accelerates the simulation relative to the dimensions of the system.

¶For the purposes of this preliminary analysis of this Phase-Field model, D was set to have a value of 10.

Given that natural interfaces have a with of just a few monolayers, k would have to have a very small value. In numerical simulations, however, it is not currently possible to simulate systems with such small interface widths, and therefore, the following relationship (see Appendix E) was used:

$$k = K\left(\frac{3}{2}h\right)^2 \tag{7.19}$$

where h is the width of the computational grid (in units of length), while K is a proportionality constant that is adjustable.

7.6.1 Numerical Simulations: Influence of k Parameter

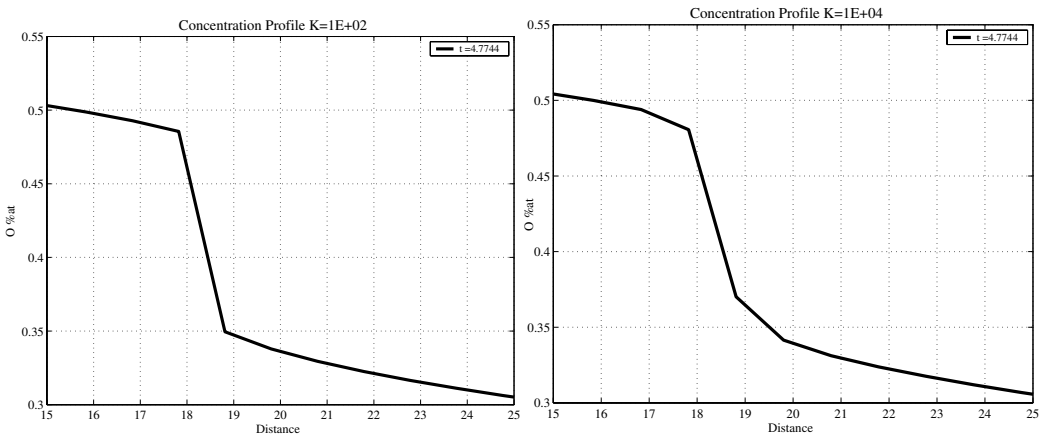

(a) Concentration Profile. $nx = 100$, $K = 1E+02$

(b) Concentration Profile. $nx = 100$, $K = 1E+04$

Figure 7-9: Effect of the value of k on the width of interfaces created trough the evolution of the *Cahn-Hilliard* equation.

As noted above in this section, the value assigned to the parameter k has a great influence on the properties of the interfaces formed during diffusional transformations governed by the *Cahn-Hilliard* equation. In principle, by increasing the value of k, the interfaces in the system would become increasingly diffuse, as can be seen in Fig. 7-9. Fig. 7-9(a) shows the calculation results for a system for which the adjustable constant, K (see Eq. 7.19) has been set with a value of 1×10^2. Note that the width of the fcc/hcp interface is noticeably less diffuse than that shown in Fig. 7-9(b), which was obtained through the evolution of the *Cahn-Hilliard* equation using $K = 1 \times 10^4$. This discrepancy can be reconciled by considering that a diffuse interface, by its very nature, is impossible to define in a precise manner*.

*In principle, a diffuse interface extends from $-\infty$ to $+\infty$

Besides its effect on the interface width, k has another, rather unexpected, effect on the behavior of systems evolving under the kinetics described by the *Cahn-Hilliard* equation: the value of k has a noticeable effect on the global mass conservation behavior of the numerical simulation.

In order to calculate the total mass in the system, at any given time, it is possible to integrate, over time, the flux of *oxygen* entering the system through its left (fixed) boundary:

$$Mass\,(t) = \int_0^t J(t)_{x=0} \tag{7.20}$$

Additionally, one can calculate the total mass in the system at any given time t, by integrating the concentration profile over the entire dimension of the computational domain:

$$Mass\,(t) = \int_{x=0}^{x=L} Conc.(x)_t dx \tag{7.21}$$

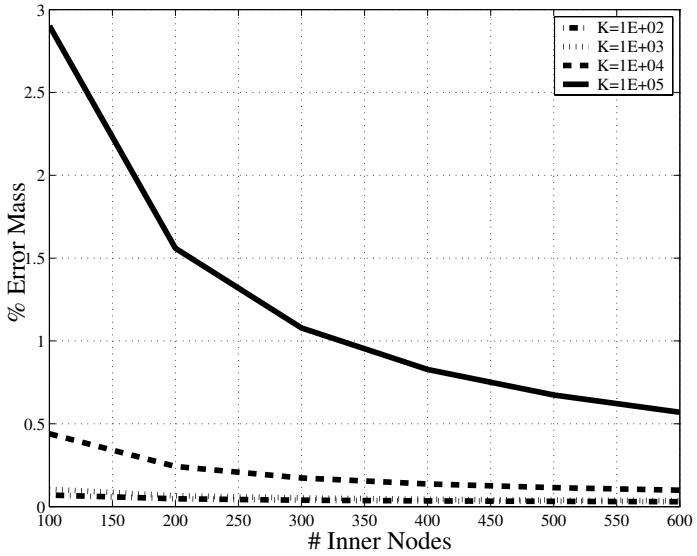

Figure 7-10: Global mass error as a function of number of inner nodes.

In principle, the results obtained from Eq. 7.20 and Eq. 7.21 should not differ. However, as can be seen in Fig. 7-11, k has a marked effect on the global mass conservation error present during the numerical simulations. For relatively small values for the adjustable parameter K ($K < 1 \times 10^4$), the global mass error lies within acceptable ranges. The discrepancies within this range are mostly determined by the numerical approximations utilized in the discretization of the $C - H$ equation, the numerical integration of the concentration profile, and the numerical approximation

of the local flux at the left-hand boundary of the simulation domain, as shown in Fig. 7-10, where the global mass error in the numerical simulations decreases as the number of grid points in the computational domain increases*. Beyond $K = 1 \times 10^5$, however, the global mass error increases in a rapid manner, becoming unacceptable at values of $K \sim 1 \times 10^5$. As of now, there is no clear explanation for this discrepancy. However, it may be linked to the fact that, as k increases, the interface becomes increasingly diffuse (see Fig. 7-9) and more material is transferred into the non-equilibrium interfacial region. This result may be of fundamental importance when using Phase-Field models to describe phase transformations in systems with large interfacial areas, compared to their volume (or total area, in the case of 2-D simulations).

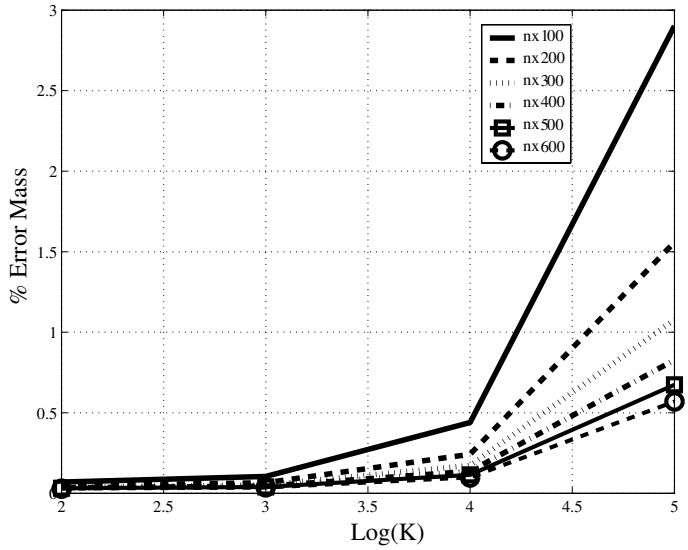

Figure 7-11: Effect of K on the global mass error of *C-H* numerical simulations of coupled oxide growth. Different numbers of inner grid points are examined.

7.6.2 Analysis of Numerical Results

In Fig. 7-12, the concentration and chemical potential profiles at a given time $t^\dagger$ are presented. From this figure, two important results are worth mentioning:

i) Despite the relative shallowness of the *interfacial excess energy* hump‡ of the Gibbs free energy function of the $Ti - O$ system§, the equilibrium interfacial compositions are well defined in the plot¶. According to the figure, the $bcc - Ti(O)$ phase is already saturated with oxygen at this stage of the simulation so

*That is, as the numerical approximations become increasingly precise.

†Refer to the figure caption for simulation parameters.

‡This 'hump' can be considered to correspond to a non-equilibrium region.

§Compare Fig. 7-5 to Fig. 7-7.

¶This is not surprising, since it is always possible to find a linear transformation of the analytical description of the Gibbs energy of the system that can amplify its non-equilibrium regions.

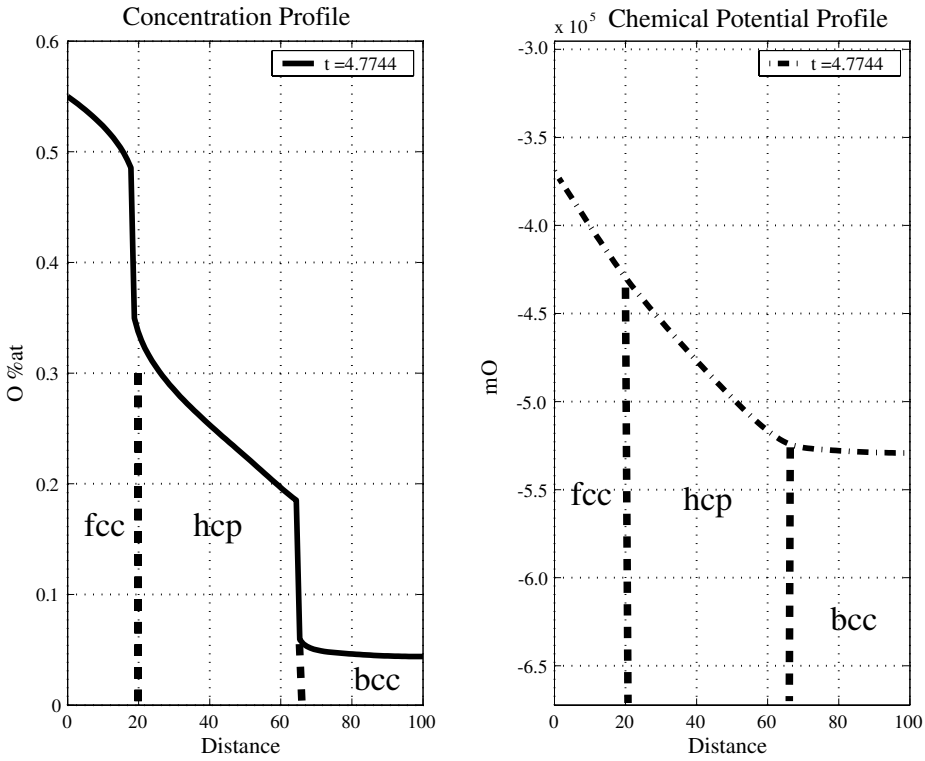

Figure 7-12: Concentration and chemical potential profiles. Phase-Field simulation of coupled oxide growth at $T = 1573$. The K factor in Eq. 7.19 has been set at $K = 100$. The number of inner grid points is 600.

there is only a $hcp \rightarrow bcc$ phase transformation occurring in those regions of the simulation domain.

ii) The system, therefore, 'finds' the correct equilibrium interfacial compositions by 'itself' without the need for performing Gibbs free energy minimizations at each point of the computational domain. Solving the *Cahn-Hilliard* equation effectively minimizes the *global* energy of the system.

iii) It is worth noting that the calculated profile for the oxygen chemical potential, $\mu(O)$, is continuous along the length of the simulation domain. This is consistent with the fact that the system is always at local equilibrium, even in the non-equilibrium regions (from the global perspective) at the interfaces. This local equilibrium approximation is also used in simulation methods that rely on sharp interface models, such as the one described by Lee and Oh [150].

As noted in 7.6.1, the value of k greatly influence the mass conservation properties of numerical integrations of the *Cahn-Hilliard* equation. However, with the proper selection of the gradient energy coefficient term, global mass conservation discrepancies lie within reasonable ranges, considering the discretization of the model. Fig. 7-13 shows that, for values of K smaller than $1,000$, the general condition:

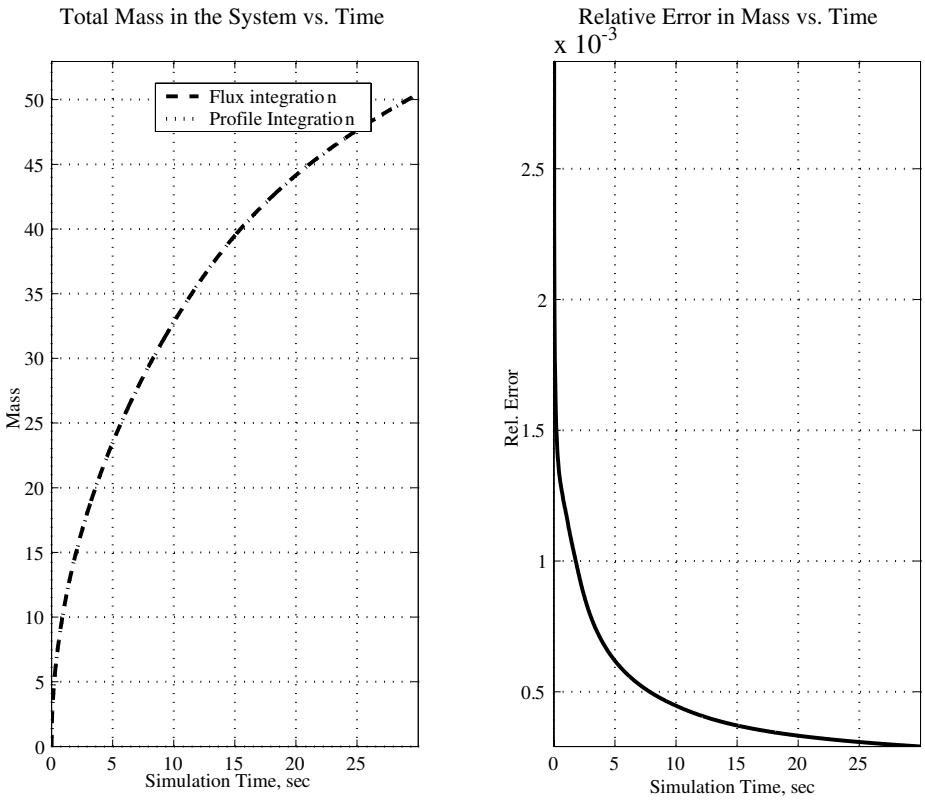

Figure 7-13: Global mass conservation for the solution of the *Cahn-Hilliard* equation. 600 grid points and $K = 100$.

$$\int_0^t J(t)_{x=0} dt = \int_{x=0}^{x=L} Conc.(x)_t \tag{7.22}$$

is satisfied. Moreover, it is also evident (right graph, in Fig. 7-13), that the discrepancy between the

flux integration and profile integration calculations to determine the total mass of the system decreases exponentially as time progresses. Initial transients as the system starts to evolve, are therefore the greatest factor in determining conservation inconsistencies.

It can be assumed that at the high temperatures ($T \sim 1,000^0 C$) at which these diffusional processes take place, coupled oxide growth in the $Ti - O$ system is a diffusion limited problem*. Therefore, it is to be expected that the displacement of the interfaces is governed by the square root law:

$$\delta x \propto \sqrt{t} \tag{7.23}$$

*The mobility of the interface constitutes no limiting factor whatsoever on the behavior of the system.

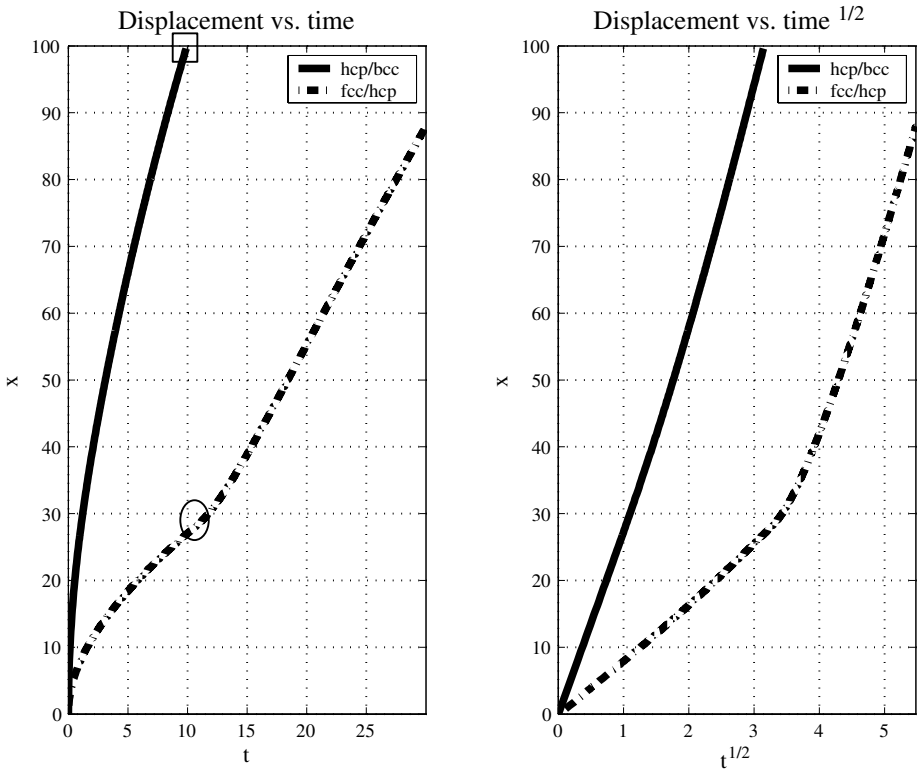

Figure 7-14: *Displacement* of interfaces versus *time* and $time^{1/2}$.

Fig. 7-14 shows that the displacement of the *bcc/hcp* interface is faster than that of the fcc/hcp interface. Unnam et al. [156] reported that generally, the *bcc/hcp* rate of transformation is much faster than the one involving a higher oxide, such as TiO_{1-x} (as in this case) or TiO_2, as reported in [156]. As can be seen in Fig. 7-14, at very short times after the simulation commences, both interfaces seem to obey the square root law. As soon as the fast-moving *hcp/bcc* interface disappears* (see square in Fig. 7-14), the slower interface accelerates (transition point indicated by a circle in Fig. 7-14).

As long as the $bcc - Ti(O)$ phase is present in the system, the equilibrium concentrations at the *hcp/bcc* and fcc/hcp interfaces are fixed. The flux of oxygen atoms across the $hcp - Ti(O)$ phase (from the $fcc - Ti(O)$ towards the $bcc - Ti(O)$) is controlled by the gradient in the chemical potential within this phase, which in turn is given by the difference in chemical potential at both interfaces, $\Delta\mu(O)$, divided by the thickness of the $hcp - Ti(O)$ layer,h:

$$J \propto \frac{\Delta\mu(O)}{h} \tag{7.24}$$

*I.e., the $bcc - Ti(O)$ phase has completely transformed into $hcp - Ti(O)$.

Since the difference in the equilibrium in chemical potentials stays constant (as long as both interfaces are present), the oxygen flux within the $hcp - Ti(O)$ layer is controlled by its instantaneous thickness, which increases as the square root of time. The flux will therefore tend to decrease over time until the $bcc - Ti(O)$ layer disappears. At this stage, the $hcp - Ti(O)$ layer stops growing and begins saturating with oxygen. It is at this point when the $fcc \rightarrow hcp$ phase transformation begins to accelerate, as can be seen in Fig. 7-14. The change in the rate of this phase transformation is due to the fact the $hcp - Ti(O)$ layer saturates rapidly with oxygen, in the absence of the $bcc - Ti(O)$ phase. As the saturation progresses, any additional amount of oxygen entering this layer leads to its immediate transformation into $fcc - Ti(O)$. From an alternative point of view, it could be said that the *hcp/bcc* interface exerts a *back pressure* over the slow-moving *fcc/hcp* interface, as soon as the *hcp/bcc* interface disappears, the *back pressure* is relieved and the displacement of the remaining *fcc/hcp* interface accelerates. It is thus evident that the growth of the three individual phases considered in this system is *coupled* through the thermodynamic properties of the interfaces.

Although the system conserves mass and behaves as if it were controlled by volume-diffusion processes (as indicated by the $\delta x \, vs. \, t^{1/2}$ plot in Fig. 7-14), it is worth examining its behavior with respect to the *Stefan Condition**, as should be applied at each of the interfaces:

$$J(t)_{in} - J(t)_{out}|_{X(t)} = (c_L - c_R) \cdot \frac{dX\,(t)}{dt} \tag{7.25}$$

where $X\,(t)$ represents the position of the interface at any given time, t, c_L and c_R represent the equilibrium compositions at the left and right-hand sides of the interface, and $J(t)_{in}$, $J(t)_{out}$ are the inward and outward mass fluxes evaluated at the interface.

Eq. 7.25 basically states the local condition for mass conservation at any interface, X. Since the global mass conservation condition (depicted in Fig. 7-13) holds, this local condition must also hold, and it should be possible to test it by analyzing the local behavior of the interfaces resulting from the simulation. Due to the very nature of a diffuse interface (no sharp boundaries divide the phases), a rigorous test of the *Stefan Condition* is impossible unless one integrates the fluxes over an infinite range, which is basically what the plot of Fig. 7-13 does.

Fig. 7-15 presents, in a very crude way, a verification of the *Stefan Condition*. Note that although it is not possible to precisely determine the difference in equilibrium compositions, the product of such approximate differences and the interfacial velocities at that time roughly correspond to the equally approximate difference in the fluxes coming in and out of both interfaces. A larger difference in the fluxes at

*In the limit where the diffuse interface approaches a sharp one.

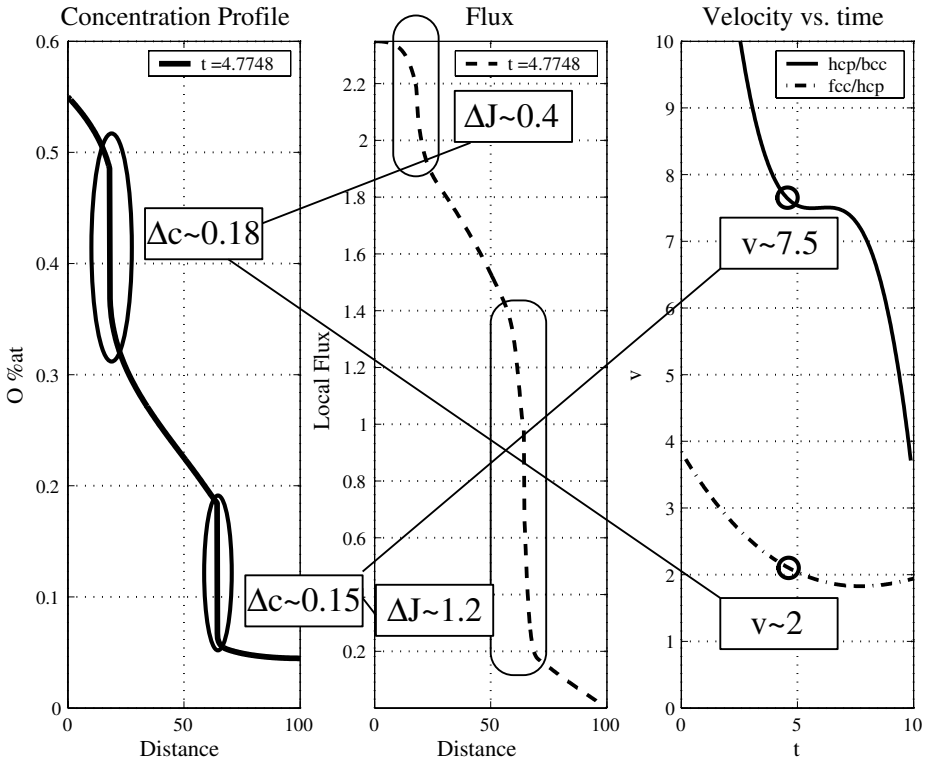

Figure 7-15: Stefan condition at the *hcp/bcc* and fcc/hcp interfaces.

the *bcc/hcp* interface naturally leads to a greater interface displacement rate.

Fig. 7-16 shows the concentration profiles at different times for the simulation of coupled-oxide growth using the kinetics described by the *Cahn-Hilliard* equation. Note that, due to fast interstitial diffusion, the $bcc - Ti(O)$ phase reaches the saturation composition* in a fast manner. As this saturation progresses, the *hcp/bcc* and fcc/hcp interfaces keep advancing at different rates, as indicated in Fig. 7-14. Note that, due to local equilibrium considerations, the oxygen mole fraction at both ends of the field corresponding to the *hcp* phase remain fixed. Consequently, the gradient in composition (And chemical potential) decreases as the phase field expands, decreasing the transformation rates and characteristic evolution rate of the system as a whole.

Fig. 7-17 shows the calculated profiles for the oxygen chemical potential† at different times during the simulation. It is evident that, according to the principle of local equilibrium, the profile for the oxygen chemical potential constitutes a smooth, monotonically-decreasing function of distance and the system evolves down the gradient in the oxygen chemical potential until it reaches an equilibrium at which further minimization of the Gibbs free energy is not possible.

*It reaches the $bcc - Ti(O)$ equilibrium composition in the $bcc + hcp$ two-phase field, according to Fig. 7-2.

†Reference State: $O_{2,g}$

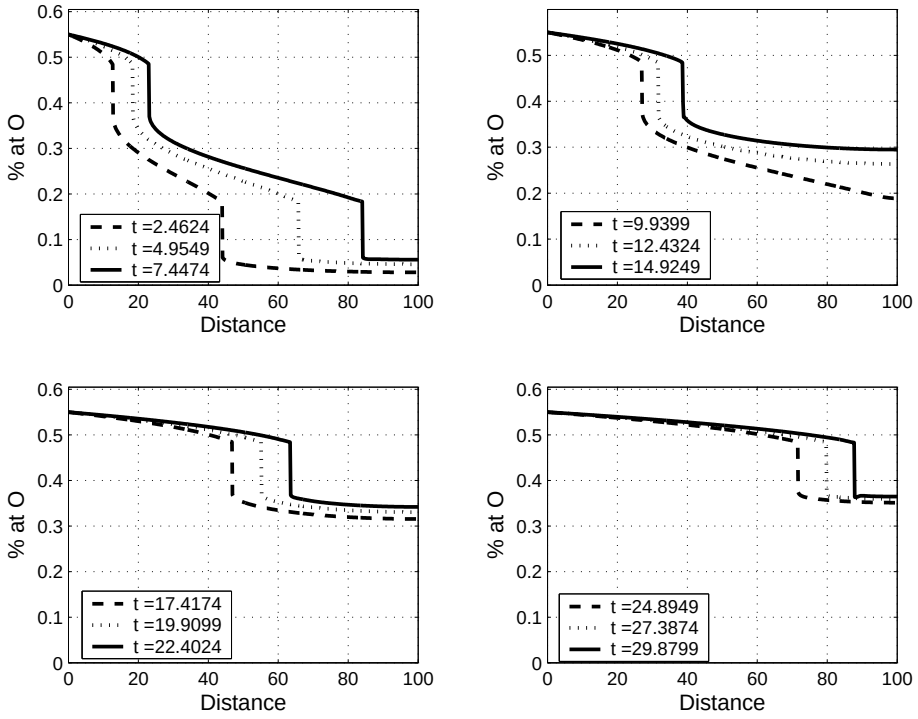

Figure 7-16: Concentration profiles at different times.

7.7 2D Simulation Results

In Section 7.6, it has been shown that it is possible to model the coupled growth of $Ti-O$ phases using CALPHAD descriptions of their thermodynamic behavior, together with a diffuse interface description of the kinetics of the phase transformation. As has been demonstrated, the displacement of the multiple interfaces follows the square-root law, which is to be expected if the phase transformation processes are diffusion-controlled. It has also been shown that the model satisfies global mass conservation conditions. Moreover, it has been demonstrated, in a somewhat crude manner, that the *Stefan* condition* is satisfied at each of the interfaces.
Given that the present model is physically-sound†, it is interesting to explore its behavior at higher dimensions. To this effect, a $2-D$ simulation of the coupled oxide growth model described in Section 7.6 has been implemented. Fig. 7-18 presents a $2-D$ simulation of the coupled oxide growth in the $Ti-O$ system, where the only phases considered are *bcc*, *hcp* and the $fcc\ Ti-O$ oxide solid solutions.

The simulation represented by Fig. 7-18 uses, as initial condition, a uniform composition on the bottom boundary of the computational domain, corresponding to the $fcc-Ti(O)$ phase field. Because of this initial condition, the behavior of the system

*Essentially, the *Stefan* condition is a local mass-conservation condition for each of the moving interfaces.

†It is important to note that realistic values for the atomic mobilities of oxygen in each of the phases have not been incorporated yet in the model. A concentration-dependent mobility field can, however, be incorporated to the model, provided reliable data for each of the phases is available.

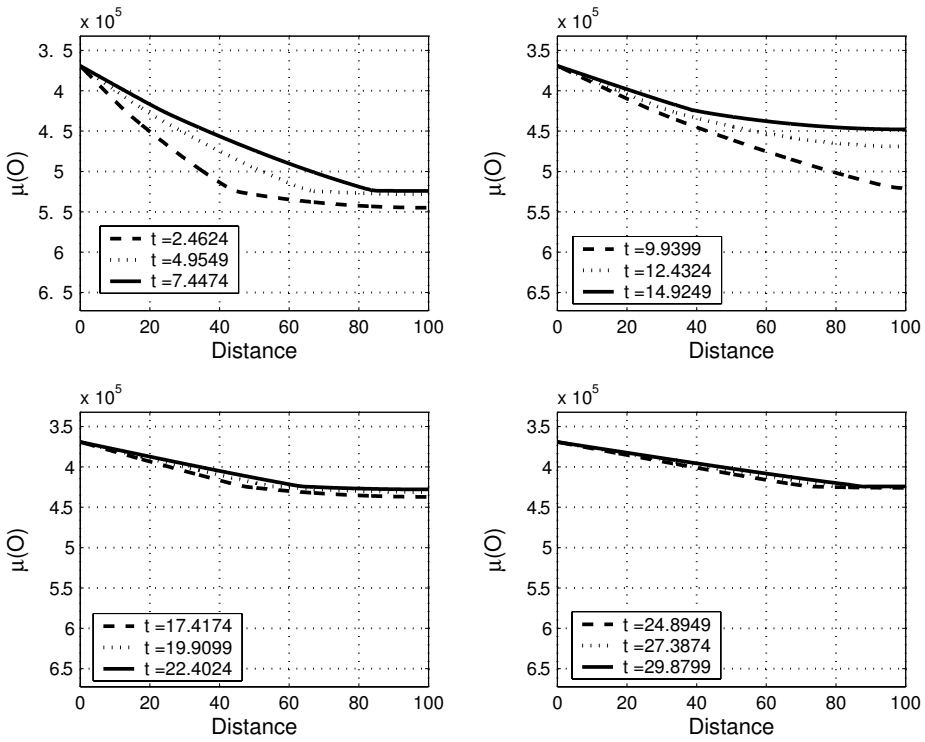

Figure 7-17: Chemical potential profiles at different times for coupled-oxide growth simulation using the *Cahn-Hilliard* formalism.

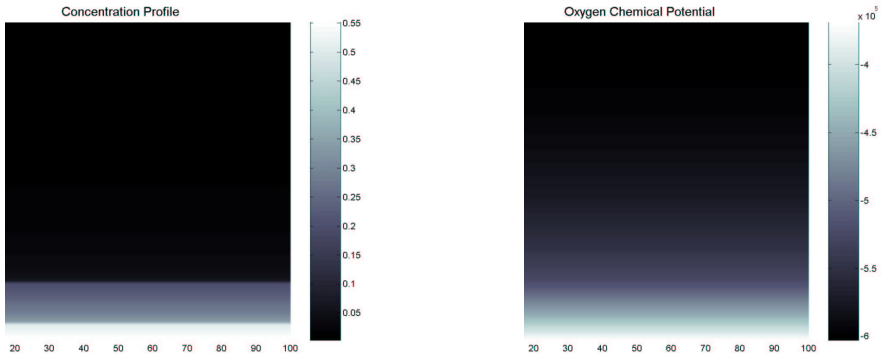

(a) Concentration profile in 2-D simulation.

(b) Chemical potential profile in 2-D simulation.

Figure 7-18: 2-D simulation of coupled oxide growth. Planar initial conditions.

is basically the same as the one that has been observed in the $1-D$ simulations presented in the previous section. It is perhaps more interesting to analyze the behavior of the system when the initial condition corresponds to a perturbation in the concentration field.

Fig. 7-19 shows a $2-D$ calculation of the coupled growth of multiple $Ti-O$ layers

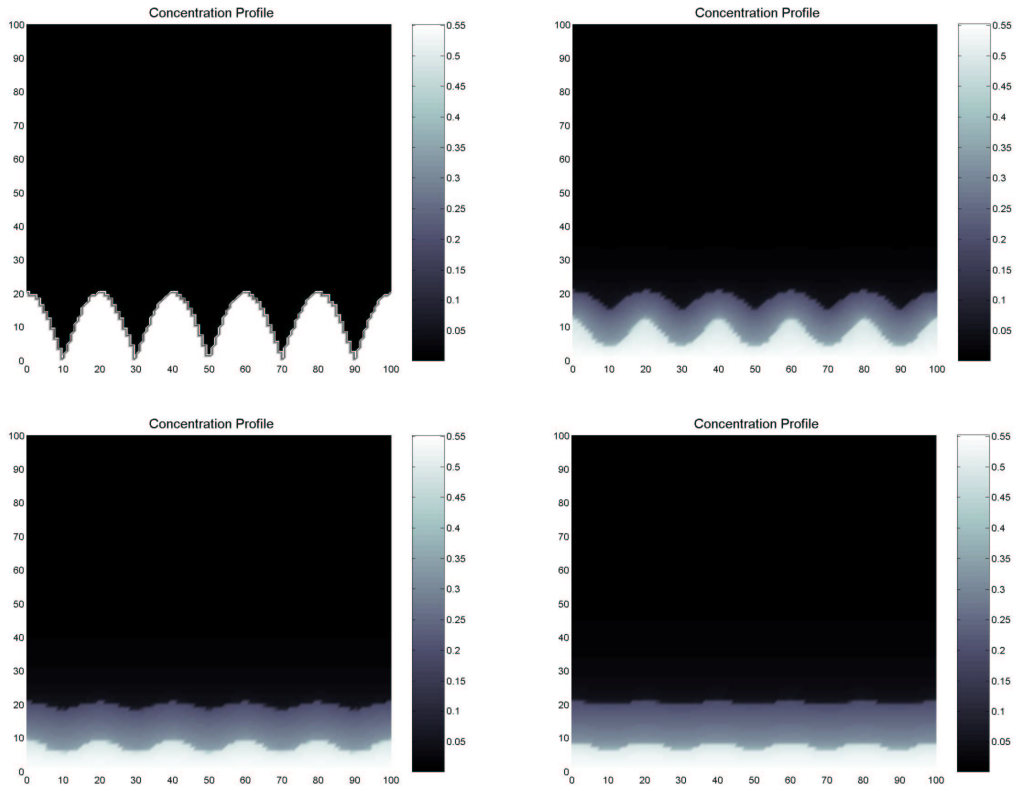

Figure 7-19: 2-D simulation. Perturbations in the concentration profile were incorporated as initial conditions.

considering, as initial condition, a semi-sinusoidal region with an initial composition corresponding to the $fcc - Ti(O)$ phase. As seen in Section 7.6, the growth of the $fcc - Ti(O)$ phase is much slower*, than the growth of the $hcp - Ti(O)$ phase. In this $2 - D$ simulation, therefore, it is to be expected that diffusion across the initial $fcc - Ti(O)$ region is so slow compared to the diffusion across the $bcc - Ti(O)$ and $hcp - Ti(O)$ regions, that any perturbation in the concentration profile would tend to disappear over time. According to this simulation, however, in addition to the much slower $fcc - Ti(O) \rightarrow hcp - Ti(O)$ transformation, it is observed that in fact the initial $fcc - Ti(O)/bcc - Ti(O)$ interfaces actually recedes, since it is thermodynamically unstable with respect to an $hcp - Ti(O)/bcc - Ti(O)$ interface. It is seen then that, according to this model, a sequence of planar reaction layers is the most stable interfacial configuration. In the next section it will be shown that experiments, reported elsewhere, confirm this finding.

7.8 Experimental Verification of Phase-Field Model

Although there is no experimental work reproducing the exact conditions that were simulated in this chapter, it is still possible to establish the validity of the assump-

*Due to a lower diffusion coefficient

tions made while developing the model, as well as the main findings regarding the qualitative behavior of the coupled layer growth simulation. To this effect, in this last section several of the key aspects of the model described in Section 7.7 through Section 7.7 will be compared against experimental facts obtained elsewhere.

7.8.1 Examining the Local Equilibrium Hypothesis

The assumption of local thermodynamic equilibrium is one of the key hypothesis regarding both diffuse and sharp interface phase transformation models. This implies that there are no abrupt changes in the chemical potentials of the system's components. In diffusional transformations, this assumption of local equilibrium implies that the chemical composition at both sides of the interface corresponds to the equilibrium compositions given by the equilibrium phase diagram. Although the local equilibrium assumption seems to be acceptable apriori, there are some experimental results that question its validity [156].

In his early experiments on the oxidation of titanium, Jenkins [157] found that the oxygen content in the $hcp-Ti(O)$ side of the $hcp-Ti(O)/oxide$ interface did not reach the saturation limit ($\sim 30\,at.\%$, see Fig. 4-11(b)) that would be expected if the $hcp-Ti(O)/oxide$ interface were at equilibrium. In those experiments, it was found that, after holding the samples for $72\,hr.$, the concentration at the $hcp-Ti(O)/oxide$ interface was $12\,at.\%$ at 650^0C, $19\,at.\%$ at 800^0C, and $25\,at.\%$ at 900^0C. In later oxidation experiments ($650-700^0C$), Hurlen [158] found that the initial oxygen content of the $hcp-Ti(O)$ phase in contact with the oxide layer was within the $14-15\,at.\%$.After analyzing the samples, Hurlen [158] concluded that the composition at the ceramic/metal interface corresponded to that of the Ti_6O^*. In a much more recent series of experiments, Unnam et al. [156] found that the saturation concentration of the $hcp-Ti(O)$ phase, in equilibrium with oxide phases, was not reached at low temperatures (590^0C). However, at temperatures above 800^0C the $hcp-Ti(O)$ saturation composition ($\sim 30\,at.\%$) was reached in very short times.

It is important to note that the fact that non-equilibrium compositions are found at the interfaces corresponding to low-temperature oxidation may be explained by low interface mobilities Martin et al. [159, p. 80]. In this case, the model develop in this chapter could not be applied, unless it is modified to incorporate the phase state of the system in an implicit manner.

In a very recent experiment on the early stages of laser-induced oxidation of titanium, Lavisse et al. [160] verified the local equilibrium condition for $Ti-O$ phases through *XRD*, *GIXRD*, *XPS* and *EDX* analyses of their samples. At least at the early stages of their oxidation experiments, Lavisse et al. [160] were able to identify several hexagonal compounds with compositions in agreement with the Ti_6O,

*This Ti_6O is an hcp-based phase in which oxygen and vacancy interstitials are ordered in alternating sequences along the perpendicular axis to the basal plane [58].

Ti_3O and Ti_2O stoichiometries. The last stoichiometry, Ti_2O, corresponds to the $hcp - Ti(O)$ solution, fully saturated with oxygen interstitials. In some of their samples, the authors were able to identify (using *GIXRD*) the TiO_x*.

Even if the local-equilibrium condition were not to be reached at low temperatures, the evidence available in the literature appears to confirm the local equilibrium hypothesis for diffusional transformations in the $Ti - O$ system, at least for temperatures above $\sim 750^0C$. Since the simulations performed in this chapter at at 100^0C, the local-equilibrium implications of the *Cahn-Hilliard* model seem to be acceptable.

7.8.2 Experimental Verification of Diffusion-Controlled Kinetics

As has been shown in Section 7.6, the *Phase-Field* model developed in this chapter produces a sequence of different $Ti - O$ phases, whose time evolution is controlled by volume diffusion†. According to this model, there are no surface-attachment limiting effects occurring at the interface. This behavior seems to be confirmed by a number of experimental works on the oxidation of Ti-based metals:

In their work on the low-temperature oxidation in titanium, Rogers et al. [161] explored the diffusion of oxygen in Ti within the $127 - 527^0C$ range, for periods ranging from 1 to 100 hr. under several pressure conditions. Oxygen concentration profiles were measured using *Auger* spectrography. From their analysis on the behavior of the oxygen concentration profile, as a function of time, Rogers et al. [161] observed that the sequence of $Ti - O$ compounds (including TiO_2, TiO, Ti_2O, and so forth) appeared to grow following the square-root-of-time law, and therefore were diffusion controlled.

In a higher-temperature series of experiments, Unnam et al. [156] studied the oxidation kinetics of Ti sheets within the $593 - 760^0C$ range. The thickness of the oxide resulting from the oxidation was measured by optical means, while the oxygen concentration in the $hcp - Ti(O)$ layer was determined using previously calibrated micro-hardness measurements. According to their measurements, the solid-state phase transformation processes occurring in all their samples were diffusion-controlled, since all the moving interfaces that were observed in the samples followed the square-root-of-time law.

As has been noted in Section 7.4 and Section 7.5, in cases when the kinetics of the phase transformations are not limited by interface mobility effects, the *Cahn-Hilliard* equation should be capable of describing the relevant kinetic behavior of such transformations. Given the evidence presented above, it is reasonable to expect that the coupled layer growth in the $Ti - O$ system at even higher temperatures will be

*This phase is an $fcc - Ti(O)$ solid solution, with a structure identical to the $NaCl$ prototype.

†The displacement of the different interfaces is governed by the square-root-of-time law, $X(t) \propto \sqrt{t}$.

controlled by volume diffusion. Therefore, the use of the *Cahn-Hilliard* equation for this particular problem seems to be justified.

7.8.3 Experimental Evidence for the Stability of Planar vs. Undulated Interfaces in the $Ti-O$ System

In Section 7.7, it was shown that, according to the *Cahn-Hilliard* model described in this chapter, a planar sequence of layered $Ti-O$ phases is more stable than an undulated-type of interface. This is to be expected if, during the phase transformations, any possible capillary effects due to the local curvature of the interfaces created, were suppressed by the dissipative nature of the diffusion-controlled kinetics described by the model.

Although there has been a considerable amount of experimental work on the oxidation behavior of titanium and titanium alloys [156–158, 160, 161], there has only been, to the best of this author's knowledge, one report on the behavior of multiple moving boundaries as a result of oxygen transport across $Ti-O$ phases. In their work on the oxidation of commercially pure titanium, Unnam et al. [156] subjected several titanium samples to an air atmosphere at different temperatures (see 7.8.2). In their experiments, Unnam et al. [156] were able to observe the formation of a titanium oxide (TiO_2, or rutile), as well as the formation of a $Ti-O$ solid solution, corresponding to the $hcp-Ti(O)$ phase. Within the $hcp-Ti(O)$ phase they were also able to determine, through metallographic etching techniques, a moving boundary, parallel to the oxide-metal interface. From their observations, Unnam et al. [156] were able to determine the following:

i) The moving boundary represented a demarcation between relatively oxygen-rich and oxygen-poor regions of the $hcp-Ti(O)$ matrix. From their micro-hardness measurements*, however, they were not able to determine any discontinuity in the oxygen concentration across the interface.

ii) The displacement of this moving boundary, $X(t)$, had a definite correlation with time and temperature, and its displacement obeyed the square-root-of-time law.

iii) The composition of this moving boundary was found to be, according to the micro-hardness measurements, around $5\,at.\%$.

Since the oxidation experiments by Unnam et al. [156] were performed below the temperature ($t < 800^0C$) at which the $bcc-Ti(O)$ phase becomes stable ($\sim 890^0C$), the formation of the moving boundary could not be attributed to the $hcp-Ti(O) \rightarrow bcc-Ti(O)$ transformation that should occur at high temperatures. In principle, it may be possible that this moving boundary resulted from the formation

*As has been noted in 7.8.2, Unnam et al. [156] used calibrated micro-hardness measurements on the $hcp-Ti(O)$ phase in order to determine its oxygen content.

of an *hcp*-based ordered interstitial solution [58]. However, the measured oxygen concentration ($\sim 5\,at.\%$) does not correspond to any reported $Ti-O$ interstitial solution.

Despite the fact that the experimental conditions in the experiments by Unnam et al. [156] do not correspond to the conditions of the simulations presented in Section 7.6 and Section 7.7*, it is perhaps interesting to observe the interfacial structure resulting from these experiments. Fig. 7-20 shows a typical result from the titanium oxidation experiments by Unnam et al. [156]. As can be seen, the interphase morphology is planar and there are two clearly identifiable interfaces within the $Ti-O$ region. As has been noted above, the experimental conditions that produce the interfacial morphology in Fig. 7-20 do not correspond to the simulations presented in Section 7.6 and Section 7.7. However, the similarity between Fig. 7-20 and Fig. 7-18(a) is remarkable.

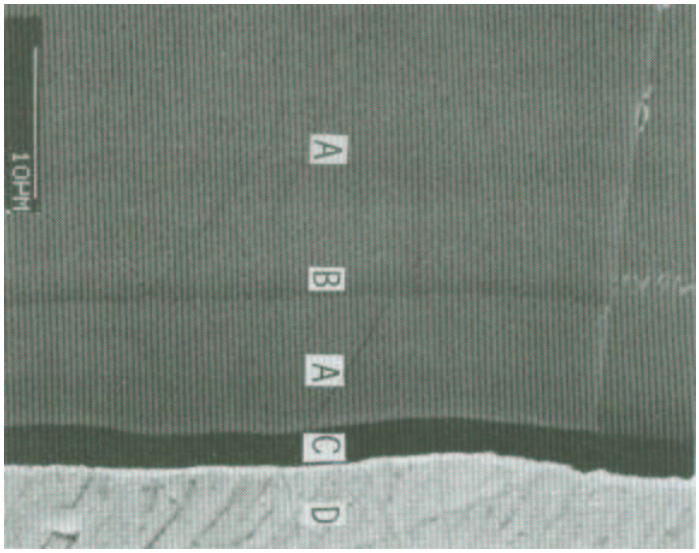

Figure 7-20: SEM micrograph of a $Ti-A55$ sample oxidized at 649^0C for $65.9hr$. A=matrix, B=moving boundary, C=oxide and D=copper coating. Originally, Fig. 7 in Unnam et al. [156, page 242]. Reproduced with permission from the publisher (Kluwer Academic Publishers).

Metin and Inal [162] studied the layer growth during titanium ion-nitridation in nitrogen plasma, at different nitrogen partial pressures within the $800-1080^0C$ range. In their work, the authors found that the layers formed corresponded to what could be expected from the $Ti-N$ phase diagram. As can be seen in Fig. 7-21, the $Ti-N$ phase diagram closely resembles the $Ti-O$ phase diagram (see Fig. 4-11(b)), at compositions of nitrogen and oxygen below $50\,at.\%$. Even more significantly, in the $Ti-N$ solid solutions, N behaves as an interstitial and the crystal structures of

*The oxidation experiments by Unnam et al. [156] were performed under air, so the formation of the rutile, TiO_2 oxide was thermodynamically favorable, compared to that of lower oxides, such as TiO or Ti_2O_3.

these phases [163] have a one-to-one correspondence with the respective $Ti-O$ phases ($bcc-Ti(O) \rightarrow bcc-Ti(N)$, $hcp-Ti(O) \rightarrow hcp-Ti(N)$, $fcc-Ti(O) \rightarrow fcc-Ti(N)$).

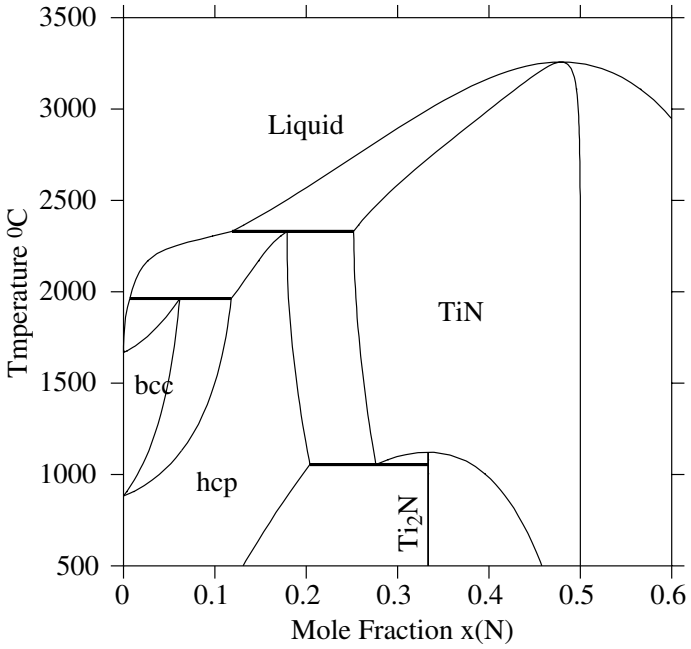

Figure 7-21: $Ti-N$ phase diagram, calculated from the thermodynamic model by Othani and Hillert [164].

In Fig. 7-22, an optical micrograph of one of the ion-nitridation experiments by Metin and Inal [162] is presented. This nitridation experiment was performed at 900^0C. As can be seen by examining the $Ti-N$ phase diagram in Fig. 7-21, the layering sequence ($TiN/Ti_2N/hcp/bcc$) observed, corresponds to what could be expected from a series of coupled phase transformations in the $Ti-N$ system, along a N chemical potential gradient. By comparing Fig. 7-22 to Fig. 7-18(a), it is possible to identify several similarities between the calculation for the $Ti-O$ system and the titanium nitridation experimental results reported by Metin and Inal [162]:

i) The layering sequence corresponds, in both cases, to what should be expected if the diffusional transformations occurred along a chemical potential gradient of the interstitial element (oxygen or nitrogen).

ii) Excluding the Ti_2N nitride, the rate of the $fcc \rightarrow hcp$ transformation is much slower than that of the $hcp \rightarrow bcc$ transformation*.

*In all the solid solution phases in both the $Ti-O$ and $Ti-N$ systems, the diffusion of the interstitial is expected to be fast, with similar atomic mobilities for all the phases. However, the site occupancy of both N and O interstitials, relative to interstitial vacancies in the fcc phase is significantly less that that of the bcc and even the hcp phases.

iii) A planar interfacial morphology seems to be more stable than an undulated one. Thus, capillary effects, due to local curvature of the different moving interfaces do not play an important role on the morphology of the reaction product layering.

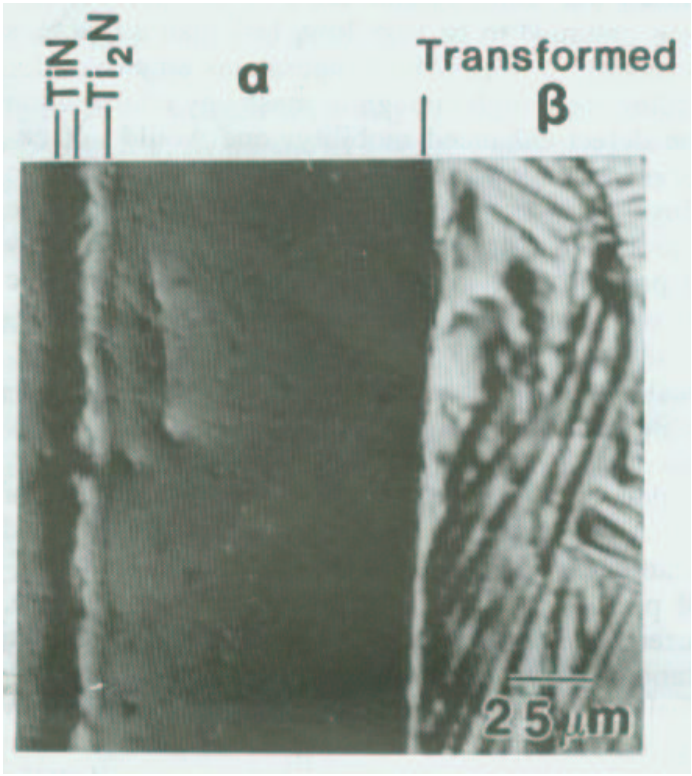

Figure 7-22: Optical micrograph of the cross-sections of the ion-nitrided titanium at 900^0C. Original figure appeared as Fig. 4 a) in Metin and Inal [162, page 1823]. Reprinted with permission from the publishers (TMS).

As can be seen from Fig. 7-22, the stability of planar interfaces with respect to undulated ones in these types of phase transformations seems to be justified from the experimental point of view.

7.9 Sensitivity of the Model To the Thermodynamic Description

Before closing this chapter, it is necessary to consider how the thermodynamic descriptions of the different phases in the system affect the dynamics of the simulation. As was seen in this section, by solving the *Cahn-Hilliard* equation using the the thermodynamic models for the $Ti - O$ system it was possible for the system to 'find' the equilibrium compositions at each of the interfaces created. In principle, any function for which common tangent constructions yield the same equilibrium compositions should be equivalent and should yield the same interfacial arrangement as the one shown here. One could, for example, linearly transform the Gibbs free energy function and still find the same common tangents. The problem with this transformation

is that, unless the transformation involves just changing the reference state for the elements in the system, the kinetics of the system will be affected since the diffusion rates within each of the regions of the system are also dependent on the local thermodynamics through:

$$D_O \cong \left[1 + \frac{\partial \ln \gamma_O}{\partial \ln X_O}\right] \cdot M_O RT$$

A linear transformation other than a constant shift of the Gibbs free energy curve would yield a different 'thermodynamic factor', which multiplies the atomic mobility to yield the chemical diffusion coefficient. In highly non-ideal systems, such as the $Ti-O$ system treated in this work, the thermodynamic correction is very important. In summary, an accurate model for the system described here requires not only that the Gibbs free energy functions used yield common tangent constructions compatible with the equilibrium phase diagram but also accurate thermodynamic descriptions that make it possible, provided diffusion data is available, to relate the observed diffusion rates to atomic mobilities and to the compositional dependence of the chemical potential of the diffusion species.

A much more critical question is whether the model presented in this work is robust enough with respect to small variations in the actual thermodynamic description of the system. As can be seen in Fig. 7-6, the Gibbs free energy curves corresponding to the *bcc*, *hcp* and fcc phases in the $Ti-O$ system are very close to each other. A valid question to ask is whether a small variation in the parameters used to describe the thermodynamics of the system will have a significant effect on the common tangent construction that leads to the equilibrium phase diagram of the system. Moreover, a change in the thermodynamic parameters used to describe the system may also have a significant effect on the heterogeneous Gibbs free energy regions, above the equilibrium tie-lines and therefore lead to different values for the interfacial energies of the system. By inspecting the results regarding the influence of the value for the gradient energy coefficient (see 7.6.1), k (see Eq. 7.13), on the dynamics of the system, one may speculate that this last effect is not as important, although it is necessary to perform a much more rigorous analysis. Although these questions are beyond the scope of this thesis, it will be necessary to answer them in the near future if this model is to be generalized to more complicated multi-component, multi-phase systems.

7.10 Conclusions and Future Work

7.10.1 Conclusions for this Chapter

In this chapter, the *Cahn-Hilliard* equation was solved to describe the coupled growth of multiple oxide phases during ceramic/metal joining operations. Although the present paper focuses on the study of the thermochemical interactions between zirconia-based ceramics and pure titanium, it is possible to apply it to other similar systems.

With the methodology developed in this paper, it was possible to use real thermodynamic descriptions (based on the *CALPHAD* formalism) of the system and incorporate them in a Phase-Field simulation in which the *Cahn-Hilliard* equation is used to describe the kinetics of the phase transformations. By solving a single kinetic equation it was possible to model the coupled growth of multiple phases without having to track the movement of every boundary in an individual manner. The system was shown to satisfy the global mass conservation condition without actually having to apply any local correction to the displacement of the individual boundaries. It was also shown that an improper value for the gradient energy coefficient could lead to mass conservation problems which become more dominant as the interfacial-area/volume ratio of the system increases.

Through this chapter it was shown that the growth of the different phases is governed by bulk-diffusion processes, following the square-root-of-time law. Furthermore, it was demonstrated that the *Stefan* condition appears to be followed at all the moving interfaces present in the system. From the one-dimensional simulations it was evident that the actual rates of growth of the three different phases involved in the simulations were coupled through the thermodynamic properties at the moving interfaces. Finally, it was demonstrated that the oxygen chemical is a monotonically-decreasing function of distance, which is consistent with the fact that the *Cahn-Hilliard* equation is based on the fundamental assumption of local thermodynamic equilibrium. From the two-dimensional simulations, it was determined that, for these type of diffusional transformations, capillary effects due to local curvatures at the different moving interfaces do not play a role in determining the stable layering morphology to be expected in these type of ceramic/metal interfacial reactions.

Although there is no experimental work reproducing the exact conditions that were simulated in this chapter, it was still possible to establish the validity of the assumptions made while developing the model, as well as the main findings regarding the qualitative behavior of the coupled layer growth simulation. The local equilibrium hypothesis, which is central to the development of both sharp and diffuse interface models, has been determined to valid, at least for the temperatures of interest in this work. Additionally, the fact that the different phase transformations occurring in the $Ti - O$ system are diffusion-controlled has been verified by a series of experiments on the oxidation of titanium and titanium alloys. Finally, the stability of planar interfaces, with respect to undulated ones, seems to be confirmed by the available literature.

Although there has been no attempt to make quantitative predictions regarding the coupled growth of multiple oxide phases during ceramic/metal joining operations in the $Ti - O$ system, the model developed in this work seems to represent the relevant physics of the system in an acceptable manner. By relaxing the assumption of constant mobility in this model, while using realistic values for the oxygen mobilities in the different phases considered, it may be possible, in the future, to completely

validate the model and extend its applicability to other complex multi-phase moving boundary problems of relevance not only in ceramic/metal interfacial interactions, but in other material systems and technologies.

7.10.2 Future Improvements on the Model

Although the model presented in this chapter accounts for the formation and evolution of interfacial structures in this relatively simple system, there are a number of improvements that need to be made in order for this model to the applicable to the general problem of ceramic/metal interfacial formation and evolution. Two important improvements are listed below:

i) The model considers that the oxygen chemical potential on one side of the computational domain is fixed at one particular value. Although this is a realistic assumption in oxidation experiments, when zirconia-based ceramics interact with titanium, the oxygen chemical potential at the zirconia/titanium interface is expected to change as the partial reduction progresses. This implies the incorporation in the present phase-field model of a zirconia phase.

ii) Fig. 5-23 illustrates the interfaces observed when a zirconia substrate interacts with a $Cu - Zr$ melt. In Section 5.7, it was shown that bulk thermodynamics cannot explain the dissolution reaction observed. In that section, it was hypothesized that grain boundary attack by the $Cu - Zr$ melt could account for the interface observed. If one were to reproduce this interface through phase-field modelling, it would be necessary to incorporate a model to account for the energy related to the formation and evolution of grain boundaries. Such a model has been successfully used by Bishop [165] in her study of $Si_3N_4{-}CaO$ inter-granular structures. Incorporating the insights of that excellent work into the particular problem of this interface could lead to a model for ceramic/metal dissolution interactions.

Chapter 8

Conclusions and Future Work

The study of ceramic/metal interface formation and evolution is very important from both an engineering and a scientific point of views. Better understanding of C/M interface formation allows the improvement of important technological applications that require the formation of synthetic C/M composites, such as solid oxide fuel cells, ceramic-metal composites, ceramic-coated turbine blades and so forth. Additionally, the diffusional reactions and phase transformations occurring in these complex systems offer the opportunity to test several methodologies of analysis and develop new models that can be used in the study of other equally complex phase transformation systems.

8.1 General Conclusions

In this work, the study of zirconia/metal interfaces has been used as a model system to illustrate the use of basic thermodynamics and kinetics concepts to analyze complex interfacial interactions. The selection of zirconia-based ceramics is not accidental, as it constitutes one of the ceramic families with numerous potential uses in energy-related technologies, which will become increasingly important over time, due to increased emphasis in efficiency and clean energy access.

With regard to the formation of zirconia/active-metal interfaces, several conclusions can be made:

i) Perhaps the most general conclusion of this work is that it is possible to use thermodynamic analysis to understand the complex diffusional reactions and phase precipitations occurring at ceramic/metal interfaces. Through the use of metastable phase diagrams, activity maps and chemical equilibria it is possible to understand the nature of zirconia/active-metal interfacial reactions under several thermal and chemical conditions.

ii) In the particular case of zirconia/titanium reactions, it has been possible to establish, at least in a qualitative manner, the possible diffusion paths that the system has to take, based on simple assumptions regarding the kinetics of diffusion and

dissolution.

iii) As has been shown in this work, it is the wide range of non-stoichiometry of zirconia-based ceramics what mostly determines the diffusion paths observed in zirconia/titanium interfacial reactions.

iv) In the particular case of solid/solid zirconia/titanium interfacial interactions, the relative size of the system plays an important role in the reaction sequences observed. When the amount of titanium in the system is comparable to that of zirconia, the initial partial reduction of the zirconia lattice is followed by a complete decomposition of the ceramic when the maximum non-stoichiometry has been reached. In cases where titanium films are put in contact with zirconia substrates, this decomposition does not take place, and the diffusion path observed moves across the $Ti-O$ binary system.

v) As mentioned in this thesis, the particular reaction product formed at the ceramic/braze interface determines the effectiveness of any given ceramic/metal brazing procedure. By carefully designing the brazing alloy it is possible to precipitate wettable products that, put in contact with a liquid metal, promote complete wetting of the ceramic substrate.

vi) Through the use of activity maps, it has been shown that the reaction products observed in zirconia/active-braze interactions (the brazes could belong to the $Ag-Cu-Ti$ or $Cu-Ti-Al$ systems) can be interpreted using the criterion of monotonic decrease in the chemical potentials of the reacting species.

vii) Although there have been some attempts at analyzing the thermochemistry of ceramic/metal joining prior to this work, the effect of the metal substrate effect on the thermochemistry of the brazing alloy has not been quantitatively determined. In this work, it has been shown that extensive solubility of the base metal in the braze, coupled with high chemical affinity between the base metal and the active additive of the braze can affect, in a dramatic manner, the nature of the interfacial interactions observed at the ceramic/braze interface.

viii) Besides the nature of the reaction products observed at ceramic/metal interfaces, morphology plays an important role in determining the final mechanical properties of ceramic/metal interfaces. By using simple thermodynamics and diffusion simulations it is not possible to gain insight into the nature of ceramic/metal interfacial morphology and evolution. In this work, the *Cahn-Hilliard* equation has been coupled to a *CALPHAD* model for the $Ti-O$ system in order to study the coupled oxide growth occurring at a zirconia/titaniun interface. Although the model so far is only qualitative, several general results and implications of this model have been validated by examining the available literature. Comparison to the analogous $Ti-N$ system during nitriding processes suggests that the model can be further used to understand other complex interfacial phenomena important in several important technologies.

Within the limited scope of this work, a few contributions have been made that not only can be applied to the analysis of the particular problem of this work, but also to other important material-related problems. These contributions are mainly through the development of thermodynamic models for several industrially important systems:

i) A thermodynamic model of the $Ag-Cu-Ti$ system has been developed through the critical assessment of the existing experimental information. The fact that the reaction products observed in zirconia/active-braze interactions in Section 5.5 can be understood using the results of this model provides additional support for the model.

ii) A model for the $Cu-Ti-Zr$ system has also been assessed and the calculated thermochemical properties of this system agree well with the experimental results. Although this model has not been explicitly used in this work, amorphous alloys based on this system may be widely used as a high-temperature substitute of $Ag-Cu-Ti$ systems.

iii) Despite having been studied and used for several decades, it was until this work that a complete model for the $Zr-O$ system has been obtained. This model is essential to understand the thermochemical reactions at ziconia/metal interfaces. Moreover, this model can be expanded to more complex systems that are important as structural materials or solid oxide electrolytes for solid oxide fuel cells, such as YSZ, MGZ, CSZ, and so forth.

iv) The $Ti-Zr-O$ and $Cu-Ti-O$ systems have also been thermodynamically assessed. Although the application of these models is somewhat constrained to the study of zirconia/mtal interactions, the $Ti-Zr-O$ system may be used in other studies that focus on the oxidation phenomena occurring in titanium alloys.

8.2 Future Work

Even though it has been shown in this thesis that thermodynamic descriptions, based on the *CALPHAD* methodology, can be used to understand the interfacial interactions observed in some zirconia/metal systems, there are several refinements that remain to be made and questions to be answered.

With regard to the thermodynamic models proposed in this work, several improvements remain to be made in some of the systems studied. For example, the thermodynamic description of the $Ti-Zr-O$ system presents some discrepancies with available experimental results, especially with regard to the experimental verification of several invariant reactions involving the liquid phase. Although these discrepancies had no impact in the present work, they need to be resolved, especially if this model is to be applied to other problems involving ionic melts with high titanium contents.

Considerable work is still required if one is interested not only in understanding the nature of ceramic/metal interfacial interactions, but also in predicting and controlling them. Although this work indicates that it is feasible to predict the nature of interfacial interactions for simple ceramic/metal systems, a more modest success has been achieved in the prediction of such interactions in more complex systems, where more components and phases play a dominant role.

The absence, in some zirconia/braze interaction experiments, of predicted phases, such as the Ti_3Cu_3O phase in zirconia/zirconia brazing operations may be due to kinetic factors. However, this has not been proved in this work and further experimental and theoretical effort is needed if one is to resolve these discrepancies.

With regard to the evolution of ceramic/metal interfacial reaction products, a need still exists for quantitative growth models, using information regarding the diffusion rates of the reacting species. Moreover, since many of these reaction products are ionic in nature, the kinetic studies must incorporate coupled charge and mass transfer mechanisms, which imply a more accurate model for the point defects in these phases. The *CALPHAD* models used in this work do not, except for the model for the TiO phase, incorporate charged species. Without this, a diffusion model using experimental data on ionic and electronic mobilities cannot be used.

An example of a technology where growth models for interfacial reaction products is of fundamental importance is the use of zirconia-based ceramics as thermal barriers for turbine blades. In these systems, high operating temperatures promote the interdiffusion and reaction of oxygen and active elements within the alloy in the turbine blade. The formation of an interfacial reaction product at the interface between the blade and the thermal barrier eventually leads to the formation of interfacial cracks and spalling of the protective zirconia barrier. In order to predict the operating life of this system it is necessary to successfully account for the growth of the thermally grown reaction products.

Although it has been shown that the *Cahn-Hilliard* equation can be successfully coupled to a thermodynamic description of the likely interfacial reaction products during zirconia/titanium interactions, the model is qualitative in nature, and quantitative validation is necessary. Real data on diffusion rates are therefore necessary. In principle, the model presented in this work my be applied to systems with a greater number of components and field variables other than composition, such as charge, for example. Although this was not within the scope of this work, the incorporation of these improvements may make this model applicable to other complex phase transformation and growth systems.

Appendix A

The Calphad Approach to Thermodynamic Modelling: Developing models for Ceramic/Metal Systems

A.1 The CALPHAD Methodology: An Introduction

In order to facilitate the development of novel materials and processes it is essential to understand the thermochemical behavior of the materials of interest as well as of the equilibrium state that the system would reach under a particular set of conditions. Because of the lack of comprehensive thermodynamic descriptions for many important material systems, the actual use of thermodynamics in materials design has been limited to few materials families, such as steels, aluminum alloys, etc. Over the past decades, and thanks to the pioneering work of Kaufman and Hillert and many more researchers, a powerful methodology that enables the application of thermodynamics to the development of material applications has slowly emerged. This methodology is sometimes referred to as the CALPHAD Method and has as its main objective the coupling of both thermochemistry and phase diagram information through the use of semi-empirical models and computational techniques*.

In general, it is possible to define the Gibbs free energy of a phase ϕ using an empirical function of the pressure, temperature and composition:

$$G^{\phi} = G^{\phi} f\left(P, T, C_i\right) \tag{A.1}$$

The particular choice of the model used to describe the thermodynamic properties of a phase depends on its chemical behavior and its internal structure†. Over the

*An excellent reference to this method can be found in the book by Saunders and Miodownik [21]

†Note that these empirical models do not contain information regarding the actual crystal struc-

years, models have been developed to describe random liquid and solid substitutional and interstitial solutions, order/disorder transformations, phases with defined sublattice occupancies, intermetallic compounds, and so forth [21].

In this work, the general sublattice formalism is used to describe the thermodynamic properties of all the phases involved in the systems studied. In the remaining sections of the present chapter the appropriate sublattice formalism notation will be used to describe the underlying 'structure' of the thermodynamic model for each of the phases. Briefly, a phase will be described using a similar expression to:

$$(A, B)_{N1} (C, D)_{N2} \tag{A.2}$$

The model represented by Eq. A.2 indicates, for example, that the phase in question has two sub-structures (or *sublattices*) with different number of sites ($N1$ and $N2$, respectively), and that the different components of such phase (*A,B,C and D*) occupy distinct spatial regions within the phase.

The models developed using the formalism represented in Eq. A.2 are then thermodynamically optimized through a fitting process whereby the adjustable coefficients in the Gibbs energy equations (such as Eq. A.1) are varied until the best (optimal) representation of both thermochemical experiments* and phase diagram determinations† are obtained. By using procedures such as least-square minimizations [90] it is possible to give this fitting procedure a mathematical rigorousness. The optimizations and further thermochemical calculations in this work were performed with the aid of the Thermo-Calc® program[144].

A.2 Calphad Models: A Brief Description

As noted in Section A.1, the development of models capable of accurately describing the thermodynamic properties of chemical systems constitutes an essential aspect of the *CALPHAD* methodology. In this section, a comprehensive description of the thermodynamic models used (and their mathematical formalism) in this work is presented ‡. In order to better illustrate the applicability of the models described, examples using phases relevant to the systems of interest for this work will be presented.

When dealing with *CALPHAD* modelling, it is necessary to consider only two main types of phases: stoichiometric compounds and solution phases (these solution phases can then be classified as random, sublattice, ionic, etc.). The major difference

ture of the phase. The term 'internal structure' should be therefore understood as the arrangement of the different species within the phase. Energetic relations between different structures are externally imposed on the models, as adjustable coefficients.

*Measurements of chemical activities, enthalpies of formation, enthalpies of solution, etc.

†Phase boundaries, invariant points, melting points, and so forth.

‡For a much more rigorous treatment on thermodynamic modelling and its relationship to the *CALPHAD* methodology, one could refer to the work by Saunders and Miodownik [21].

between both types of phases is that a solution phase, contrary to a stoichiometric compound, allows a finite solubility of more than one component or species within the structural components of the phase. The remainder of this section contains a brief description of the models used for the different kinds of phases assessed in this work.

A.2.1 Stoichiometric Compounds

The integral Gibbs energy of a pure species or stoichiometric compound G^{ϕ}_{ij} (in this case a binary ij compound) is given by the equation:

$$G^{\phi}_{ij} - H^{SER} = {}^{0}\Delta H^{\phi}_{ij,f} - T{}^{0}\Delta S^{\phi}_{ij,f} + GHSER_i + GHSER_j \tag{A.3}$$

where ${}^{0}\Delta H^{\phi}_{ij,f}$ is the standard enthalpy of formation for the compound ij (that has the crystal structure ϕ), ${}^{0}\Delta S^{\phi}_{ij,f}$ is the entropy of formation, and $GHSER$ can in turn be defined as $G_i - H^{SER}_i$, where H^{SER}_i is the enthalpy of the element i in its defined reference state at $298.15\,K$.

A.2.2 Random Substitutional Phases

Random substitutional models are used with phases* whose components can mix on any spatial position available to that phase (in a crystal structure, it is possible to think of lattice sites, for example). In general, the Gibbs energy G^{ϕ} of such a phase can be represented by

$$G^{\phi} = {}^{0}G + {}^{id}G^{\phi}_{m} + {}^{xs}G^{\phi}_{m} \tag{A.4}$$

where ${}^{0}G$ represents the contribution of the pure components of the phase to the total Gibbs energy, ${}^{id}G^{\phi}_{m}$ is the ideal mixing contribution (considering non-interaction components) and ${}^{xs}G^{\phi}_{m}$ represents any interaction between components within the phase.

Since there is no interaction energy between components in an ideal solution, the ideal mixing energy is only determined by the configurational entropy of the solution:

$${}^{id}G^{\phi}_{m} = RT \sum_{i} x^{\phi}_{i} \ln\left(x^{\phi}_{i}\right) \tag{A.5}$$

where x_i is the molar fraction of component i in phase ϕ.

*substitutional solid solutions, simple liquids, gas phase

In an ideal solution, ${}^{xs}G_m^{\phi} = 0$. In most cases, however, it is necessary to consider the energetic interactions between components within the phase. One of the first attempts to use a mathematical description for the excess Gibbs energy of a phase was that of Van Laar in 1908 [166]:

$$G_{mix}^{\phi,xs} = x_i x_j L_{ij} \tag{A.6}$$

where L_{ij} is the interaction parameter between components i and j of the solution. In general L_{ij} can be composition- (higher order terms are necessary) as well as temperature- (there is an excess entropy of mixing) dependent. In the case where there are more than two components and the higher order interactions become important, additional interaction parameters can be added to the expression for the Gibbs energy. The general expression for a random solution (in this case, a third order solution) is then given by:

$$G^{\phi} = \sum_i x_i^{\phi 0} G_i^{\phi} + RT \sum_i x_i^{\phi} \ln\left(x_i^{\phi}\right) + \sum_i^{n-1} \sum_{j=i+1}^{n} x_i^{\phi} x_j^{\phi} L_{i,j}^{\phi} + x_i^{\phi} x_{j\neq i\neq k}^{\phi} x_{k\neq j\neq i}^{\phi} L_{i,j,k}^{\phi} \tag{A.7}$$

where L_{ij}^{ϕ} can be also a function of temperature and composition:

$$L_{ij}^{\phi} = \sum_k \left\{ {}^k a + {}^k b \cdot T \right\} \left(x_i^{\phi} - x_j^{\phi}\right)^k \tag{A.8}$$

In cases when the Gibbs free energy of a ternary system is highly asymmetrical*, it may be necessary to have a ternary interaction parameter with greater degrees of freedom if an accurate description of the energy of the ternary system is desired. In order to do this, the ternary term appearing in Eq. A.7 would be given by:

$${}^3G^{\phi} = x_i x_j x_k \left(v_i L_{i,jk}^{\phi} + v_j L_{j,ik}^{\phi} + v_k L_{k,ij}^{\phi} \right) \tag{A.9}$$

where v_i is given by:

$$v_i = x_i + \frac{1 - x_i - x_j - x_k}{3} \tag{A.10}$$

Note that v_i is identical to x_i when the system is a ternary. In the case of a higher-order system that is not the case. Additionally, the sum over all v_i is unity in all cases, while the sum of x_i is only unity in the case of a ternary system.

Perhaps the best example of a random substitutional phase is a metallic liquid solution. An important random solution phase assessed in this work, for example, is the liquid $Ag - Cu - Ti$ phase. This phase has very interesting properties (the existence of a ternary miscibility gap) that define clear operational limits for ceramic/metal

*Take for example a case were two of the binary subsystems have strong negative deviations from ideal behavior while the third sub-system has strong positive deviations.

joining techniques using such alloys.

A.2.3 The Sublattice Model

Although the random solution model described in A.2.2 is very useful and widely applicable, it has some limitations, for example:

- This model cannot take into account preferential site occupation in intermetallic phases *.
- The random solution model does not constitute a realistic representation of solid interstitial solutions since interstitial atoms occupy clearly distinct sites in the solution†.
- The complex behavior of ionic melts, where charge neutrality must be taken into account as a further constraint to the system, cannot be described using random solution models‡.

The limitations listed above come from the fact that, in the random solution formalism, all regions of space must be treated equivalently. It is obvious that to overcome its limitations, it is necessary to expand this model so unlike types of sites within a phase are treated differently§. Such a model was developed some 20 years ago, by Sundman and Ågren [167]. This model, appropriately called the *sublattice model*, relies on the explicit differentiation of the structural components within a phase (sublattices)¶. Thanks to its practical success, this formalism has become one of the principal methods used to describe a wide range of phases with diverse chemical and physical behaviors [21]. Its flexibility allows its application to the description of phases with widely differing behavior, from solid interstitial solution phases to ionic liquid solutions, to phases undergoing order/disorder transformations, and so forth.

Fig. A-1 shows an example of a crystalline phase having two distinct sublattices. In this particular example, we have four species‖ (A,B,C,D), with species A and B allowed to occupy only the body-centered sites while species C and D occupy the corner sites. Note that although in the figure we can distinguish between species in each sublattice, a central characteristic of the sublattice model is that the species within

*See for example the Wagner-Shottky model used in Hari Kumar et al. [30] to describe the $CuTi$ and Cu_4Ti phases in the $Cu-Ti$ system.

†For example the β phase in the $Zr-O$ system [52]. In this phase, oxygen occupies the interstitial sites of the BCC structure.

‡The two-sublattice ionic liquid model has been used to describe the liquid phase in the $Zr-O$ system assessed by Arroyave et al. [52].

§The distinction among different sites can be artificial, like in an ionic melt or natural, like in an interstitial solution.

¶It is important to note, however, that this model is phenomenological in nature and it does not attempt to represent structural relationships between the different sublattices present in any given phase (crystalline or non-crystalline).

‖These species could be elements, stable molecules, metastable complexes, etc.

each sublattice behave as if they were in a random solution, that is, they randomly mix. Using the sublattice model, it is possible to describe chemical interactions between species located in different sublattices (through the *Compound Energy Method* [168]) as well as within the same sublattice. Therefore it is possible to represent the behavior of complex phases.

In the remainder of this subsection, a brief description of the mathematical formalism of the general *Sublattice Model* is presented. The original description of this model was published by Sundman and Ågren [167]. A general overview of the application of the *Sublattice Model* to the description of several types of solutions is given in Saunders and Miodownik [21].

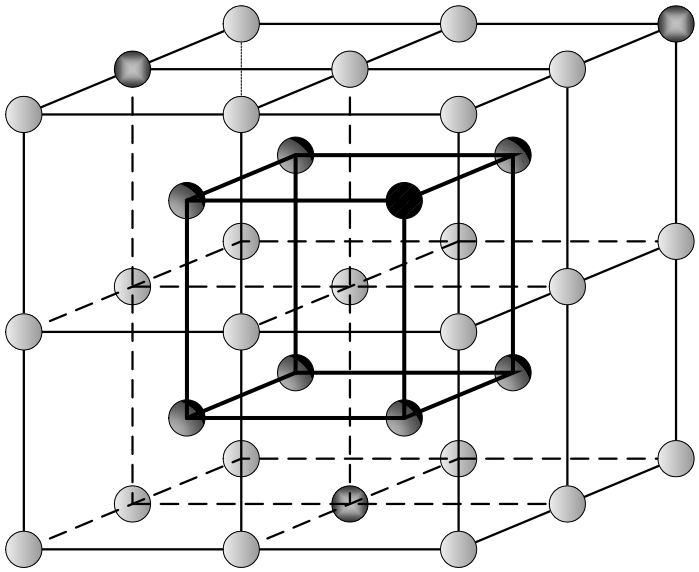

Figure A-1: Body-centered crystalline structure. Observe that there is preferential occupation of atoms in two distinct sites: 'blue' (A) and 'black' (B) species in body-centered sites, 'red' (C) and 'green' (D) species in corner sites.

A.2.3.1 Mathematical Description of Sublattice Model

Perhaps one of the most important things to understand about the sublattice formalism is its notation. We can take, as an example, the phase depicted in Fig. A-1. In the sublattice formalism, such a phase is described as

$$(A, B)_{N^1} (C, D)_{N^2} \tag{A.11}$$

Eq. A.11 can be understood as follows: the phase has two distinct sublattices (or clearly defined crystallographic positions). The number of sites in sublattices 1 and 2 are N^1 and N^2, respectively. The first sublattice is occupied by species A and B. The second sublattice is occupied by species C and D.

The occupancy of each sublattice can be defined using the site-fraction matrix Y defined by Sundman and Ågren [167]:

$$Y = \begin{matrix} y_A^1 & y_B^1 & y_C^1 & y_D^1 \\ y_A^2 & y_B^2 & y_C^2 & y_D^2 \end{matrix} \tag{A.12}$$

where y_i^s corresponds to the site fraction of species i (n_i^s is the mole number of i in sublattice s) in sublattice s (N^s is the total number of moles in sublattice s) ($y_i^s = {}^{n_i^s}/_{N^s}$). Note that for this particular case $y_C^1 = y_D^1 = y_A^2 = y_B^2 = 0$.

Following a description analogous to that of a random solution (see Eq. A.4), the Gibbs energy of a sublattice phase is given by:

$$G^\phi = {}^{ref}G_m^\phi + {}^{id}G_m^\phi + {}^{xs}G_m^\phi \tag{A.13}$$

The first term ${}^{ref}G_m^\phi$ corresponds to the Gibbs energy reference state. This reference state corresponds to the state at which there is complete site occupation by only one of the species in each sublattice:

$${}^{ref}G^\phi = y_A^1 y_C^2 \cdot {}^0G^\phi_{(A)_1(C)_1} + y_A^1 y_D^2 \cdot {}^0G^\phi_{(A)_1(D)_1} + y_B^1 y_C^2 \cdot {}^0G^\phi_{(B)_1(C)_1} + y_B^1 y_D^2 \cdot {}^0G^\phi_{(B)_1(D)_1} \tag{A.14}$$

where ${}^0G^\phi_{(i)_1(j)_1}$ corresponds to the Gibbs free energy of the reference compound ij in the crystal structure ϕ analogous to the expression found in Eq. A.3. The Gibbs free energy of the reference compound represents a chemical interaction between atoms occupying different sites within the structure. Eq. A.14 can be generalized using:

$${}^{ref}G^\phi = \sum_I P_{I0}\left(Y\right) \cdot {}^0G^\phi_{I0} \tag{A.15}$$

where $P_{I0}\left(Y\right)$ corresponds to the zeroth-order product of site fractions (see Eq. A.12) corresponding to each of the reference compounds [167].

As noted above, a central aspect of the sublattice model is the fact that the species within each sublattice behave as if they were part of a random solution. Therefore, the ideal contribution to the total Gibbs free energy of a sublattice phase is given by the configurational entropy contribution of each of the sublattices (see Eq. A.5):

$${}^{id}G_m^\phi = RT \cdot \sum_{s=1,2} N^s \sum_{i=A,B,C,D} y_i^s \ln\left(y_i^s\right) \tag{A.16}$$

The excess Gibbs energy of a sublattice phase is given by the chemical interactions between species within each of the sublattices. In general, we can think that chemical interactions among species within the same sublattice arise by the fact that such species have nearest neighbors in the sublattice they are in[169]. Without any interaction energy, the solutions within each sublattice are ideal.

For the phase depicted in Fig. A-1, we can assume for example that there is a non-ideal chemical interaction between species C and D in the second sublattice when A or B are present in the first sublattice. For this situation, the excess Gibbs energy is given by:

$$^{ex}G_m^{\phi} = y_A^1 y_C^2 y_D^2 L_{A:C,D}^{\phi} + y_B^1 y_C^2 y_D^2 L_{B:C,D}^{\phi} \tag{A.17}$$

where $L_{A:C,D}^{\phi}$ can be a function of both temperature and composition, as in Eq. A.8. This case can be generalized using the equation:

$$^{ex}G_m^{\phi} = \sum_{Z>0} \sum_{IZ} P_{IZ}(Y) \cdot L_{IZ} \tag{A.18}$$

where Z is the order of the array necessary to define the interactions of arrangement I. For example, the interaction $A:C$ can be defined by a zeroth-order array and defines the Gibbs energy of compound $(A)_1 (C)_1$. P_{I0} will be given then by $y_A^1 y_C^2$. When the interaction arrangement I is $A:C,D$, then we are defining a chemical interaction between species C and D in the second sublattice, while A is present in the first one ($L_{A:C,D}^{\phi}$). In this case P_{IZ} would be $P_{(A):(C,D)1}$ or $y_A^1 y_C^2 y_D^2$.

Using Eq. A.14, Eq. A.16 and Eq. A.14, we have an expression for the total Gibbs energy for the phase $(A,B)_1 (C,D)_1$:

$$\begin{aligned} G^{\phi} = {} & y_A^1 y_C^2 {}^0G_{A:C}^{\phi} + y_A^1 y_D^2 {}^0G_{A:D}^{\phi} + y_B^1 y_C^2 {}^0G_{B:C}^{\phi} + y_B^1 y_D^2 {}^0G_{B:D}^{\phi} \\ & + RT \cdot \sum_{s=1,2} N^s \sum_{i=A,B,C,D} y_i^s \ln(y_i^s) \\ & + y_A^1 y_C^2 y_D^2 L_{A:C,D}^{\phi} + y_B^1 y_C^2 y_D^2 L_{B:C,D}^{\phi} \end{aligned} \tag{A.19}$$

We can generalize the expression for any sublattice phase, with any number of components and sublattices as [167]:

$$G^{\phi} = \sum_{I0} P_{I0}(Y) \cdot {}^0G_{I0}^{\phi} + RT \sum_s N^s \sum_i y_i^s \ln(y_i^s) + \sum_{Z>0} \sum_{IZ} P_{IZ}(Y) \cdot L_{IZ} \tag{A.20}$$

In order to make equilibrium calculations it is important to be able to derive mathematical expressions for partial quantities (i.e. chemical potentials). Using the

methodology described in Hillert [168, pp. 70-72], it is possible to obtain, from the extensive quantity $A(T, P, N_i)$ the partial quantity $A_j \equiv (\partial A/\partial N_j)_{T,P,N_k}$. Using $A = N \cdot A_m$, we have:

$$A_j = A_m + \frac{\partial A_m}{\partial x_j} - \sum x_i \frac{\partial A_m}{\partial x_i} \tag{A.21}$$

If one were to obtain a mathematical expression for the chemical potential of A in the phase $(A)\,(A, C)$, given the fact that the total Gibbs energy expression for this phase would be:

$$\begin{aligned} G = {} & y_A^2\,{}^0G_{A:A} + y_B^2\,{}^0G_{A:B} + RT \cdot [y_A^2 \ln(y_A^2) + y_B^2 \ln(y_B^2)] \\ & + y_A^2 y_B^2\,{}^0L_{A:A,B} \end{aligned} \tag{A.22}$$

For this particular case, the chemical potential of A, μ_A, is equivalent to the partial quantity $G_{A:A}$ *. Using Eq. A.21, the following expression is obtained:

$$\mu_A = G_{A:A} = {}^0G_{A:A} + RT \cdot y_A^2 \ln\left(y_A^2\right) + y_B^2\,{}^0L_{A:A,B} \tag{A.23}$$

A.2.4 Applications of the Sublattice Model

As noted above, the sublattice model is very powerful and versatile, as it can be applied to a broad range of phases' types. A good example of the application of the sublattice model to intermetallic phases is the description of the MTi_2 phases in the assessment of the $Cu - Ti$ system by Hari Kumar et al. [30]. In this system the phases $CuTi_2$ and $AgTi_2$ ($MoSi_2$ is their prototype structure) form a solid solution with each other and therefore it is reasonable to assume that they can both be represented by the same phase:

$$(Ag, Cu)_1\,(Ti)_2 \tag{A.24}$$

According to Eq. A.24, Ag and Cu occupy the first sublattice of the structure $MoSi_2$. Both elements would form a random solution in the first sublattice, with Ti always present in the second sublattice. The Gibbs energy of this phase would be given by:

$$\begin{aligned} G^{MTi_2} = {} & y_{Ag}^1\,{}^0G_{Ag:Ti}^{MTi_2} + y_{Cu}^1\,{}^0G_{Cu:Ti}^{MTi_2} \\ & + RT \cdot \left\{y_{Ag}^1 \ln\left(y_{Ag}^1\right) + y_{Cu}^1 \ln\left(y_{Cu}^1\right)\right\} \\ & + y_{Ag}^1 y_{Cu}^1 \cdot L_{Ag,Cu:Ti}^{MTi_2} \end{aligned} \tag{A.25}$$

*Note that, in the sublattice formalism, it is not possible to directly define a chemical potential for a pure element i. It should be derived (when possible) from the partial Gibbs energy of the components in the phase.

where ${}^0G^{MTi_2}_{Ag:Ti}$ corresponds to the Gibbs energy of the end-member $AgTi_2$ and ${}^0G^{MTi_2}_{Cu:Ti}$ is the Gibbs energy of the pure $CuTi_2$ compound. This expression can be further simplified using the constraint $y^1_{Cu} + y^1_{Ag} = 1$

Another example of an application of the sublattice model is the description of interstitial solid solutions. In these phases, small elements such as O, C, N, H occupy the interstitial sites of the structure. The system $Zr - O$ presents two such phases: β (bcc) and α (hcp). In these phases, oxygen occupies the interstitial sites* and their description is given by:

$$(Zr)_1 (O, Va)_c \tag{A.26}$$

where c corresponds to the ratio between interstitial and substitutional sites in the structure. In this system, c has a value of 3 and 0.5 for the bcc and hcp phases, respectively. In order to properly describe this phase, it is necessary consider the presence of vacancies in the interstitial sites. The Gibbs energy of this phase can be represented using

$$\begin{aligned} G^{\beta,\gamma} = {} & y^2_{Va}\, {}^0G^{\alpha,\beta}_{Zr:Va} + y^2_O\, {}^0G^{\alpha,\beta}_{Zr:O} \\ & + c \cdot RT \cdot \left\{ y^2_O \ln\left(y^2_O\right) + y^2_{Va} \ln\left(y^2_{Va}\right) \right\} + y^2_O y^2_{Va} \cdot L^{\alpha,\beta}_{Zr:O,Va} \end{aligned} \tag{A.27}$$

The reference compounds for this phase would then be ${}^0G^{\beta,\gamma}_{Zr:Va}$ and ${}^0G^{\beta,\gamma}_{Zr:O}$. ${}^0G^{\beta,\gamma}_{Zr:Va}$ corresponds to the Gibbs energy of the pure bcc or hcp phases. ${}^0G^{\beta,\gamma}_{Zr:O}$ in turn corresponds to the Gibbs energy of the hypothetical compounds ZrO_3 or $ZrO_{0.5}$ which correspond to a state at which there is full occupation of oxygen atoms in the interstitial sites†. In this model, the L interaction parameters describe the chemical interaction between species within the same sublattice‡. The G Gibbs free energy expressions correspond to the chemical interactions between species belonging to different sublattices.

The power of the sublattice model can be best illustrated by considering what would happen if a third element, say Ti, was introduced into the system. In this case, the sublattice representation of the phase would be

$$(Ti, Zr)_1 (O, Va)_c \tag{A.28}$$

Providing there was already an expression for the total Gibbs energy of the $(Ti)_1 (O, Va)_c$ and $(Ti, Zr)_1 (Va)_c$ systems, the total Gibbs energy for the ternary system described in Eq. A.28 (see Section 4.5) would be given by:

*In interstitial solutions of group IV elements with small gaseous species such as oxygen, hydrogen and nitrogen, the gas atoms occupy the octahedral interstitial sites [58].

†Such full occupation is observed in the case of the hcp solid solution.

‡In this case, vacancies and oxygen interstitials.

$$
\begin{aligned}
G^{\beta,\gamma} = & y_{Zr}^1 y_{Va}^2 {}^0G_{Zr:Va}^{\alpha,\beta} + y_{Zr}^1 y_O^2 {}^0G_{Zr:O}^{\alpha,\beta} + y_{Ti}^1 y_{Va}^2 {}^0G_{Ti:Va}^{\alpha,\beta} + y_{Ti}^1 y_O^2 {}^0G_{Ti:O}^{\alpha,\beta} \\
& + RT \cdot \left[\left\{ y_{Ti}^1 \ln\left(y_{Ti}^1\right) + y_{Zr}^1 \ln\left(y_{Zr}^1\right) \right\} + c \left\{ y_O^2 \ln\left(y_O^2\right) + y_{Va}^2 \ln\left(y_{Va}^2\right) \right\} \right] \\
& + y_{Zr}^1 y_O^2 y_{Va}^2 \cdot L_{Zr:O,Va}^{\alpha,\beta} + y_{Ti}^1 y_O^2 y_{Va}^2 \cdot L_{Ti:O,Va}^{\alpha,\beta} \\
& + y_{Zr}^1 y_{Ti}^1 y_O^2 \cdot L_{Zr,Ti:O}^{\alpha,\beta} + y_{Ti}^1 y_{Ti}^1 y_{Va}^2 \cdot L_{Zr,Ti:Va}^{\alpha,\beta}
\end{aligned}
\tag{A.29}
$$

Finally, it is possible to use the sublattice formalism to describe the thermodynamic behavior of ionic melts [170]. This model considers two types of sublattices. The electropositive ions are contained in one of the sublattices, while electronegative ions and neutral atoms are located in the other sublattice. This model also considers the *hypothetical* presence of charged vacancies so the composition of the melt can deviate towards the pure melt of the element with electropositive character, maintaining, at all times, the neutrality condition of the liquid. The sublattice formula for this model is represented by:

$$
\left(C_i^{+v_i}\right)_P \left(A_j^{-v_j}, Va, B_k^0\right)_Q \tag{A.30}
$$

where C are the cations, A anions, Va (hypothetical) vacancies and B neutrals. The charges of the ions are represented by v_i and v_j. In order to maintain electroneutrality throughout the entire compositional range of the melt, it is necessary to vary the values for P and Q:

$$
\begin{aligned}
P &= \sum_j v_j y_{A_j} + Q y_{Va} \\
Q &= \sum_i v_i y_{C_i}
\end{aligned}
\tag{A.31}
$$

From Eq. A.31 it is obvious that the *hypothetical* vacancies will have an induced (negative) charge of - $|Q|$. If neutral atoms in the anion sublattice are excluded and only one type of anion in the melt (for example oxygen) the Gibbs energy of this phase would be given by:

$$
\begin{aligned}
G = & \sum_i \sum_j y_{C_i} y_{A_i} {}^0G_{C_i:A_j} + Q y_{Va} \sum_i y_{C_i} {}^0G_{C_i} \\
& + RT \cdot \left[P \sum_i y_{C_i} \ln\left(y_{C_i}\right) + Q \left\{ \sum_j y_{A_j} \ln\left(y_{A_j}\right) + y_{Va} \ln\left(y_{Va}\right) \right\} \right] \\
& + \sum_{i_1} \sum_{i_2} \sum_j y_{i_1} y_{i_2} y_j L_{i_1,i_2:j} + \sum_{i_1} \sum_{i_2} y_{i_1} y_{i_2} y_{Va}^2 L_{i_1,i_2:Va} \\
& + \sum_i \sum_j y_i y_j y_{Va} L_{i:j,Va}
\end{aligned}
\tag{A.32}
$$

where ${}^0G_{C_i:A_j}$ is the Gibbs energy of formation for the corresponding compound and

${}^0G_{C_i}$ is the Gibbs energy of the pure liquid cation. The L interaction parameters, can be defined as:

- $L_{i_1,i_2:j}$ represents the interaction between cations i_1 and i_2 in the presence of a common anion; for example $L_{Zr^{+4},Ti^{+4}:O^{-2}}$ represents the interaction term in the (liquid) system $ZrO_2 - TiO_2$ (see Section 4.5).
- $L_{i_1,i_2:Va}$ represents interactions between metallic elements; for example $L_{Zr,Ti:Va}$ in the $Ti - Zr$ binary system.
- $L_{i_1:j,Va}$ represents interactions between an anion and the *hypothetical* vacancies in the presence of a cation i_1; for example $L_{Zr^{+4}:O^{-2},Va}$ (see Section 4.2).

An example of a phase assessed in this work would be the ionic liquid in the $Zr-O$ system (Section 4.2):

$$\left(Zr^{+4}\right)_{4-2y_O^{-2}}\left(O^{-2},Va\right)_4 \tag{A.33}$$

The Gibbs energy of this phase is given by:

$$\begin{aligned} G^{ionic} &= y_{Zr^{+4}}y_{O^{-2}}{}^0G_{(Zr^{+4})_2:(O^{-2})_4} + 4y_{Zr^{+4}}y_{Va^{-4}}{}^0G_{(Zr^{+4}):(Va^{-4})} \\ &+RT\cdot\left[\left(4-2y_{O^{-2}}\right)y_{Zr^{+4}}\ln\left(y_{Zr^{+4}}\right)\right] \\ &+RT\cdot\left[4\left\{y_{O^{-2}}\ln\left(y_{O^{-2}}\right)+y_{Va^{-4}}\ln\left(y_{Va^{-4}}\right)\right\}\right] \\ &+y_{Zr^{+4}}y_{O^{-2}}y_{Va^{-4}}L_{Zr^{+4}:O^{-2},Va^{-4}} \end{aligned} \tag{A.34}$$

Appendix B

Derivation of an expression for the Chemical Potential of an element i in a Sublattice Phase

In principle, the partial Gibbs energy with respect to a component i in a phase ϕ is equivalent to its chemical potential and is defined as:

$$G_i = \mu\left(i\right) \equiv \left.\frac{\partial G^{\phi}}{\partial n_i}\right)_{T,P.n_j} \tag{B.1}$$

In a phase that has sublattices, however, it is impossible to vary the content of one component alone, as Eq. B.1 requires, unless it is present in all the sublattices. This difficulty present in all phases with more than one sublattices can be overcome if one, instead of defining the chemical potential of an element, defines the chemical potential of a compound:

$$G_i j = \mu\left(ij\right) \equiv \left.\frac{\partial G^{\phi}}{\partial n_i j}\right)_{T,P.n_j k} \tag{B.2}$$

According to [167], it is possible to define the chemical potential of component $I0$:

$$\mu_{I0} = G^{\phi} + \sum_{s}\left(\frac{\partial G^{\phi}}{\partial y_i^s} - \sum_{j} y_j^s \frac{\partial G^{\phi}}{\partial y_j^s}\right) \tag{B.3}$$

The second term in Eq. B.3 corresponds to the sum of the partial derivatives of the expression of the Gibbs energy of the phase with respect to the site fractions of the elements present in each of the compound's sublattice. The third term corresponds to all the partial derivatives of the Gibbs free energy with respect to the site fraction of all the components of the phase in all the sublattices.

As a more concrete example, it is possible to use the model $(A)_a (B,C)_b$ to calculate the chemical potential of compound $(A)_a (B)_b$:

$$\mu_{A_aB_b} = G^\phi + \frac{\partial G^\phi}{\partial y_A} + \frac{\partial G^\phi}{\partial y_B} - y_A \frac{\partial G^\phi}{\partial y_A} - y_B \frac{\partial G^\phi}{\partial y_B} - y_C \frac{\partial G^\phi}{\partial y_C} \tag{B.4}$$

Due to the stoichiometry constrain, it is not possible to define a chemical potential for element A, as it is not present in all the sublattices of phase ϕ. However, the chemical potential of the compounds in phase ϕ and the chemical potential of the elements in phase ϕ are related through:

$$\begin{aligned} \mu_{A_aB_b} &= a\mu_A + b\mu_B \\ \mu_{A_aC_b} &= a\mu_A + b\mu_C \end{aligned} \tag{B.5}$$

According to Eq. B.5, the chemical potential of B can be obtained using a linear combination of the chemical potentials of the components A_aB_b and A_aC_b:

$$\begin{aligned} \mu_{A_aB_b} - \mu_{A_aC_b} &= a\mu_A + b\mu_B - a\mu_A + b\mu_C \\ \mu_B &= \tfrac{1}{b} \cdot (\mu_{A_aB_b} - \mu_{A_aC_b} - b\mu_C) \end{aligned} \tag{B.6}$$

Thus, the chemical potential of B can be defined with respect to that of C. C is any constituent of the sublattice. If the sublattice in question has vacancies, and it is assumed that such point defects are at thermal equilibrium, it can be considered that their chemical potential is zero and the expression for the chemical potential is greatly simplified.

Appendix C

Model Parameters

In this appendix, the model parameters for the phases that were thermodynamically assessed in Chapter 3 and Chapter 4 will be presented. The expressions for the Gibbs free energy of formation of the different phases of the pure components will not be included, as they are available in the SGTE thermodynamic databases. Unless otherwise stated, the Gibbs free energy of formation of stoichiometric compounds is also taken from the SGTE thermodynamic databases. Parameters marked with $\diamond$ were obtained in this work. For a detailed description of the *CALPHAD* models used in the optimization, refer to Chapter A. Details of the assessments are available in Chapter 3 and Chapter 4.

Table C.1: Thermodynamic parameters for the *ionic liquid* phase.

$(Ag^{+1}, Cu^{+1}, Cu^{+2}, Ti^{+2}, Ti^{+3}, Ti^{+4})_P (O^{-2}, Va)_Q$	
$Ag - Cu$ [29]	
${}^0L^{liq}_{Ag^{+1},Cu^{+1}:Va}$	$+17,534.6 - 4.45479T$
${}^1L^{liq}_{Ag^{+1},Cu^{+1}:Va}$	$+2,251.3 - 2.6733T$
${}^2L^{liq}_{Ag^{+1},Cu^{+1}:Va}$	$+492.7$
$Ag - Ti$	
${}^0L^{liq}_{Ag^{+1},Ti^{+2}:Va}$	$+25,632\diamond$
${}^1L^{liq}_{Ag^{+1},Ti^{+2}:Va}$	$-327\diamond$
$Cu - Ti$ [30]	
${}^0L^{liq}_{Cu^{+1},Ti^{+2}:Va}$	$-19,330 + 7.651T$
${}^1L^{liq}_{Cu^{+1},Ti^{+2}:Va}$	0

continued on next page

continued from previous page

$(Ag^{+1}, Cu^{+1}, Cu^{+2}, Ti^{+2}, Ti^{+3}, Ti^{+4})_P (O^{-2}, Va)_Q$	
${}^2L^{liq}_{Cu^{+1},Ti^{+2}:Va}$	$+9,382 - 5.448T$
$Ag - Cu - Ti$	
${}^0L^{liq}_{Ag^{+1},Cu^{+1},Ti^{+2}:Va}$	$+32,400\diamond$
$Cu - Zr$ [48]	
${}^0L^{liq}_{Cu^{+1},Zr^{+4}:Va}$	$-61,685.53 + 11.2924T$
${}^1L^{liq}_{Cu^{+1},Zr^{+4}:Va}$	$-8,830.66 + 5.04565T$
$Cu - Ti - Zr$ [26]	
${}^0L^{liq}_{Cu^{+1},Ti^{+2},Zr^{+4}:Va}$	$+23,828.5\diamond$
${}^1L^{liq}_{Cu^{+1},Ti^{+2},Zr^{+4}:Va}$	$-28,081.4\diamond$
${}^2L^{liq}_{Cu^{+1},Ti^{+2},Zr^{+4}:Va}$	$+23,828.5\diamond$
$Ti - Zr$ [49]	
${}^0L^{liq}_{Ti^{+2},Zr^{+4}:Va}$	-968
$Cu - O$ [71]	
${}^0G^{liq}_{Cu^{+2}:Va}$	${}^0G^{liq}_{Cu} + 600,000$
${}^0G^{liq}_{Cu^{+1}:O^{-2}}$	$3 \cdot GCU2OLIQ$
${}^0G^{liq}_{Cu^{+2}:O^{-2}}$	$4 \cdot GCU2OLIQ - 44,058 + 25T$
${}^0L^{liq}_{Cu^{+1}:O^{-2},Va}$	$+27,004 + 2.6T$
${}^1L^{liq}_{Cu^{+1}:O^{-2},Va}$	$-9,894 + 5.73T$
${}^2L^{liq}_{Cu^{+1}:O^{-2},Va}$	$20,462 - 9.8T$
${}^0L^{liq}_{Cu^{+1},Cu^{+2}:O^{-2}}$	$-6,879$
${}^2L^{liq}_{Cu^{+1},Cu^{+2}:O^{-2}}$	$8,000$
$Ti - O$ [34]	
${}^0G^{liq}_{Ti^{+3}:Va}$	${}^0G^{liq}_{Ti} + 2 \times 10^4$
${}^0G^{liq}_{Ti^{+4}:Va}$	${}^0G^{liq}_{Ti} + 4 \times 10^4$
${}^0G^{liq}_{Ti^{+2}:O^{-2}}$	$2 \cdot GTIO_A + 41,2507 - 201.62T$
${}^0G^{liq}_{Ti^{+3}:O^{-2}}$	$GTI2O3 + 190,919 - 71.49T$
${}^0G^{liq}_{Ti^{+4}:O^{-2}}$	$2 \cdot GTIO2 + 178,003 - 62.4769T$

continued on next page

continued from previous page	
$(Ag^{+1}, Cu^{+1}, Cu^{+2}, Ti^{+2}, Ti^{+3}, Ti^{+4})_P (O^{-2}, Va)_Q$	
${}^0L^{liq}_{Ti^{+2}:O^{-2},Va}$	$-249,324 + 112.42T$
$Zr - O$ [52]	
${}^0G^{liq}_{Zr^{+4}:O^{-2}}$	$2 \cdot GZRO2A + 198,026 - 71.62T\diamond$
${}^0L^{liq}_{Zr^{+4}:O^{-2},Va}$	$+136,748 - 67.01T\diamond$
${}^1L^{liq}_{Zr^{+4}:O^{-2},Va}$	$+40,050\diamond$
$Ti - Zr - O\diamond$	
${}^0L^{liq}_{Ti^{+4},Zr^{+4}:O^{-2}}$	$-105,027\diamond$
${}^1L^{liq}_{Ti^{+4},Zr^{+4}:O^{-2}}$	$+39,985\diamond$
${}^0L^{liq}_{Ti^{+4},Zr^{+4}:O^{-2},Va}$	$-30,010\diamond$
${}^1L^{liq}_{Ti^{+4},Zr^{+4}:O^{-2},Va}$	$+49,950\diamond$

Table C.2: Thermodynamic parameters for the *bcc* phase.

$(Ag, Cu, Ti, Zr)(O, Va)_3$	
$Ag - Cu$ [29]	
${}^0L^{bcc}_{Ag,Cu:Va}$	$35,000 - 8T$
$Ag - Ti\diamond$	
${}^0L^{bcc}_{Ag,Ti:Va}$	$22,900 + 0.5T\diamond$
${}^1L^{bcc}_{Ag,Ti:Va}$	$1,500\diamond$
$Cu - Ti$ [30]	
${}^0L^{bcc}_{Cu,Ti:Va}$	$3,389$
$Cu - Zr$ [48]	
${}^0L^{bcc}_{Cu,Zr:Va}$	$-7,381.13$
$Ti - Zr$ [49]	
${}^0L^{bcc}_{Ti,Zr:Va}$	$-4,346 + 5.489T$
$Cu - Ti - Zr$ [26]	
${}^0L^{bcc}_{Cu,Ti,Zr:Va}$	$-12,000\diamond$
continued on next page	

continued from previous page	
$(Ag, Cu, Ti, Zr)\,(O, Va)_3$	
$Cu - O\diamond$	
${}^0G^{bcc}_{Cu:O}$	$+1 \times 10^6 + 3 \cdot G^{HSER}_O + G^{HSER}_{Cu}\diamond$
$Ti - O$ [34]	
${}^0G^{bcc}_{Ti:O}$	$-4 \times 10^5 + 3 \cdot G^{HSER}_O + G^{HSER}_{Ti}$
${}^0L^{bcc}_{Ti:O,Va}$	$-1,207,294 + 274.32T$
$Zr - O$ [52]	
${}^0G^{bcc}_{Zr:O}$	$-405,010 + 3 \cdot G^{HSER}_O + G^{HSER}_{Zr}\diamond$
${}^0L^{bcc}_{Zr:O,Va}$	$-1,237,630 + 278.01T\diamond$
$Ti - Zr - O\diamond$	
${}^0L^{bcc}_{Ti,Zr:O}$	$-866,900 + 329T\diamond$
${}^1L^{bcc}_{Ti,Zr:O}$	$-250,000 + 146T\diamond$

Table C.3: Thermodynamic parameters for the fcc phase.

$(Ag, Cu, Ti, Zr)\,(O, Va)$	
$Ag - Cu$ [29]	
${}^0L^{fcc}_{Ag,Cu:Va}$	$+33,819 - 8.124T$
${}^1L^{fcc}_{Ag,Cu:Va}$	$-5,601.9 + 1.32997T$
$Ag - Ti\diamond$	
${}^0L^{fcc}_{Ag,Ti:Va}$	$23,405\diamond$
$Cu - Ti$ [30]	
${}^0L^{fcc}_{Cu,Ti:Va}$	$-9,882$
${}^0L^{fcc}_{Cu,Ti:Va}$	$15,777$
$Cu - Zr$ [48]	
${}^0L^{fcc}_{Cu,Zr:Va}$	$+2,233$
$Ti - Zr$ [49]	
continued on next page	

continued from previous page	
$(Ag, Cu, Ti, Zr)\,(O, Va)$	
${}^{0}L^{fcc}_{Ti,Zr:Va}$	$-4,346 + 5.489T$
$Cu - Ti - Zr$ [26]	
${}^{0}L^{fcc}_{Cu,Ti,Zr:Va}$	$0\diamond$
$Cu - O\diamond$	
${}^{0}G^{fcc}_{Cu:O}$	$+1 \times 10^{6} + G^{HSER}_{Cu} + G^{HSER}_{O}\diamond$
${}^{0}L^{fcc}_{Cu:O,Va}$	$-1,017,730 + 29.6T\diamond$
$Ti - O$ [34]	
${}^{0}G^{fcc}_{Ti:O}$	$+59741 + GTIO_{A}$
${}^{0}L^{fcc}_{Ti:O,Va}$	$-11,628 + 4.99T$
$Zr - O$ [52]	
${}^{0}G^{fcc}_{Zr:O}$	N/A
${}^{0}L^{fcc}_{Zr:O,Va}$	N/A

Table C.4: Thermodynamic parameters for the *hcp* phase.

$(Ag, Cu, Ti, Zr)\,(O, Va)_{0.5}$	
$Ag - Cu$ [29]	
${}^{0}L^{hcp}_{Ag,Cu:Va}$	$35,000 - 8T$
$Ag - Ti\diamond$	
${}^{0}L^{hcp}_{Ag,Ti:Va}$	$50,050\diamond$
${}^{1}L^{hcp}_{Ag,Ti:Va}$	$27,000\diamond$
$Cu - Ti$ [30]	
${}^{0}L^{hcp}_{Cu,Ti:Va}$	$16,334$
$Cu - Zr$ [48]	
${}^{0}L^{hcp}_{Cu,Zr:Va}$	$+11,337$
$Ti - Zr$ [49]	
continued on next page	

continued from previous page	
$(Ag, Cu, Ti, Zr)\,(O, Va)_{0.5}$	
${}^{0}L^{hcp}_{Ti,Zr:Va}$	$+5,133$
$Cu-Ti-Zr$ [26]	
${}^{0}L^{hcp}_{Cu,Ti,Zr:Va}$	$0\diamond$
$Cu-O\diamond$	
${}^{0}G^{hcp}_{Cu:O}$	$+1\times10^{6}+G^{HSER}_{Cu}+0.5\cdot G^{HSER}_{O}\diamond$
$Ti-O$ [34]	
${}^{0}G^{hcp}_{Ti:O}$	$-260,898+33.86T+G^{HSER}_{Ti}+0.5\cdot G^{HSER}_{O}$
${}^{0}L^{hcp}_{Ti:O,Va}$	$-11,628+4.99T$
$Zr-O$ [52]	
${}^{0}G^{hcp}_{Zr:O}$	$-286,672+43.99T+G^{HSER}_{Zr}+0.5\cdot G^{HSER}_{O}\diamond$
${}^{0}L^{hcp}_{Zr:O,Va}$	$-40,056+19.01T\diamond$
${}^{1}L^{hcp}_{Zr:O,Va}$	$-9,995\diamond$
$Ti-Zr-O\diamond$	
${}^{0}L^{hcp}_{Ti,Zr:O}$	$+20,000\diamond$
${}^{1}L^{hcp}_{Ti,Zr:O}$	$118,963-77.7T\diamond$
${}^{0}L^{hcp}_{Ti,Zr:O,Va}$	$-25,000\diamond$

Table C.5: Thermodynamic parameters for the $CuTi$ phase. $Cu-Ti$ parameters taken from [30]

$(Ag, Cu, Ti)\,(Ag, Cu, Ti)$,$*=Ag, Cu, Ti$	
${}^{0}G^{CuTi}_{Cu:Cu}$	$+10,000+2\cdot G^{HSER}_{Cu}$
${}^{0}G^{CuTi}_{Ti:Cu}$	$+42,412-6.544T+G^{HSER}_{Cu}+G^{HSER}_{Ti}$
${}^{0}G^{CuTi}_{Cu:Ti}$	$-22,412+6.544T+G^{HSER}_{Cu}+G^{HSER}_{Ti}$
${}^{0}G^{CuTi}_{Ti:Ti}$	$+10,000+2\cdot G^{HSER}_{Ti}$
${}^{0}G^{CuTi}_{Ag:Ag}$	$+10,000+2\cdot G^{HSER}_{Ag}\diamond$
${}^{0}G^{CuTi}_{Ti:Ag}$	$+24,080-1.32T+G^{HSER}_{Ag}+G^{HSER}_{Ti}\diamond$
continued on next page	

continued from previous page	
$(Ag, Cu, Ti)\,(Ag, Cu, Ti), * = Ag, Cu, Ti$	
${}^{0}G^{CuTi}_{Ag:Ti}$	$-4,080 + 1.32T + G^{HSER}_{Ag} + G^{HSER}_{Ti}\diamond$
${}^{0}G^{CuTi}_{Cu:Ag}$	$25,000 + G^{HSER}_{Ag} + G^{HSER}_{Cu}\diamond$
${}^{0}G^{CuTi}_{Ag:Cu}$	$25,000 + G^{HSER}_{Ag} + G^{HSER}_{Cu}\diamond$
${}^{0}L^{CuTi}_{Cu,Ti:*}$	$15,419$
${}^{0}L^{CuTi}_{*:Cu,Ti}$	$15,578$
${}^{0}L^{CuTi}_{Ag,Ti:*}$	$23,000\diamond$
${}^{0}L^{CuTi}_{*:Ag,Ti}$	$23,000\diamond$
${}^{0}L^{CuTi}_{Cu,Ag:Ag}$	$50,000\diamond$
${}^{0}L^{CuTi}_{Cu,Ag:Cu}$	$50,000\diamond$
${}^{0}L^{CuTi}_{Cu,Ag:Ti}$	$21,000\diamond$
${}^{1}L^{CuTi}_{Cu,Ag:Cu}$	$3,500\diamond$
${}^{0}L^{CuTi}_{*:Cu,Ag}$	$50,000\diamond$

Table C.6: Thermodynamic parameters for the Cu_4Ti phase. $Cu - Ti$ parameters taken from [30]

$(Cu, Ti)_4\,(Cu, Ti)$	
${}^{0}G^{Cu_4Ti}_{Cu:Cu}$	$+25,000 + 5 \cdot G^{HSER}_{Cu}$
${}^{0}G^{Cu_4Ti}_{Ti:Cu}$	$80,000 - 11.693T + G^{HSER}_{Cu} + 4 \cdot G^{HSER}_{Ti}$
${}^{0}G^{Cu_4Ti}_{Cu:Ti}$	$-30,055 + 11.693T + 4 \cdot G^{HSER}_{Cu} + G^{HSER}_{Ti}$
${}^{0}G^{Cu_4Ti}_{Ti:Ti}$	$+25,000 + 5 \cdot G^{HSER}_{Ti}$
${}^{0}L^{CuTi}_{Cu,Ti:Cu}$	$17,089$
${}^{0}L^{CuTi}_{Cu,Ti:Ti}$	$17,089$
${}^{0}L^{CuTi}_{Cu:Cu,Ti}$	$-15,767$
${}^{0}L^{CuTi}_{Ti:Cu,Ti}$	$-15,767$

Table C.7: Thermodynamic parameters for the CuM_2 phase. $Cu-Ti$ parameters taken from [30]. $Cu-Zr$ parameters taken from [48]

$(Ag, Cu)\,(Ti, Zr)$	
${}^0G^{CuM_2}_{Cu:Ti}$	$-36,393 + 14.064T + G^{HSER}_{Cu} + 2 \cdot G^{HSER}_{Ti}$
${}^0G^{CuM_2}_{Ag:Ti}$	$-8,325 + 3.3T + G^{HSER}_{Ag} + 2 \cdot G^{HSER}_{Ti}\diamond$
${}^0G^{CuM_2}_{Cu:Zr}$	$-43,904 + 5.1905T + G^{HSER}_{Cu} + 2 \cdot G^{HSER}_{Zr}$
${}^0G^{CuM_2}_{Ag:Zr}$	$-15,000 + 2.6T + G^{HSER}_{Ag} + 2 \cdot G^{HSER}_{Zr}\diamond$
${}^0L^{CuM_2}_{Ag,Cu:Ti}$	$14,500\diamond$
${}^0L^{CuM_2}_{Cu:Ti,Zr}$	$+30,250\diamond$
${}^1L^{CuM_2}_{Cu:Ti,Zr}$	$-6,205\diamond$
${}^2L^{CuM_2}_{Cu:Ti,Zr}$	$+1,028\diamond$

Table C.8: Thermodynamic parameters for stoichiometric intermetallic compounds.

Stoichiometric intermetallics	
$Cu-Ti$ [30]	
${}^0G^{Cu_2Ti}_{Cu:Ti}$	$-17,628 + 2 \cdot G^{HSER}_{Cu} + G^{HSER}_{Ti}$
${}^0G^{Cu_3Ti_2}_{Cu:Ti}$	$-46245 + 10.86T + 3 \cdot G^{HSER}_{Cu} + 2 \cdot G^{HSER}_{Ti}$
${}^0G^{Cu_4Ti_3}_{Cu:Ti}$	$-68,236 + 15.946T + 4 \cdot G^{HSER}_{Cu} + 3 \cdot G^{HSER}_{Ti}$
$Cu-Zr$ [48]	
${}^0G^{CuZr}_{Cu:Zr}$	$-2.01 \times 10^{+4} - 7.63196T + G^{HSER}_{Cu} + G^{HSER}_{Zr}$
${}^0G^{Cu_5Zr}_{Cu:Zr}$	$-6.1794 \times 10^{+4} + 5 \cdot G^{HSER}_{Cu} + G^{HSER}_{Zr}$
${}^0G^{Cu_8Zr_3}_{Cu:Zr}$	$-1.48063 \times 10^{+5} + 8 \cdot G^{HSER}_{Cu} + 3 \cdot G^{HSER}_{Zr}$
${}^0G^{Cu_{51}Zr_{14}}_{Cu:Zr}$	$-8.43412 \times 10^{+5} + 51 \cdot G^{HSER}_{Cu} + 14 \cdot G^{HSER}_{Zr}$
${}^0G^{Cu_{10}Zr_7}_{Cu:Zr}$	$-2.4174 \times 10^{+5} + 10 \cdot G^{HSER}_{Cu} + 7 \cdot G^{HSER}_{Zr}$
$Cu-Ti-Zr$ [26]	
${}^0G^{Cu_2TiZr}_{Cu:Ti:Zr}$	$-7.6377 \times 10^4 + 2.0206882 \times 10^1 T + 2 \cdot G^{HSER}_{Cu} + G^{HSER}_{Ti} + G^{HSER}_{Zr}$

Table C.9: Thermodynamic parameters for the γTiO phase. [34]

$(Ti^{+2}, Ti^{+3}, Va)\,(Ti^{0}, Va)\,(O^{-2})$	
${}^{0}G^{\gamma TiO}_{Ti^{+2}:Ti:O^{-2}}$	$-259,159 - 52.3756T + 2 \cdot G^{HSER}_{Ti} + G^{HSER}_{O}$
${}^{0}G^{\gamma TiO}_{Ti^{+3}:Ti:O^{-2}}$	$-247,865 + 2 \cdot G^{HSER}_{Ti} + G^{HSER}_{O}$
${}^{0}G^{\gamma TiO}_{Va:Ti:O^{-2}}$	$GTIO_A + 237,249 - 3.0751T$
${}^{0}G^{\gamma TiO}_{Ti^{+2}:Va:O^{-2}}$	$GTIO_A + 59,741 - 3.30751T$
${}^{0}G^{\gamma TiO}_{Ti^{+3}:Va:O^{-2}}$	$0.5 \cdot GTI2O3 + 45,030 + 6.2254T$
${}^{0}G^{\gamma TiO}_{Va:Va:O^{-2}}$	0
${}^{0}L^{\gamma TiO}_{Ti^{+2}:Ti,Va:O^{-2}}$	$-472,450 + 185.7944T$
${}^{0}L^{\gamma TiO}_{Ti^{+2},Ti^{+3}:Va:O^{-2}}$	$-173,492$

Table C.10: Thermodynamic parameters for the TiO_2 (rutile) phase. $Ti - O$ parameters from [34]

$(Ti^{+4}, Zr^{+4})\,(O^{-2}, Va^{-2})$	
${}^{0}G^{TiO_2}_{Ti^{+4}:O^{-2}}$	$+GTIO2 + 22,057.2$
${}^{0}G^{TiO_2}_{Zr^{+4}:O^{-2}}$	$+GZRO2A + 30,971 - 4.02T\diamond$
${}^{0}G^{TiO_2}_{Ti^{+4}:Va^{-2}}$	$+G^{Ti}_{HSER} + 40,000$
${}^{0}G^{TiO_2}_{Zr^{+4}:Va^{-2}}$	$+G^{Zr}_{HSER} + 40,000\diamond$
${}^{0}L^{TiO_2}_{Ti^{+4},Zr^{+4}:O^{-2}}$	$-18,625 + 4T\diamond$
${}^{0}L^{TiO_2}_{Ti^{+4}:O^{-2},Va^{-2}}$	$-150,570.4\diamond$

Table C.11: Thermodynamic parameters for the αZrO_2 phase [52].

$(Zr^{+4})\,(O^{-2}, Va^{-2})_2$	
${}^{0}G^{\alpha ZrO_2}_{Zr^{+4}:O^{-2}}$	$+GZRO2A\diamond$
continued on next page	

continued from previous page	
$(Zr^{+4})\,(O^{-2},Va^{-2})_2$	
${}^0G^{\alpha ZrO_2}_{Zr^{+4}:Va^{-2}}$	$+G^{Zr}_{HSER}+200,000\diamond$
${}^0L^{\alpha ZrO_2}_{Ti^{+4}:O^{-2},Va^{-2}}$	$-1,000\diamond$

Table C.12: Thermodynamic parameters for the βZrO_2 phase [52].

$(Ti^{+4},Zr^{+4})\,(O^{-2},Va^{-2})_2$	
${}^0G^{\beta ZrO_2}_{Ti^{+4}:O^{-2}}$	$+GTIO2+35,000\diamond$
${}^0G^{\beta ZrO_2}_{Zr^{+4}:O^{-2}}$	$+GZRO2A+5941-4.02T\diamond$
${}^0G^{\beta ZrO_2}_{Ti^{+4}:Va^{-2}}$	$+G^{HSER}_{Ti}+200,000\diamond$
${}^0G^{\beta ZrO_2}_{Zr^{+4}:Va^{-2}}$	$+G^{HSER}_{Zr}+200,000\diamond$
${}^0L^{\beta ZrO_2}_{Ti^{+4},Zr^{+4}:O^{-2}}$	$-15,000+15.01T\diamond$
${}^1L^{\beta ZrO_2}_{Ti^{+4},Zr^{+4}:O^{-2}}$	$+23,000\diamond$
${}^2L^{\beta ZrO_2}_{Ti^{+4},Zr^{+4}:O^{-2}}$	$-2,000-10T\diamond$
${}^0L^{\beta ZrO_2}_{Zr^{+4}:O^{-2},Va^{-2}}$	$-130,210+35.03T\diamond$
${}^1L^{\beta ZrO_2}_{Zr^{+4}:O^{-2},Va^{-2}}$	$-19,990\diamond$

Table C.13: Thermodynamic parameters for the γZrO_2 (rutile) phase [52].

$(Ti^{+4},Zr^{+4})\,(O^{-2},Va^{-2})_2$	
${}^0G^{\gamma ZrO_2}_{Ti^{+4}:O^{-2}}$	$+GTIO2+35,000\diamond$
${}^0G^{\gamma ZrO_2}_{Zr^{+4}:O^{-2}}$	$+GZRO2A+11,986-6.309T\diamond$
${}^0G^{\gamma ZrO_2}_{Ti^{+4}:Va^{-2}}$	$+G^{HSER}_{Ti}+200,000\diamond$
${}^0G^{\gamma ZrO_2}_{Zr^{+4}:Va^{-2}}$	$+G^{HSER}_{Zr}+200,000\diamond$
${}^0L^{\gamma ZrO_2}_{Zr^{+4}:O^{-2},Va^{-2}}$	$-235,850+23T\diamond$
continued on next page	

continued from previous page	
$(Ti^{+4}, Zr^{+4})(O^{-2}, Va^{-2})_2$	
${}^1L^{\gamma ZrO_2}_{Zr^{+4}:O^{-2},Va^{-2}}$	$-105,440\diamond$
${}^2L^{\gamma ZrO_2}_{Zr^{+4}:O^{-2},Va^{-2}}$	$+184,910\diamond$

Table C.14: Thermodynamic parameters for the $3-3$ M_6X compound.$\diamond$

$(Ti)_3(Cu)_2(Cu,Al)_1(Cu,Al)_1$	
${}^0G^{M_6X}_{Ti:Cu:Cu:O}$	$-655,832+141.67T\diamond$
${}^0G^{M_6X}_{Ti:Cu:Al:O}$	$-850,050+221T\diamond$
${}^0L^{M_6X}_{Ti:Cu:Cu,Al:O}$	$-25,000\diamond$

Table C.15: Thermodynamic parameters for stoichiometric oxides.

Stoichiometric oxides	
$Cu-O$ [71]	
${}^0G^{CuO}_{Cu:O}$	$+GCUO$
${}^0G^{Cu_2O}_{Cu:O}$	$+GCU2O$
$Ti-O$ [34]	
${}^0G^{\alpha TiO}_{Ti:O}$	$GTIO_A12,496+1.95751T$
${}^0G^{Ti_2O_3}_{Ti:O}$	$GTI2O3+19508-2.4214T$
${}^0G^{Ti_3O_2}_{Ti:O}$	$-1,064,478+178.6T+3\cdot G^{HSER}_{Ti}+2\cdot G^{HSER}_{O}$
${}^0G^{Ti_3O_5}_{Ti:O}$	$GTI3O5+15,000-T$
${}^0G^{Ti_4O_7}_{Ti:O}$	$GTI4O7+40T$
$Zr-O$ [52]	
${}^0G^{Zr_2O}_{Zr:O}$	$-650,000+145T+2\cdot G^{HSER}_{Zr}+G^{HSER}_{O}\diamond$
${}^0G^{Zr_3O}_{Ti:O}$	$-605,000+97T+3\cdot G^{HSER}_{Zr}+G^{HSER}_{O}\diamond$
continued on next page	

continued from previous page	
Stoichiometric oxides	
${}^0G^{Zr_6O}_{Ti:O}$	$-594,500 + 110.1T + 6 \cdot G^{HSER}_{Zr} + G^{HSER}_{O}\diamond$
$Ti - Zr - O\diamond$	
${}^0G^{ZrTi_2O_6}_{Zr:Ti:O}$	$GZrO2A + 2 \cdot GTIO2 - 7250 + 25T\diamond$
${}^0G^{ZrTiO_4}_{Zr:Ti:O}$	$GZrO2A + GTIO2 + 38493 - 20T\diamond$
$Cu - Ti - O\diamond$	
${}^0G^{Ti_4Cu_2O}_{Ti:Cu:O}$	$-631,814 + 116.51T + 4 \cdot G^{HSER}_{Ti} + 2 \cdot G^{HSER}_{Cu} + G^{HSER}_{O}$

Table C.16: Functions used in the models.

Name	Function	Range, K
$Cu - O$ functions [71]		
GCU2OLIQ	$-47734 + 148.5T - 28T\ln(T)$	N/A
GCUO	$172,735 + 291.78T - 49.03T\ln(T)$ $-3.47 \times 10^{-3}T^2 + \frac{390,000}{T}$	N/A
GCU2O	$193,230 + 360.057T - 66.26T\ln(T)$ $-7.96 \times 10^{-3}T^2 + \frac{374,000}{T}$	N/A
$Ti - O$ functions [34]		
$GTIO_A$	$-551,056.8 + 252.17T - 41.99T\ln(T) - 8.898 \times 10^{-3}T^2$ $+1.097 \times 10^{-8}T^3 + \frac{327,015}{T}$	N/A
GTI2O3	$-1,581,243 + 940.17T - 147.67T\ln(T) - 1.74 \times 10^{-3}T^2$ $-1.53 \times 10^{-10}T^3 + \frac{2,395,423.5}{T}$ $-159,0717.7 + 1012.15T - 156.9T\ln(T)$	470-2,115 2,115-3500
GTIO2	$-966,880.6 + 348.55T - 57.02T\ln(T) - 2.017 \times 10^{-2}T^2$ $+3.86 \times 10^{-6}T^3 + \frac{528,343}{T}$ $-974,253 + 461.2T - 74.519T\ln(T) - 1.356 \times 10^{-3}T^2$ $+2.102 \times 10^{-8}T^3 + \frac{1,126,927}{T}$ $-1,022,606 + 679.833T - 100.42T\ln(T)$	300-700 700-2,130 2,130-4,000
continued on next page		

continued from previous page		
Name	Function	Range, K
GTI3O5	$-2,514,503 + 1056.2T - 174.75T\ln(T) - 1.682 \times 10^{-2}T^2$	450-900
	$-1,772,107 - 6,305.1T + 882.36T\ln(T) - 6.808 \times 10^{-1}T^2$ $+7.767 \times 10^{-5}T^3 - \frac{96,994,950}{T}$	900-1,200
	$-2,514,675.5 + 1056.66T - 174.79T\ln(T) - 1.682 \times 10^{-2}T^2$	1,200-2,047
	$-2,566,064.8 + 1501.09T - 234.304T\ln(T)$	2,047-3,000
GTI4O7	$-3,510,274 + 1643.59T - 267.04T\ln(T) - 2.467 \times 10^{-2}T^2$ $+2.377 \times 10^{-6}T^3 + \frac{3,660,393.5}{T}$	500-1,000
	$-3,523,423.8 + 1791.65T - 288.799T\ln(T) - 8.51 \times 10^{-3}T^2$ $+1.118704 \times 10^{-7}T^3 + \frac{5,171,905}{T}$	1,000-1,950
	$-3,642,234.5 + 2439.22T - 368.19T\ln(T)$	1,950-4,000
$Zr - O$ functions [52]		
GZRO2A	$-1,125,582 + 417.51T - 68.328T\ln(T) - 4.542 \times 10^{-3}T^2$ $+1.724 \times 10^{-10}T^3 + \frac{671,863}{T}$	298-1,445
	$-1,129,291 + 484.94T - 78.1T\ln(T) - 1.0845 \times 10^{-16}T^2$ $+7.815 \times 10^{-21}T^3 - \frac{7.623 \times 10^{-8}}{T}$	1,445-2620
	$-1,134,269 + 501.79T - 80T\ln(T) - 2.0127 \times 10^{-14}T^2$ $+9.192 \times 10^{-19}T^3 - \frac{5.1278 \times 10^{-5}}{T}$	2,620-2983
	$-1,193,929 + 681.804T - 100T\ln(T) + 3.041 \times 10^{-16}T^2$ $-8.75 \times 10^{-21}T^3 + \frac{2.467 \times 10^{-6}}{T}$	2,983-6,000

Appendix D

Qualitative Assessment of Diffusion Paths in AgCu-Ti Couples

The $Ag - Cu - Ti$ System is of great importance in the development of ceramic/metal joining techniques. This brief work has the intention of illustrating how simple thermodynamic calculations and reasonable assumptions regarding the kinetic behavior of the system can shed some light on the diffusion paths followed by diffusion couples involving systems pertaining to this ternary once particular initial conditions are established.

D.1 Estimation of Diffusion Paths

When two different phases of different compositions and brought into contact, the different chemical potentials of the elements comprising the two phases constitute the driving force for mass diffusion. The components of each phase would follow a diffusion path determined by the experimental conditions and the actual thermochemical properties of the system. In theory, in a system of third and higher order, the diffusion path actually followed by a diffusion couple constructed from two distinct phases within the system could not be determined without any knowledge on the actual kinetic properties of the phases in question. The reason for this is the infinite number of trajectories through which a system can achieve thermodynamic equilibrium.

Despite this, thermodynamic calculations can be of use in determining possible diffusion paths if some simple and reasonable assumptions are made, as has been shown by [120]. One can assume, for example that there exist local equilibrium conditions at each one of the interfaces. If this holds true, it is reasonable to calculate metastable equilibrium conditions and assume that it is possible to determine which phases are formed by simply calculating the driving forces for precipitation of the remaining phases in the system. To find the actual metastable equilibrium state, inferences regarding the kinetics of the system could be made. For example, if the diffusion rates in both phases are very different from each other reasonable assumptions regarding the ratio of the components concentration profiles can be made.

With these simple assumptions, a possible metastable equilibrium state can be calculated. At this particular point in thermodynamic space it is possible to calculate the driving force for precipitation of the rest of the phases not playing a role in the mestastable equilibrium:

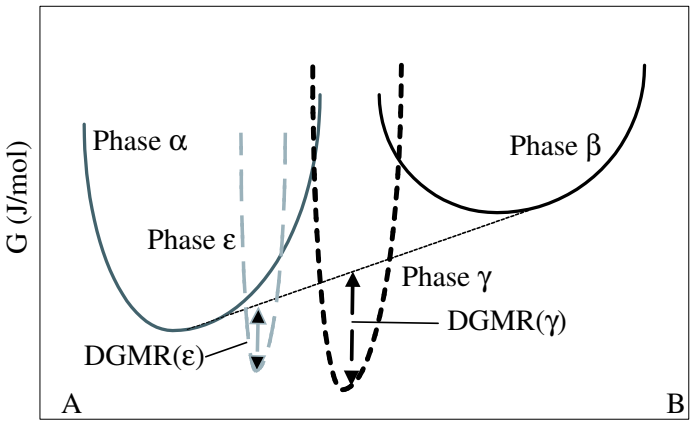

Figure D-1: Schematics of Metastable Equilibrium.

Fig. D-1 illustrates a mestastable equilibrium condition between two phases, while two other phases have positive driving forces for precipitation but are limited by kinetics. The initial condition is a diffusion couple between phases α and β. At the beginning of this reaction, a mestastable equilibrium between these two phases is established. Although phases ϵ and γ are thermodynamically stable, energy barriers due to surface energy or mechanical strains may prevent them from nucleating. To determine which of the two "dormant" phases precipitates first, we could use elementary nucleation theory:

$$J = f\,(T)\,e^{\frac{16\cdot\pi\cdot\gamma^3}{3(\Delta G_v-\Delta G_s)^2}} \tag{D.1}$$

where J is the nucleation rate; γ is the interfacial energy between the nucleus and the matrix;ΔG_v corresponds to the driving force of precipitation of the phase; and ΔG_s is the elastic strain energy contribution to the volumetric energy.

As can be seen, to estimate the relative nucleation rates for competing phases ϵ and γ, it would be necessary to have information regarding interfacial and elastic strain energies which, due to their nature, are extremely difficult to obtain experimentally. However, it is reasonable to assume that interfacial and strain energies would be in the same order of magnitude for each of the phases in question. Therefore, the difference in the value for the driving force for precipitation would then be the determining factor to establish which of the two "dormant" phases would precipitate first, under the particular metastable equilibrium conditions [120].

D.2 Application to the AgCu-Ti Diffusion Couple

In their experiments regarding the $Ag-Cu-Ti$ System, Paulasto et al. [22] studied the thermochemical interactions between several liquid $AgCu$ alloys* and Ti. Due to the reactivity of Ti and the high vapor pressure of Ag, the $AgCu$ alloys were placed inside Ti ampules, which were later evacuated and sealed. The samples were heated to 900^0C, 950^0C and 1000^0C for several periods of time and were later water-quenched. Based on the microstructural and compositional analysis of the phases present, they were able to confirm the main features of the $Ag-Cu-Ti$ system, as described by Eremenko et al. [41, 42, 43, 44]. Using the approach outlined above, it is possible to rationalize the findings reported in the work by Paulasto et al. [22] and propose a possible diffusion-reaction path consistent with both the existing thermodynamic information on the $Ag-Cu-Ti$ (see Section 3.2) system and reasonable assumptions regarding the kinetic behavior of the phases involved.

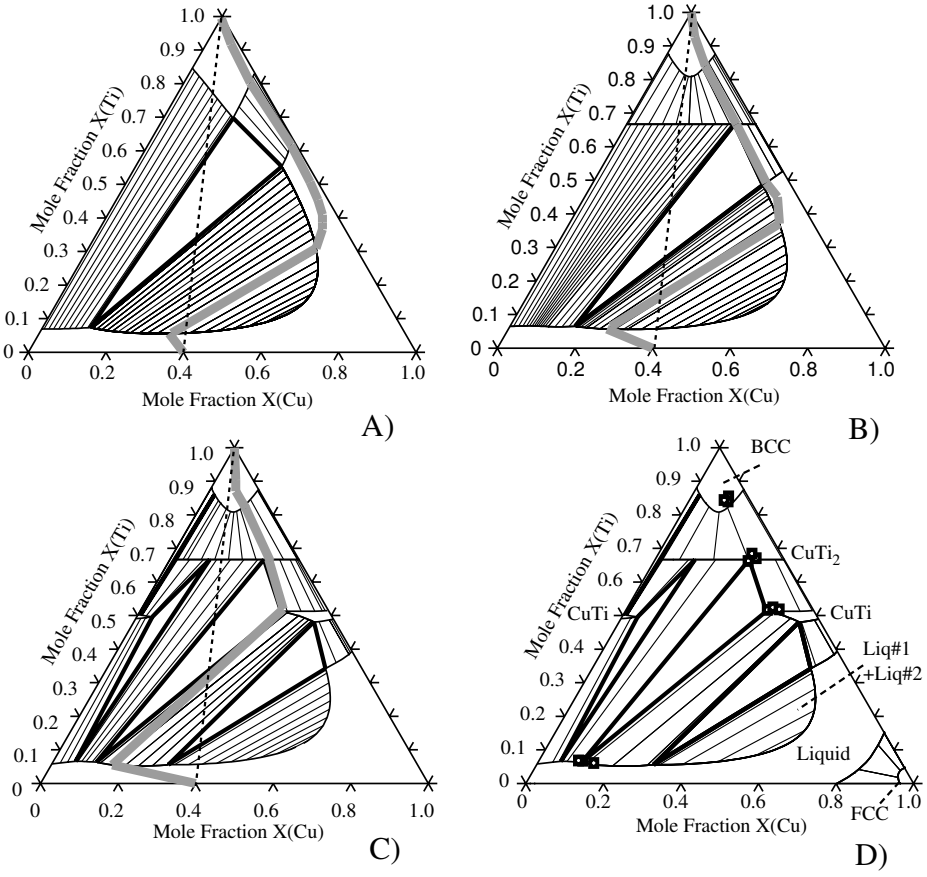

Figure D-2: Proposed diffusion paths and experimental results by Paulasto et al. [22].

Fig. D-2 A) shows the proposed initial conditions of the system: At the beginning of the reaction, βTi is in contact with a liquid $AgCu$ eutectic alloy. The eutectic

*One eutectic and three non-eutectic alloys.

composition is approximately $60\,\%Ag - 40\,\%Cu$. To study this initial condition, a mestastable equilibrium ternary diagram involving the liquid* and the solid *bcc* phases is calculated. When the interfacial reaction starts, Ti would rapidly diffuse out and dissolve into the liquid continuously until the liquid is saturated with the element†. During the initial stages of this interfacial reaction, the concentration of Ti at the interface can be assumed to lie somewhere at the $(bcc+liquid)/liquid$ phase boundary‡.

On the other hand, the elements in the liquid phase (Ag and Cu) will also start do diffuse into the *bcc* phase. Because of the expected difference in the diffusion rates of Ag and Cu in $bcc-Ti$, it would be expected that the ratio $\frac{n(Ag)}{n(Cu)}$ would be different from the initial conditions. To examine this, it is important to consider the ratio of the diffusivities in the liquid and *bcc* phases. To a first approximation, tracer diffusivities in the liquid state can be reasonably assumed to be in the order of $1 \times 10^{-2}\ \frac{m^2}{s}$, while diffusion coefficients in the solid state would be in the order of $1 \times 10^{-12}\ \frac{m^2}{s}$. Concentration gradients in the liquid state would be negligible compared to those of the solid phase and this fact could be use to estimate the proper concentration at the $liquid/(bcc + Liquid)$ phase boundary. A complication arises, however, due to the existence of a miscibility gap in the liquid phase.

To establish a reasonable diffusion path at the onset of the interfacial reaction, the combined observations regarding the behavior of the liquid and solid phases could be used:

Starting from the $AgCu$ eutectic point, a line fulfilling the condition $\frac{x_{Ag}}{x_{Cu}} = 1.5$ could be traced for increasing amounts of Ti, which would represent continuous Ti dissolution in the liquid phase. As can be seen from Fig. D-2 A), this line intersects the miscibility gap boundary§ at around $x_{Ti} = 0.1$. Since the system must be at equilibrium¶, we can assume that the interface between *Liquid* 1 and *Liquid* 2 is defined by a tie-line, which implies a planar *liquid/liquid* interface.

To complete the analysis, the diffusion processes occurring at the solid interface must also be considered. The actual composition at the metastable *Liquid* $2/bcc$ interface must be determined. It is reasonable to assume that the Ti content at this interface must be such that a high Ti chemical potential is obtained, since, as the reaction progresses, the chemical potential of Ti at the interface is expected to decrease. The candidate composition at the $bcc/(bcc + liquid\ 2)$ phase boundary would then be located at the $x_{Cu} \sim 0.2$, $x_{Ti} \sim 0.8$ compositional coordinate. By assuming again a planar *liquid* $2/bcc$ interface, it is possible to find a tie-line that connects the

*Including the well-established miscibility gap.

†When the chemical potential of Ti is the same in the liquid and the solid phases.

‡This assumption, however, is complicated by the existence of a miscibility gap in the liquid phase.

§*Liquid* $1 +$ *Liquid* 2

¶A simplifying assumption would be that the two liquid phases have the same density and therefore the interfaces remain unchanged throughout the reaction

compositions at the $bcc/(bcc + liquid\ 2)$ and $(bcc + liquid\ 2)/liquid\ 2$ phase boundaries. The rest of the proposed diffusion path is shown in Fig. D-2 A). *It is important to note that the proposed diffusion path crosses the dotted line connecting the $AgCu$ eutectic and the pure Ti compositions. This is a necessary condition if mass is to be conserved in the system..*

To estimate which phase would precipitate next under the already defined metastable conditions, it is necessary to calculate the driving force for precipitation for all the stable phases. Fig. D-3 shows the calculated ratio of the driving forces for precipitation for the $CuTi_2$ and $CuTi$ phases along the $bcc/(bcc+liquid\ 2)$ phase boundary as a function of Ti composition. The $x_{Ti} \sim 0.8$ corresponds to the $x_{Cu} \sim 0.2$, $x_{Ti} \sim 0.8$ compositional coordinate. As noted above, this point has the highest Ti chemical potential and it seems reasonable to consider that it represents the initial interfacial condition at the onset of the reaction. Fig. D-3 shows that at this composition, the driving force for precipitation of the $CuTi_2$ is five times as large as that of the $CuTi$ phase. It is therefore reasonable to expect that this phase would be the first to form under these diffusion/reaction conditions.

Fig. D-2 B) shows a diffusion path at $t = t_1 > t_0$. By this time, the $CuTi_2$ phase is assumed to have already precipitated. Since the expected Cu content of this phase at this time is higher than that of Ag, the liquid phase would be depleted of Cu and the $\frac{x_{Ag}}{x_{Cu}}$ ratio would have increased. This is shown by decreasing the slope of the diffusion path connecting the $AgCu$ eutectic point and the $liquid\ 1 + liquid\ 2$ phase boundary. At the same time, the Ti content at the bcc side of the $bcc/liquid\ 2$ interface would have decreased, due to the formation of the $CuTi_2$ particles and the continuing dissolution of Ti in the liquid phase, accompanied by the enrichment of the bcc phase with Ag and Cu. The tie-line connecting the two liquid phases corresponds to a higher Ti chemical potential, as expected due to the further Ti enrichment of the liquid.

Fig. D-2 C) shows yet another diffusion path at $t = t_2 > t_1 > t_0$. It is assumed that the $CuTi$ phase has already precipitated and therefore, a metastable equilibrium between βTi, $CuTi_2$, $CuTi$, $Liquid\ 1$ and $Liquid\ 2$ has to be calculated. The composition of the $CuTi$ phase is richer in Cu than in Ag and a further decrease in the slope connecting the $AgCu$ eutectic point and the $Liquid\ 1 + Liquid\ 2$ phase boundary is expected. As the chemical potential of Ti at the βTi side of the $\beta Ti/Liquid\ 2$ interface decreases, the diffusion path indicates that the $CuTi_2$ phase would increase its Ag content. The tie-line connecting the two liquid phases would correspond to a higher Ti chemical potential, due to further dissolution of Ti into the liquid.

Fig. D-2 D) shows the experimental compositions at 950^0C after annealing for $30\,min.$. As can be seen, the compositions observed are consistent with the ternary phase diagram. Moreover, the experimental compositions are consistent with the diffusion path proposed in this work. The validity of the analysis and the assumptions made are thus justified. A similar approach can be used to analyze diffusion reactions

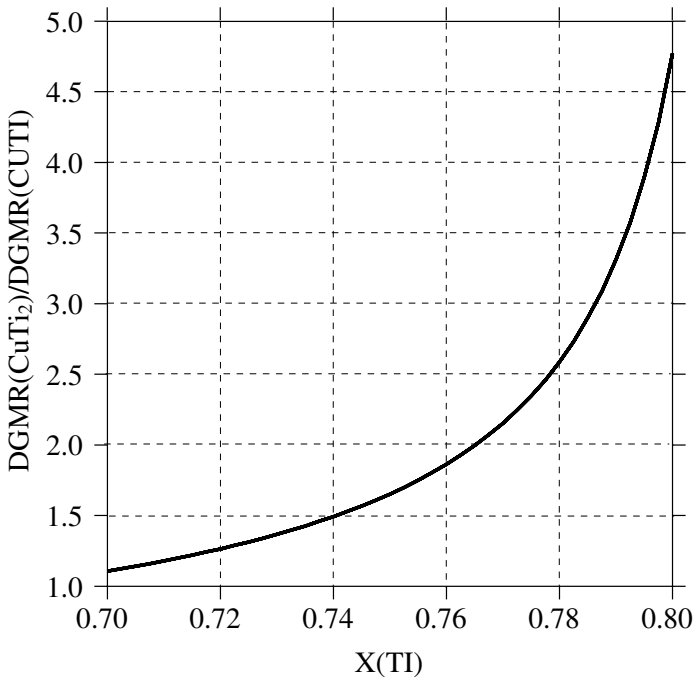

Figure D-3: $\frac{DGMR(CuTi_2}{DGMR(CuTi)}$ ratio at the $\beta Ti/(\beta Ti + Liquid\ 2)$ phase boundary as a function of Ti content.

of this system at other temperatures of interest.

D.3 Summary

In this appendix, following a similar approach by Lee et al. [120] it has been demonstrated the usefulness of metastable thermodynamic calculations to establish possible diffusion paths in diffusion couples in ternary systems. Diffusion experiments on the $Ag - Cu - Ti$ system have been rationalized using the complete thermodynamic description of the $Ag - Cu - Ti$ system.

Appendix E

Numerical Implementation of Phase Field Model of Coupled Oxide Layers Growth

E.1 Finite Difference Formulation

To solve the Cahn-Hilliard equation (Eq. 7.13) for this system, a finite difference formulation was used. For simplicity, a one-dimensional problem was considered. For the first term of the C-H equation, three uniformly spaced grid points (h spacing) were used. The discretization error of this finite difference formulation is $O(h^2)$:

$$\nabla \cdot M \cdot \nabla \left(\frac{\partial f}{\partial c}\right) = \nabla \cdot M \cdot \nabla \left(\mu\left(O\right)\right)$$
$$M \cdot \nabla^2 \left(\mu\left(O\right)\right) = M \cdot \frac{\mu_{i-1} - 2\mu_i + \mu_{i+1}}{h^2}$$

For the second term, five equally spaced grid points were used and a central fourth order difference equation of discretization error $O(h^2)$ was obtained:

$$\nabla \cdot M \cdot \nabla \left(-2k\nabla^2 c(x)\right) = \nabla \cdot M \cdot \nabla \left(-2k\nabla^2 x(O)\right)$$
$$-2kM \cdot \nabla^4 x(O) = -2kM \cdot \frac{x(O)_{i-2} - 4x(O)_{i-1} + 6x(O)_i - 4x(O)_{i+1} + x(O)_{i+2}}{h^4}$$

E.2 Treatment of Boundary Conditions

To simplify the implementation of the numerical simulation, central differences were used also at both boundaries. The system was treated as if it had symmetric boundary conditions. The computational domain to the right is the mirror image to the one on the left:

Therefore, special finite difference equations were implemented at the boundaries. The code was written so the boundary conditions could be easily modified in case different physical situations were to be simulated. As can be seen, in the simplified model, the zirconia is not considered and instead, a concentration is fixed at one end

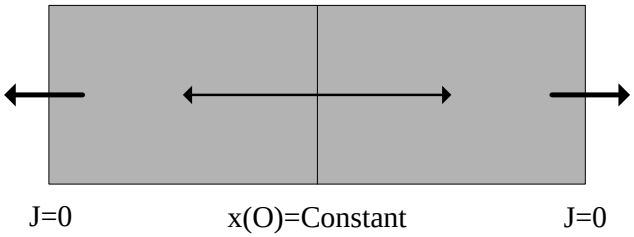

Figure E-1: Boundary conditions for simulations.

of the computational domain. Although this is not entirely correct, it still resembles the physics of the original problem.

E.3 Value of the gradient energy term

In the diffuse-interface formalism, one of the key parameters determining the interface characteristic thickness is the gradient energy coefficient (See Eq. 7.13), k. As described in Section 7.4, the gradient energy coefficient is related to the energy penalty that the system has to pay in order to have abrupt changes in composition (i.e. interfaces). The larger this parameter is, the greater the importance of the second parameter in Eq. 7.13. It is therefore important to be able to assign a value for this parameter. It is known (See Section 7.4) that $k \propto \left(\frac{\delta}{2}\right)^2$, where δ is the interface thickness. By assuming that:

$$\delta = 3 \cdot h \tag{E.1}$$

k can be obtained through

$$k = K\left(\frac{3}{2}h\right)^2 \tag{E.2}$$

where K is a constant that reflects the uncertainties in the value for the parameter k. It is obvious that, given the actual widths of real interfaces*,the parameter K must be modified in order to make the calculations practical. Although the actual interface is not accurately described (its dimension is increased by several orders of magnitude), the essential aspects of the diffuse-interface approached are retained through the approximation shown in Eq. E.2.

E.4 Numerical Scheme: Explicit Euler

The simplest way to numerically integrate the marching time Cahn-Hilliard equation is to implement a simple forward Euler numerical scheme in time:

$$x(O)_i^{n+1} = x(O)_i^n + \Delta t \cdot \left[M \cdot D^2 \cdot (\mu(O)_i^n) - 2 \cdot \kappa \cdot D^4 \cdot (x(O)_i^n)\right] \tag{E.3}$$

where Δt is the time interval, n denotes the previous time interval, n+1 corresponds to the interval to calculate, D^2 is the discrete second spatial derivative operator and

*A typical value is about 10 monatomic layers, or 30 Å.

D^4 is the fourth order finite difference operator.

Since this numerical scheme is conditionally stable, there is a maximum allowable $\triangle t$, beyond which the solution becomes unstable and the simulation diverges. An additional problem is the fact that at the beginning of the simulation, the system develops the interfaces quite rapidly and as the simulation proceeds, the evolution of the system becomes increasingly slower. This means that there are different time scales during the simulation and thus an adaptive time stepping scheme was implemented. To ensure stability of the simulation, the maximum change in the concentration was fixed.

The algorithm is designed so the Δt used in the integration reaches a steady state and the simulation remains stable. Basically, three different time scales in the simulation can be observed. The first one involves the initial formation of the two diffuse interfaces. At this stage, large concentration gradients develop and large local fluxes are present. As the simulation continues, Dt increases at a slower pace. Eventually, the simulation reaches a stage in which local variations in the composition profile occur slowly. The large variation at some stages of the simulation can be minimized by decreasing the tolerance.

E.5 Numerical Scheme: Semi-implicit Crank-Nicholson

For the conventional diffusion equation, semi-implicit schemes such as C-N are unconditionally stable. Unfortunately, this is not true for the *C-H* equation, because of the non-linearity and the bi-harmonic term . Despite this, it is expected that the maximum allowable Dt is greater than that of the simple explicit scheme. It will be shown that this is indeed the case. Furthermore, it will be proven that as the required accuracy of the numerical simulation is increased, the use of semi-implicit schemes is increasingly more advantageous.

The C-N numerical scheme can be represented by:

$$x(O)_i^{n+1} = x(O)_i^n + \Delta t \cdot \frac{\left\{ \begin{array}{l} \left[M \cdot D^2 \cdot (\mu(O)_i^n) - 2 \cdot \kappa \cdot D^4 \cdot (x(O)_i^n)\right] \\ + \left[M \cdot D^2 \cdot \left(\mu(O)_i^{n+1}\right) - 2 \cdot \kappa \cdot D^4 \cdot \left(x(O)_i^{n+1}\right)\right] \end{array} \right\}}{2} \quad \text{(E.4)}$$

In this method, the PDE is supposed to be satisfied at a mid-point between the actual time and the immediate next time in the future. Therefore, the solution in time is related to the average to the spatial solutions in both the actual time and the immediately next one.

E.6 Newton Method

As can be seen in Eq. E.4, the C-N method involves the solution of a non-linear system of equations. Because of the non-linearity of the system of equations, an iterative method must be used. For this particular problem, the multi-dimensional Newton method was used.

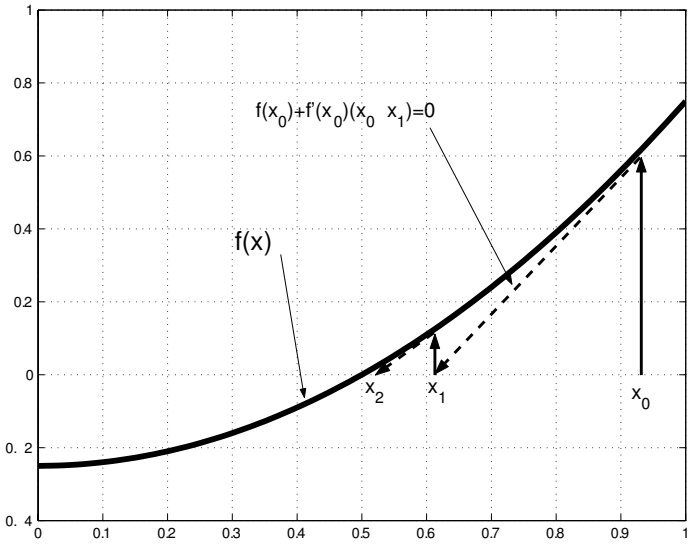

Figure E-2: One-dimensional Newton method.

Fig. E-2 shows the concept of the Newton method applied to a simple one-dimensional problem. This method relies on the use of the local derivative of the function evaluated at the initial guess (X_0) to approach the solution (X_1) . The procedure continues until the solution has been reached (converged) within a pre-defined tolerance (X_2). In the case of the multidimensional Newton method, the algorithm would be:

To solve $F(\vec{x})$ where $\vec{x}$ is a vector to obtain $\vec{x}^{n+1}$, do:

1) x^0 = initial guess, k=0

2) Repeat {

3) Compute $F(\vec{x}^k)$, $J_F(\vec{x}^k)$ (Jacobian Matrix)

4) Solve $J_F(\vec{x}^k) \cdot (\vec{x}^{k+1} - \vec{x}^k) = -F(\vec{x}^k)$ for x^{k+1}

5) $k = n + 1$

6) } Until $\left\|x^{k+1} - x^k\right\|$ AND $\left\|f\left(x^{k+1}\right)\right\|$ are small enough and where $J_F(\vec{x}^k)$ is the

Jacobian matrix and is defined as:

$$J_F\left(\vec{x}^n, \vec{x}^k\right) \cdot \Delta x \equiv \begin{bmatrix} \frac{\partial F_1(\vec{x})}{\partial x_1} & \cdots & \frac{\partial F_1(\vec{x})}{\partial c_N} \\ \vdots & \ddots & \vdots \\ \frac{\partial F_N(\vec{x})}{\partial x_1} & \cdots & \frac{\partial F_N(\vec{c})}{\partial x_N} \end{bmatrix} \begin{bmatrix} \Delta x_1 \\ \vdots \\ \Delta x_N \end{bmatrix}$$

For the problem at hand:

$$F(x_i) = -x_i^{n+1} + x_i^n + \Delta t \cdot \frac{\left\{ \begin{array}{l} \left[M \cdot D^2 \cdot (\mu_i^n) - 2 \cdot \kappa \cdot D^4 \cdot (x_i^n)\right] \\ + \left[M \cdot D^2 \cdot \left(\mu_i^{n+1}\right) - 2 \cdot \kappa \cdot D^4 \cdot \left(x_i^{n+1}\right)\right] \end{array} \right\}}{2} \tag{E.5}$$

One of the main difficulties in implementing *Newton* iterative methods is the calculation of the *Jacobian* matrix. The algebraic expression describing how the chemical potential, μ, changes with composition will have to be used and the solver would have to be modified each time this expression changes. Thus, if a general C-H semi-implicit solver is to be implemented, other ways for approximating the *Jacobian* must be found:

For this work, a *Jacobian*-free *Newton* iteration method [171, 172] was used. The *Jacobian* was approximated using a Gradient Conjugate Residual *GCR* algorithm. This algorithm attempts to minimize

$$r^{k+1} = -F\left(x^k\right) - J_F\left(x^k\right) \cdot \left(x^{k+1} - x^k\right) \tag{E.6}$$

At each iteration of the GCR, $J_F(x^k)$ can be approximated by

$$J_F\left(x^k\right) \cdot p = \frac{1}{\varepsilon}\left[F\left(x^k + \varepsilon \cdot p\right) - F\left(x^k\right)\right] \tag{E.7}$$

where p is an orthogonalized search direction for the particular GCR iteration.

E.7 Implementation of Semi-Implicit Numerical Scheme

For this implementation, the different time-scales of the simulation were also considered and an adaptive time-stepping scheme was implemented. This adaptive time-stepping was designed such that the simulation would minimize the number of Newton iterations required to solve each time interval and at the same time it would maximize the integrating $\triangle t$.

Appendix F

Experimental Apparatus

Reactive brazing involves the use of highly reactive elements that are susceptible to oxidation. For reactive brazing of zirconia to be successful, it is necessary to ensure that the only possible source of oxygen (for the oxidation of the reactive element) is the zirconia itself and not the atmosphere surrounding the specimen.

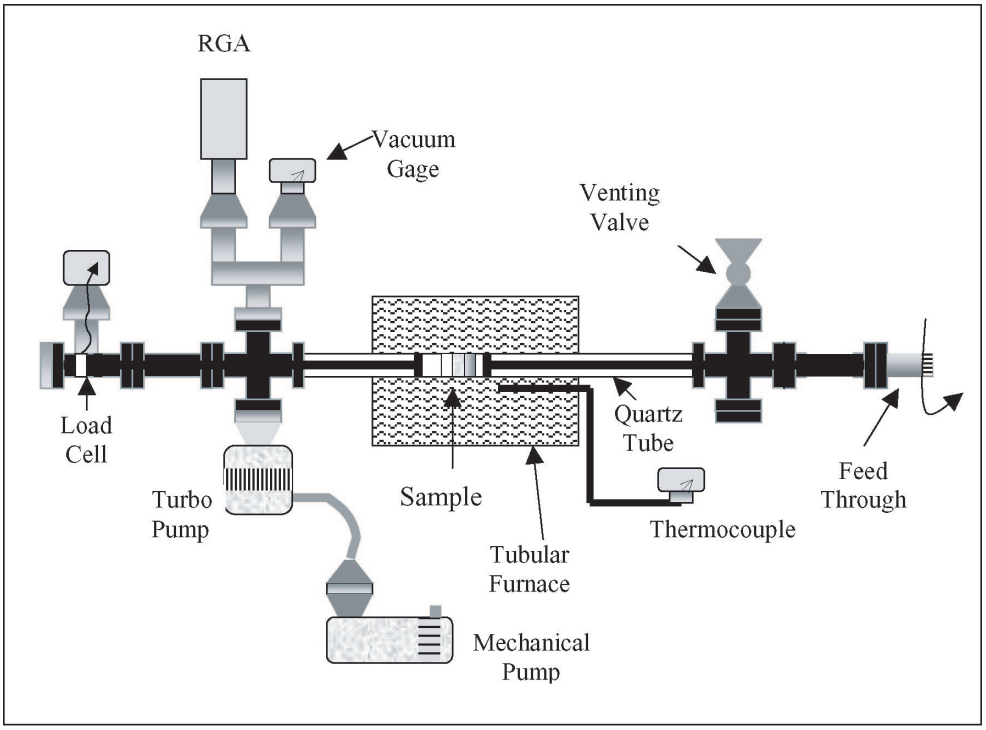

Figure F-1: Experimental apparatus.

Fig. F-1 presents a schematics of the experimental apparatus designed for the experimental part of this work. With this experimental apparatus it was possible to control the thermal history of the samples studied, while maintaining the oxygen partial pressure low enough so no reaction between the active alloys and the atmosphere would take place. The compressive on the load was controlled through a load gauge that was positioned at one of the ends of the sample holder. With this furnace,

vacuum pressures of $10^{-6}\,torr$ were routinely obtained. The maximum operating temperature of this furnace was 1250^0C. An actual picture of the experimental setup is presented in Fig. F-2

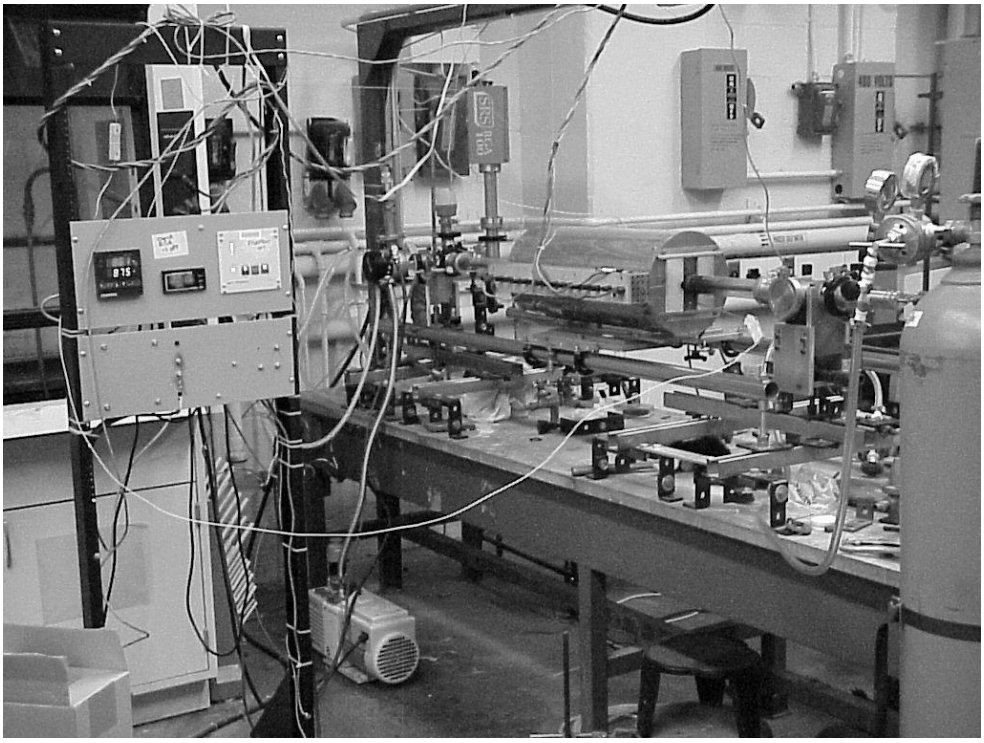

Figure F-2: Vacuum high-temperature furnace.

Arroyave [51] provides a more detailed description of the characteristics and capabilities of the experimental apparatus presented in this appendix.

Bibliography

[1] M. G. Nicholas. Ceramic-Metal Interfaces. In *Surfaces and Interfaces of Ceramic Materials*, pages 393–417, United Kingdom, 1989. Kluwer Academic Publishers.

[2] J.-W. Park, P. F. Mendez, and T. W. Eagar. Strain Enegy Distribution in Ceramic/Metal Joints. *Acta Mater.*, 50:883–899, 2002.

[3] J. M. Howe. Bonding, Structure and Properties of Metal/Ceramic Interfaces: Part 1 Chemical Bonding, Chemical Reaction and Interfacial Structure. *Int. Mater. Rev.*, 38:233–255, 1993.

[4] A. Dupré. *Théorie Mécanique de la Chaleur*, chapter IX. Gauthier-Villars, Paris, 1869.

[5] N. Eustathopoulos, M. G. Nicholas, and B. Drevet. *Wettability at High Temperatures*. Pergamon, 1999.

[6] J. E. MacDonald and J. G. Eberhart. Adhesion in Aluminum Oxide-Metal Systems. *Trans. Metall. Soc. AIME*, 233:512–517, 1965.

[7] B. M. Gallois. Wetting in Non-reactive Liquid-Metal Systems. *JOM*, 49(6): 48–51, 1997.

[8] M. W. Chase. *JANAF Thermochemical Tables*. American Chemical Society, Washington DC, 1983.

[9] J.-G. Li. Wetting and Interfacial Bonding of Metals with Ioncovalent Oxides. *J. Am. Ceram. Soc.*, 75:3118–3126, 1992.

[10] F. R. de Boer, R. Boom, W. C. M. Mattens, A. R. Miedema, and A. K. Niessen. *Cohesion in Metals, Transition Metal Alloys*. North-Holland, Amsterdam, 1988.

[11] I. Rivollet. *Contact Angle and Thermodynamic Adhesion in Nonreactive Metal-Alumina Systems*. PhD thesis, Institut National Polytechnique, 1986.

[12] W. H. Strehlow and E. L. Cook. Compilation of Energy Band Gaps in Element and Binary Compound Semiconductors and Insulators. *J. Phys. Chem. Ref. Data*, 2:163–93, 1973.

[13] O. Kubaschewski, C. B. Alcock, and P. J. Spencer. *Materials Thermochemistry*. Pergamon Press, Oxford, sixth edition, 1993.

[14] R. M. Pilliar and J. Nutting. Solid-Solid Interfacial Energy Determinations in Metal-Ceramic Systems. *Philos. Mag.*, 16:181–188, 1967.

[15] M. G. Nicholas. Active Metal Brazing. *Br. Ceram. Trans. and J.*, 85:144–146, 1986.

[16] N. Eustathopoulos and B. Drevet. Mechanisms of Wetting in Reactive Metal/Oxide Systems. *Mater. Res. Soc.*, 314:15–25, 1993.

[17] N. Eustathopoulos, M. G. Nicholas, and B. Drevet. *Wetting at High Temperatures*, chapter 2, pages 91–92. Pergamon, 1999.

[18] F. Moret and Eustathopoulos. Ceramic to Metal Direct Brazing. *J. de Physique IV*, 3:1043–1052, 1993.

[19] C. H. Lupis. *Chemical Thermodynamics of Materials*. Prentice Hall, New York, 1993.

[20] Y. Naidich. The Wettability of Solids by Liquid Metals. In D. A. Cadenhead and J. F. Danielli, editors, *Progress in Surface and Membrane Science*, page 353, New York, 1981. Academic Press.

[21] N. Saunders and A. P. Miodownik. *CALPHAD - A Comprehensive Guide*. Pergamon, New York, 1998.

[22] M. Paulasto, F. J. J. Van Loo, and J. K. Kivilahti. Thermodynamic and experimental study of Ti-Ag-Cu alloys. *J. Alloy. Compd*, 220:136–141, 1995.

[23] G. P. Kelkar and A. H. Carim. Synthesis, Properties, and Ternary Phase Stability of M_6X Compounds in the Ti-Cu-O System. *J. Am. Ceram. Soc.*, 76: 1815–1820, 1993.

[24] O Botstein, A. Schwarzman, and A. Rabinkin. Induction Brazing of Ti-6Al-4V Alloy with Amorphous 25Ti-25Zr-50Cu Brazing Filler Metal. *Mater. Sci. Eng. A*, A206:14–23, 1996.

[25] Z. S. Yu, M. F. Wu, C. Liang, and K. Wang, F. J. Amd Qi. Interfacial Morphology and Strength of Al_2O_3/Nb Joint Brazed with Cu-Ti-Zr Filler Metal. *Mater. Sci. Technol.*, 18:99–102, 2002.

[26] R. Arroyave and T. W. Eagar. Thermodynamic Assessment of the System Cu-Ti-Zr. *J. Alloys Compd.*, 351:158–170, 2002.

[27] R. Arroyave. Assessment of the Ag-Ti System. Technical report, Massachusetts Institute of Technology, 2002.

[28] J. J. Pak, M. L. Santella, and R. J. Fruehan. Thermodynamics of Ti in Ag-Cu Alloys. *Metall. Trans. B.*, 21B:349–355, 1990.

[29] F. H. Hayes, L. Lukas, G¿ Effenberg, and G. Petzow. A Thermodynamic Optimization of the Cu-Ag-Pb System. *Z. Metallkd.*, 77:749–754, 1986.

[30] K. C. Hari Kumar, I. Ansara, P. Wollants, and L. Delaey. Thermodynamic Optimization of the Cu-Ti System. *Z. Metallkd.*, 87:666–672, 1996.

[31] J. L. Murray and K. J. Bhansali. The Ag-Ti (Silver-Titanium) System. *Bull. Alloy Phase Diagrams*, 4:178–182, 1983.

[32] K. Fitzner and O. J. Kleppa. Thermochemistry of Binary Alloys of Transition Metals: The Me-Ti, Me-Zr, and Me-Hf (Me=Ag,Au) Systems. *Metall. Mater. Trans. A*, 23A:997–1003, 1992.

[33] P. Wei, L. Rongti, C. Jian, S. Ruifeng, and L. Jie. Thermodynamic Properties of Ti in Ag-Ti Alloys. *Mater. Sci. Eng. A*, A287:72–77, 2000.

[34] B. J. Lee. Thermodynamic Evaluation of the $Ti-O$ Binary System. *J. Korean Inst. Metals and Materials*, 32:869–877, 1994.

[35] C. Wagner. *Thermodynamics of Alloys*, chapter 2, pages 54–58. Addison-Wesley, 1952.

[36] L. Kaufman. Thermodynamic Database for the Ag-Ti System, 2002. Personal Communication, MIT, 2002.

[37] M. R. Plichta and H. I. Aaronson. The $\beta \rightarrow \alpha$ Transformation in Three Ti-X Systems. *Acta Metall.*, 26:1293–1305, 1978.

[38] R. Reinbach and D. Fischmann. Diffusion in the Titanium-Silver System. *Z. Metallkd.*, 54:314–316, 1963.

[39] M. K. McQuillan. A Study of the Titanium-Silver System. *J. Inst. Met.*, 88: 235–239, 1960.

[40] H. Bakker. *Enthalpies in Alloys: Miedema's Semi-Empirical Model*. Trans Tech Publications Ltd, Zurich, 1998.

[41] V. N. Eremenko, Y. I. Buyanov, and N. M. Panchenko. Phase Separation in the Molten State in the Ti-Cu-Ag System. *Izv. Akad. Nauk SSSR, Metally*, 5: 200–202, 1969.

[42] K. Eremenko, Yu. I. Buyanov, and N. M. Panchenko. Phase Equilibrium in the Ti-Cu-Ag System at $700^0\,C$. *Izv. Akad. Nauk. USSSR, Metally*, 3:188–193, 1969.

[43] N. M. Eremenko, Yu. I. Buyanov, and N. M. Panchenko. The Liquidus Surface of the System Titanium-Copper-Silver. *Sov. Powder Metall. Met. Ceram.*, 10: 301–304, 1970.

[44] N. M. Eremenko, Yu. I. Buyanov, and N. M. Pancheno. Polythermal and Isothermal Sections of the System Titanium-Copper-Silver. *Sov. Powder Metall. Met. Ceram.*, 10:410–414, 1970.

[45] C. G. Woychik and T. B. Massalski. Phase Diagram Relationships in the System Cu-Ti-Zr. *Z. Metallkd.*, 79:149–153, 1988.

[46] W. D. MacDonald and T. W. Eagar. Transient-liquid-phase Bonding. *Annu. Rev. Mater. Sci.*, 22:23–46, 1992.

[47] V. N. Chebotnikov and V. V. Molokanov. Structures and Properties of Amorphous and Crystalline Alloys in the Ti_2Cu-Zr_2Cu Section in the Cu-Ti-Zr System. *Inorg. Mater.*, 26:808–811, 1990.

[48] K. J. Zeng, Håmålåinen, and H. L. Lukas. A New Thermodynamic Description of the Cu-Zr System. *J. Phase Equilib.*, 15:577–586, 1994.

[49] C. C. H. Kumar, P. Wollants, and L. Delaey. Thermodynamic Assessment of the Ti-Zr System and Calculation of the Nb-Ti-Zr Phase Diagram. *J. Alloys Compd.*, 206:121–127, 1994.

[50] BJ. Lee. Prediction of Ti/Al_2O_3 Interface Reaction Products by Diffusion Simulation. *Acta. Mater.*, 45:3993–3999, 1997.

[51] Raymundo Arroyave. Reactive Brazing of Zirconia to Nickel-Based Super Alloys. Master's thesis, Massachusetts Institute of Technology, 2000.

[52] R. Arroyave, L. Kaufman, and T. W. Eagar. Thermodynamic Modelling of the Zr-O System. *CALPHAD*, 26:95–118, 2002.

[53] L. Kaufman and E. V. Clougherty. Thermodynamic Factors Controlling the Stability of Solid Phases at High Temperatures and Pressures. In AIME Metall. Soc., editor, *Metallurgy at High Pressures and High Temperatures*, pages 322–379, New York, 1964. Gordon and Breach, Science Publishers.

[54] J. P. Abriata and R. Versaci. The O-Zr (Oxygen-Zirconium) System. *Bull. of Alloy Phase Diagrams*, 7(2):116–124, 1986.

[55] M. Hillert, B. Jansson, B. Sundman, and Ågren. A Two-Sublattice Model for Molten Solutions With Different Tendency for Ionization. *Metall. Mater. Trans. A*, 16A:261, 1985.

[56] T. Tsuji. Thermochemistry of IVA Transition Metal-Oxygen Solid Solutions. *J. Nucl. Mater.*, 247:63–71, 1997.

[57] P. Waldner and G. Eriksson. Thermodynamic Modelling of the System Titanium-Oxygen. *CALPHAD*, 23:189–218, 1999.

[58] M. Hirabayashi, S. Yamaguci, H. Asano, and K. Hiraga. Order-Disorder transformations of Interstitial Solutes in Transition Metals of IV and V Groups. In H. Warlimont, editor, *Order-Disorder Transformations in Alloys*, pages 266–302, Berlin, 1974.

[59] R. W. Vest, N. M. Tallan, and W. C. Tripp. Electrical Properties and Defect Structure of Zirconia: I, Monoclinic Phase. *J. Am. Ceram. Soc.*, 47:635–640, 1964.

[60] R. W. Vest and N. M. Tallan. Electrical Properties and Defect Structure of Zirconia: II, Tetragonal Phase and Inversion. *J. Am. Ceram. Soc.*, 48:472–475, 1965.

[61] M. Hillert and B. Jansson. Thermodynamic Model for Non-stoichiometric Ionic Phases. Application to CeO_{2-x}. *J. Am. Ceram. Soc.*, 69:732–734, 1986.

[62] S. C. Carniglia, S. D. Brown, and T. F. Schroeder. Phase Equilbria and Physical Properties of Oxygen-Defficient Zirconia and Thoria. *J. Am. Ceram. Soc.*, 54: 13–17, 1970.

[63] R. J. Ackerman, S. P. Garg, and E. G. Rauh. High-Temperature Phase diagram for the System Zr-O. *J. Am. Ceram. Soc.*, 60:341–345, 1977.

[64] R. J. Ackerman, S. P. Garg, and E. G. Rauh. The Lower Phase Boundary of ZrO_{2-x}. *J. Am. Ceram. Soc.*, 61:275–276, 1978.

[65] E. G. Rauh and P. Garg. The ZrO_{2-x} (cubic)- ZrO_{2-x} (cubic+tetragonal) Phase Boundary. *J. Am. Ceram. Soc.*, 63:239–240, 1980.

[66] E. Gebhardt, H. D. Seghezzi, and W. Durrschenabel. Research on the System Zirconium-Oxygen. *J. Nucl. Mater.*, 4:255–268, 1961.

[67] G. Boureau and P. Gerdanian. Use of a Tian-Calvet Microcalorimeter at 1300^oC Direct Measurement of $h^M_{O_2}$ in the Metal-Oxygen Systems. *Can. Metall. Q.*, 13: 339–343, 1974.

[68] G. Boureau and P. Gerdanian. High Temperature Thermodynamics of Solutions of Oxygen in Zirconium and Hafnium. *J. Phys. Chem. Solids*, 45:141–145, 1984.

[69] K. L. Komarek and M. Silver. Thermodynamic Properties of Zirconium-Oxygen, Titanium-Oxygen and Hafnium-Oxygen Alloys. In *Thermodynamics of Nuclear Materials*, pages 749–774, Vienna, Austria, 1962. International Atomic Energy Agency.

[70] R. J. Ackerman, S. P. Garg, and E. G. Rauh. The Thermodynamic Properties of Substoichiometric Zirconium Dioxide at the Lower Phase Boundary. *High. Temp. Sci.*, 11:199–210, 1979.

[71] B. Hallstedt, D. Risold, and L. J. Gauckler. Thermodynamic Assessment of the Copper-Oxygen System. *J. Phase Equilib.*, 15:483–499, 1994.

[72] G. P. Kelkar, K. E. Spear, and Carim A. H. Thermodynamic Evaluation of Reaction Products and Layering in Brazed Alumina Joints. *J. Mater. Res.*, 9: 2244–2250, 1994.

[73] M. H. Mueller and H. W. Knott. The Crystal Structures of Ti_2Cu, Ti_2Ni, Ti_4Ni_2O and Ti_4Cu_2O. *Trans. Metall. Soc. AIME*, 227:674–78, 1963.

[74] G. P. Kelkar and A. H. Carim. Al solubility in M_6X Compounds in the Ti-Cu-O System. *Mat. Letters*, 23:231–235, 1995.

[75] C. Peytour, F. Barbier, P. Berhet, and A. Revcolevschi. Characterization of $Al_2O_3/TA6V$ and $ZrO_2/TA6V$ Ceramic-Metal Interfaces. *J. de Phys.*, 51, $Suppl.C1{:}C1_897 - -C1_902$, 1990.

[76] M. L. Santella, J. A. Horton, and J. J. Pak. Microstructure of Alumina Brazed with a Silver-Copper-Titanium Alloy. *J. Am. Ceram. Soc.*, 73:1785–1787, 1990.

[77] H. Haessler, H. Kippenberg, and A. G. Siemens. Possibilities of degassing alloys based on copper with elements having an oxygen affinity such as chromium, zirconium, titanium in relation to the material of the crucible. In J. G. Krueger, editor, *Proc. Int. Conf. Vac. Metall. Electroslag Remelting Processes*, pages 87–89, Hanau, Germany, 1977. Leybold-Heraeus GmbH Co.

[78] V. S. Sudavtsova. Thermodynamic Properties of the Cu-O-Zr System. *J. Ukrainian Chem.*, 59:1149–1150, 1993.

[79] C. H. Lupis. *Chemical Thermodynamics of Materials*. Prentice-Hall, New York, 1983.

[80] B. Sundman. Modification of the Two-Sublattice Model for Liquids. *CALPHAD*, 15:109–119, 1991.

[81] J. Assal, B. Hallstedt, and L. J. Gauckler. Thermodynamic Assessment of the Ag-Cu-O System. *J. Phase Equilib.*, 19:351–361, 1998.

[82] C. Wagner. The Activity Coefficient of Oxygen and Other Nonmetallic Elements in Binary Liquid Alloys as a Function of Alloy Composition. *Acta Metall.*, 21: 1297–1303, 1973.

[83] H. M. Ondik and H. F. (Editors) McMurdie. *Phase Diagrams for Zirconium and Zirconia Systems*. The American Ceramic Society, Westerville, Ohio, USA, 1998.

[84] J.-H. Park, P. Liang, H. J. Seifert, F. Aldinger, B.-K. Koo, and H.-G. Kim. Thermodynamic Assessment of the ZrO_2 and TiO_2 System. *Kor. J. Ceram.*, 7:11–15, 2001.

[85] F. H. Brown and P. Duwez. The Zirconia-Titania System. *J. Am. Ceram. Soc.*, 37:129–132, 1954.

[86] A. H. Webster, R. C. MacDonald, and W. S. Bowman. The System PbO-ZrO_2-TiO_2 at 1100. *J. Canad. Ceram. Soc.*, 34:97–102, 1965.

[87] M. Hoch and R. L. Dean. The System Titanium-Zirconium-Oxygen. *Trans. Metall. Soc. AIME*, 221:1162–1173, 1961.

[88] A. V. Shevchenko, L. M. Lopato, I. M. Maister, and O. S. Gorbunov. The $TiO_2 - ZrO_2$ System. *Russ. J. Inorg. Chem.*, 25:1379–1381, 1980.

[89] T. Noguchi and M. Mizuno. Phase Changes in Solids Measured in Solar Furnace, ZrO_2-TiO_2 System. *Solar Energy*, 11:56–61, 1967.

[90] B. Jansson. Evaluation of Parameters in Thermochemical Models using different types of Conditions. Technical Report TRITA-MAC-0234, Division of Metallurgy, Royal Institute of Technology, Stockholm, Sweden, 1984.

[91] L. W. Coughanour, R. S. Roth, and V. A. DeProsse. Phase Equilibrium Relations in the Systems Lime-Titania and Zirconia-Titania. *J. Res. Natl. Bur. Std.*, 52:37–42, 1954.

[92] T. Noguchi and M. Mizuno. Phase Changes in the $ZrO_2 - TiO_2$ System. *Bull. Ceram. Soc. (Jap.)*, 41:2895–2899, 1968.

[93] A. E. McHale and R. S. Roth. Low Temperature Phase Relationships in the System ZrO_2-TiO_2. *J. Am. Ceram. Soc.*, 69:827–832, 1986.

[94] W. Weppner. Tetragonal Zirconia Polycrystals- a High Performance Solid Oxygen Conductor. *Solid State Ionics*, 52:15–21, 1992.

[95] R. V Allen, W. E. Borbidge, and P. T. Whelan. The Reaction-Bonded Zirconia Oxygen Sensor: An Application for Solid-State Metal-Ceramic Reaction-Bonding. *Advances in Ceram.*, 12:537–43, 1984.

[96] W. B. Hanson, K. I. Ironside, and J. A. Fernie. Active Metal Brazing of Zirconia. *Acta Mater.*, 48:4673–4676, 2000.

[97] R. C. Garvie. Structural Applications of Zirconia-bearing Materials. *Advances in Ceramics*, 12:465–479, 1984.

[98] R. L. Jones. The Development of Hot-Corrosion-Resistant Zirconia Thermal Barrier Coatings. *Mater. High Temp.*, 9:228–236, 1991.

[99] A. Tsoga, A. Naoumidis, and P. Nikolopoulos. Wettability and Interfacial Reactions in the Systems Ni/YSZ and $Ni/Ti - TiO_2/YSZ$. *Acta Mater.*, 44: 3679–3692, 1996.

[100] E. A. G. Shillington and D. R. Clarke. Spalling Failure of a Thermal Barrier Coating Associated with Aluminum Depletion in the Bond-Coat. *Acta Mater.*, 47:1297–1305, 1999.

[101] J. H. Park and R. N. Blumenthal. Thermodynamic Properties of Nonstoichiometric Yttria-Stabilized Zirconia at Low Oxygen Pressures. *J. Am. Ceram. Soc.*, 72:1485–1487, 1989.

[102] M. Hillert and T. Sakuma. Thermodynamic Modeling of the $c \rightarrow t$ Transformation in ZrO_2 Alloys. *Acta Metall. Mater.*, 39:1111–1115, 1991.

[103] J. Katamura and T. Sakuma. Thermodynamic Analysis of the Cubic-Tetragonal Phase Equilibria in the System $ZrO_2 - YO_{1.5}$. *J. Am. Ceram. Soc.*, 80:2685–2688, 1997.

[104] H. Kanda, Atushi Saiki, K. Shinozaki, and N. Mizutani. Formation Mechanism of Oxygen Deficient Region in Electrochemically Reduced Y-PSZ Crystal. *J. Ceram. Soc. Jap. (English Translation)*, 101:344–348, 1993.

[105] J. Janek and C. Korte. Electrochemical Blackening of Yttria-Stabilized Zirconia-Morphological Instability of the Moving Reaction Front. *Solid State Ionics*, 116:181–195, 1999.

[106] H. Solmon, J. Chaumont, C. Dolin, and C. Monty. Zirconium, Yttrium and Oxygen Self Diffusion in Yttria-stabilized Zirconia $Zr_{1-x}Y_xO_{2-\frac{x}{2}}$. *Ceram. Trans.*, 24:175–184, 1991.

[107] G. Wang and J. J. Lannutti. Chemical Thermodynamics as a Predictive Tool in the Reactive Metal Brazing of Ceramics. *Metal. Mater. Trans. A*, 26A:1499–1505, 1995.

[108] H. Inaba and H. Yokokawa. Analysis of Interfacial Reactions by the Use of Chemical Potential Diagrams. *J. Phase Equilib.*, 17:278–289, 1996.

[109] H. Yokokawa, T. Kawada, and M. Dokiya. Construction of Chemical Potential Diagrams for Metal-Metal-Nonmetal Systems: Applications to the Decomposition of Double Oxides. *J. Am. Ceram. Soc.*, 72:2104–2110, 1989.

[110] H. Yokokawa, N. Sakai, T. Kawada, and M. Dokiya. Chemical Thermodynamic Stabilities of the Interface. In S. P. S. Badwal, M. J. Bannister, and R. J. H. Hannik, editors, *Sci. Technolog. Zirconia V*, pages 752–763, Lancaster PA, 1993. Technomic Pub. Co.

[111] R. Metselaar and F. J. J. Van Loo. The Use of Phase Diagrams for The Study of Metal-Ceramic Interdiffusion. *Mater. Sci. Forum*, 34-36:413–420, 1988.

[112] X. L. Li, R. Hillel, F. Teyssandier, S. K. Choi, and F. J. J. Van Loo. Reactions and Phase Relations in the Titanium-Aluminum-Oxygen System. *Acta. Metall. Mater.*, 40:3149–3157, 1992.

[113] B.J. Lee and N. Saunders. Thermodynamic Evaluation of the Ti-Al-O Ternary System. *Z. Metallkd.*, 88:153–161, 1997.

[114] S. Turan. Reactions at Ceramic-Metal Intrfaces in Capacitor-Discharge Joined Ceramics. In *Materials Science Forum Vols. 294-296*, pages 345–348, Switzerland, 1999. Trans. Tech. Publications.

[115] J. V. Emiliano, R. N. Correia, P. Moretto, and S. D. Peteves. Zirconia-Titanium Joint Interfaces. In *Materials Science Forum. Vols. 207-209*, pages 145–148. Transtec Publications, Switzerland, 1996.

[116] J. Zhu, A. Kamiya, T. Yamada, W. Shi, K. Naganuma, and K. Mukai. Surface Tension, Wettability and Reactivity of Molten Titanium in Ti/Yttria-Stabilized Zirconia System. *Mater. Sci. Eng. A*, A327:117–127, 2002.

[117] K.-F. Lin and C.-C. Lin. Interfacial Reactions between Zirconia and Titanium. *Scripta Mater.*, 39:1333–1338, 1998.

[118] K.-F. Lin and C.-C. Lin. Transmission Electron Microscope Investigation of the Interface between Titanium and Zirconia. *J. Am. Ceram. Soc.*, 82:3179–3185, 1999.

[119] K.-F. Lin and C.-C. Lin. Interfacial Reactions between Ti-6Al-4V Alloy and Zirconia Mold During Casting. *J. Mater. Sci.*, 34:5899–5906, 1999.

[120] B. J. Lee, N. M. Hwang, and Lee H. M. Prediction of Interface Reaction Products Between Cu and Various Solder Alloys By Thermodynamic Calculation. *Acta Metall.*, 45:1867–1857, 1996.

[121] C. J. Smithells. *Smithells Metals Reference Book*. Butterworth Heinemann, 1992.

[122] J. S. Kirkarldy and D. J. Young. *Diffusion in the Condensed State*. The Institute of Metals, 1987.

[123] K. Suganuma, T. Okamoto, and M. Koizumi. Solid-state Bonding of Partially Stabilized Zirconia to Steel with Titanium Interlayer. *J. Mater. Sci. Lett.*, 5: 1099–1100, 1986.

[124] R. N. Correia, J. V. Emiliano, and P. Moretto. Microstructure of Diffusional Zirconia-Titanium and Zirconia-(Ti-6 wt%Al-4 wt%V) Alloy Joints. *J. Mater. Sci.*, 33:215–221, 1998.

[125] N. Shinozaki, M. Suenaga, and K. Mukai. Wettability of Zirconia and Alumina Ceramics by Molten Zinc. *Mater. Trans., JIM*, 40:52–56, 1999.

[126] X. M. Xue, J. T. Wang, and Z. T. Sui. Wettability and Interfacial Reaction of Alumina and Zirconia by Reactive Silver-Indium Base Alloy at Mid-temperatures. *J. Mater. Sci.*, 28:1317–1322, 1991.

[127] C. Peytour, F. Barbier, O. Berthet, and A. Revcolevschi. Characterization of Aluminum Oxide/TA6V and Zirconium Dioxide/TA6V Ceramic-Metal Interfaces. *J. Phys., Colloque 1*, pages 897–902, 1990.

[128] T. Yamazaki and A. Suzumura. Monitoring of Reactive Metal's Diffusion and Reaction at $Ag - Cu - Ti/ZrO_2 Brazed Interface$. *Mater. Trans., JIM*, 37: 1103–1108, 1996.

[129] T. H. Chuang, M. S. Yeh, and Y. H. Chai. Brazing of Zirconia with AgCuTi and SnAgTi Active Filler Metals. *Metall. Mater. Trans. A*, 31A:1591–1597, 2000.

[130] A. J. Moorhead and H.-E. Kim. Oxidation Behaviour of Titanium-containing Brazing Filler Metals. *J. Mater. Sci.*, 26:4067–4075, 1991.

[131] R. R. Kapoor and T. W. Eagar. Oxidation Behavior of Silver- and Copper-Based Brazing Filler Metals for Silicon Nitride/Metal Joints. *J. Am. Ceram. Soc.*, 72:448–454, 1989.

[132] D. Sciti, A. Bellosi, and L. Esposito. Bonding of Zirconia to Super Alloy with the Active Brazing Technique. *J. Eur. Ceram. Soc.*, 21:42–52, 2001.

[133] R. Arroyave and T. W. Eagar. Metal Substrate Effects on the Thermochemistry of Active Brazing Interfaces. *Acta Mater.*, 51:4871–4880, 2003.

[134] C. J. Barry and G. L. Leatherman. The Effects of Brazing Temperature on the Strength of Ceramic to Metal Seals. *British Ceram. Trans.*, 91:83–85, 1992.

[135] J. J. Stephens, P.T. Vianco, P.F. Hlava, and C. A. Walker. Microstructure and Performance of Kovar/alumina Joints made with Silve-Copper Base Active Metal Braze Alloys. In *Advanced Brazing and Soldering Technologies*, pages 240–251, Metals Park, OH, USA, 2000. ASM International.

[136] T. W. Kim, H. Chang, and S. W. Park. Mechanical Properties of Silicon Nitride/Steel Joint with Ni-interlayer. In *Ceramic Engineering and Science Proceedings*, pages 843–848, USA, 2002. American Ceramic Society.

[137] L. A. Bucklow. Ceramic/Metal Bonding: a Study of Joining Zirconia to Cast Iron, and Silicon Carbide to Steel. *TWI Journal*, 2:129–162, 1993.

[138] S. Jonsson. Assessment of the Fe-Ti System. *Metall. Mater. Trans. B*, 29B: 361–370, 1998.

[139] L Kaufman. KP Public Binary Thermodynamic Data Base. Technical report, Thermocalc, AB, ca. 1970.

[140] P. Bellen, H.C. Hari Kumar, and Wollants P. Thermodynamic Assessment of the Ni-Ti Phase Diagram. *Z. Metallkd.*, 87:972–978, 1996.

[141] C. Servant, B. Sundman, and O. Lyon. Thermodynamic Assessment of the Cu-Fe-Ni System. *CALPHAD*, 25:79–95, 2001.

[142] B. Sundman, B. Jansson, and J. O. Andersson. The Thermo-Calc Databank System. *CALPHAD*, 9:153–90, 1985.

[143] J. O. Andersson and J. Ågren. Models for Numerical Treatment of Multicomponent Diffusion in Simple Phases. *J. Appl. Phys.*, 72:1350–1355, 1992.

[144] J. O. Andersson, T. Helander, L. Hoglund, P. Shi, and B. Sundman. Thermo-Calc and DICTRA, Computational Tools for Materials Science. *CALPHAD*, 26:273–312, 2002.

[145] H. Zhou and R.-N. Singh. Kinetics for the Growth of Silicon Carbide by the Reaction of Liquid Silicon and Carbon. *J. Am. Ceram.*, 78:2456–2462, 1995.

[146] Y. Paransky, L. Klinger, and I. Gotman. Kinetics of two-phase Layer Growth during Reactive Diffusion. *Mater. Sci. Eng. A*, A270:231–236, 1999.

[147] J. W. Cahn and J. E. Hilliard. Free Energy of a Nonuniform System I. Interfacial Free Energy. *J. Chem. Phys.*, 28:258–267, 1958.

[148] J. W. Cahn. On Spinodal Decomposition. *Acta Metall.*, 9:795–801, 1961.

[149] T. Torvund, Ø. Grong, O. M. Akselsen, and M. Ulvensøen. A Model for Coupled Growth of Reaction Layers in Reactive Brazing of ZrO_2-Toughened Al_2O_3. *Metall. and Mater. Trans. A*, 27A:3630–3638, 1996.

[150] B. J. Lee and K. H. Oh. Numerical Treatment of the Moving Interface in Diffusional Reactions. *Z. Metallkd.*, 87:195–204, 1996.

[151] R. W. Balluffi, S. M. Allen, and W. C. Carter. *Kinetic Processes in Materials*. John Wiley & Sons, New York, 2002.

[152] R. E. Collins. *Mathematical Methods for Physicists and Engineers*, chapter 12, page 290. Dover Publications, 1999.

[153] E. Fischer. Thermodynamic Calculation of the O-Ti System. *J. Phase Equilib.*, 18:338–343, 1997.

[154] I. Loginova, J. Odqvist, G. Amber, and J. Ågren. The Phase-Field Approach and Solute Drag Modeling of the Transition $\gamma \rightarrow \alpha$ Transformation in Binary $Fe - C$ alloys. *Acta Mater.*, 51:1327–1339, 2003.

[155] S. M. Allen and J. W. Cahn. Microscopic Theory for Antiphase Boundary Motion and its Application to Antiphase Domain Coarsening. *Acta Metall.*, 27: 1085–1095, 1979.

[156] J. Unnam, R. N. Shenoy, and R. K. Clark. Oxidation of Commercially Pure Titanium. *Oxid. Met.*, 26:231–251, 1986.

[157] A. E. Jenkins. A further Study of the Oxidation of Titanium and its Alloys at High Temperatures. *J. Inst. Met.*, 82:213–221, 1955.

[158] T. Hurlen. Oxidation of Titanium. *J. Inst. Met.*, 89:128–136, 1960.

[159] J. W. Martin, R. D. Doherty, and B. Cantor. *Stability of Microstructure in Metallic Systems*. Cambridge University Press, United Kingdom, 1997.

[160] L. Lavisse, D. Grevey, C. Langlade, and B. Vannes. The Early Stage of Laser-induced Oxidation of Titanium Substrates. *Appl. Surf. Sci.*, 186:150–155, 2002.

[161] J. W. Rogers, K. L. Erickson, D. N. Belton, R. W. Springer, T. N. Taylor, and J. G. Beery. Low Temperature Diffusion of Oxygen in Titanium and Titanium Oxide Films. *Appl. Surf. Sci.*, 35:137–152, 1988-89.

[162] E. Metin and O. T. Inal. Kinetics of Layer Growth and Multiphase Diffusion in Ion-Nitrided Titanium. *Met. Trans. A*, 20A:1819–1832, 1989.

[163] H. A. Wriedt and J. L. Murray. The N-Ti (nitrogen-titanium) System. *Bull. Alloy Phase Diagrams*, 8:378–388, 1987.

[164] H. Othani and M. Hillert. Thermodynamic Assessment of the N-Ti System. *CALPHAD*, 14:289–306, 1990.

[165] C. M. Bishop. *Continuum Models for Intergranular Films in Silicon Nitride and Comparison to Atomistic Simulations*. PhD thesis, Massachusetts Institute of Technology, 2003.

[166] T. Nishizawa. Progress of CALPHAD. *Mat. Trans. JIM*, 33:713–722, 1992.

[167] B. Sundman and J. Ågren. A Regular Solution Model for Phases with Several Components and Sublattices, Suitable for Computer Calculations. *J. Phys. Chem. Solids*, 42:297–301, 1981.

[168] M. Hillert. *Phase Equilibria Phase Diagrams and Phase Transformations. Their Thermodynamic Basis*, chapter 3, page 71. Cambridge University Press, 1998.

[169] M. Hillert. The Compound Energy Formalism. *J. Alloys Compd.*, 320:161–176, 2001.

[170] M. Hillert, B. Jansson, B. Sundman, and J. Ågren. A two-sublattice Model for Molten Solutions with Different Tendency for Ionization. *Metall. Trans. A*, 16A:261–266, 1985.

[171] David Dussault. Personal Communication, 2001. MIT.

[172] J. White. Lectures on Intruduction to Simulation, 2001. MIT.